Orsay
N° d'ordre: 184

UNIVERSITE PARIS XI

U.F.R. SCIENTIFIQUE D'ORSAY

THESE

présentée pour obtenir

le TITRE de DOCTEUR EN SCIENCES

par

Viatcheslav KOKOOULINE

Titre:

TRAITEMENT THÉORIQUE DES MOLECULES FROIDES: MISE AU POINT DE MÉTHODES NUMERIQUES.

Soutenue le 1er décembre 1999 devant la commission d'examen:

Mr	François AGUILLON	
Mr.	Olivier DULIEU	*Membre invité*
Mr	Jean-Michel LAUNAY,	*Rapporteur*
Mme.	Françoise MASNOU-SEEUWS	
Mr.	Valentin OSTROVSKY	
Mr.	Christophe SALOMON	*Président*
Mr.	Eberhard TIEMANN	*Rapporteur*
Mr.	Carl WILLIAMS	*Membre invité*

UNIVERSITE PARIS XI

U.F.R. SCIENTIFIQUE D'ORSAY

THESIS

submitted for

the DEGREE of DOCTOR IN SCIENCE

by

Viatcheslav KOKOOULINE

Title:

THEORETICAL APPROACH TO COLD MOLECULES: DEVELOPMENT OF NUMERICAL METHODS.

Defended 1 December 1999 before the Examination Commission

Mr	François AGUILLON	
Mr.	Olivier DULIEU	*Invited member*
Mr	Jean-Michel LAUNAY,	*Official referee*
Mme.	Françoise MASNOU-SEEUWS	
Mr.	Valentin OSTROVSKY	
Mr.	Christophe SALOMON	*President*
Mr.	Eberhard TIEMANN	*Official referee*
Mr.	Carl WILLIAMS	*Invited member*

Remerciements.

Je voudrais tout d'abord exprimer ma profonde gratitude à Mme Françoise Masnou-Seeuws pour son sens pédagogique, pour les connaissances qu'elle m'avait transmises, pour son soutien permanent pendant toute la période de la thèse.

Je tiens vivement à remercier M. Valentin Ostrovsky qui m'a aidé et encouragé au début de la thèse. Grâce à Mme Françoise Masnou-Seeuws, M. Valentin Ostrovsky et la collaboration Franco-Russe, mon travail de recherche a été effectué au Laboratoire Aimé Cotton.

C'est difficile à estimer les connaissances que j'ai obtenues pendant des discussions avec Olivier Dulieu. Qu'il soit remercié aussi pour son extrême disponibilité et pour sa bonne volonté.

J'adresse ma reconnaissance également à M. Jean-Michel Launay et à M. Eberhard Tiemann pour avoir accepté d'être rapporteurs de cette thèse. Leur avis est particulièrement important pour moi. De même, je remercie MM. François Aguillon, Christophe Salomon et Carl Williams d'avoir accepté d'évaluer ma thèse et de participer au jury.

Je voudrais exprimer ma gratitude à toutes les personnes avec qui j'ai pu avoir des discussions fructueuses.

Notamment je voudrais faire ressortir la collaboration avec M. Ronnie Kosloff.

Je suis reconnaissant à Patrice Cacciani pour une partie des résultats de la thèse qui a été faite avec lui et grâce à lui.

Je remercie Vladimir Akouline et Igor Mourachko pour le soutien qu'ils m'apportaient.

A toute l'équipe des chercheurs, techniciens et administratifs du Laboratoire Aimé Cotton, mes vifs remerciements. Je suis particulièrement reconnaissant à M. Christian Colliex de m'avoir fait bénéficier au Laboratoire Aimé Cotton d'excellentes conditions de travail, ainsi qu'à Mme Jocelyne Sinzelle pour l'aide en informatique et à Claude Dion pour ses remarques et corrections.

Contents

1 Introduction. **9**

1.1 Photo-associative spectroscopy of homonuclear dimers 10
1.2 "Laser cooling" of molecules 15
1.3 Heteronuclear alkali diatoms 16
1.4 Theoretical techniques for cold diatoms 17
1.4.1 Time-independent methods 17
1.4.2 Time-dependent methods. The Chebyshev polynomial expansion method 18
1.5 Organization of the Thesis 19

2 Mapped Fourier Grid Representation Method for Cold Collisions. **21**

2.1 Functions and operators in the FGR method 22
2.1.1 Expansion basis. Wave function on the grid 22
2.1.2 Exponential basis. Coordinate grid 24
2.1.3 Choice of the basis 26
2.1.4 Operators in FGR 27
2.1.5 Multi-channel potential. Example of two-channel potential. . . 30
2.2 Hermicity of the Hamiltonian in the basis of FGR. 31
2.3 Mapped FGR method for a long-range potential. 32
2.3.1 Mapping procedure 33
2.3.2 Transformation of the Hamiltonian 37
2.3.3 Mapping using R^{-3} and R^{-6} analytical potentials and a repulsive wall 38
2.3.4 Comparison of the numerical and the analytical mapping procedures 40
2.3.5 Occupation of the phase space domain after coordinate transformation 41
2.4 Mapping for Hamiltonian containing non-adiabatic coupling term . . 44
2.4.1 Reducing adiabatic Hamiltonian to hermitian matrix in FGR . 44
2.4.2 Application to the problem of bound states 46
2.4.3 Adiabatic basis: long-range potentials. Diabatization procedure 49
2.4.4 The numerical evaluation. An error estimation 51
2.5 Mapped time-independent FGR method for lifetime calculations . . . 51
2.6 Time-dependent FGR method. 52

2.6.1 General description 53
2.6.2 Chebyshev expansion 54
2.6.3 Hermicity in the time-dependent FGR method 55
2.6.4 Mapping 56
2.7 Mapped time-dependent FGR method for calculation of lifetimes. . . 57
2.8 Choice of the enveloping potential 60
2.9 Conclusion 65

3 Precision. Comparison with Other Methods. 67
3.1 Vibrational levels of Na_2 ($^1\Pi_g$). Comparison with the Numerov method. 67
3.2 Example of a wave function extending at long range: potential Cs_2 (1_g). 71
3.3 Wave function in the mapped FGR method. 71
3.4 Comparison of methods for calculations of lifetimes 75
3.4.1 Considering example 75
3.4.2 Time-dependent method 76
3.4.3 Time-independent method 78
3.4.4 Comparison of results 78
3.5 Conclusion 79

4 Photo-association Spectroscopy of Alkali Diatom near the Dissociation Limit. 81
4.1 Introduction 81
4.2 Perturbations in spectra 0_u^+ of Rb_2 and Cs_2. 84
4.2.1 Perturbations in the Rb_2 spectrum 84
4.2.2 Perturbations in the Cs_2 spectrum 100
4.3 Lifetimes of pre-dissociated levels of 0_u^+ symmetry of Rb_2 and Cs_2. . . 104
4.3.1 Rb_2 105
4.3.2 Cs_2 113
4.4 Conclusion 115

5 Other Applications of the Mapped Fourier Grid Method. 117
5.1 Tunneling in the Cs_2 0_g^- photo-association spectrum. 117
5.2 Symmetry breaking between $B^1\Pi_u$ and $1^1\Pi_g$ states in $^6Li^7Li$. 118
5.2.1 Introduction 118
5.2.2 The pre-dissociation through the potential barrier 119
5.2.3 Theoretical model for coupling between $B^1\Pi_u$ and $1^1\Pi_g$ states in $^6Li^7Li$. 121
5.2.4 Results of calculations 124
5.2.5 Comparison with the experiment 126
5.2.6 Conclusion 127

6 Conclusion and Perspectives. 129
6.1 Results obtained in the Thesis 130
6.2 Some perspectives 133
6.3 Résumé 135

A Classification and Calculation of Molecular Terms **139**
A.1 General scheme of the construction of molecular terms 140
A.1.1 Symmetry groups and quantum numbers of electronic states of the diatomic system 140
A.1.2 Molecular wave functions on large internuclear distance 141
A.2 Molecular terms of $nS + nP$ and $nP + nP$ alkali diatoms. 144
A.2.1 Quantum numbers 144
A.2.2 Transformation matrix between a and c bases. 145

B Adiabatic Schrödinger Equation for the Alkali Diatom **147**

C Article: *"Mapped Fourier methods for long-range molecules: Application to perturbations in the Rb_2 0_u^+ photo-association spectrum"* **153**

D Article: *"Theoretical treatment of channel mixing in excited Rb_2 and Cs_2 ultra-cold molecules. I Perturbations in (0_u^+) photoassociation and fluorescence spectra"*, **Submitted to Phys Rev. A** **167**

Chapter 1

Introduction.

During the last fifteen years, successful theoretical and experimental work have led to the creation of a new domain of atomic and molecular physics - the *cooling* and *trapping* of atoms using light and electro-magnetic fields. Cooling means that the mean energy (i.e. temperature, $E = kT$) of the kinetic motion of atoms becomes smaller. For example, in typical magneto-optical traps with cesium atoms, velocities of atoms are of the order of 0.1 cm/s ($\approx$ 100 μK), whereas at the room temperature atoms have velocities of about 200 cm/s. Part of the interest in cooling was stimulated by a large number of applications of cold atoms. At the fundamental level applications include high resolution photo-association spectroscopy (reviewed by J. Weiner *et al.* [142] and by W. C. Stwalley and H. Wang *et al.* [121]) and the study of collisions at ultra-low energies (several μK) [31, 41]. More practical applications include atomic clocks, atomic lasers and interferometers, the development of instruments for atomic optics and atomic lithography. An additional impressive phenomenon, recently experimentally observed is Bose-Einstein condensation [8, 23, 33].

The principle of trapping and cooling is based on the mechanical effect of light. The first theoretical and experimental works on the laser *trapping* of atoms were begun over 30 years ago. In 1968 V. Letokhov proposed that atom could be trapped in a light beam using the dipole force [80, 81]. He and his coworkers defined a so-called Doppler limit of laser *cooling* of atoms [82] – a temperature minimum, determined by the heating due to the spontaneous emission into a lower state. The first proposal to cool neutral atoms in counter-propagating laser beams was made by T.W.Hänsch and A. L. Schawlow in 1975 [49]. At the same time, a similar proposal was put forward by D. J. Wineland and H.G. Dehmelt [143], to be used for ions in ion traps. Hänsch and Schawlow proposed to cool neutral atoms in pairs of counter-propagating laser beams detuned slightly below a resonance transition of the atoms.

Alkali atoms were the first species to be trapped and cooled to ultra-low temperature due to their relatively simple structure. The method of the laser cooling, proposed by Hänsch and Schawlow, was experimentally carried out first by S. Chu in 1985 [26]. S. Chu used six red-shifted laser beams in order to stop sodium atoms

(see Fig. 1.1). This type of cooling was called Doppler cooling. Another method was

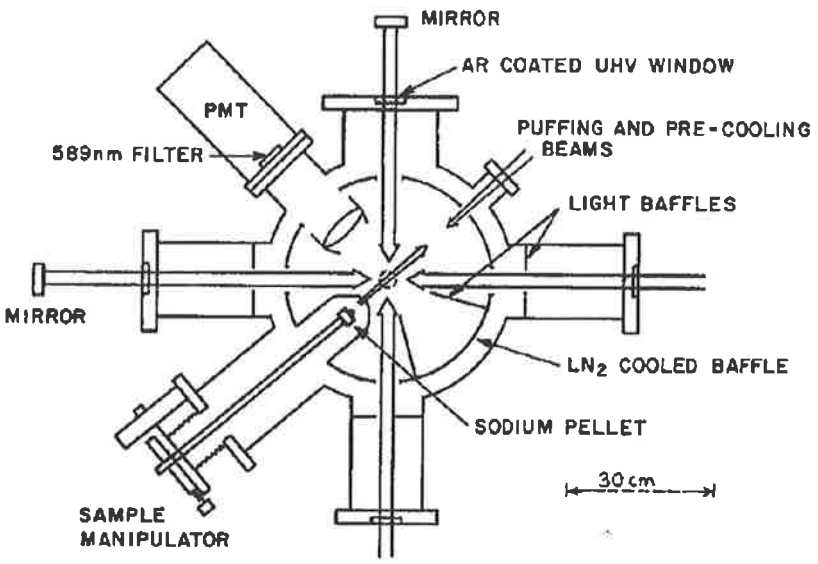

Figure 1.1: The first experiment using the Doppler cooling. Schematic drawing of the vacuum chamber, intersecting laser beams and atomic beam [145].

proposed by W. Phillips *et al.* [19]. W. Phillips using Zeeman slower and optical molasses obtained a temperature of about 40 μK for Na atoms. This temperature was lower than the Doppler limit. The explanation of this effect and further development was made by C. Cohen-Tannoudji *et al.* [28]. This polarization gradient cooling below the Doppler limit, is limited by the recoil energy of a single photon. It was called the Sisyphus cooling. In 1987 J. Dalibard from the École Normale first proposed a "magneto-optical" trap, using a weak magnetic field and circularly polarized light. After that the magneto-optical trap has become the most widely used setup for the cooling. The subsequent works by Cohen-Tannoudji, A. Aspect, E. Arimondo, R. Kaiser, N. Van-Steenkiste, C. Salomon [9, 10, 29, 60, 10] led to the creation of another ingenious cooling scheme based on velocity-selective optical pumping of atoms into a non-absorbing coherent superposition of states (so-called "dark" state). Using this method helium atoms were cooled to a temperature of 0.25 μK.

1.1 Photo-associative spectroscopy of homonuclear dimers

One of the most impressive experimental achievements carried out on trapped and cooled atoms is photo-association spectroscopy (PAS).

The principle of PAS is based on possibility for two free atoms to absorb one photon being excited into a bound molecular state (see, for example, Ref. [142] and Fig. 1.2). The reaction for a pair of identical ground-state atoms A can be written

in a form:

$$A(nS) + A(nS) + \omega_b \rightarrow A_2(\Omega_{g,u}(nS, nP_{1/2,3/2}); \nu, J) \tag{1.1}$$

where the frequency ω_b is smaller than the resonant atomic transition $nS \rightarrow nP$ frequency ω_a. The energy difference $\omega_a - \omega_b$ defines the bound energy of vibrational level (ν_b, J) (Fig. 1.2):

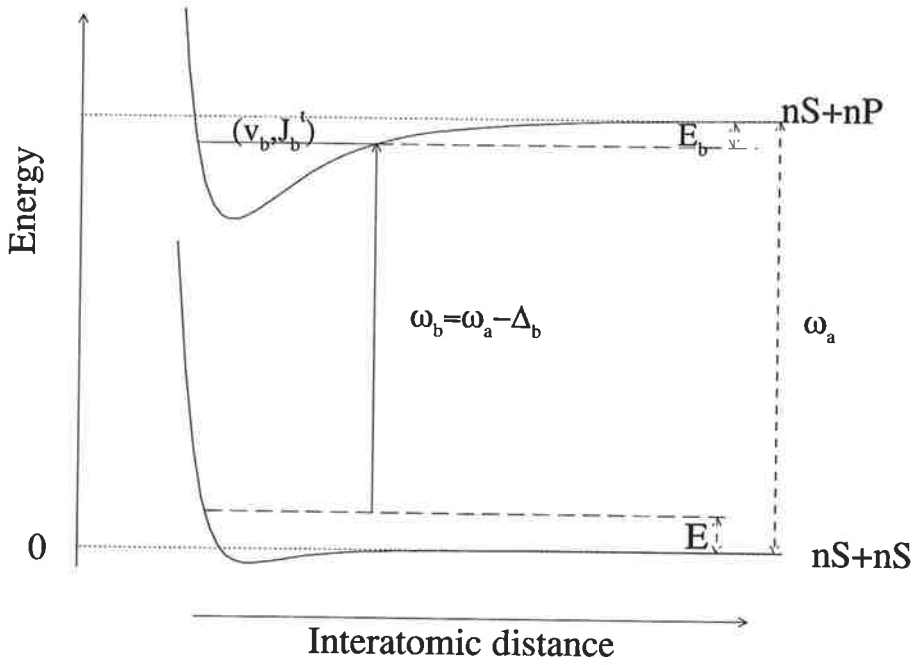

Figure 1.2: The photo-association scheme. The energy ω_a corresponds to the atomic transition $nS \rightarrow nP$. Photon ω_b ($\omega_b < \omega_a$) is the photo-association step. It populates a ro-vibrational level ν_b, J_b of the upper molecular state $nS + nP$ starting from the two free atoms with the asymptotic kinetic energy E.

$$\omega_a - \omega_b = E_b + E \tag{1.2}$$

where E is a relative asymptotic kinetic energy of two ground atoms. By scanning the frequency ω_b, different vibrational levels (ν_b, J) can be populated. The resolution of photo-association experiment is limited by the width of the statistical distribution of E. For a gas of atoms in a thermal equilibrium at temperature $300K$, the width is of order 200 cm^{-1}; at temperature about 100 μK the width is of order 1 MHz [106]. At this temperature (100 μK), the statistical distribution width become comparable and even smaller than the natural width. For example, for rubidium, the natural width of the $^1\Sigma_u$ $(5S + 5P)$ state is 12 MHz.

Since the method of laser (Doppler) cooling works for two-levels atoms, the best experimental realization of the ideal two-level system is provided by alkali atoms. The ground state ns and the first excited state np of a single electron in alkali atoms give the two-level system. Therefore, in most cases, photo-association experiments

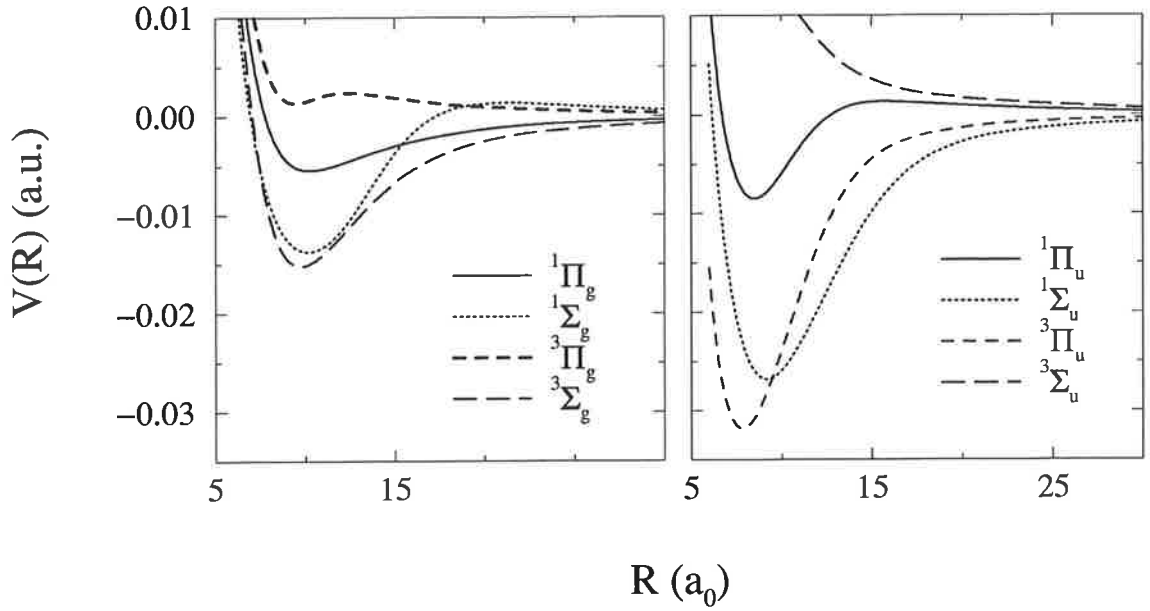

Figure 1.3: Potential curves of Rb_2 correlated to the $5S + 5P$ dissociation limit of free atoms, calculated without the spin-orbit interaction. (Calculated by Foucrault *et al.* [43] at small distances and by M.Marinescu and A.Dalgarno [92] at large distances.)

are able to investigate molecular states of alkali dimers, which have dissociation limits corresponding to $nS + nP$ and $nP + nP$ free atoms.

The potential curves of all homonuclear alkali molecules are very similar. Figure 1.3 shows all potential curves of Rb_2 having the $5S + 5P$ dissociation limit. A difference between various alkali atoms that plays an important role in the behavior of related molecules is the the spin-orbit splitting of the np electronic state. It gives two different dissociation limits of the $nS + nP$ molecule. The spin-orbit splitting is large for heavy alkali atoms, Rb and Cs where it should be taken into account. Figure 1.4 shows the potential curves for Rb_2 calculated after account for the spin-orbit coupling.

The first experiments with free-bound photo-absorption were carried out before the development of laser cooling [112, 55]. In those experiments the population of the initial free state was very broad due to high temperature of ground-state atoms. As a result the fluorescence spectrum obtained was not very selective. One way to improve the selectivity would be to use slow ground-state atoms in a PAS experiment. H. Thorsheim *et al.* were the first who proposed to use trapped and cooled atoms for the free-bound spectroscopy [126]. In that paper many features of PAS were predicted: (1) precision measurement of rotational-vibrational progression from which accurate potentials could be determined, (2) line profile measurements, (3) spectral intensity modulation from which the ground-state potential and the scattering length could be determined. In next several years many experimentalists investigated these

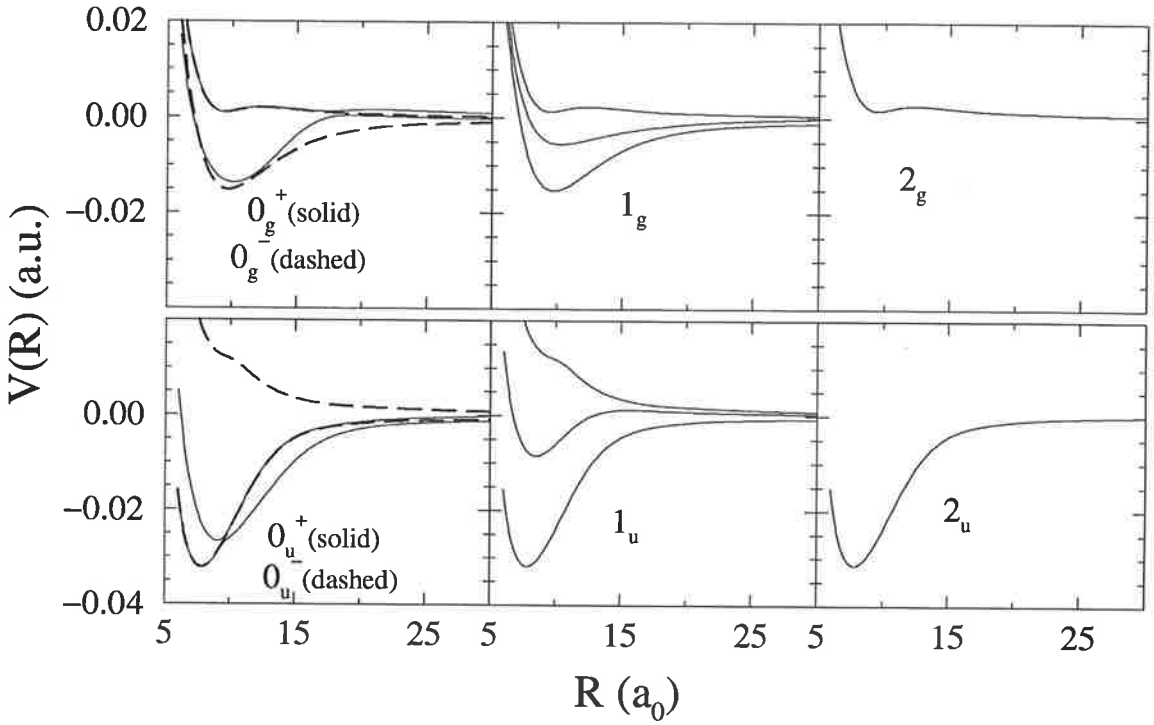

Figure 1.4: The Rb_2 potential curves calculated from curves presented on the Fig. 1.3 with accounting of the spin-orbit coupling (details of calculations are in the Appendix).

PAS features. The breakthrough in PAS and PAI experiments was achieved by two separated experiments by P. Lett *et al.* [83] using sodium in a magneto-optical trap (MOT) and by Miller *et al.* [51] in a far-off-resonance optical trap (FORT) [96] using rubidium atoms in 1993.

In the photo-association experiment [83] with **Sodium**, two regular progression were observed, corresponding to different vibrational levels of single excited potential curve of Na_2 molecule correlated to the $3S + 3P_{3/2}$ limit of free atoms. These series were attributed to 1_g and 0_u^+ potential curves. The experiment allowed to determine these potential curves with high accuracy. Since the long-range potentials correlated to the $3S + 3P_{3/2}$ limit have the asymptotic behavior C_3/R^3, the experimental spectral series can serve for determination of coefficients C_3, using the law of Leroy-Bernstein [78]. In 1994 Ratliff *et al.* [109] improved the experiment [83] using so-called "dark-spot" MOT [63] and increasing the ionic signal by two orders of magnitude. This experiment revealed new series of $3S + 3P_{3/2}$ manifold attributed to 1_g, 0_u^+ and 0_g^- vibrational series. Due to their high experimental resolution the rotational and hyperfine structure was observed as well. Furthermore, in this experiment it was shown that measurements of the fluorescence loss during the trap phase and measurements of the ionization production can serve to better attribute different peaks in the spectra [142].

In the experiment of Miller *et al.* [51] with **Rubidium** another interesting feature was revealed. The spectrum exhibits slow oscillations of line intensities. The transi-

tion probability for PA is defined by the matrix element of dipole transition moment. The latter is governed by the overlap of ground state and excited state wave functions. The main contribution to this overlap is given by the outer turning point R_c of the nuclear wave function in the excited potential. If the wave function of ground state has a maximum at this internuclear distance, then the transition probability is large. If the ground-state wave function has a node at $R = R_c$, then the transition probability is small. Thus the oscillations of transition probability reflect nodes and anti-nodes of the scattering wave function [126, 142]. By scanning the excitation frequency one can obtain the shape of the ground state wave function. In particular, the scattering length can be determined. In an improved experiment (Heinzen *et al.*) [27] the C_3 coefficients were determined for the 1_g and 0_u^+ potentials.

The photo-association experiments with **Lithium** (^{6}Li and ^{7}Li) were performed by the Hulet group in 1995. C_3 coefficients, atomic lifetimes and scattering lengths were determined [1, 93]. The C_3 coefficient was defined with very high precision. In 1996 Abraham *et al.* [2] reported spectra with a resolved hyperfine structure for both isotopes.

The experiments with **Potassium** were carried out by the groups of Stwalley and Gould [135, 136, 139]. 0_g^-, 1_g and 0_u^+ series were identified in the obtained spectrum. Later, Wang *et al.* [137] reported a full study of the six long-range states of 0_u^+, 1_g and 0_g^- symmetries, three states dissociating to the $4S + 4P_{3/2}$ asymptote and other three states dissociating to the $4S + 4P_{1/2}$ asymptote. This authors determined C_3 constants, radiative lifetimes and reported also, for the first time, the pure long range 1_u state [138].

In 1998 the group of P. Pillet reported for the first time PAS experiments with **Cesium** [41] (see below). A spectrum of 0_g^- $(6S + 6P_{3/2})$ state was observed. The C_3 coefficient of 0_g^- $(6S + 6P_{3/2})$ was defined as well. More recently, several papers [42, 31] reported the 1_u, 1_g, 0_u^+ PA spectra of Cs_2, $(6S + 6P_{3/2})$. An accurate RKR potential 0_g^- $(6S + 6P_{3/2})$ has been determined using the experimental data.

Recently, the first results of PAS experiments with polarized **Hydrogen** were published [101]. The group from Utrecht reported the first experiment with cold meta-stable **Helium** atoms [144]. They observed for the first time vibrational levels in $He^*(2^3S)$.

Another feature present in PA spectra is the broadening of spectral lines caused by various pre-dissociation processes. The loss of atoms from the trap is connected to finite lifetimes of excited molecular state. In many cases the mechanism of the trap loss is not well described theoretically. Among the experiments with the trap loss and measurements of line widths are direct measurements of fine-structure collision losses of Cs [40], isotopic difference in trap loss collisions [134], pre-dissociation of 0_u^+ $(5S + 5P_{3/2})$ of Rb_2 [27] and K_2 [139].

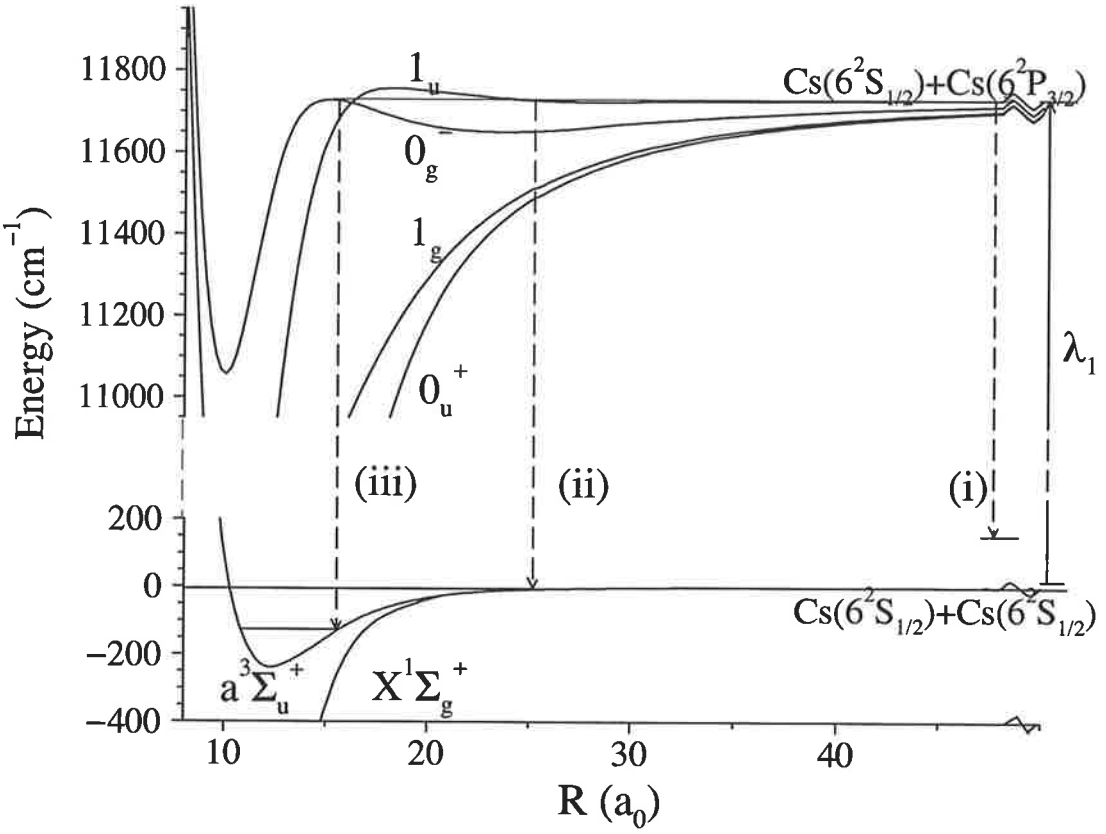

Figure 1.5: Diagram of the Cs_2 optical transitions and molecular states relevant for the photoassociation experiment. The vibrational level shown represents schematically a level of one of the four curves. Spontaneous emission leads to: (i) trap-loss by desexcitation in two free atoms occurring from the four curves. (ii) and (iii) formation of translationally cold molecules in the $X^1\Sigma_g^+$ and $a^3\Sigma_u^+$, by desexcitation of the 1_u and 0_g^- states respectively. (Taken from [42])

1.2 "Laser cooling" of molecules

With the development of laser cooling techniques and PAS, it became possible to observe and study cold molecules. Despite the great progress, the technique of atoms cooling cannot be applied to molecules directly. The direct cooling of molecules remains a difficult problem, mostly because of enhanced spectral complexity of molecules and multiple spontaneous decay channels. Excited molecules have many more decay channels. All these channels must be re-pumped again into the excited state. It requires many different laser frequencies [13, 31]. The situation is similar to cooling of atoms with hyperfine structure, when one needs an additional laser frequency in order to re-pump non-resonant hyperfine level to which the spontaneous emission from the excited level occurs.

Translationally cold molecules were reported for the first time [41] in the **Cesium** trap at the temperature about $300\mu K$ (corresponding to the velocity 13 cm/s). The originality of the experiment was in detection of Cs_2^+ molecular ions by photoionization of Cs_2 triplet ground state molecules, produced by spontaneous decay of

the excited molecular state formed by photo-association. The experimental scheme is shown in figure 1.5. The formation of cold ground-state molecules in this experiment is favored due to the particular shape of the 0_g^- and 1_u potential curves (see the figure). These curves have the second shallow well at distances about 25 a_0. Therefore they also possess a Condon point at intermediate internuclear distances (near $15 - 18$ a_0) [42] that favours spontaneous emission to the ground molecular state (arrows *ii* and *iii* in Fig. 1.5).

Later on several experiments were reported with the cold molecules produced in different ways.

Knize *et al.* observed cold cesium molecules formed not by photo-association, but by the trap laser. The number of molecules was very small, about 20-30. The molecules stayed in the trap for 0.5 s. [122].

The group of Stwalley reported the observation of ultra-cold ground-state **Potassium** molecules [103]. For potassium, the intermediate Condon point is situated at very large distances. However, using the fact that K_2 spectroscopy is very well known, the authors could predict for which transition $0_u^+ \rightarrow {}^1\Sigma_g^+$ the Franck-Condon factor is favourable. They could observe cold molecules in the ground molecular state ${}^1\Sigma_g^+$.

C. Gabbanini *et al.* have initiated experiments with **Rubidium** atoms.

The future research in cooling of molecules involves several aspects: 1) improving and optimizing formation of ultra-cold molecules; 2) trapping cold molecules; 3) cooling the internal degrees of freedom; 4) achieving non-destructive techniques of detection; 5) working toward realization of a Bose-Einstein condensate of molecules. The feasible applications of ultra-cold molecules are in metrology, chemistry, interferometry of molecules, and a molecular laser. In order to realize these programs one needs to develop new theoretical and computing techniques.

1.3 Heteronuclear alkali diatoms

Another promising direction is the possibility to trap and study heteronuclear systems. Heteronuclear diatoms are interesting because they have a permanent dipole moment, that allows to trap them by an electrostatic field. Another particularly important difference is that the interaction of a ground-excited-state heteronuclear pair lacks the long-range resonant dipole contribution ($V \approx C_3/R^3$) which plays a decisive role in the homonuclear case. Instead, the long-range part of the heteronuclear pair potential is generally dominated by a comparatively shorter range interaction ($V \approx C_6/R^6$ or C_8/R^8, for example). One consequence of this difference is that the absorption of the photo-associating photon occurs at a much smaller internuclear spacing (R_{ex}) for a heteronuclear as compared to a homonuclear pair. In the photo-association experiment with Na_2 one has $R_{ex} \approx 1800$ a_0, whereas for NaCs the separation R_{ex} is estimated as $\approx 40 - 100$ a_0 in case of 10 MHz detuning from the resonant frequency [116]. Some experiments with heteronuclear alkali atoms have been published. Weidemüller *et al.* reported their observation of cold collisions in lithium-cesium MOT [113]. In the experiment of J. Shaffer *et al.* [116] NaCs cold

collisions have been observed. The theoretical study of heteronuclear systems in the context of PAS was presented by Stwalley *et al.* [140].

1.4 Theoretical techniques for cold diatoms

In many cases theoretical description of cold diatomic systems within the Born-Oppenheimer approximation can be subdivided in two parts: 1) definition of potential curves in this approximation and 2) simulation of dynamics on these potentials. The first problem is beyond of the scope of the present thesis. There are two approaches to the second problem corresponding to two forms of the Schrödinger equation: time-independent and time-dependent.

The time-independent method is used for many physical problems, in particular, for calculation of bound states, resonances and lifetimes, wave functions of bound and pre-dissociated states (this is considered in the present thesis). The time-dependent approach is generally applied when a subject of interest is the temporal evolution of an initial state. But the same approach can be used also for calculation of bound states and wave function, resonances and lifetimes.

1.4.1 Time-independent methods

There are many different numerical methods for integration of the Schrödinger equation. Among the most commonly used, the Runge-Kutta methods [146] for numerical integration of ordinary differential equations are popular because of their simplicity and efficiency (see, for example, the book by M. Abramowitz and I. Stegun [3]). The Numerov [146] method is also frequently used (see, for example, the book by W.Press *et al.*, [108]). This is a two-step, fifth order predictor-corrector method for a second-order ordinary differential equation. The Numerov method was found to be more precise for this problem than the Runge-Kutta methods. In both Runge-Kutta and Numerov methods the variable step in coordinate can be introduced in order to adapt it to fast or slow variation of the integrand. A variable step was introduced in the Numerov method by Simos and Mousadis [118, 119] and by Coté and Jamieson [32]. Runge-Kutta and Numerov methods are so-called **finite-order difference methods**. They are based on a local polynomial approximation of the function and therefore the convergence of these methods follows a power low Δx^n, where Δx is a grid step and n is the order of the finite difference approximation. Due to their *local* character, the finite difference methods usually need grids with very large number of points.

An alternative to the Numerov method is the method of the variational matrix representation in which an orthonormal basis of N functions is used, and variational coefficients are determined by diagonalization. In this variational basis representation (VBR), the operators are represented in terms of their projections onto a basis of L^2 functions. The eigenvalues of truncated $(N \times N)$ matrix are usually determined by diagonalization.

In 1982-1984 J. Light *et al.* [85, 86] have developed the Discrete Variable Representation (DVR) method. The method is based on the representation of the wave function on a grid of points, and in the same time, a unitary transformation maps N functions to a unique set of N points. The DVR basis is constructed in such a way that the amplitudes of a wave function on grid points directly give expansion coefficients of the wave function over the related basis. Thus the DVR method includes some properties of Numerov method and VBR method. All operators in DVR are represented by matrices $N \times N$ (as it is in VBR method) where N is a number of grid points. Eigenvalues and eigenfunctions of a multichannel potential are defined by a simple diagonalization of the Hamiltonian matrix. In some sense, both DVR and VBR methods are isomorphic - the DVR grid can be "constructed" from the VBR basis. In 1983-1993 R. Kosloff and D. Kosloff ([67, 68, 70]) reported a special case of VBR methods - the Fourier grid representation (FGR) method, where the basis of of exponential functions was employed. The great advantage of the method is the simple connection between the truncated L^2 basis of functions and equally spaced grids in coordinate spaces. The transformation between split spaces (between grids) is carried out by a discrete Fourier transform. Now the FGR method is widely used (see, for instance, [30, 35, 127, 34, 99, 100]). In application to the time-independent Schrödinger equation it is referred to as the Fourier Grid Hamiltonian method [35].

1.4.2 Time-dependent methods. The Chebyshev polynomial expansion method

When solving the time-dependent Schrödinger equation in most cases one employs the second-order difference, split operator propagation, Chebyshev polynomial expansion or Lanczos method. The brief description together with comparative discussion of precision and efficiency of these methods can be found in [77, 98].

One of the most frequently used methods is the split operator method. It is based on the fact that in most cases the Hamiltonian $\mathbf{H}$ can be split into two non-commuting parts with a simple transformation between them, namely the kinetic energy term $\mathbf{T}$ and the potential term $\mathbf{V}$ [77]. The time-propagation operator $U(\Delta t) = \exp(-i\mathbf{H}\Delta t)$ in this case is presented as a product of three operators:

$$U(\Delta t) = \exp(-\frac{i}{2}\mathbf{T}\Delta t)\exp(-i\mathbf{V}\Delta t)\exp(-\frac{i}{2}\mathbf{T}\Delta t)\ . \tag{1.3}$$

The kinetic part of the Hamiltonian is diagonal in the momentum space, the potential is diagonal in the coordinate representation. Therefore, the propagation operator $U(\Delta t)$ can be easily evaluated by the matrix multiplication. The transformation between the configuration and the momentum spaces are performed by the Fourier transformation.

The Lanczos method is recommended for time-dependent potentials. It is a short-time propagation scheme. It does not impose any restriction on the form of the Hamiltonian [77, 98].

Among the time-dependent methods the most precise one is expansion of propagator over Chebyshev polynomials as proposed by R. Kosloff and H. Tal-Ezer in series of papers [123, 71, 72]. Later E. Fattal and R. Kosloff [72] proposed to adapt the working grid in order to improve distribution of points over the grid. They used an analytical transformation of the coordinate (the mapping). The mapping was applied to the time-dependent and time-independent Schrödinger equations. Such a mapped grid was used for solution of the Coulomb problems with a singularity. The multi-dimensional version of the Fourier grid representation method is also discussed in Ref. [72].

1.5 Organization of the Thesis

The subject of this thesis is a further development of both time-independent and time-dependent approaches adapted for diatomic systems when the energy is close (below and above) to the molecular dissociation limit. As an applications, the thesis discusses the most typical problems of the theoretical interpretation of experiment with cold diatoms: calculations of bound levels for one- or multi-channel potentials, calculations of lifetimes and resonances of pre-dissociated vibrational levels, simulation of dynamics of cold atom collisions.

The thesis is organized as follows. Chapter 2 describes the Mapped Fourier Grid Representation (MFGR) method. The method is adapted for calculation of bound levels for a multi-channel potential in diabatic and adiabatic representation. By introducing the absorptive potential into the method we are able to calculate lifetimes of pre-dissociated vibrational levels. Further on, the method is used for solution of the time-dependent Schrödinger equation. It is demonstrated that the mapped time-dependent techniques is an efficient tool for simulation of dynamics of slow atomic collisions. The lifetimes are calculated by two methods: by the time-dependent method and by the time-independent method with an absorptive potential. This allows us to verify the applicability of both approaches.

Chapter 3 is devoted to the accuracy of the developed techniques (time-dependent and time-independent) method and to the comparison with other methods.

In chapter 4 the techniques are applied to various problems. The bound levels of 0_u^+ symmetries of Cs_2 and Rb_2 diatoms are calculated. It is found that for this symmetry small variation of the molecular fine structure coupling can have strong effect of the perturbations in the spectrum. These perturbations are investigated and parameterized using the Multichannel Quantum Defect theory. Lifetimes of pre-dissociated levels of the 0_u^+ symmetry of Rb_2 and Cs_2 are determined with two methods – by the time-independent method with the absorptive potential and by the time-dependent method using the Chebyshev propagator. We find strong isotopic difference in lifetimes of pre-dissociated levels of 0_u^+ symmetry for two isotopes: $^{85}Rb_2$ and $^{87}Rb_2$.

Chapter 5 describes another application. The symmetry breaking between $^1\Pi_u$ and $^1\Pi_g$ states of $^6Li^7Li$ observed in the experiment is explained using the developed

method and a simple model of coupling between $^1\Pi_u$ and $^1\Pi_g$ molecular states.

The Appendix contains description and calculation of potential curves of $nS+nP$-symmetry with the spin-orbit coupling and some features of diabatic and adiabatic representations of the Schrödinger equation.

Chapter 2

Mapped Fourier Grid Representation Method for Cold Collisions.

As discussed in the Introduction, the Fourier grid representation (FGR) method is one of the most effective methods for solution of the Schrödinger equation. It is widely used for applications (for example, works by M. Monnerville and J. M. Robbe [99, 100], by O. Dulieu *et al.* [35]). The FGR method has many advantages of both, finite-order difference and VBR, methods. The FGR method represents the wave function by coefficients of expansion over basis functions as in VBR method. At the same time these coefficients represent values of the wave function on the coordinate grid, as in the Numerov-type methods. As a result, the Hamiltonian is represented by a matrix, but the elements of the matrix are related to the values of the Hamiltonian on the grid. A second advantage of the FGR method is the choice of expansion functions (complex exponents) allows one to easily switch from momentum to coordinate representations of the wave function and vice versa. The third advantage is that, knowing the initial conditions of the problem and using properties of the representation by exponential basis, one can determine the number of basis functions and the accuracy of the representation by this basis prior to calculations. The disadvantage of the ordinary FGR method is the constant grid step. Since the step cannot be too big, a Hamiltonian with a long-range potential demands a grid with a large number of mesh points. Therefore it becomes virtually impossible to apply the FGR method to the problems of cold collisions and to calculation of bound vibrational levels for long-range potentials.

This chapter of the Thesis describes how the FGR method can be modified in order to include large internuclear separations into consideration. It is made by an adaptive coordinate transformation (or mapping) of the Schrödinger equation in such way that "local completeness" of the basis would be sufficient to correctly represent the wave function locally. In other words, the coordinate grid defined by the exponential basis with the mapping would be more dense in regions where wave function varies more rapidly. The mapping uniformly "distributes" the grid points between oscillations of

wave functions. It allows one to introduce a unique parameter of the points density, i.e. number of mesh points per oscillation (the $1/\beta$ parameter). This parameter defines *a priori* the accuracy of the calculation.

In section 2.1 the ordinary FGR method is described and the completeness of the Fourier basis is discussed. Section 2.2 is devoted to the hermicity of the matrix of the Hamiltonian in the Fourier grid representation. The hermicity of different terms in the Hamiltonian is discussed. After that in section 2.3 we develop the mapped FGR method for the Schrödinger equation in the diabatic basis. Section 2.4 describes the mapped FGR (MFGR) method for the adiabatic representation. The next section 2.5 is devoted to the time-independent calculation of lifetimes by using the mapped FGR method. Section 2.6 describes the mapped time-dependent FGR method that employs the Chebyshev expansion scheme. Section 2.7 applies it to calculation of lifetimes. The last section 2.8 describes how the mapping must be chosen. The enveloping potential is introduced in order to make the proper choice.

2.1 Functions and operators in the FGR method

This section briefly reviews the Fourier grid method for representing the wave functions. The scheme presented here, was developed mainly by R. Kosloff in 1983-1993 [70]. The FGR method can be considered as a special case of the General Collocation Scheme [70] or Discrete Variable Representation (DVR) [85]. Functions are represented on grid points. On the other hand, FGR method is also a special case of the Variable Basis Representation (VBR) with the exponential functional basis. We describe a general scheme for representing functions and operators on a grid.

2.1.1 Expansion basis. Wave function on the grid

An approximation of a wave function $\psi(R)$ by a finite set of N_f analytical linear-independent functions $g_n(R)$ is given by formula

$$\psi(R) \approx \bar{\psi}(R) = \sum_{n=1}^{N_f} a_n g_n(R) \ . \tag{2.1}$$

The wave function is represented by the N_f-component vector of coefficients a_n.

If the wave function $\psi(R)$ is represented on a grid of N_g points R_j $(j = 1, \ldots N_g)$, then at grid points one has

$$\psi(R_j) = \bar{\psi}(R_j) = \sum_{n=1}^{N_f} a_n g_n(R_j) \ , \tag{2.2}$$

or in the matrix form

$$\psi = \mathbf{G}a, \tag{2.3}$$

where ψ and a are N_f-component vectors, and $\mathbf{G}$ is $N_f \times N_g$ matrix:

$$\psi_j = \psi(R_j); \quad G_{j,n} = g_n(R_j) \ . \tag{2.4}$$

If $N_g = N_f = N$, the matrix $\mathbf{G}$ is invertible provided g_n are linear-independent. The coefficients a_n in a vector form are expressed as

$$\mathbf{a} = \mathbf{G^{-1}}\psi \ . \tag{2.5}$$

The two last equations demonstrate that descriptions of the vector ψ by coefficients a_n and by sampling points $\psi(R_j)$ are identical. In other words these descriptions are different representations of one discrete function ψ. The connection between these representation is provided by the matrix $\mathbf{G}$.

If the grid points are chosen so that the expansion functions obey the orthogonality relation:

$$\sum_{n=1}^{N_g} g_n^*(R_i) g_n(R_j) = \delta_{i,j} \ , \tag{2.6}$$

then according to Eq. (2.5) the coefficients a_n are calculated in a very simple way:

$$a_n = \sum_{j=1}^{N_g} \psi_n^*(R_j) g_n(R_j) \ . \tag{2.7}$$

If the basis set ψ_n $(n = 1, \ldots N_g)$ is orthogonal and normalized:

$$\int_{R_{min}}^{R_{max}} g_n^*(R) g_m(R) dR = \delta_{nm}, \tag{2.8}$$

then the scalar product of two wave-functions

$$\psi(R) = \sum_{n=1}^{N_g} a_n g_n(R) \ , \tag{2.9}$$

and

$$\phi(R) = \sum_{n=1}^{N_g} b_n g_n(R) \tag{2.10}$$

is expressed as

$$< \psi | \phi > = \sum_{j=1}^{N_g} \psi^*(R_j) \phi(R_j) \ . \tag{2.11}$$

One can consider linear space $\mathcal{G}$ constructed on the finite basis of L^2 functions defined on the grid. As a consequence of the orthogonality relations this space becomes a discrete vector space with a unitary transformation between the discrete sampling points R_j and the discrete functional basis g_n.

2.1.2 Exponential basis. Coordinate grid

In the Fourier grid method the expansion basis $\{g_k(R)\}$ is a set of N complex exponential functions:

$$g_k(R) = \frac{1}{\sqrt{N}} e^{i2\pi kR/L}, \qquad k = -(N/2-1), \ldots, 0, \ldots, (N/2) , \tag{2.12}$$

where index k is related to the momentum p. This choice of the basis has an advantage that functions (2.12) are eigenfunctions of the momentum operator with eigenvalues $p_k = 2\pi k/L$. Thus the expansion coefficients of the wave function $\psi(R)$ over basis functions (2.12) have a meaning of values of the wave function in the momentum space. This basis will be referred to as the **coordinate** basis, since the argument is the coordinate R. It will be designated also $\{|p_k > (R)\}$:

$$|p_k > (R) = \frac{1}{\sqrt{N}} e^{ip_k R}, \quad \text{where } p_k = \frac{2\pi k}{L} . \tag{2.13}$$

It is important that Eq. (2.13) gives relation between the smallest momentum Δp that can be presented by such a basis and the length of the coordinate grid L.

$$\Delta p = \frac{2\pi}{L} . \tag{2.14}$$

A coordinate grid, corresponding to this basis and satisfying Eqs. (2.6) and (2.8) is a set of equally-spaced points $(R_{min};\ R_{max})$: $R_j = R_{min} + (j-1) * \Delta R;\ j = 1, N;\ \Delta R = L/N;\ L = R_{max} - R_{min}$. Indeed, the functions $g_k(R)$ on this grid obey Eq. (2.6):

$$\sum_{k=-N/2+1}^{N/2} g_k(R_n) g_k^*(R_m) = \frac{1}{N} \sum_{k=-N/2+1}^{N/2} e^{i2\pi kR_n/L} e^{-i2\pi kR_m/L} =$$

$$\frac{1}{N} \sum_{k=-N/2+1}^{N/2} e^{i2\pi kn/L} e^{-i2\pi km/L} = \frac{1}{N} e^{-i2\pi(n-m)/N} \frac{1 - e^{i2\pi(n-m)}}{1 - e^{i2\pi(n-m)/N}} = \delta_{n,m} . \tag{2.15}$$

The orthogonality relation (2.8) in a discrete form is also satisfied:

$$\sum_{j=1}^{N} g_k(R_j) g_l^*(R_j) = \delta_{k,l} . \tag{2.16}$$

Here Eq. (2.15) are used. Now the wave-function $\psi(R)$ is expanded over $\frac{1}{\sqrt{N}} e^{i2\pi kR/L}$ functions:

$$\psi(R) \approx \frac{1}{\sqrt{N}} \sum_{k=-N/2+1}^{N/2} a_k e^{i2\pi kR/L} . \tag{2.17}$$

The expansion coefficients a_k are coefficients of the discrete Fourier expansion. They are calculated as

$$a_k = \frac{1}{\sqrt{N}} \sum_{j=1}^{N} \psi(R_j) e^{-i2\pi k R_j / L} \ . \tag{2.18}$$

These coefficients a_k represent the amplitude of wave-function in the space k, i.e. in the momentum space, at the points $|p_k>$. The expansion functions $\frac{1}{\sqrt{N}} e^{-i2\pi k R_j / L}$ define a basis in the momentum space. This space is canonically conjugate to the coordinate space. The basis functions are designated as $|R_j>(p)$.

Thus two conjugated bases are defined:

$$|p_k>(R) = \frac{1}{\sqrt{N}} e^{ip_k R}, \tag{2.19}$$

$$|R_j>(p) = \frac{1}{\sqrt{N}} e^{-ipR_j}, \tag{2.20}$$

where R is a discrete variable of the basis (2.19) in the **coordinate** representation, and p is a discrete variable of the basis (2.20) in the **momentum** representation.

In order to avoid confusion, one must note, that basis functions of the coordinate representation are numerated by the index k, which is related to the grid in the momentum space. Each function of the **momentum** representation (2.20) corresponds to single **coordinate** grid point R_j. Therefore one must be careful in notations of both basis. Below the representation using the first basis is referred to also as a **momentum-grid** or simply a **coordinate** representation. The second representation is referred to as a **coordinate-grid** or a **momentum** representation.

Both bases are related to the corresponding grids. The notation "grid" will be more frequent since the grid representation has a simple sense - wave functions are represented by values of the function on the grid points in the corresponding basis.

The maximum absolute value of the momentum that can be presented by these bases is given by Eq. (2.13) with $k = N/2$. It gives an important relation between the step of the Fourier grid ΔR and the maximum momentum that can be represented by the chosen grid:

$$p^g_{max} = \frac{\pi}{\Delta R} \ . \tag{2.21}$$

For completeness, continuous versions of bases are:

$$|p_k>(R) = \frac{1}{\sqrt{L}} e^{ip_k R}, \quad R \in [R_{min}, R_{min} + L] \ ,$$

$$|R_j>(p) = \frac{1}{\sqrt{2D_p}} e^{-ipR_j}, \quad p \in [-D_p, D_p] \ . \tag{2.22}$$

Consider now the M-channel function $\vec{\psi}(R)$.

$$\vec{\psi}(R) = \begin{pmatrix} \psi_1(R) \\ \psi_2(R) \\ \vdots \\ \psi_M(R) \end{pmatrix} . \tag{2.23}$$

In the Fourier grid representation the channel index must be introduced to label components of $\vec{\psi}(R)$. A pair of indexes of FGR-components (j) and channel components (γ) will be designated by Greek characters

$$\alpha = (\gamma, j) . \tag{2.24}$$

With account for both indexes the vector-function $\vec{\psi}(R)$ in FGR has $M \times N$ components. The same consideration is valid in the conjugate momentum representation.

2.1.3 Choice of the basis

The basis (2.12) is characterized by two parameters: by the length of the coordinate grid L and by the number of basis functions N. These parameters have to be determined from the physical content of the problem.

At first we discuss definition of the grid length L when the *bound levels* are considered. In the crudest approximation L is size region where the motion is allowed classically allowed. However, if the potential is not infinite at ends of the grid the bound state wave functions have exponentially decreasing tails situated in the classically forbidden domain. If such a tail is not negligible, one has to extend properly the length L into the classically forbidden region. For the *pre-dissociated levels* $\psi^p(R)$ the wave functions $\psi^p(R)$ do not vanish at the asymptotic region. In this case the ends of the grid must be chosen in the region, where wave functions become the purely asymptotic: $\psi^p(R) \approx \sin kR$. The grid must be extended in this case up to the distances where variation of the potential energy becomes much smaller than the asymptotic kinetic energy.

Since the second parameter N defines the maximum momentum p^g_{max} representing by the grid:

$$p^g_{max} = \pi N p^g_{max}/L = \frac{\pi}{\Delta R} , \tag{2.25}$$

the parameter N is chosen using the same reasoning as above but now considering domain of possible variation of the momentum. From Eq. (2.25) one sees that if p^g_{max} increases then the density of grid points (ΔR decreases) is to be enhanced. This improves accuracy of the wave function representation. Thus the basis needed for the calculations is defined simply from the physical content of the problem and the desirable accuracy.

The size of the basis N must be chosen in such way that p^g_{max} is larger than the maximum possible momentum in the problem p_{max}

$$p_{max} < p^g_{max} . \tag{2.26}$$

As p_{max} is defined by the maximum kinetic energy $p_{max} = \sqrt{2\mu E_{max}}$ (μ is a reduced mass), the size of the basis is

$$N > \frac{\sqrt{2\mu E_{max}} L}{\pi} . \tag{2.27}$$

For the grid step $\Delta R = L/N$ this gives

$$\Delta R = \frac{\pi}{\sqrt{2\mu E_{max}}} . \tag{2.28}$$

Note that the relations (2.25) and (2.26) state that each oscillation of the wave function is represented at least by one sampling point. Since the basis is exponential one sees that the more oscillations of the wave function are harmonic, the better the wave function is represented by the basis. If oscillations are not harmonic, the accuracy of the representation can be improved by increasing of density of points, i.e. by increasing N.

2.1.4 Operators in FGR

Once the basis is chosen, the operators are defined in the usual way, i.e. by its matrix elements on the basis functions. For example, in the coordinate grid representation (on the points $\{R_j\}$) the action of the operator $\mathbf{A}$ on a wave function $\psi(R)$ is presented as:

$$\mathbf{A}\psi(R)|_{R=R_j} = \sum_{l=1}^{N} A_{j,l}\psi(R_l) , \tag{2.29}$$

where $A_{j,l}$ is a matrix element in $\{R_j\}$ representation which will be referred to also as $< R_j|A|R_l >$.

In case of M-channel problem, all operators are represented in FGR by $MN \times MN$ matrices. As discussed above the label of basis states in FGR consists of a pair of indexes (γ, j).

Consider now the Hamiltonian in the FGR method. The matrix element $H_{\alpha,\beta}$ is to be be considered with two pairs of indices α and β:

$$\alpha = (\gamma, j) ,$$

$$\beta = (\gamma', l) . \tag{2.30}$$

Here j, l label the grid points R_j whereas γ, γ' channels.

Now we discuss kinetic and potential energy operators.

One-channel potential operator

The operator of potential energy V in FGR is the operator of multiplication in the coordinate space; it is diagonal in variable R:

$$\mathbf{V}\psi(R)|_{R=R_j} = V(R_j)\psi(R_j) . \tag{2.31}$$

As a result the correspondent matrix element in coordinate grid representation is simply a value of the potential V at the related point:

$$V_{\alpha,\beta} = V(R_j)\,\delta_{j,l}\ . \tag{2.32}$$

Multi-channel potential operator

In the multi-channel case potential operator is applied to the wave function as

$$\mathbf{V}\psi(R)|_{R=R_j} = \sum_{\gamma'} V_{\gamma,\gamma'}(R_j)\psi_{\gamma'}(R_j) \tag{2.33}$$

that implies

$$V_{\alpha,\beta} = V_{\gamma,\gamma'}(R_j)\,\delta_{j,l}\ . \tag{2.34}$$

Kinetic energy term

The kinetic energy term implies evaluation of the second (and, sometimes, also the first) derivative over R. Derivative operators are diagonal in the momentum space, and, thus, can be calculated in coordinate space using the Fourier transform. Their explicit form in the R_j basis is given by I. Tuvi and Y. Band [127]: The n^{th} derivative of $\psi(R)$ is written:

$$\psi(R)^{(n)}|_{R=R_j} = \left(\sum_{k=-N/2+1}^{n/2} a_k e^{ikR\frac{2\pi}{L}}\right)^{(n)}_{R=R_j} = \sum_{k=-N/2+1}^{N/2} a_k e^{ikj\frac{2\pi}{N}}\left(ik\frac{2\pi}{L}\right)^n$$

$$= \sum_{k=-N/2+1}^{N/2}\frac{1}{N}\sum_{l=1}^{N}\psi(R_l)e^{-ikl\frac{2\pi}{N}}e^{ikj\frac{2\pi}{N}}\left(ik\frac{2\pi}{L}\right)^n$$

$$= \frac{1}{N}\sum_{k=-N/2+1}^{N/2}\sum_{l=1}^{N}\psi(R_l)e^{ik(j-l)\frac{2\pi}{N}}\left(ik\frac{2\pi}{L}\right)^n\ . \tag{2.35}$$

Comparing Eq. (2.35) with (2.29), the matrix elements of the operator $\frac{\mathbf{d^{(n)}}}{\mathbf{dR^{(n)}}}$ can be written in the form

$$\left\{\frac{\mathbf{d^{(n)}}}{\mathbf{dR^{(n)}}}\right\}_{j,l} = \frac{1}{N}\sum_{l=1}^{N} e^{ik(j-l)\frac{2\pi}{N}}\left(ik\frac{2\pi}{L}\right)^n\ . \tag{2.36}$$

The sum in this equation can be evaluated analytically for the first and second derivatives [127]. For an even number N of grid points one has

$$\langle R_j|\frac{d^2}{dR^2}|R_l\rangle = \begin{cases} -\frac{\pi^2}{L^2}\frac{N^2+2}{3}, & j = l \\ -(-1)^{l-j}\frac{2\pi^2}{L^2}\frac{1}{sin^2[(j-l)\pi/N]}, & j \neq l \end{cases} \tag{2.37}$$

$$\langle R_j|\frac{d}{dR}|R_l\rangle = \begin{cases} i\frac{\pi}{L}, \ j=l \\ \\ (-1)^{j-l}\frac{\pi}{L}(i+cot[(j-l)\pi/N]), \ j\neq l \end{cases} . \tag{2.38}$$

Derivative matrix elements in the multichannel case are diagonal over the **channel** indexes:

$$\langle\alpha|\frac{d}{dR}|\beta\rangle = \langle R_j|\frac{d}{dR}|R_l\rangle\delta_{\gamma,\gamma'} . \tag{2.39}$$

Non-adiabatic term

Consider now a term which mixes channels and grid points. An example of such a term is the non-adiabatic coupling term in the adiabatic Schrödinger equation. Due to the nuclei motion the adiabatic potential channels are coupled. This coupling is described by non-adiabatic term which contains a first derivative multiplied by a factor mixing the channel components (see, for instance, the Appendix B):

$$\mathcal{W} = \left(<\gamma|\frac{\partial}{\partial R}|\gamma'>\frac{d}{dR}\right) = \left(\mathbf{A}_{\gamma,\gamma'}\frac{d}{dR}\right) . \tag{2.40}$$

The matrix element of $\langle\alpha|\mathcal{W}|\beta\rangle$ is

$$\langle\alpha|\mathcal{W}|\beta\rangle =< R_j|\mathbf{A}_{\gamma,\gamma'}\frac{d}{dR}|R_l >= \mathbf{A}_{\gamma,\gamma'}(R_j) < R_j|\frac{d}{dR}|R_l > . \tag{2.41}$$

In Eq. (2.40) the operators $\mathbf{A}$ and $\frac{d}{dR}$ do not commute. Indeed, consider the operator

$$\mathcal{W}' = \frac{d}{dR}\mathbf{A}_{\gamma,\gamma'} , \tag{2.42}$$

where the matrix $\mathbf{A}_{\gamma,\gamma'}(R)$ has the same form as in the preceding equations. Its matrix elements is

$$\langle\alpha|\mathcal{W}'|\beta\rangle =< R_j|\frac{d}{dR}\mathbf{A}_{\gamma,\gamma'}|R_l >= \mathbf{A}_{\gamma,\gamma'}(R_l) < R_j|\frac{d}{dR}|R_l > . \tag{2.43}$$

The right hand sides of (2.41) and (2.43) are different since $\mathbf{A}_{\gamma,\gamma'}(R_j) \neq \mathbf{A}_{\gamma,\gamma'}(R_l)$.

Now all the terms in the Hamiltonian are written in terms of matrix elements in the FGR basis. In FGR the entire Hamiltonian for M-channel problem is presented by the matrix $MN \times MN$. The diagonalization of this matrix gives eigenenergies of the Hamiltonian. The eigenvectors obtained in course of diagonalization give the wave functions of related states evaluated at the grid points. These eigenvectors have MN components, which are labeled by the index $\alpha = (\gamma, j)$. The α-component, $|\alpha>$, of the wave function in the coordinate grid representation gives value of the wave function in the γ channel at a distances R_j:

$$|\alpha >= \psi_\gamma(R_j) . \tag{2.44}$$

Kinetic energy term in the time-propagation

For the time-propagation the use of the matrix form of the derivative d^2R/dR^2 for calculations of the kinetic energy term $\mathbf{T}$ implies multiplication of related matrix on the vector ψ at every step of propagation. It takes each time $O(N^2)$ operations. The fact that $\mathbf{T}$ is diagonal in the momentum space, gives a possibility to reduce a number of operations for evaluation of $\mathbf{T}$. If $\bar{\psi}(p)$ is the wave function in the momentum space, then

$$\mathbf{T}\bar{\psi}(p) = \frac{p^2}{2\mu}\bar{\psi}(p) \ . \tag{2.45}$$

Therefore procedure of calculation $\mathbf{T}\psi(R)$ consists of three steps:

1. The Fourier image $\bar{\psi}(p)$ of $\psi(R)$ is calculated;
2. The function $\bar{\psi}(p)$ is multiplied by $\frac{p^2}{2\mu}$;
3. The inverse Fourier transformation of the product gives the result $\mathbf{T}\psi(R)$.

If the number of points is a power of 2, each evaluation of $\mathbf{T}\psi(R)$ takes $O(N \log N)$ operations provided the fast Fourier procedure is employed[70, 72].

2.1.5 Multi-channel potential. Example of two-channel potential.

The principle of generalization of the ordinary FGR method to the multi-channel problems is well known and was widely used (M.Monnerville and J.Robbe [99, 100], O. Dulieu and P. Julienne [34], O. Dulieu *et al.* [35]). Although the principle of representing the multichannel problem was already outlined in the general scheme (section 2.1.4), these problems are so important that this subsection describes them in more detail.

Below we give only one example. Consider Hamiltonian for the two-channel problem. For the grid $\{R_j\}$ with N points the kinetic energy matrix T has dimension $N \times N$ ($\mathbf{T} = -\frac{d^2}{2\mu dR^2}$) (subsection 2.1.4) for the one-channel potential. The potential $\mathbf{V}(R)$ depends upon R and has channel components $V_{1,1}(R)$, $V_{1,2}(R)$, $V_{2,1}(R)$, $V_{2,2}(R)$. Let $\mathbf{V}_{1,1}$, $\mathbf{V}_{1,2}$, $\mathbf{V}_{2,1}$, $\mathbf{V}_{2,2}$ be diagonal $N \times N$ matrices with the diagonal elements $< R_j|V_{\gamma,\gamma'}|R_j >= V_{\gamma,\gamma'}(R_j)$. The total matrix $\mathbf{H}$ of the Hamiltonian in the FGR has dimension $2N \times 2N$:

$$\mathbf{H} = \mathbf{T} + \mathbf{V} = \begin{pmatrix} T & 0 \\ 0 & T \end{pmatrix} + \begin{pmatrix} V_{1,1}(R) & V_{1,2}(R) \\ V_{2,1}(R) & V_{2,2}(R) \end{pmatrix} \ . \tag{2.46}$$

The diagonalization of this matrix gives eigenenergies of the Hamiltonian $\mathbf{H}$. The eigenfunctions obtained in course of diagonalization are presented as two-component wave functions. The first N values of wave functions give the first *channel* component on grid points while the second half gives the second *channel* component.

2.2 Hermicity of the Hamiltonian in the basis of FGR.

The Hamiltonian in the FGR method are represented usually by a very large matrix $NM \times NM$. In applications, the number NM can be very large. Bound levels of the Hamiltonian are obtained by a diagonalization of such large matrix. In this case it is preferable to minimize calculational efforts.

One possible approach is to look for an *hermitian* representation of the Hamiltonian. The diagonalization of the hermitian matrix is much cheaper. On the other hand, for the time propagation, the using of an hermitian matrix is also necessary – the propagation scheme using the Chebyshev polynomials does not work for non-hermitian matrix (see section on propagation).

The Hamiltonian H is always hermitian over channels γ, but its matrix in FGR is not obliged to be hermitian over grid index j. In this section, symmetry properties of the Hamiltonian in FGR are reviewed mainly as it was given by I.Tuvi and Y.Band [127]. .

A hermicity of the Hamiltonian over channel indexes reads:

$$H_{\gamma,\gamma'} = \langle \psi_\gamma | H | \psi_{\gamma'} \rangle_R = \int \psi^*_\gamma(R)(H\psi_{\gamma'})(R)dR = \langle \psi_{\gamma'} | H | \psi_\gamma \rangle^*_R = H^*_{\gamma',\gamma} \tag{2.47}$$

where the notation $\langle\rangle_R$ means integration over the internuclear variable R.

The Hermicity of the Hamiltonian in FGR means that:

$$< \alpha | H | \beta > = < \beta | H | \alpha >^*, \tag{2.48}$$

where α, β are defined by Eq. (2.30).

The hermicity of the total Hamiltonian can be checked as the hermicity of all consisting terms.

One-channel potential operator

It is diagonal over indexes α and β, since it is diagonal over j and l.

Multi-channel potential operator

The operator $\mathbf{V}$ is hermitian over channels. $\mathbf{V}$ is diagonal over grid indexes. $\Rightarrow$ $\mathbf{V}$ is hermitian over a permutation of α and β. From equation (2.34):

$$< \alpha | V | \beta > = < \beta | V | \alpha >^*, \tag{2.49}$$

Second derivative and kinetic energy term $-\frac{1}{2\mu}\frac{d^2}{dR^2}$

Indexes j and l enter symmetrically into Eq. (2.37). Changing j and l does not change matrix elements. $\Rightarrow$ The second derivative and the kinetic energy term $-\frac{1}{2\mu}\frac{d^2}{dR^2}$ are hermitian in FGR.

Terms with a first derivative

From Eq. (2.38), the matrix of the first derivative operator in FGR is anti-hermitian:

$$< R_j|\frac{d}{dR}|R_l >= - < R_l|\frac{d}{dR}|R_j >^* . \tag{2.50}$$

Therefore, in general, terms containing the first derivative are not hermitian in FGR. There are two ways that these terms can be symmetrized. If the first derivative is multiplied by an operator, which is anti-hermitian over channels and R-independent, the whole product will be hermitian over indexes α and β. This property will be used for the adiabatic Schrödinger equation, containing a term of a such type. Another way is to try to exclude the first derivative by a proper transformation of the wave function. This approach will be used for the mapped Schrödinger equation.

2.3 Mapped FGR method for a long-range potential.

As it was discussed already in the introduction of the Thesis, the calculations of bound vibrational levels near the dissociation limit with long range potential requires modifications of existing numerical methods. Wave functions of the most excited vibrational levels have an important tail located at very large distances. The situation becomes even more difficult, when the potential energy is rapidly decreasing near the dissociation limit and, as a consequence, an important part of the wave function can be beyond the region of the classical motion. C.Boisseau *et al.* [20, 21] have shown that for the Lennard-Jones potential, a part of the norm of the most excited level situated at the classically forbidden region can be very close to 100%. The ordinary FGR methods, using the constant grid step, are not able to treat too long-range potentials, since corresponding grids have too large a number of points. R. Kosloff, E. Fattal *et al.* [38, 70, 39] have proposed the mapped FGR method, optimizing the working grid. For the optimization, the estimation of the working phase space was used. But their method was adapted only for the short-range potential with singularities, and it does not propose any uniform procedure for the choice of the mapping. The recent work by E.Tiesinga *et al.* [125] discusses also the mapped FGR method in application to the highly-excited bound levels. There are two main disadvantages in the proposed method. There is no a preliminary criteria for the precision of results, and the mapping is analytical and must be adapted for any new potential curve. Côté and M.Jamieson in their work [32] have used for the solution of the Schrödinger equation the Numerov method with the variable step, adapted to local oscillations of the wave functions. The step was changing during the integration. The method proposed in the Thesis can be viewed as a combination of the FGR method with the *preliminary* adapted grid step. The procedure of this step adaptation will be refereed as a *mapping*.

This section presents mainly the theoretical part of an article [64] by V. Kokoouline, O. Dulieu, R. Kosloff and F. Masnou-Seeuws. In order to keep the logical progression of the Thesis, the part of the article concerning applications is included in the subsection 4.2.1. The whole paper is included at the end of the Thesis (Appendix C). The text taken from the paper will be typed by this font. Some corrections added to the article's text will be typed by the normal letters.

The subsection 2.3.1 describes the procedure of a choice of the potential-adapted grid-step – the mapping. Then, the Schrödinger equation in the mapped coordinate is presented. The hermicity of the Hamiltonian in FGR is discussed also. After, the analytic mapping adapted for potentials with the C_n/R^n asymptotic behavior is discussed. Finally, the phase space approach is presented for the estimation of the efficiency of working grids with and without the mapping.

2.3.1 Mapping procedure

In order to compute bound vibrational states of a diatomic molecule, a method, originally proposed by Kosloff [69] and by Colbert and Miller [30] , was further developed by Monnerville and Robbe [99], Dulieu and Julienne [34] and by Dulieu et al [35]. Let us recall briefly the principle of this method, hereafter referred to as Fourier Grid Representation Method (FGR). In the paper [64] the FGR method for time-independent Schrödinger equation is called the FGR method. This notation is used also in [34, 35]. The radial Schrödinger equation for eigenvalues problem is written:

$$[\mathbf{T} + V(R)]\psi(R) = E\psi(R) \tag{2.51}$$

A grid of N points equally spaced over coordinate R is defined as: $R_i, (i = 1, N)$. We introduce a set of functions defined at the grid points :

$$\varphi_i(R_j) = \delta(R_i - R_j), (i, j = 1, N) \tag{2.52}$$

(see the subsection 2.1.2). In this basis, both $\mathbf{T}$ and $\mathbf{V}(R)$ are represented by $N \times N$ matrices . The potential operator $\mathbf{V}(R)$ is diagonal in this representation, while the kinetic energy $\mathbf{T}$ is diagonal in the momentum representation which is connected by Fourier transform to the coordinate representation. Using well-known properties of the Fourier transform, the elements of the operator $\mathbf{T}$ can be written explicitly as a function of the number of points N -assumed to be even- and total length L of the grid [95] :

$$T_{ii} = \frac{\pi^2}{\mu L^2}\frac{N^2+2}{6} \tag{2.53}$$

$$T_{ij} = (-1)^{i-j}\frac{\pi^2}{\mu L^2}\frac{1}{sin^2[(i-j)\pi/N]} \tag{2.54}$$

In Eqs. (2.53) and (2.54), μ is the reduced mass of the system. Eigenvalues E_i are obtained by diagonalization of the $N \times N$ matrix $\mathbf{T} + V$.

Is is important to note that for the vibrational levels considered, the energy is close to the asymptotic value of the potential, hereafter taken as the energy origin. The maximum kinetic energy in the problem can be estimated by the depth $(V_{max} - V_{min})$ of the potential well. In most applications $V_{max} = 0$, nonzero positive values corresponding to situations where the potential has a hump. For a grid of length L, the two-dimension phase space should occupy at least a rectangular-shaped area :

$$A \geq 2Lp_{max}, \tag{2.55}$$

where p_{max} is the maximum momentum which has to be considered, corresponding to the maximum value of the kinetic energy:

$$p_{max} = \sqrt{2\mu(V_{max} - V_{min})}, \tag{2.56}$$

In practice, for a grid with N points, with a constant grid step $\Delta R = L/N$, the FGR method [72] considers a momentum domain extending from $-p_{grid}$ to $+p_{grid}$, so that the phase space is a rectangle with area:

$$A_N = 2\pi N\hbar = 2Lp_{grid}. \tag{2.57}$$

where, using atomic units, $\hbar = 1$. Therefore the constant grid step should verify:

$$\Delta R = \frac{\pi}{p_{grid}} \leq \frac{\pi}{\sqrt{2\mu(V_{max} - V_{min})}}. \tag{2.58}$$

When the vibrational motion extends at very long range, the length L has to be very large and calculations involve diagonalization of huge matrices $\mathbf{H} = T + V$. In fact, the grid contains too many points in the asymptotic region: indeed, at each distance R, the grid step needs only to be small enough to represent correctly the local kinetic energy. It is then sufficient to consider a local grid step $s(R)$ satisfying to the condition:

$$s(R) = \frac{\pi}{\sqrt{2\mu(V_{max} - V(R))}}. \tag{2.59}$$

For the class of problems that we are considering (see below section 3) the computation effort of the diagonalization procedure scales as the cube of the number of grid points. We propose to apply coordinate transformation in order to "compress" the grid at large distances. To that purpose, we define a transformation function $g(R)$ to set a working grid $x_i = g(R_i), i = 1, N$, with a constant step Δx related to the variable step in the physical grid through:

$$s(R) = \frac{\Delta x}{g'(R)}. \tag{2.60}$$

The transformation function is obtained, by comparing Eqs. (2.60) and (2.59), as:

$$x = g(R) = \int_{R_0}^{R} \frac{\sqrt{2\mu(V_{max} - V(r))}}{\pi} dr. \tag{2.61}$$

It is easy to check that in the working grid the minimum step is:

$$\Delta x = 1. \tag{2.62}$$

In Eq. (2.61), the integration domain starts at a distance R_0 slightly smaller than the position of the repulsive potential wall at short range. Now the physical grid is well adapted to different regions of the potential, since in the asymptotic region the local step $s(R)$ becomes much larger than at short inter-nuclear distances . In Fig. 2.1, we have illustrated this behavior considering various potentials for Na_2 [89] or Cs_2 [94] with either R^{-3} or R^{-6} asymptotic behavior. For a constant step $\Delta x = 1$ in the working grid, we

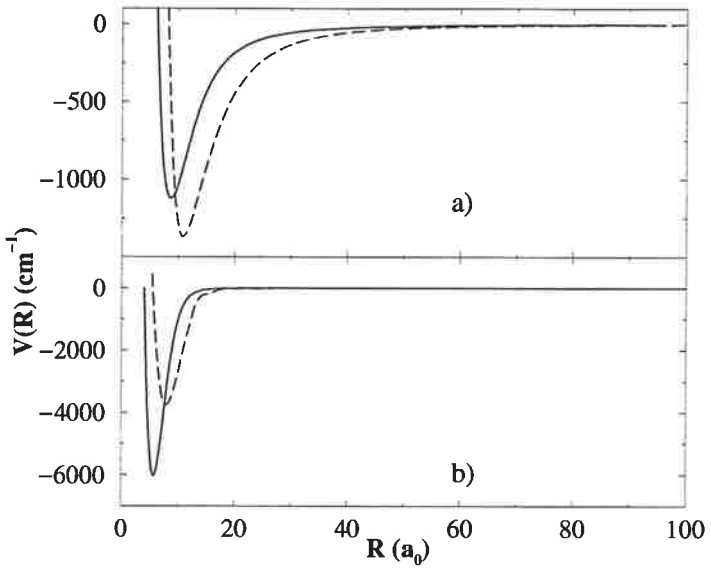

Figure 2.1: Examples of potential curves used in the paper. a) Two potentials with R^{-3}asymptotic behavior. Solid line: Na_2 $(^1\Pi_g, 3s + 3p)$, dashed line: $Cs_2(1_g, 6s + 6p^2P_{3/2})$. b) Two ground state potentials with R^{-6} asymptotic behavior. Solid line: $Na_2(^1\Sigma_g^+, 3s+3s)$, dashed line: $Cs_2(^1\Sigma_g^+, 6s+6s)$. For all curves, the energy origin is taken at the dissociation limit.

have represented in Fig. 2.2 the variation of $s(R)$ as a function of the distance R. The marked dependence upon the value of the n exponent manifests itself clearly, the step $s(R)$ increasing more rapidly with the distance in case of a R^{-6} potential. Besides, due

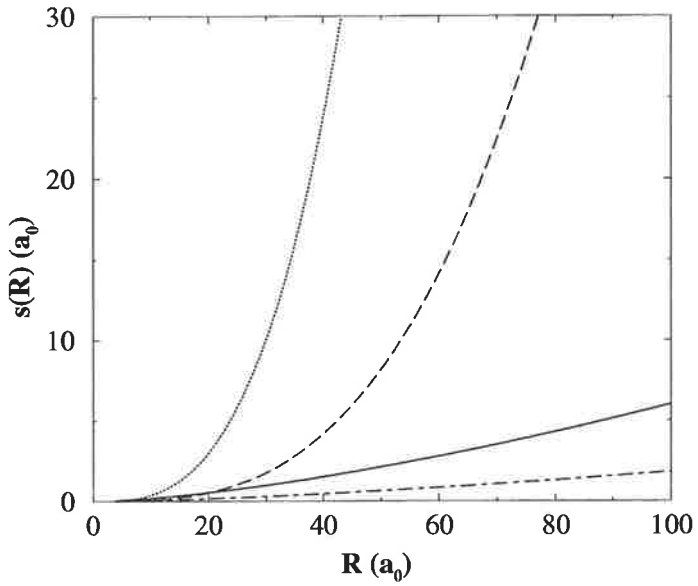

Figure 2.2: Variation of the grid-step $s(R)$ in the physical grid, for the four potentials in Fig. 2.1. Dotted line: $Na_2(^1\Sigma_g^+, 3s+3s)$, dashed line: $Cs_2(^1\Sigma_g^+, 6s+6s)$, solid line: $Na_2(^1\Pi_g, 3s+3p)$, dash-dotted line: $Cs_2(1_g, 6s+6p^2P_{3/2})$.

to the mass factor present in Eq. (2.59) the R variation is more rapid for Na_2 than for Cs_2. These features, as well as the role of the position R_0 of the inner repulsive potential wall, will be discussed more explicitly in paragraph 2.3.3.

Alternatively, in Eq. (2.59 defining a maximum local grid step, the real potential $V(R)$ can be replaced by another potential $V_{env}(R)$ provided the local kinetic energy stays larger than or equal to the real one. We shall call $V_{env}(R)$ an "enveloping potential" as the corresponding potential curve lies below the real one. The local grid step is now such that:

$$s_{env}(R) = \frac{\pi}{\sqrt{2\mu(V_{max} - V_{env}(R))}} \leq s(r). \tag{2.63}$$

Therefore the number of points on the grid is necessarily increased compared to the previous one. We discuss in the paragraph 2.3.3 examples where the asymptotic expression of the potential is considered.

Finally, for the discussion of the convergence of the calculations, it is convenient to introduce an auxiliary parameter $\beta_R = s_{env}(R)/s(R)$. If the enveloping potential differs from the real one, β_R depends upon R, with the restriction $\beta_R \leq 1$ so that the number of grid points is sufficient. Moreover, we can, starting from the real potential, calculate $s(R)$, and choose a constant $\beta < 1$ (for instance the minimum value of β_R) in order to define a local grid step such that $s_\beta(R) = \beta s(R)$. It means that the density of points is $\frac{1}{\beta}$ time larger than the critical density defined by Eq. (2.62), the step in the working grid

being now:

$$\Delta x = \beta \tag{2.64}$$

corresponding in the physical grid to a larger extension of the momentum, from $-p_{grid}$ to $p_{grid} = p_{max}/\beta$

2.3.2 Transformation of the Hamiltonian

Changing in the Schrödinger equation :

$$-\frac{1}{2\mu}\frac{d^2}{dR^2}\psi + V(R)\psi = E\psi \tag{2.65}$$

the variable R into another x with the transformation:

$$R = f(x),\ dR = J(x)dx,\ J(x) = f'(x) \tag{2.66}$$

one gets:

$$\left(-\frac{1}{2\mu J^2}\frac{d^2}{dx^2} + \frac{J'}{2\mu J^3}\frac{d}{dx}\right)\psi + V(x)\psi = E\psi, \tag{2.67}$$

where $J' = \frac{dJ}{dx}$. As discussed in the Appendix, the elements $T_{i,j}$ and $T_{j,i}$ of the kinetic energy operator in FGR are generally different, leading to the diagonalization of a non-symmetric matrix.

In order to introduce a Hamiltonian matrix symmetric in FGR, we define a new wave function $\phi(x)$:

$$\psi(x) = J^{-\frac{1}{2}}(x)\phi(x), \tag{2.68}$$

so that Eq. (2.67) becomes:

$$\left(-\frac{1}{2\mu J^2}\frac{d^2}{dx^2} + \frac{J'}{\mu J^3}\frac{d}{dx} + V + \frac{1}{2\mu}\left(-\frac{5}{4}\frac{(J')^2}{J^4} + \frac{1}{2}\frac{J''}{J^3}\right)\right)\phi(x) = E\phi(x) \tag{2.69}$$

We can rewrite this equation in a symmetrical form as:

$$\left(-\frac{1}{4\mu}\left(\frac{1}{J^2}\frac{d^2}{dx^2} + \frac{d^2}{dx^2}\frac{1}{J^2}\right) + \bar{V}\right)\phi = E\phi \tag{2.70}$$

where we have introduced an effective potential by:

$$\bar{V}(x) = V(x) + \frac{1}{2\mu}\left(\frac{7}{4}\frac{(J')^2}{J^4} - \frac{1}{2}\frac{J''}{J^3}\right) \tag{2.71}$$

We can check that the indexes i and j now play the same role in the expression of the kinetic operator $\mathbf{T}$ matrix elements :

$$T_{i,j} = (-1)^{i-j} \frac{\pi^2}{2\mu L^2} \frac{1}{sin^2[(i-j)\pi/N]} \left(\frac{1}{J_i^2} + \frac{1}{J_j^2} \right), \tag{2.72}$$

if $i \neq j$, while

$$T_{i,i} = \frac{\pi^2}{\mu L^2} \frac{N^2+2}{6} \frac{1}{J_i^2}, \tag{2.73}$$

As a consequence, FGR yields a symmetrical Hamiltonian matrix, so that efficient diagonalization procedures designed for triangular matrices can be implemented.

2.3.3 Mapping using R^{-3} and R^{-6} analytical potentials and a repulsive wall

In the derivation of the mapping procedure, we can use as an "enveloping potential" in equation (2.63) any analytic potential $V_{env}(R) = -C_n^{env}/R^n$, such that the corresponding potential curve lies below $V(R)$.

The Schrödinger equation for a potential with R^{-n} behavior, n being an integer value such that $n \geq 3$, was discussed by many authors: in Refs. [75, 104, 47], a change of variable is introduced in order to transform the Schrödinger equation into Bessel equation for which analytical solutions can be found. In the present approach, performing integration of the right hand side of Eq. (2.61), we get :

$$x_n = g_n(R) = x_{0,n} \frac{2\alpha_n}{(n-2)} \frac{1}{R^{\frac{n-2}{2}}} \tag{2.74}$$

where we have defined:

$$\alpha_n = \frac{\sqrt{2\mu C_n^{env}}}{\pi} \tag{2.75}$$

$$x_{0,n} = \frac{2\alpha_n}{(n-2)} \frac{1}{R_0^{\frac{n-2}{2}}} \tag{2.76}$$

Whereas the physical grid is extending from R_0 (chosen at a distance shorter than the position of the repulsive wall of the actual potential) to R_{max}, the new grid is varying from 0 to a maximum value which is limited by the finite value $x_{0,n}$, depending both of the asymptotic behavior of the potential (through α_n and n) and of R_0. There is therefore an accumulation of points in the vicinity of $x_{0,n}$, which is never explicitly reached. At small distances, due to the existence of a repulsive wall in our potential, we do not encounter the problem of the accumulation of points at the origin that had to be considered in Ref. [38] for the Coulomb problem.

The relation between the constant step Δx on the working grid and the variable step $s_n(R)$ on the physical grid is readily obtained as:

$$s_n(R) = \frac{R^{n/2}}{\alpha_n}\Delta x \tag{2.77}$$

The role of the exponent n and of the mass factor in α_n appears clearly in Eq. (2.77) and has been illustrated in fig.2.2 . We also display as an example in fig. (2.3), in a case where $n = 3$, corresponding to the asymptotic behavior of the upper 1_g curve of Cs_2, the repartition of the grid points for the working grid and for the physical grid : the adaptive character of the mapping procedure is demonstrated by the fewer number of points in the working grid when inter-nuclear distance is increasing. In the case of asymptotic potential

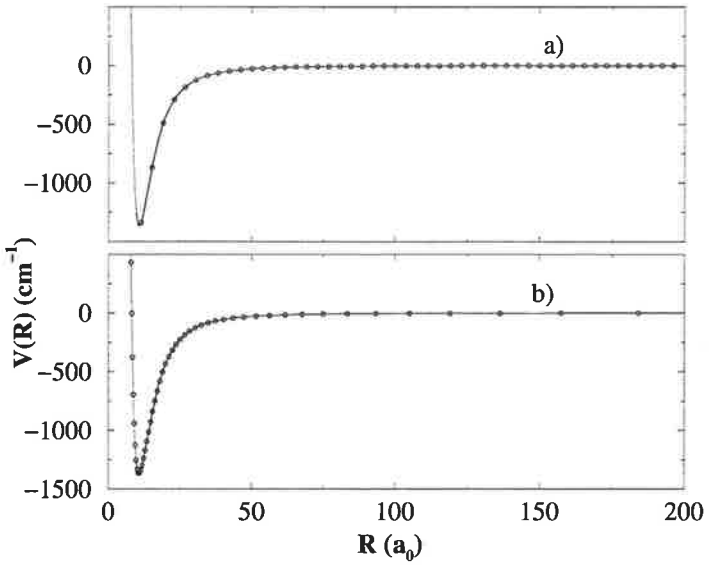

Figure 2.3: Distribution of the grid points for a potential with asymptotic R^{-3} behavior: example of $Cs_2(1_g, 6s + 6p^2P_{3/2})$. a) - without mapping; b) - with the mapping defined by Eq. (2.74).

$-C_3^{env}/R^3$, the change of variable should be:

$$x_3 = x_{0,3} - 2\alpha_3 R^{-\frac{1}{2}} \tag{2.78}$$

where we have defined $\alpha_3 = \sqrt{2\mu C_3^{env}}/\pi$ through Eq. (2.75. The inverse transformation is then analytical:

$$R = f_3(x_3) = \frac{(2\alpha_3)^2}{(x_{0,3} - x_3)^2} \tag{2.79}$$

As the change of function described in section 2.3.2 differs from what was proposed in the references quoted above [75, 104, 47], our new Schrödinger equation differs from a

Bessel equation. It is more convenient for numerical calculations as it leads to symmetrical matrices in FGR:

$$\left(-\frac{1}{2\mu}\left(\frac{(x_{0,3}-x_3)^6}{2^7(\alpha_3)^4}\frac{d^2}{dx_3^2}+\frac{d^2}{dx_3^2}\frac{(x_{0,3}-x_3)^6}{2^7(\alpha_3)^4}\right)+\bar{V}\,(x_3)\right)\phi(x_3)=E\phi(x_3) \tag{2.80}$$

with new potential $\bar{V}$:

$$\bar{V}\,(x_3)=V(x_3)+\frac{1}{2\mu}\frac{39}{2^8(\alpha_3)^4}(x_{0,3}-x_3)^4 \tag{2.81}$$

In the new coordinate x_3, the asymptotic behavior of $V(x_3)$ obtained by transformation of $-C_3/R^{-3}$ is:

$$V_{as}(x)=-\frac{1}{2\mu}\frac{4\pi^2}{2^8(\alpha_3)^4}(x_{0,3}-x_3)^6 \tag{2.82}$$

so that when $C_3^{env}=C_3$, the effective potential, in the asymptotic region, may be written:

$$\bar{V}_{as}\,(x_3)=\frac{1}{2\mu}\left(-\frac{4\pi^2}{2^8(\alpha_3)^4}(x_{0,3}-x_3)^6+\frac{39}{2^8(\alpha_3)^4}(x_{0,3}-x_3)^4\right). \tag{2.83}$$

The matrix elements for the kinetic energy operator are now:

$$T_{i,j}=(-1)^{i-j}\frac{\pi^2}{2\mu L^2}\frac{1}{sin^2[(i-j)\pi/N]}\left(\frac{(x_{0,3}-x_{3,i})^6}{2^6(\alpha_3)^4}+\frac{(x_{0,3}-x_{3,j})^6}{2^6(\alpha_3)^4}\right), \tag{2.84}$$

if $i\neq j$, while

$$T_{i,i}=\frac{\pi^2}{\mu L^2}\frac{N^2+2}{6}\frac{(x_{0,3}-x_{3,i})^6}{2^6(\alpha_3)^4}. \tag{2.85}$$

2.3.4 Comparison of the numerical and the analytical mapping procedures

The analytic approach enables a simple assessment of the procedure. However, the computing code has to be modified for potentials differing in their asymptotic expression, which is not the case for the general numerical procedure.

Another disadvantage of the analytical approach lies in the definition of an enveloping potential. In many cases, due to the existence of higher order attractive terms in the multi-pole expansion, the asymptotic curve $-C_3/R^3$ crosses the $V(R)$ curve. Therefore

the value of C_3^{env} should be chosen much larger than the actual C_3 value. For example, as illustrated in Fig. 2.4, the asymptotic behavior of Na_2 $^3\Pi_u$ $(3s, 3p\ ^2P)$ is $-6.48/R^3$ [92], but only the enveloping curve with $C_3^{env} = 18.0$ lies under $V(R)$ for all inter-nuclear distances. In the latter case, the use of an enveloping analytical potential in Eq. (2.63) results into a number of grid points four times larger than when the real potential is used in Eq. (2.61). This drawback is particularly important for cases corresponding to

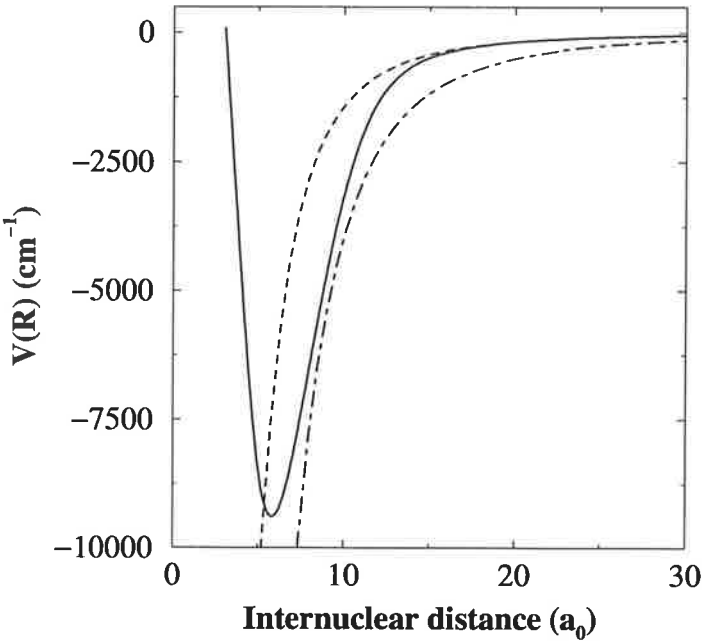

Figure 2.4: Comparison of the computed potential curve for Na_2 ($^3\Pi_u$, $3s, 3p$) [89] (full line) with the asymptotic curve $V(R) = -C_3/R^3$, $C_3 = 6.48$ $a.u.$, (dashed line) and the enveloping curve $V(R) = -C_3^{env}/R^3$, $C_3^{env} = 18$ $a.u.$ (dash-dotted line).

small values of R_0, the divergence of C_3/R^3 near the origin resulting into a significant increase of the number of grid points N. Moreover, increasing the phase space of the problem when using small grid steps near the origin may lead to spurious eigenvalues in the numerical diagonalization procedure. It also increases significantly the spectral range of the Hamiltonian operator. This will hinder the use of direct propagation methods.

It seems therefore more convenient to use the real potential in Eq. (2.61). The mapping transformation is calculated for any potential whatever is the asymptotic behavior. The integral in Eq. (2.61) and all derivatives of $g(R)$ are then obtained through purely numerical procedures .

2.3.5 Occupation of the phase space domain after coordinate transformation

As discussed by Fattal et al [38] and by Kosloff [72], mapping procedures are capable of optimizing the use of the phase space volume of the representation. As a first approximation, the phase space domain necessary to describe the system can be estimated by

considering the classical trajectory corresponding to the highest vibrational level which we want to compute. This is illustrated in Fig. 2.5, where we have drawn the phase domain in distance R and momentum p spanned by a classical trajectory corresponding to a vibrational motion with binding energy $E = 1.3 \cdot 10^{-7}$, i.e. $E_u = -0.295\ cm^{-1}$, in the potential $Cs_2(1_g)$ displayed in Figs. 2.1 and 2.2.

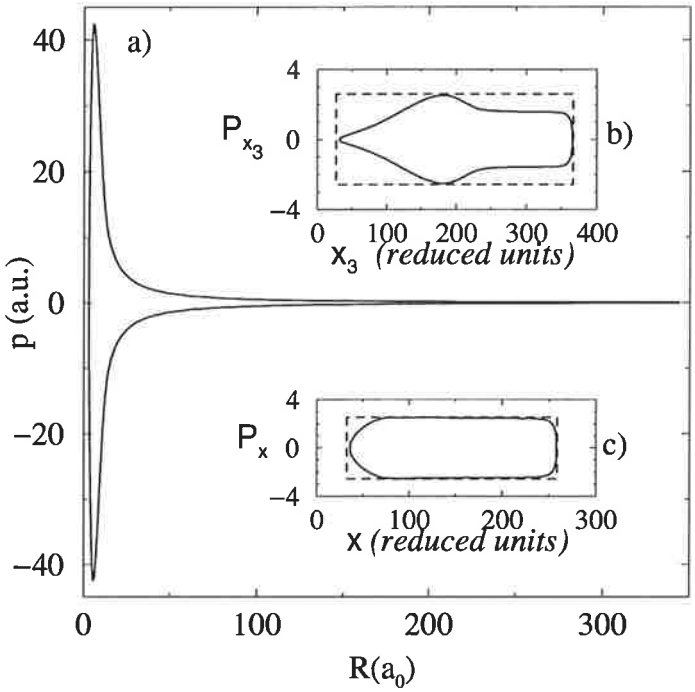

Figure 2.5: Solid lines: The classical energy shell in phase space with and without the coordinate transformation, for the vibrational level with binding energy $E_u = -0.295\ cm^{-1}$ in the potential Cs_2 $(1_g, 6s, 6p^2P_{3/2})$. a) - The main figure shows the energy shell in phase space without any mapping. b) - The upper inset displays the energy shell with the mapping defined by the enveloping potential $-C_3^{env}/R^3$ with $C_3^{eff} = 24.42$. c)- The lower inset displays the energy shell in phase space with the mapping using the real behavior of the potential. The area $S = 1034\ a.u.$ defined by contour is the same for all three cases. The number of phase cells N_c is connected with S through $S = 2\pi * N_c$. Broken lines: The rectangles defining the phase space used in the calculations. One can see that without the mapping a larger phase volume is used in the calculation, that requires proportionally more grid points. The third case is most efficient in that sense.

The shape differs markedly from rectangular, showing that at large distances, due to the very small value of the local momentum, only a very small part of the phase space defined by a grid with a constant grid step is occupied.

The same domain in the new variables x and P_x is presented also. In the working grid, the variable x is defined in Eq. (2.61) while the variable P_x , canonically conjugated to x in the new phase space, can be found [74] from the Poisson bracket:

$$\frac{\partial P_x}{\partial p}\frac{\partial x}{\partial R} - \frac{\partial x}{\partial p}\frac{\partial P_x}{\partial R} = 1. \tag{2.86}$$

As from Eq. (2.66) $dR = J(x)dx$ and as $\frac{\partial x}{\partial p} = 0$ then:

$$P_x = pJ(x) \tag{2.87}$$

On the lower inset of Fig.2.5 we display the phase space spanned by the classical trajectory in the new variables x, P_x. The area confined by the contour is the same as in previous case, $S = 1034\ a.u.$, but the shape is now very close to a rectangle.

In the upper inset of the figure we show also the same trajectory in the x_3, P_{x3} space - using Eq. (2.78) and generalizing Eq. (2.87) – for mapping with the analytical enveloping potential $-C_3^{env}/R^3$ where $C^{env} = 24.42$, larger than the value $C_3 = 18$ associated with the Cs_2 (1_g) potential. The contour now differs from a rectangular shape, especially at short x_3, where the extension of the momentum space is due to overestimation of local kinetic energy. The efficiency of the occupation of the phase space can easily be discussed by comparing the equivalent area $S = 1034\ a.u.$ spanned by the three contours with the area of the rectangles associated to the three grids. In the physical problem, treated with a classical picture, the number of phase cells $N_c = 165$ is deduced from the area S through $S = 2\pi \times N_c$. Without mapping, the rectangle associated with the physical grid has an area, defined in Eq. (2.55), such that $A \leq 28730 \approx 2\pi \times 4573$. The numerical treatment should therefore involve at least $N = 4573$ grid points. After mapping with enveloping potential, the area spanned by the grid is defined as $A_3^{mapp} \leq 2x_{3,max}\ P_{x_{3,max}}$, so that in the chosen ax-ample we have $A_3^{mapp} \leq 1705 \approx 2\pi \times 272$, so that the minimum number of grid points is reduced to 272. Finally, when the mapping procedure based on the real potential, the area $A^{mapp} \leq 2x_{max}P_{x_{max}}$ now is at least 1077, corresponding to a minimum number of grid points of 172 only, very close to the number $N_c = 165$ of cells estimated from the classical phase space restricted to the same energy. The efficiency of the numerical mapping method is therefore clearly demonstrated by this figure.

One should note that this approach to the estimation of phase space confined by the problem is completely classical. It assumes that the quantum density in phase space decays exponentially fast in the classical forbidden region. The definition of the phase space in quantum mechanics was done by M. Hillery et al in [53]. Using the Wigner distribution function the exponential decay of the quantum density outside the classical allowed region is clearly evident [72]. If tunneling is important, the phase space region involved, both in coordinate and momentum has to be included in the grid, so that a larger number of grid points should be considered. The introduction of a parameter β, as defined in Eq. (2.64), in order to reduce the step in the working grid is then justified, and this parameter needs to be optimized in the calculations.

The efficiency of the method can be further improved if classically forbidden region is taken into account. This problem was briefly discussed in the subsection 2.1.3. A possible improvement could be the including of the domain of the classically forbidden motion, $[R_{min}, R_{min} + L]$, which accounts exponentially decreasing tails of wave functions. An estimation of a such domain can be made in the semi-classical approximation.

2.4 Mapping for Hamiltonian containing non-adiabatic coupling term

The previous sections considered the Schrödinger equation containing terms which are hermitian in FGR. It was assumed that the Hamiltonian does not contain a term with the first derivative, which is not-hermitian in FGR. The Schrödinger equation with the multi-channels adiabatic potential includes such a term that couples the adiabatic channels.

If such a term with the first derivatives is directly introduced into the Schrödinger equation, the total matrix of the Hamiltonian becomes non-hermitian in FGR. It means that in the time-independent approach one has to diagonalize a non-symmetric matrix, that takes much more time as compared with the diagonalization of a hermitian matrix (see discussion by M. Monnerville and J. Robbe [100]). Unfortunately, this approach does not work at all for the time propagation based on the Chebyshev polynomial expansion. Therefore, it is useful to construct the matrix of adiabatic Hamiltonian hermitian in the FGR.

In this section two different approaches to the problem of non-hermicity are considered. First, the non-hermitian terms of the Hamiltonian are combined in such a way that they become hermitian in FGR. This approach is valid only for the uniform (non-mapped) FGR method. It was developed mainly by I. Tuvi and Y. Band [127]. The second approach employs *diabatization* of the adiabatic potential, i.e. excluding the non-adiabatic terms by changing the basis of molecular states (F. Smith [120], M. Baer [12]).

2.4.1 Reducing adiabatic Hamiltonian to hermitian matrix in FGR

In this subsection the hermitian representation of the adiabatic Schrödinger equation without mapping is briefly discussed. The procedure was suggested by I. Tuvi and Y. Band [127] in order to explicitly obtain a hermitian matrix for the adiabatic Hamiltonian in the FGR. In the Thesis small modifications are added that simplifies understanding. The time-independent Schrödinger equation is used, but all results are also valid for the time-dependent equation.

The following form of the adiabatic Schrödinger equation is used:

$$\left(-\frac{1}{2\mu}\frac{d^2}{dR^2}+V_\gamma\right)\psi_\gamma-\frac{1}{2\mu}\sum_{\gamma'}\left(2\tau^{(1)}_{\gamma,\gamma'}\frac{d}{dR}+\tau^{(2)}_{\gamma,\gamma'}\right)\psi_{\gamma'}=E\psi_\gamma \qquad (2.88)$$

with non-adiabatic radial coupling terms:

$$\tau^{(1)}_{\gamma,\gamma'}(R)=<\gamma|\frac{\partial}{\partial R}|\gamma'>_r$$

$$\tau^{(2)}_{\gamma,\gamma'}(R)=<\gamma|\frac{\partial^2}{\partial R^2}|\gamma'>_r . \qquad (2.89)$$

The notation $< \mid >_r$ means integrating over the electronic variable. Quantities $\tau^{(1)}_{\gamma,\gamma'}(R)$ and $\tau^{(2)}_{\gamma,\gamma'}(R)$ do not depend upon the electronic coordinates. It is supposed that $\tau^{(1)}_{\gamma,\gamma'}(R)$, $\tau^{(2)}_{\gamma,\gamma'}(R)$ are known as well as $V_\gamma(R)$.

Equation (2.88) looks like Eq. (2.67). Indeed, the first derivative is present in both cases. However, from the point of view of the FGR, there is a large difference. Eq. (2.67) contains the term with the first derivative multiplied by a function of R. This function does not mix potential channels. Due to that, the term with the first derivative can be excluded by multiplication of the wave function by $J^{1/2}(x)$ as it was discussed above. In Eq. (2.88) the term with the first derivative contains a factor mixing the channels, and therefore, it cannot be excluded by a simple multiplication of the wave function by some factor like $J^{1/2}(x)$.

The matrix $\tau^{(1)}$ is anti-hermitian over channel indices γ and γ':

$$< \gamma|\gamma' >_r = \delta_{\gamma,\gamma'} \tag{2.90}$$

$$\frac{\partial}{\partial R} < \gamma|\gamma' >_r = < \frac{\partial}{\partial R}\gamma|\gamma' >_r + < \gamma|\frac{\partial}{\partial R}\gamma' >_r =$$

$$< \gamma'|\frac{\partial}{\partial R}\gamma >^*_r + < \gamma|\frac{\partial}{\partial R}\gamma' >_r = 0 \tag{2.91}$$

and, therefore,

$$< \gamma'|\frac{\partial}{\partial R}|\gamma >^*_r = - < \gamma|\frac{\partial}{\partial R}|\gamma' >_r \ . \tag{2.92}$$

The matrix $\tau^{(2)}$ is hermitian over channel indices

$$< \gamma'|\frac{\partial^2}{\partial R^2}|\gamma >^*_r = < \gamma|\frac{\partial^2}{\partial R^2}|\gamma' >_r \ . \tag{2.93}$$

The matrix element $\langle\alpha|H|\beta\rangle$ of the Hamiltonian in the coordinate-grid basis is:

$$\langle\alpha|H|\beta\rangle = -\frac{1}{2\mu}\langle R_j|\frac{d^2}{dR^2}|R_l\rangle\delta_{\gamma,\gamma'} + V_{\gamma,\gamma'}(R_l)\delta_{j,l}$$

$$-\frac{1}{2\mu}\left(2\tau^{(1)}_{\gamma,\gamma'}(R_j)\langle R_j|\frac{d}{dR}|R_l\rangle + \tau^{(2)}_{\gamma,\gamma'}(R_j)\delta_{j,l}\right) \tag{2.94}$$

where α and β are defined by Eq. (2.30).

The first two terms of the right hand side in the last equation are hermitian over α and β. Since $\tau^{(1)}_{\gamma,\gamma'}$, $\tau^{(2)}_{\gamma,\gamma'}$ depend of the variable R, one has

$$\tau^{(1,2)}_{\gamma,\gamma'}(R_j) \neq \tau^{(1,2)}_{\gamma,\gamma'}(R_l) \ . \tag{2.95}$$

Therefore the third and fourth terms are not hermitian. As a result the entire matrix is not hermitian:

$$\langle\alpha|H|\beta\rangle \neq \langle\beta|H|\alpha\rangle^* \ . \tag{2.96}$$

In order to overcome this difficulty, I. Tuvi and Y. Band [127] proposed to represent the non-adiabatic radial terms in alternative form. Using the identity

$$\frac{d}{dR}(\tau^{(1)}\psi) \equiv \psi\frac{d}{dR}\tau^{(1)} + \tau^{(1)}\frac{d}{dR}\psi \tag{2.97}$$

the adiabatic Schrödinger equation is rewritten as

$$\left(-\frac{1}{2\mu}\frac{d^2}{dR^2} + V_\gamma\right)\psi_\gamma - \frac{1}{2\mu}\sum_{\gamma'}\left(\tau^{(1)}_{\gamma,\gamma'}\frac{d}{dR} + \frac{d}{dR}\tau^{(1)}_{\gamma,\gamma'} + \bar{\tau}^{(2)}_{\gamma,\gamma'}\right)\psi_{\gamma'} = E\psi_\gamma \ , \tag{2.98}$$

where

$$\bar{\tau}^{(2)}_{\gamma,\gamma'} = \tau^{(2)}_{\gamma,\gamma'} - \frac{d}{dR}\tau^{(1)}_{\gamma,\gamma'} \ . \tag{2.99}$$

The equation (2.99) is equivalent to Eq. (2.88), but in the latter form all the terms in the Hamiltonian are hermitian in FGR.

For matrix elements of the non-adiabatic interaction one has

$$\langle\alpha|\tau^{(1)}\frac{d}{dR} + \frac{d}{dR}\tau^{(1)}|\beta\rangle = \left(\tau^{(1)}_{\gamma,\gamma'}(R_j) + \tau^{(1)}_{\gamma,\gamma'}(R_l)\right)\langle j|\frac{d}{dR}|l\rangle =$$

$$\left(-\tau^{(1)*}_{\gamma',\gamma}(R_j) - \tau^{(1)*}_{\gamma',\gamma}(R_l)\right)\left(-\langle l|\frac{d}{dR}|j\rangle^*\right) = \langle\beta|\tau^{(1)}\frac{d}{dR} + \frac{d}{dR}\tau^{(1)}|\alpha\rangle^* \ . \tag{2.100}$$

The term $\bar{\tau}^{(2)}$ is hermitian over channel indices and diagonal over j and l. Therefore it is hermitian in FGR:

$$\langle\alpha|\,\bar{\tau}^{(2)}\,|\beta\rangle = \langle\beta|\,\bar{\tau}^{(2)}\,|\alpha\rangle^* \ . \tag{2.101}$$

Thus $\bar{\tau}^{(2)}$ is the additional term in the potential.

2.4.2 Application to the problem of bound states

The results of previous subsection are valid for the multi-channel problem. Below, a numerical example with a two-channel potential is considered to demonstrate that the proposed method is workable. We consider example based on the potential curves calculated numerically for real diatomic molecules. I. Tuvi and Y. Band [127] have also tested the same method but using analytical Morse potential.

Specifically we consider two states of 0^+_u $(5S + 5P)$ symmetry of Rb_2 (see more discussion in section 4.2). We compare calculations in diabatic and adiabatic representations.

In the diabatic form the Schrödinger equation reads

$$\left[-\frac{1}{2\mu}\frac{d^2}{dR^2} + \mathbf{V^{diab}}\right]\psi = E\psi \ . \tag{2.102}$$

The potential $\mathbf{V^{diab}}$ is constructed from two Hund's case a potential curves of Rb_2: $A^1\Sigma_u^+(5S + 5P)$ and $b^3\Pi_u(5S + 5P)$ (the graph 1.3). The non-diagonal adiabatic coupling is a constant spin-orbit interaction (see section 4.2). The corresponding adiabatic equation is

$$\left[-\frac{1}{2\mu}\frac{d^2}{dR^2} + \mathbf{V^{adiab}} - \frac{1}{2\mu}\left(\tau^{(1)}\frac{d}{dR} + \frac{d}{dR}\tau^{(1)} + \tilde{\tau}^{(2)}\right)\right]\psi = E\psi \ . \tag{2.103}$$

The adiabatic potential curves $\mathbf{V^{adiab}}$ are obtained by diagonalization of Hund's case a potentials (with the adiabatic coupling) at each internuclear distance (see Fig. 1.4).

Consider now relation between these two representations. If the diabatic potential for the two-states problem is

$$\mathbf{V^{diab}} = \begin{pmatrix} U_1(R) & a(R) \\ a(R) & U_2(R) \end{pmatrix} , \tag{2.104}$$

then the related adiabatic representation of $\mathbf{V^{adiab}}$ is

$$\mathbf{V^{adiab}} =$$

$$\begin{pmatrix} \frac{1}{2}\left[U_1(R) + U_2(R) - \Delta U(R)\right] & 0 \\ 0 & \frac{1}{2}\left[U_1(R) + U_2(R) + \Delta U(R)\right] \end{pmatrix} , \tag{2.105}$$

where

$$\Delta U(R) = \sqrt{(U_1(R) - U_2(R))^2 + 4a^2(R)}. \tag{2.106}$$

The matrix $\mathbf{S}$ of transformation between diabatic and adiabatic representations

$$\mathbf{V^{diab}} = \mathbf{S^{-1}V^{adiab}S} \tag{2.107}$$

is defined by the diabatic curves and the interaction a:

$$\mathbf{S} = \begin{pmatrix} \cos\chi & \sin\chi \\ -\sin\chi & \cos\chi \end{pmatrix} , \tag{2.108}$$

where

$$\chi = \frac{1}{2}\arctan\left[\frac{a(R)}{U_2(R) - U_1(R)}\right] \ . \tag{2.109}$$

The matrices of non-adiabatic coupling operators in the adiabatic equation are calculated by inserting the identity (2.107) into Eq. (2.102) and comparing it with Eq. (2.103). They are

$$\tau^{(1)} = \mathbf{S}\left(\frac{d\mathbf{S}}{dR}\right)^T , \tag{2.110}$$

$$\tau^{(2)} = \mathbf{S}\left(\frac{d^2\mathbf{S}}{dR^2}\right)^T , \tag{2.111}$$

$$\tilde{\tau}^{(2)} = -\frac{d\mathbf{S}}{dR}\left(\frac{d\mathbf{S}}{dR}\right)^T . \tag{2.112}$$

A uniform equally-spaced grid was used for the test, because the mapping can not be implemented directly for the equation with non-adiabatic terms (this problem is considered in the next section.)

The matrix elements for derivatives with even number N of points are given by Eqs. (2.37) and (2.38). The matrix elements of the first order derivative are complex, whereas these elements for odd N are real [127]. Therefore, in order to exclude complex variables from the program, the odd number of points was chosen for the adiabatic equation. The matrix elements for odd N are:

$$\langle R_i|\frac{d^2}{dR^2}|R_i\rangle = \begin{cases} -\frac{\pi^2}{L^2}\frac{N^2-1}{3}, & i = j \\ -(-1)^{i-j}\frac{2\pi^2}{L^2}\frac{\cos[(i-j)\pi/N]}{\sin^2[(i-j)\pi/N]}, & i \neq j \ , \end{cases} \tag{2.113}$$

$$\langle R_i|\frac{d}{dR}|R_i\rangle = \begin{cases} 0, & i = j \\ -(-1)^{i-j}\frac{\pi}{L}\frac{1}{\sin[(i-j)\pi/N]}, & i \neq j \ . \end{cases} \tag{2.114}$$

The first test verifies that calculations with even and odd N give the same results. The diabatic equation was used for the Cs_2 (1_g) state was considered using $N = 564$ and 565 for even and odd cases respectively. Tests show that eigenvalues calculated by using odd and even grids are the same with the relative difference $\frac{E_{even}-E_{odd}}{E_{even}} = 10^{-12}$ for deeply bound levels. The relative difference is of order of 10^{-6} for the highest calculated level $v = 330$ (in this energy region the error comes from exponentially decreasing tails of wave functions, extending to the classically forbidden region). In addition, the two-channel case of Rb_2 (0_u^+) has also been tested. The precision is of the same order of magnitude.

The second test is a comparison of results for adiabatic and diabatic equations. The equations (2.103) and (2.65) should give identical results. The two-channel potential of symmetry 0_u^+ for Rb_2 was used. The relative difference between results of two approaches for vibrational levels is of order of $10^{-6} - 10^{-5}$ (or $10^{-2} - 10^{-1}$ cm^{-1}). As one can see the error is quite large. It is attributed to the imperfection of the present code. There are numerous spline procedures which reduce the accuracy and have to be excluded.

Unfortunately only preliminary tests were carried out. The work will be continued. But even these preliminary tests have demonstrated that the proposed approach is working.

2.4.3 Adiabatic basis: long-range potentials. Diabatization procedure

In contrast to the results of Ref. [127] it seems to be impossible to obtain a symmetric form of the Hamiltonian with the adiabatic terms in the grid representation, using an arbitrary mapping. It is not enough to multiply a wave function by some combination of $J(x)$ and its derivatives and to combine the derivative operators as it was done in the previous section. A possible way is to choose some transformation of the basis of adiabatic functions $|\gamma>$ into another set ($|\gamma> \rightarrow |\phi>$) for which the first-derivative operator vanishes or, by others words, to apply to the Hamiltonian the diabatization procedure.

The diabatization procedure is not new. As early as in 1969 F. Smith [120] and M. Baer in 1976 [12] proposed to exclude $\frac{d}{dR}$ terms from the equation using a unitary transformation of the basis of electronic wave functions. Later, many other authors examined advantages and disadvantages of both representations (see also [117], V. Sidis 1989).

In this section, it is shown how the transformation matrix $\mathbf{S}$ can be found using the non-adiabatic terms. The procedure of the numerical evaluation is proposed.

Consider the adiabatic Schrödinger equation in the form of (2.103). Applying a linear transformation S of the basis of molecular states

$$\psi = \mathbf{S}\phi \tag{2.115}$$

the equation is reduced to the form

$$\mathbf{S^T H S}\phi = E\phi \ , \tag{2.116}$$

where $\mathbf{H}$ is the Hamiltonian from Eq. (2.103). The new Hamiltonian $\mathbf{H^d} = \mathbf{S^T H S}$ has form:

$$-\frac{1}{2\mu}\mathbf{S^T}\Big[\mathbf{S}\frac{d^2}{dR^2} + 2\mathbf{S'}\frac{d}{dR} + \mathbf{S''} + 2\tau^{(1)}\mathbf{S}\frac{d}{dR} +$$

$$+2\tau^{(1)}\mathbf{S'} + \tau^{(2)}\mathbf{S} - 2\mu\mathbf{V^{adiab}S}\Big], \tag{2.117}$$

or

$$-\frac{1}{2\mu}\Big[\frac{d^2}{dR^2} + 2(\mathbf{S^T S'} + \mathbf{S^T}\tau^{(1)}\mathbf{S})\frac{d}{dR} +$$

$$\mathbf{S^T S''} + 2\mathbf{S^T}\tau^{(1)}\mathbf{S'} + \mathbf{S^T}\tau^{(2)}\mathbf{S} - 2\mu\mathbf{S^T V^{adiab}S}\Big] \tag{2.118}$$

The condition for the diabatic functions ϕ is:

$$\mathbf{S^T S'} + \mathbf{S^T}\tau^{(1)}\mathbf{S} = 0 \ ,$$

$$\mathbf{S'} = -\tau^{(1)}\mathbf{S} \ ,$$

$$\tau^{(1)} = -\mathbf{S}'\mathbf{S}^{\mathbf{T}} = \mathbf{S}(\mathbf{S}^{\mathbf{T}})' \,. \tag{2.119}$$

It is exactly Eq. (2.110). For the matrix $\tau^{(2)}$ the condition (2.111) is satisfied also. The formal solution of Eq. (2.119) is

$$\mathbf{S} = \mathbf{C}\mathbf{e}^{-\tau^{(1)}\mathbf{R}} \,. \tag{2.120}$$

Using expressions (2.119) and (2.111) for $\tau^{(1)}$, $\tau^{(2)}$ and the fact that

$$\mathbf{S}^{\mathbf{T}}\mathbf{S}'' + 2\mathbf{S}^{\mathbf{T}}\tau^{(1)}\mathbf{S}' + \mathbf{S}^{\mathbf{T}}\tau^{(2)}\mathbf{S} =$$

$$\mathbf{S}^{\mathbf{T}}\mathbf{S}'' + 2\mathbf{S}^{\mathbf{T}}\mathbf{S}\mathbf{S}'^{\mathbf{T}}\mathbf{S}' + \mathbf{S}^{\mathbf{T}}\mathbf{S}\mathbf{S}''^{\mathbf{T}}\mathbf{S} = \mathbf{S}^{\mathbf{T}}\mathbf{S}'' + 2\mathbf{S}'^{T}S' + \mathbf{S}''^{\mathbf{T}}\mathbf{S} = (\mathbf{S}^{\mathbf{T}}\mathbf{S})'' = 0 \,, \tag{2.121}$$

we reduce the Schrödinger to the form

$$\left[-\frac{1}{2\mu}\frac{d^2}{dR^2} + \mathbf{S}^{\mathbf{T}}\mathbf{V}^{\mathbf{adiab}}(\mathbf{R})\mathbf{S}\right]\phi = E\phi \,. \tag{2.122}$$

Since the kinetic energy in this representation is diagonal over channel indexes, this representation is diabatic representation. The matrices $\mathbf{S}$ and $\mathbf{e}^{-\tau^{(1)}\mathbf{R}}$ are unitary. As a result, $\mathbf{C}$ is a unitary matrix independent of R. A choice of arbitrary constant $\mathbf{C}$ gives different diabatic presentations, which are interconnected by a unitary transformation. From the physical point of view it gives a possibility to choose $\mathbf{S}$ as a unity matrix $\mathbf{I}$ for a some desirable distance ($R = \infty$, for example), and, as a result, at this distance the potential operator is diagonal and equivalent to the adiabatic curves.

Let some diabatic representation be known. The corresponding equation (2.122) is written in a form:

$$\left[-\frac{1}{2\mu}\frac{d^2}{dR^2} + \mathbf{V}^{\mathbf{diab}}(\mathbf{R})\right]\phi = E\phi \,. \tag{2.123}$$

Any other diabatic equation can be written in a form:

$$\left[-\frac{1}{2\mu}\frac{d^2}{dR^2} + \mathbf{C}^{\mathbf{T}}\mathbf{V}^{\mathbf{diab}}(\mathbf{R})\mathbf{C}\right]\varphi = E\varphi, \tag{2.124}$$

where

$$\phi = \mathbf{C}\varphi \,. \tag{2.125}$$

It can be useful for the case when there is diabatic equation with non-vanishing interaction between diabatic states in the asymptotic region (for example, the diabatic representation of the 0_u^+ symmetry). This asymptotic coupling can be excluded by the corresponding unitary transformation (2.125).

Everything concerning the mapping and the adiabatic and the diabatic representations can be extended for the time-dependent Schrödinger equation.

2.4.4 The numerical evaluation. An error estimation

If adiabatic potential curves V^{adiab} and matrices $\tau^{(1)}$ and $\tau^{(2)}$ are known, the Schrödinger equation with long-range potentials can be solved in two steps. In the first step, the non-diagonal diabatic potential operator is defined. After that the Schrödinger equation is solved in diabatic representation using coordinate transformation, as described already.

For the definition of $\mathbf{S}$ one needs to find out solution of the equation (2.122). Numerically the integration is carried out by the procedure:

$$\mathbf{S}(R+\Delta R) = \mathbf{S} - \Delta R \tau^{(1)} \mathbf{S},$$

$$\mathbf{S} = \mathbf{S}(R). \tag{2.126}$$

Let us estimate the precision of the procedure (2.126) for calculations of the transformation matrix S. The error accumulated during one step ΔR can be estimated from the unitary relation. Let $\mathbf{S}$ is unitary at the distance R. Then for $\mathbf{S}(R+\Delta R)$:

$$\mathbf{S}(R+\Delta R)\mathbf{S}^{\mathbf{T}}(R+\Delta R) =$$

$$\mathbf{S}\mathbf{S}^{\mathbf{T}} - \Delta R \mathbf{S}(\tau^{(1)}\mathbf{S})^{\mathbf{T}} - \Delta R \tau^{(1)}\mathbf{S}\mathbf{S}^{\mathbf{T}} + \Delta R^2 \tau^{(1)}\mathbf{S}(\tau^{(1)}\mathbf{S})^{\mathbf{T}} =$$

$$\mathbf{I} - \Delta R \mathbf{S}\mathbf{S}^{\mathbf{T}}(\tau^{(1)})^{\mathbf{T}} - \Delta R \tau^{(1)}\mathbf{S}\mathbf{S}^{\mathbf{T}} + \Delta R^2 \tau^{(1)}\mathbf{S}\mathbf{S}^{\mathbf{T}}(\tau^{(1)})^{\mathbf{T}} =$$

$$\mathbf{I} - \Delta R((\tau^{(1)})^{\mathbf{T}} + \tau^{(1)}) + \Delta R^2 \tau^{(1)}(\tau^{(1)})^{\mathbf{T}} = \mathbf{I} - \Delta R^2 \tilde{\tau}^{(2)} \,. \tag{2.127}$$

The error is $\Delta R^2 \tilde{\tau}^{(2)}$. If the integration distance $R_{max} - R_{min}$ is divided on N equidistant intervals ΔR, the total error for N intervals can be estimated as:

$$\mathbf{S}_{\mathbf{er}} = \frac{(R_{max} - R_{min})^2}{N} MAX(\tilde{\tau}^{(2)})_R. \tag{2.128}$$

Here $MAX(\tilde{\tau}^{(2)})_R$ means a matrix constructed from maximum values of each $\tilde{\tau}^{(2)}_{i,j}$ matrix element defined on entire interval $[R_{min};\ R_{max}]$. Thus, the error can be reduced by reducing the integration step. The error for each element of $\mathbf{S}$ is defined by the maximum value of the matrix element of $\tilde{\tau}^{(2)}$ and by the number of partition intervals.

2.5 Mapped time-independent FGR method for lifetime calculations

The applicability of the FGR method is not limited to the bound states calculations. In 1994-1999 M. Monnerville and J. M. Robbe [99, 100] have successfully applied the FGR method for calculations of lifetimes of pre-dissociated vibrational levels,

introducing the absorptive potential at one end of the grid. The method of absorptive potential itself originally was proposed by G. Jolicard *et al.* [58]. Á. Vibók and G. G. Balint-Kurti in 1991-1992 [131, 132] have proposed different forms of absorptive potential and have checked their efficiency using the time-dependent approach.

The pre-dissociated vibrational levels often have a small asymptotic kinetic energy (E_{as}) in comparison with the potential depth at small distances. In this case, it is worthwhile to use a non-uniform grid, i.e. to apply mapping.

This section describes how the mapping is introduced into the FGR method together with the absorptive potential.

The transformation of the Schrödinger equation induced the coordinate transformation is the same as for the ordinary potential. The principle of definition of the enveloping potential is the same: one has to define the maximum local energy for all internuclear distances. But there is one difference. The asymptotic kinetic energy E_{as} now is not zero and the grid step becomes constant at asymptotic region. This energy E_{as} should be taken into account. The general scheme of calculation of the enveloping potential is described in the section 2.8.

Following the recommendations by Á. Vibók and G. G. Balint-Kurti [131] and M. Monnerville and J. M. Robbe [99, 100], the optical potential is chosen as

$$V_{opt.} = -iA_5 \left[N \exp\left(-\frac{2L}{R - R_0} \right) \right] \tag{2.129}$$

with parameters calculated according to Ref. [131]. N is a constant $N = 13.22$, L is the effective length of the optical potential, R_0 is a starting point of the optical potential, A is a constant defining the absorption intensity.

Since the absorptive potential introduces imaginary part into diagonal elements of the matrix of the Hamiltonian in FGR, this matrix can not be made hermitian. Thus, the diagonalizing procedure takes much more time than in case of the hermitian matrix (especially, when the eigenfunctions are calculated).

An imaginary parts of an eigenvalue gives a half-width of the corresponding pre-dissociated level. The inverse of the width is a lifetime τ of this state.

2.6 Time-dependent FGR method.

In previous sections the time-independent Schrödinger equation was considered in application to the problem of vibrational and pre-dissociation levels of the diatom near the dissociation limit. But, the time-independent approach can not be applied for all problems, especially, when a temporal description of the process is required. Thus, for completeness, the supplementary approach - the mapped time-dependent method is considered in this section. All results of the previous sections, concerning the mapping procedure are generalized for the time-dependent approach. As a base method, a propagation scheme, developed mainly by R. Kosloff (for instance, [72]) is taken.

In this chapter, first, the ordinary (without the mapping) method of propagation [72] is briefly described. Then, the mapping is introduced into the method, and features of the mapped time-dependent method are discussed – a choice of the enveloping potential, the phase domain domain, the absorbing conditions.

2.6.1 General description

The propagation using the FGR method and the Chebyshev expansion (FGR-C) is one of numerous pseudo-spectral techniques of the time propagation, among those are also the Krylov method, the method based on Newton's interpolation formulas. A clear and whole description of these methods as well as of those based on the Chebyshev expansion one can find in Refs. [69, 70, 71, 62, 72]. A comparison with other propagation and time-dependent methods has been done by C. Leforestier *et al.* [77]. A complete description and analysis of several time-propagation techniques including the scheme with the Chebyshev polynomials are given by M.Monnerville [98]. Since FGR-C is used for the application of the mapping to the time propagation, it is briefly described below.

The time-dependent Schrödinger equation:

$$\mathbf{H}\psi(t,R) = i\hbar\frac{d\psi(t,R)}{dt}. \tag{2.130}$$

Here, $\mathbf{H}$ is a time-independent hermitian (in the ordinary sense) . $\psi(t,R)$ is a multi-component wave function. The solution is an exponential operator $e^{-\frac{i}{\hbar}\mathbf{H}t}$:

$$\psi(t_0+\Delta t,R) = e^{-\frac{i}{\hbar}\mathbf{H}\Delta t}\psi(t_0,R) \equiv \mathbf{U}(\Delta t)\psi(t_0,R). \tag{2.131}$$

The problem of the propagation in time can be separated in two essential parts. The first is a choice of a basis $\{g_n(R)\}$ of the representation of the wave function $\psi(t_0,R)$.

$$\psi(t_0,R) = \sum_n a_n(t_0)g_n(R) \tag{2.132}$$

The second is the procedure of the evaluation of $e^{-\frac{i}{\hbar}\mathbf{H}\Delta t}\psi(t_0,R)$

The R-grid basis in FGR-C is the same as in the time-independent FGR (Eq. (2.20)). The propagation (2.131) is carried out using an expansion of the propagation operator $e^{-\frac{i}{\hbar}\mathbf{H}\Delta t}$ as a function of t in Chebyshev polynomials with a variable t.

Thus, in two words, the technic committed below is following.

1. The wave function $\psi(t_0,R)$ at time t_0 is presented on grid points $\{R_j\}$. (Or $\psi(t_0)$ can be presented on the grid $\{p_k\}$ in the momentum space. See the section 2.1).

2. If the wave-function $\psi(t_0)$ in the moment t_0 is known, the $\psi(t_0+\Delta t)$ is calculated using Eq. (2.131). The exponent operator (2.131) is approximated by a sum of Chebyshev polynomials ϕ_n as

$$e^{-\frac{i}{\hbar}\mathbf{H}\Delta t} \approx \sum_{n=0}^{N_c} b_n(\Delta t)\phi_n \equiv \mathbf{P}(\Delta t). \tag{2.133}$$

The number N_c in the sum $\sum_{n=0}^{N_c} b_n\phi_n$ is sufficiently large to provide a desirable precision. The argument of functions ϕ_n is an operator $-\frac{i}{\hbar}\mathbf{H}\Delta t$, and a results of ϕ is an operator also. (If the time step is fixed, the operator $-\frac{i}{\hbar}\mathbf{H}\Delta t$ can be simply presented as a constant matrix $N \times N$, where N is a number of grid points or a number of basis functions $g_n(R)$.) Since the Hamiltonian is suppose to be time-independent, the operator $\mathbf{P}(\Delta t)$ does not depend of time and can be also presented by a constant $N \times N$ matrix in FGR. Coefficients b_n are calculated as it is described below. In order to reduce the calculation efforts the propagation in time is not organized simply as a consecutive multiplication of the wave function $\psi(R_j)$ by the constant matrix of $\mathbf{P}(\Delta t)$. The applied procedure is described below.

2.6.2 Chebyshev expansion

In this subsection a procedure of calculation of the evolution operator $\mathbf{U} = e^{-\frac{i}{\hbar}\mathbf{H}\Delta t}$ of Eq. 2.131 (more strictly speaking the procedure of calculation of $\mathbf{P}(\Delta t)$) is described as it is presented in [123]:

The operator $\mathbf{U}$ is expanded in polynomial series of the operator $-\frac{i}{\hbar}\mathbf{H}\Delta t$. The problem is reduced to an approximation of the scalar function e^z by a polynomial expansion, where z belongs to the domain which includes all eigenvalues of the operator $-\frac{i}{\hbar}\mathbf{H}\Delta t$. As the considering problem is limited over energies, the spectrum of $\mathbf{H}$ is limited, and this analogue with a scalar function is possible. The expansion by complex Chebyshev polynomials φ_k gives the best approximation among other possible expansions [123].

The complex Chebyshev polynomials φ_k are defined by the recurrence relation:

$$\varphi_k(z) = 2z\varphi_{k-1}(z) + \varphi_{k-2}(z)$$

$$\varphi_0(z) = 1, \quad \varphi_1(z) = z \tag{2.134}$$

with $z \in [-i; i]$.

In order to calculate polynomials with an operator argument, first, one should remove the energy spectrum of the operator $H\Delta t$ to the interval $[-1; 1]$. The maximum kinetic energy represented by the grid (see subsection 2.1.2) is $\frac{(p^g_{max})^2}{2\mu} = \frac{\pi^2}{2\mu\Delta R^2}$ (Eq. (2.25)). And the whole spectrum of the discrete Hamiltonian is in the interval:

$$\left[V_{min}; V_{max} + \frac{\pi^2}{2\mu\Delta R^2}\right]. \tag{2.135}$$

With a transformation from z to ω:

$$\omega = \frac{z - i(r+g)}{r}, \tag{2.136}$$

where r and g are:

$$r = \frac{\Delta t \left(\frac{\pi^2}{2\mu\Delta R^2} + V_{max} - V_{min}\right)}{2}, \quad g = V_{min}\Delta t, \tag{2.137}$$

one obtains:

$$e^z = e^{i(r+g)}e^{r\omega}, \qquad \omega \in [-i, i]. \tag{2.138}$$

At this step, e^z is expanded in the Chebyshev series:

$$e^z \approx \sum_{k=0}^{N_c} a_k \varphi_k(\omega), \tag{2.139}$$

where coefficients a_k are:

$$a_k = e^{i(r+g)} C_k J_k(r), \tag{2.140}$$

and $C_k = 1$ for $k = 1$ and $C_k = 2$ for $k > 1$, $J_k(r)$ are Bessel functions of the first kind of order k. The high accuracy of this expansion is provided by the fact that when $k > r$, $J_k(r)$ goes to zero exponentially fast. Thus, N_c has to be at least greater than r. In the working code $N_c = 1.2 \cdot r$.

The propagation scheme is then obtained by substituting $\hat{Z} = -\frac{i}{\hbar}\mathbf{H}t$ instead of z into Eq. (2.139) and using Eq. (2.140):

$$\mathbf{U}(\Delta t) \approx \mathbf{P}(\Delta t) = \sum_{k=0}^{N_c} a_k \varphi_k \left(\frac{-i\mathbf{H}\Delta t}{r}\right), \tag{2.141}$$

with $\varphi_k(\hat{Z})$

$$\varphi_k(\hat{Z}) = 2\hat{Z}\varphi_{k-1}(\hat{Z}) + \varphi_{k-2}(\hat{Z})$$

$$\varphi_0(\hat{Z}) = 1, \quad \varphi_1(\hat{Z}) = \hat{Z}. \tag{2.142}$$

The refinement of the scheme is based on increasing of the order of the expansion and not of decreasing the time step Δt.

2.6.3 Hermicity in the time-dependent FGR method

In (2.135), (2.139), (2.141), it was implicitly supposed that the potential and the total Hamiltonian are hermitian in FGR in order to the variable ω will be purely imaginary. For this, the whole spectrum of the operator $\mathbf{H}$ must be real. Even a small imaginary part in the spectrum leads to the exponential error during the propagation. The

spectrum of hermitian Hamiltonian is always real irrespective of a representation, if this representation is complete. But, in practice, if the non-hermitian representation is used, matrix elements are calculated numerically, and, as a sequence, the spectrum of the *matrix* of the Hamiltonian has a small imaginary part because of roundoff error of calculation of matrix elements. Thus, even if the Hamiltonian has a purely real spectrum, the spectrum of corresponding matrix can have complex eigenvalues. The issue is to use representations where the matrix of the Hamiltonian is hermitian explicitly. Because of non-completeness of the used basis, This matrix is always an approximation of the Hamiltonian, but it is better adapted for numerical calculation. Thus, all discussions concerning the hermicity of different terms of Hamiltonian, and also the discussion of the FGR-hermicity of the adiabatic equation are still valid and important for the time-dependent method using the Chebyshev expansion scheme.

2.6.4 Mapping

The mapping procedure is applied to the time-dependent Schrödinger equation by the same way as for the time-independent equation. Starting from the equation analogous to Eq. (2.65):

$$-\frac{1}{2\mu}\frac{d^2}{dR^2}\psi + V(R)\psi = i\frac{d}{dt}\psi \tag{2.143}$$

and repeating all steps of changing of the variable $R \to x$, the mapped time-dependent equation in a symmetric form becomes:

$$\left(-\frac{1}{4\mu}\left[\frac{1}{J^2}\frac{d^2}{dx^2} + \frac{d^2}{dx^2}\frac{1}{J^2}\right] + \bar{V}\right)\phi = i\frac{d}{dt}\phi \tag{2.144}$$

with the same effective potential defined by (2.71).

The only difference from the time-independent method is that the enveloping potential is not going to zero at the asymptotic region (The time-independent approach can use also the enveloping potential with the non-zero asymptotic energy, if resonances are calculated). V_{env} must provide the free asymptotic kinetic energy of the system. Thus, step size tends to a constant in the asymptotic region. The size of the grid and, as a sequence, a number of points are chosen in dependence of the problem. If the asymptotic kinetic energy is comparable with the depth of the potential, there is no a large advantage of applying of the mapping. The mapping is favorable if the the total energy energy is close to the dissociation limit, that corresponds to cold collisions. In this case, the asymptotic kinetic energy is much smaller that the depth of the potential well, and grid step can vary sufficiently, providing the effectiveness of the mapping.

The choice of the enveloping potential depends of the potential and of the problem and is discussed in details in the section 2.8.

In order to apply the Chebyshev propagation scheme to the mapped Schrödinger equation it is necessary to estimate the energy spectrum of the Hamiltonian and,

then, to define a volume of the time-energy phase space r from Eqs. (2.137). An interval of the energetic spectrum of the Hamiltonian in the MFGR:

$$\frac{(p^g_{max})^2}{2\mu} + V_{max} - V_{min} \tag{2.145}$$

p^g_{max} is defined from the smallest step of the real grid ΔR after the coordinate transformation:

$$p^g_{max} = \frac{\pi}{\Delta R_{min}} = \frac{\pi}{\min J(x)|_x}, \tag{2.146}$$

where Δx is suppose to be 1.

And the argument of Bessel functions is defined in the usual way:

$$z = \Delta t \Delta E/2 \tag{2.147}$$

The norm in the new representation can be written as:

$$1 = \int |\psi(R)|^2 dR = \int |\psi(x)|^2 J(x) dx =$$

$$\int |\phi(x) J^{-\frac{1}{2}}(x)|^2 J(x) dx = \int |\phi(x)|^2 dx \tag{2.148}$$

Thus the form of calculation of the norm stays the same.

The energy is calculated using the fact:

$$\mathbf{H}\psi(R) = J^{-\frac{1}{2}}(x)\mathbf{H}\phi(x). \tag{2.149}$$

And then

$$E = \int \psi^*(R)\mathbf{H}\psi(R) dR = \int J^{-1}(x)\phi^*(x)\mathbf{H}\phi(x) J(x) dx =$$

$$\int \phi^*(x)\mathbf{H}\phi(x) dx \tag{2.150}$$

Thus, the form of calculation of the energy stays also the same.

2.7 Mapped time-dependent FGR method for calculation of lifetimes.

The one of numerous applications of the time-dependent method is calculations of lifetimes. The method using the Chebyshev expansion was successfully applied for lifetime calculations of short-range pre-dissociated levels of symmetry 0^+_g of alkali

diatoms by O. Dulieu *et al.* [35]. Very often, in applications the pre-dissociated wave function is not limited by small internuclear distances. This is a case, for example, for the problem of ultra cold molecules, when the pre-dissociated vibrational wave function can reach of distances till 1000 a_0. The mapped time-dependent method is adapted for this kind of problems.

In order to absorb the outgoing flux reaching an end of the grid, the wave function is smoothly cut at the end of the grid after each time step. The procedure is similar to the procedure proposed by R. Heather and H.Metiu [50] and have been used by by O. Dulieu *et al.* [35]. The difference is that in the present calculations, instead of transferring on the new grid, the cut portion of the outgoing flux is not propagated at all, but it is taken into account for calculation of the norms. Using the optical potential for absorbing of the outgoing flux seems to be more difficult since the Chebyshev scheme is not adapted for the non-hermitian Hamiltonian (subsection 2.6.3). A discussion of the effectiveness of the absorbing boundary condition can be found in [68] (R.Kosloff and D.Kosloff).

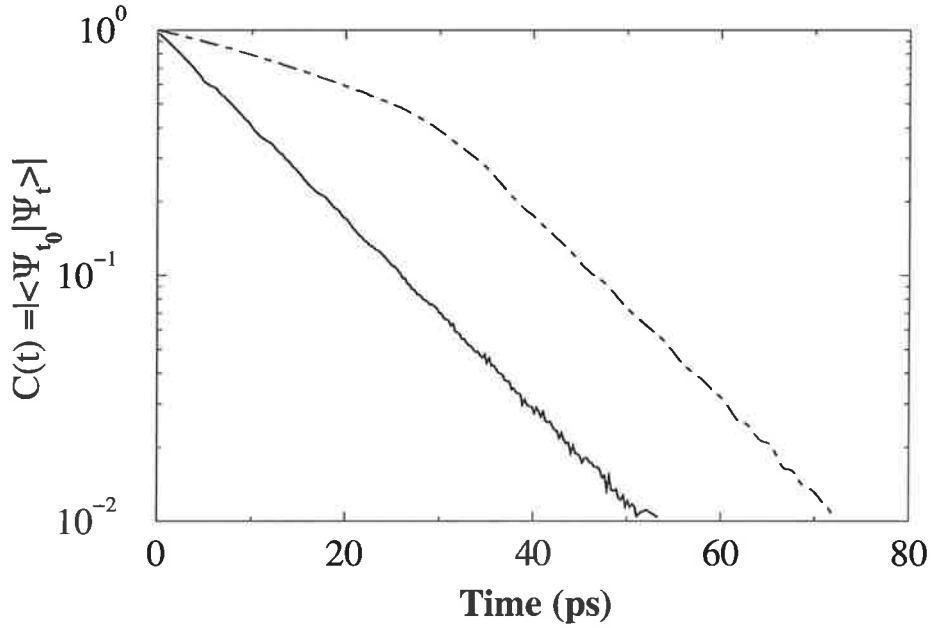

Figure 2.6: Two examples of $C(t)$ for one pre-dissociated level of 0_u^+ $(5S + 5P)$ symmetry of $^{87}Rb_2$. The energy of the level is 26.13 cm^{-1} over the $P_{1/2}$ dissociation limit. Full line – the initial wave function is purely pre-dissociated, dot-dashed line corresponds to the initial wave function containing the non-pre-dissociated $P_{1/2}$ component.

The method of the extraction of lifetimes during the propagation is following. The initial wave function ψ_0 for the propagation is an approximate pre-dissociated wave function. This wave function is propagated during the time. Since the propagation works as a filter for eigen states, components of the initial wave functions which do not belong to the exact pre-dissociated wave function, decay much faster (R.Bisseling *et al.* [17], O. Dulieu *et al.* [35]). After enough time, only components of the exact pre-dissociated wave function will rest in the interacting region of the potential. The lifetime of the pre-dissociated level ψ_0 is defined by a projection, $C(t)$, of the initial wave function on the wave function "filtered" by the time t [35].

The projection $C(t)$:

$$C(t) =< \psi_0|e^{-i\hbar\mathbf{H}t}|\psi_0 >=< \psi_0|\psi_t >, \tag{2.151}$$

The function $C(t)$ is called a correlation function. If the initial (pre-dissociated) wave function is decaying exponentially with a lifetime 2τ (τ corresponds to the decay of the norm):

$$\psi_t = e^{-\frac{t}{2\tau}}\psi_0, \tag{2.152}$$

then τ is extracted from the correlation function as:

$$\tau = -\frac{\log t_1 - \log t_2}{2(t_1 - t_2)}. \tag{2.153}$$

The initial wave function ψ_0 can be calculated, for example, in the time-independent FGR method when the coupling with continuum levels is switched off.

The graph 2.6 shows examples of the correlation function. Both examples correspond to the same pre-dissociated level. Initial wave functions are different. One initial wave function is purely pre-dissociated. The decay of this wave function is purely exponential (full line). Another curve represents the initial wave function containing continuum $P_{1/2}$ components. The initial behavior of the decay is not exponential — the dot-dashed line is not direct. After some time ($t_0 \approx 30\ ps$), the continuum components go away, the decay becomes exponential and a slope of the dot-dashed curve becomes the same as for the solid line, demonstrating the same lifetime.

2.8 Choice of the enveloping potential

This section describes how the maximum kinetic energy, i.e. the enveloping potential, must be calculated for different types of potentials.

A correctness and completeness of the representation of wave functions in FGR depends of a choice of the expansion basis $\{g_n\}$. A choice of the grid in R defines maximum momentum, which the grid can represent (see Eq. (2.59)):

$$\Delta R = \frac{\pi}{p^g(R)} \tag{2.154}$$

This momentum must be larger than the momentum $p(R)$ proposed by physical conditions of the problem:

$$p^g \geq p_{max} \tag{2.155}$$

or, defining the enveloping potential:

$$V_{env}(R) = -\frac{(p^g)^2}{2\mu} \tag{2.156}$$

$$-V_{env}(R) \geq E_{max}(R) = \frac{p^2(R)}{2\mu} \tag{2.157}$$

From (2.154) and (2.157):

$$\Delta R = \frac{\pi}{\sqrt{-2\mu V_{env}}}. \tag{2.158}$$

For the coordinate transformation $R = f(x)$:

$$\Delta R = \frac{dR}{dx}\Delta x = \frac{\pi}{\sqrt{-2\mu V_{env}}}. \tag{2.159}$$

Δx can be always chosen to be equal to 1. And with $J = \frac{dR}{dx}$:

$$\Delta R = J = \frac{\pi}{\sqrt{-2\mu V_{env}}}. \tag{2.160}$$

Thus, J determines the step of the real grid and is determined by the enveloping potential. As it was discussed, $|V_{env}(R)|$ is a curve with values which are larger than local maximum kinetic energy $E_{max}(R)$.

Thus, the problem of the mapping is reduced to the definition of the quantity $E_{max}(R)$.

The wave function does not vanish in the classically forbidden region where the momentum becomes imaginary. This part of the wave function is exponentially decreasing. It previous classical consideration of the enveloping potential, it was supposed that this exponential tail is small in comparison with the rest of the wave function. If it is not a case one has to include into consideration a domain of the phase space (R, p), where the wave function are not negligible.

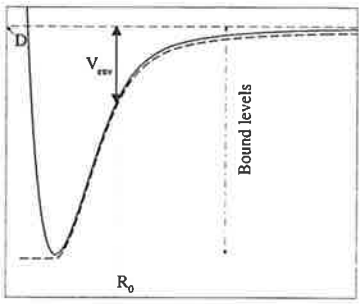

Figure 2.7: The enveloping potential (the dashed line) for the one-channel potential (solid line).

The correlation between ΔR and p in the classically allowed region is defined from classical relations between p and ΔR like Eq. (2.158). In the classically forbidden region it can be done using semi-classical estimations. Implicitly, the present method takes into account the classically forbidden regions, if the parameter β is slightly smaller than unity. By the same way the accuracy of the representation of high momentum components can be improved. A more elaborated semi-classical analysis rests for the future work.

The definition of the enveloping potential depends of the problem and the potential $\mathbf{V}$. Here some of cases are considered. (D means the first dissociation limit $\mathbf{V}$.)

One-channel potential, bound levels.

If $\mathbf{V}$ is a one-channel potential, and only bound states are under consideration, then the enveloping potential is simply the potential curve $V(R)$:

$$V_{env}(R) = V(R) - D. \tag{2.161}$$

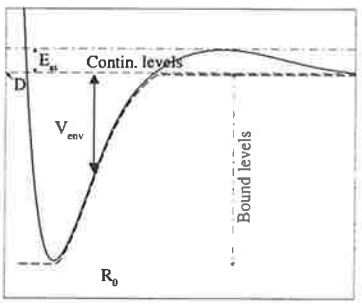

Figure 2.8: The enveloping potential for the one-channel potential with a hump.

In a case of one potential curve $D = V(\infty)$. As it was discussed in the section 2.3, the enveloping potential in the present calculations does not repeat the behavior of the potential at small distances – from the beginning of the grid to the minimum of the potential. The grid step in this region stays constant. In this region the potential energy varies quickly, and the exponential tail of a wave function in the classically forbidden region can be sufficient. The constant minimum step provides

the correctness of the representation of wave function. This procedure introduces only a few additional grid points.

This case of the enveloping potential is demonstrated on the graph 2.7. A length of a full line with big arrows corresponds to the value of $V_{env}(R_0)$ at the distance R_0.

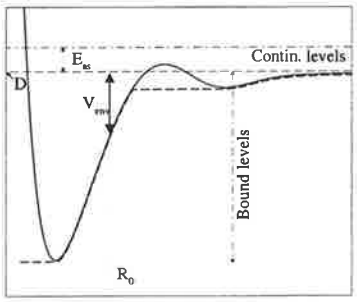

Figure 2.9: The enveloping potential for the potential with a hump and a well.

If the potential has a hump at some distance (for example, graphs 2.8 and 2.9) with the potential energy larger than the dissociation limit, from the classical estimations, the enveloping potential must be zero for all R, where $V(R) > D$. But due to the tunneling effect the probability of the presence is not zero there, and V_{env} must provide the representation of the wave function in this region. In the practice, $V_{env}(R)$ in such region is chosen to be constant and equal to the minimal value of $V(R)$ at the right side from the hump.

If the potential never becomes lower than D ($V(R) > D$) at right of the hump, then $V_{env}(R) = 0$ at the right (the graph 2.8). If not, it means that there is an outer well, and $V_{env}(R)$ on points of the hump is equal to depth of the well (the graph 2.9). The lines with two big arrows show the value $V_{env}(R_0)$ of the enveloping potential for bound level calculations.

Bound levels. Analytical mapping.

In the previous case $V_{env}(R)$ can be also an analytical curve, situated under the potential curve of $V(R) - D$. In this case $f(x)$ and all its derivatives J, J', J'' are calculated analytically [64]). The most natural choice of this analytical curve is a curve repeating the asymptotic behavior of the potential – as a rule – a C_n/R^n curve. A similar approach was proposed by E.Tiesinga *et al.* [125].

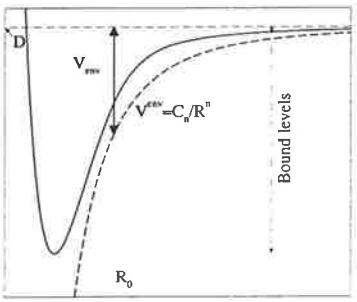

Figure 2.10: The analytical enveloping potential.

The obvious advantage of the analytical approach is a possibility of the exact evaluation of quantities f, J, J', J''. (The analytical enveloping potential could be useful for estimations of the accuracy of the method using an analytical potential curve.) This advantage becomes not so important if the potential is not analytical – the error of the calculation of the potential in intermediate points and the error of numerical valuation of f, J, J', J'' are comparable.

The graph 2.10 demonstrates the case of the analytical potential. A full line with big arrows shows again a value of $V_{env}(R_0)$ at the distance R_0. It is evident, that the phase space defined by this enveloping potential (and as a sequence — the basis size, N) is larger than in the previous case due to the high density of points at small distances, where $V_{env}(R)$ and $V(R)$ are different.

One-channel potential, continuum levels

The enveloping potential for calculations of levels of continuum in potential $\mathbf{V}$ is easily defined if the enveloping potential for bound levels is known. Let V^b_{env} is the enveloping potential for $\mathbf{V}$, determined only for bound levels calculations. Levels of the continuum with asymptotic energies from 0 to E_{as} can be included into the consideration by addition of the constant E_{as} to V_{env}:

$$V_{env}(R) = V^b_{env}(R) - E_{as}. \tag{2.162}$$

The enveloping potential with the non-zero asymptotic energy is used for the mapping in the time-dependent equation for lifetimes calculations and for the simulation of cold collisions. It is also used in the time-independent approach coupled with the method of the optical potential where the grid must provide the kinetic energy of the outgoing flux. This situation is demonstrated by graphs 2.8, 2.9 and 2.11. The value $V_{env}(R_0)$ (demonstrated by the length of a full line with big arrows) must be now increased on the quantity E_{as} in comparison with previous cases. (At all graphs these lines are drawn for bound levels only.)

Multi-channel adiabatic potential.

Consider now the multi-channel problem with the adiabatic potential. Since the non-adiabatic coupling term $\tau^{(1)}_{\gamma,\gamma'}\frac{d}{dR}$ does not introduce the additional kinetic energy in the Hamiltonian, it does not increase the momentum. Thus, the curve $V_{env}(R)$ coincides with the lower adiabatic curve (let say $V_1(R)$). For bound levels:

$$V_{env}(R) = V_1(R) - V_1(\infty), \tag{2.163}$$

for the continuum levels:

$$V_{env}(R) = V_1(R) - V_1(\infty) - E_{as}, \tag{2.164}$$

At the figure 2.11 this case of the potential is demonstrated.

The full line with two big arrows show the local value V_{env} with accounting the asymptotic energy E_{as}. The including of E_{as} provides the correct representation of continuum levels.

Multi-channel diabatic potential.

The simplest way of the calculation of V_{env} for the multi-channel diabatic potential is to compute the corresponding adiabatic curves and to use, then, the method described in the previous case.

An example of the two-channel diabatic potential.

An alternative way of the calculation of V_{env} for diabatic potential is to estimate how adiabatic curves can be deep. Consider the two-channel example with the adiabatic coupling between channels – $V_{1,2}(R)$. $V_{env}(R)$ for *bound levels* is defined in two steps. First, the preliminary enveloping potential $V^p_{env}(R)$ is calculated for each distance R as the minimum of two quantities

$$V^p_{env}(R) = \min(V_1(R) - D, V_2(R) - D) \tag{2.165}$$

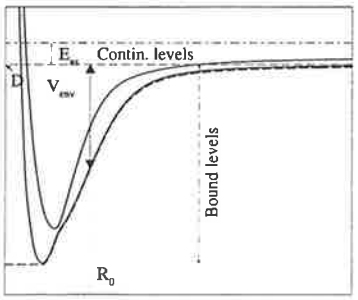

Figure 2.11: The enveloping potential for the two-channel adiabatic potential. The enveloping potential follows the behavior of the lower potential.

The second step takes into account the effect of the coupling. The coupling changes (slightly, in general) potential curves, that may increase the local kinetic energy. The most change is in the region of the crossing R_c. This change is equal to $V_{1,2}(R_c)$. Thus, the coupling $V_{1,2}(R)$ must be accounted in the enveloping potential. For the bound levels:

$$V_{env} = V^p_{env} - |V_{1,2}(R)| + |V_{1,2}(\infty)|. \tag{2.166}$$

Here, the enveloping potential overestimates the maximum local energy, since the additional increasing of local kinetic energy due to the coupling is smaller than $|V_{1,2}(R)|$ everywhere outside of crossings. The last term is added, since continuum states, introduced by a asymptotic shift $|V_{1,2}(R)|$ at $R = \infty$, must be excluded from the consideration. Continuum levels can be accounted by an addition of the corresponding E_{as}:

$$V_{env} = V^1_{env} - |V_{1,2}(R)| + |V_{1,2}(\infty)| - E_{as}. \tag{2.167}$$

Once the enveloping potential is known, the mapping functions $J(x)$ and $f(x)$ are calculated using Eq. (2.160). There is a technical difficulty with a calculation of $J(x)$. If the potential $\mathbf{V}$ is quite complex, the enveloping potential, obtained as described above, will have breaks. It occurs, for example, in the place where two potential curves are crossing. In this region, the mapping functions J, J', J'' have big breaks or are not defined at all. On the graph 2.12 an example of two-channel potential of Rb_2 near the crossing is demonstrated (full lines on the upper panel). The enveloping potential V_{env} calculated as described above is shown by a dashed line. At the lower panel one mapping function J', calculated from V_{env}, is also shown. J' is broken in the region of the crossing . This break reduces the accuracy of representation of the mapping and, as sequence, reduce the accuracy of obtained bound levels.

In order to obtain more smooth V_{env} the next procedure of the smoothing is proposed.

$$\tilde{V}_{env}(R) = \frac{1}{a\sqrt{\pi}} \int_{-\infty}^{+\infty} exp\left(\frac{r-R}{a}\right)^2 V_{env}(r)dr \tag{2.168}$$

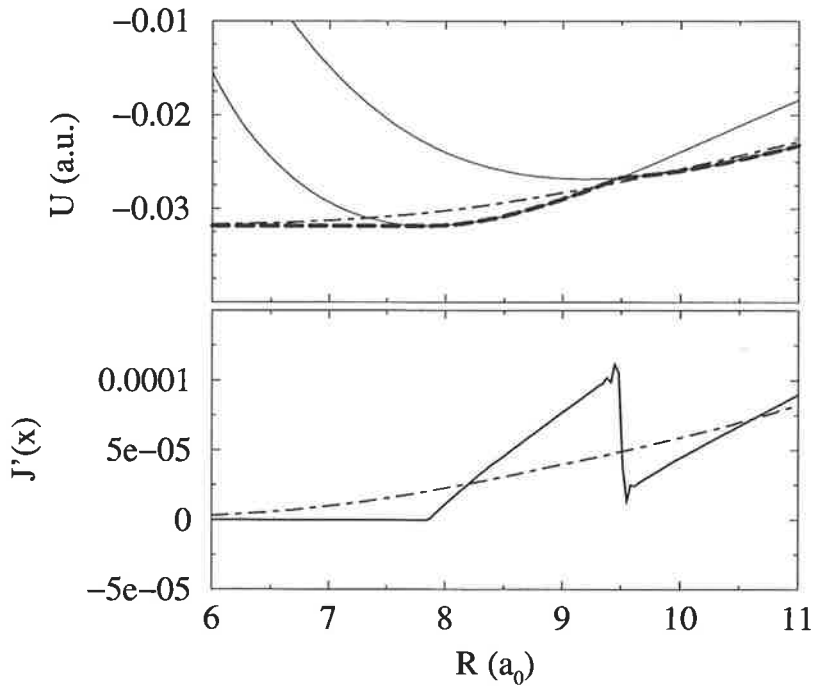

Figure 2.12: Efficiency of smoothness of the enveloping potential calculated for two-channel system 0_u^+, $5S + 5P$ of Rb_2. Upper panel: full lines – potential curves of the 0_u^+ symmetry, dashed line – non-smoothed enveloping potential, dot-dashed line - smoothed potential according to Eq. (2.168) with $a = 2\ a_0$. Lower panel: Curves represented the quantity $J'(x)$ as a functions or R. Full line is $J'(x)$ calculated from the non-smoothed V_{env}, dot-dashed line represents the smoothed $\tilde{V}_{env}$.

Each point of $\tilde{V}_{env}$ is now correlated with neighboring points. As one can see from Eq. (2.168) that all derivatives of $\tilde{V}_{env}$ over R are defined and continuous. The new enveloping potential is shown by the dot-dashed line on the upper panel of the graph 2.12, the dot-dashed line of the lower panel shows the new J'.

2.9 Conclusion

In this chapter of the Thesis the mapped Fourier grid representation method was developed. Comparing with the uniform method, a main advantage and a main idea of the proposed method is to adapt the local grid step to the local de Broglie wave length of the most oscillating wave function. Since the ordinary FGR basis determines the equally-spaced grid, the coordinate R in the Schrödinger is transformed into the new variable x in such way that in this new coordinate x, the grid rests equally-spaced, whereas the most oscillating wave function has almost the constant frequency in coordinate x, that reduces needed basis and, as a sequence, the computation efforts to the minimum.

The matrix of the Hamiltonian is written in grid over the variable x in FGR. As in the uniform method, diagonalization of this matrix gives eigen energies and eigen wave functions of the Hamiltonian. The efficiency of the mapping is demonstrated by

$\{p, R\}$ curves in the phase space. Using the uniform distribution of grid points in the coordinate x between oscillations of the most excited level allows also to introduce a unique parameter β, which controls *a priori* the accuracy of calculations.

The proposed phase space approach for the choice of the basis can be made more accurate including a consideration of the classically forbidden region. This problem rests opened.

MFGR can be used not only for calculations of bound levels. Using MFGR together with the method of the optical potential, energies and widths of levels of the continuum levels can be calculated, that is also very frequent problem of cold collisions.

The chapter describes also some aspects of the application of the method at the adiabatic Schrödinger equation. It can be useful if a use of a hermitian representation of the Hamiltonian is preferable, that is a case, for example, of the time-propagation techniques using the Chebyshev expansion.

It was shown that MFGR can be used also for the time-dependent Schrödinger equation. In the chapter it is demonstrated that MFGR can be coupled with the time-propagation scheme using the Chebyshev polynomials, that can be used for a dynamics simulations of cold collisions.

Chapter 3

Precision. Comparison with Other Methods.

The FGR method is a spectral-type numerical technique [70]. This means that, in principle, the error, as a function of a points number N, decreases faster then any power of N. It is valid if a potential of the Hamiltonian is analytic - the potential and its derivatives can be calculated exactly. R.Kosloff [70] has shown that for a harmonic oscillator a relative precision of calculation of vibrational levels is of order 10^{-14}. It was demonstrated that the precision increases exponentially with the density of points.

An alternative Numerov method is widely used for the solution of differential equations. It is a finite difference method and its error is decreasing as $O(N^{-5})$ with increasing of N. Thus, the FGR method is superior over the Numerov method. On the hand, the Numerov method have proved its applicability and can be used for the estimation of the precision of the developed FGR method.

In practice, the potential is presented numerically by grid points and, usually, its derivatives on intermediate points are calculated using the spline procedure (As it is done in the present program) . It limits the precision of both methods.

This chapter is devoted to the comparing of the precision of the FGR method with the Numerov method using realistic potentials. First, two examples, the Na_2 ($^1\Pi_g$) and Cs_2 (1_g), of potentials are taken for the comparison of results for bound level calculation. Then, the precision of calculations of wave functions is discussed for both methods. In the section 3.4 the precision of lifetime calculations is considered. Time-dependent and time-independent FGR methods are analyzed with this goal.

3.1 Vibrational levels of Na_2 ($^1\Pi_g$). Comparison with the Numerov method.

a) *Tests carried out in the article [64]. The text taken from the paper will be typed again by* this font.

The efficiency and accuracy of the mapped FGR method described above can be

checked by comparison with a standard method, such as the well known Numerov Cooley algorithm [18], as well as with the usual FGR method.

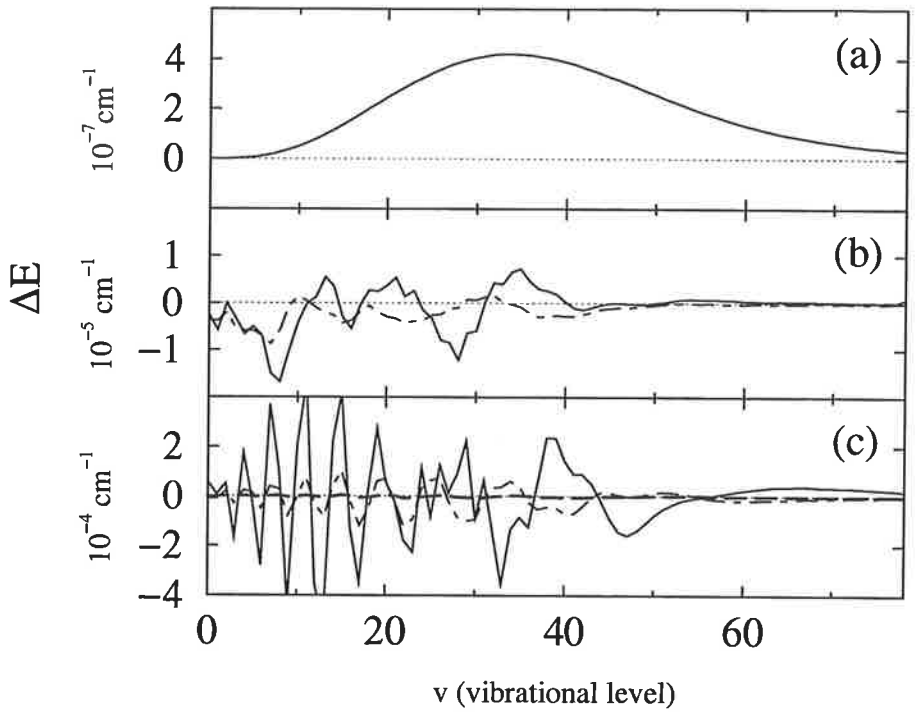

Figure 3.1: Accuracy ΔE of the computed energies for the 80 lowest $Na_2(1_g)$ vibrational levels in the $Na_2(^1\Pi_g, 3s+3p)$ potential. The three figures represent a) - ΔE, from Numerov integration with $\Delta R = 0.0025$ (34000 points). b) - ΔE, for energies computed by the FGR method with uniform grid. Solid line: N=950 points; dash-dotted line: N=1140 points. c) - ΔE, for the FGR method with the mapping defined by Eq. (2.61), considering different values of the parameter β. Solid line: $\beta = 0.6$, N=170 points; dash-dotted line: $\beta = 0.4$, N =254 points; dashed line: $\beta = 0.2$, N=506 points.

We have performed accuracy tests computing the energies of the first 80 vibrational levels in the potential Na_2 $^1\Pi_g$, $3S+3P$ [89] already displayed in Fig.2.1 extended at long range by the asymptotic $-6.48/R^3$ curve predicted in [92]. We chose a grid extending from 5.0 a_0 to 90 a_0, and we display in Fig 3.1 the results of the convergence tests. The precision of the Numerov method itself is illustrated in the upper panel, where we show that the computed vibrational energies E_v vary by less than $4 \cdot 10^{-7}$ cm^{-1} when the step size is modified from $\Delta R = 0.00125$ a_0 (68000 points) to $\Delta R = 0.0025$ a_0 (34000 points). The binding energies extend from 1103.78 cm^{-1} to 2.44 cm^{-1}. Taking as a reference the first calculations with the Numerov algorithm, we show that a typical 10^{-5} cm^{-1} accuracy can be obtained with the FGR method using a constant step and a number of points of the order of 1000.

The convergence tests for the mapped FGR method varying the β parameter are also given in the figure. The same level of accuracy can be reached with $\beta = 0.2$ and $N = 506$ grid points, thus reducing N by a factor of 2. We should note that the accuracy obtained with $\beta = 0.6$ is already better than 10^{-3} cm^{-1}, and corresponds only to 170 grid points for

determination of 80 vibrational levels. In contrast, for $\beta = 1$, only the 20 lowest levels are obtained accurately, the error on the energy of levels $v \geq 40$ reaching 0.5 cm^{-1}. Finally, we have checked that for $\beta > 1$, the method is not even yielding all the eigen-energies.

The calculated error on the energy resulting from the Numerov calculation Fig. 3.1 is clearly non-uniform. Indeed, changing the number of grid points modifies the local description of the potential curve, which will affect mainly energy levels with outer turning points located in the region $10\ a_0 < R < 16\ a_0$ where the slope of the potential is large. In contrast, the calculated error in the FGR method is uniformly distributed on all levels, due to the global character of the method.

b) *Additional tests carried out in the Thesis using an improved version of the program*

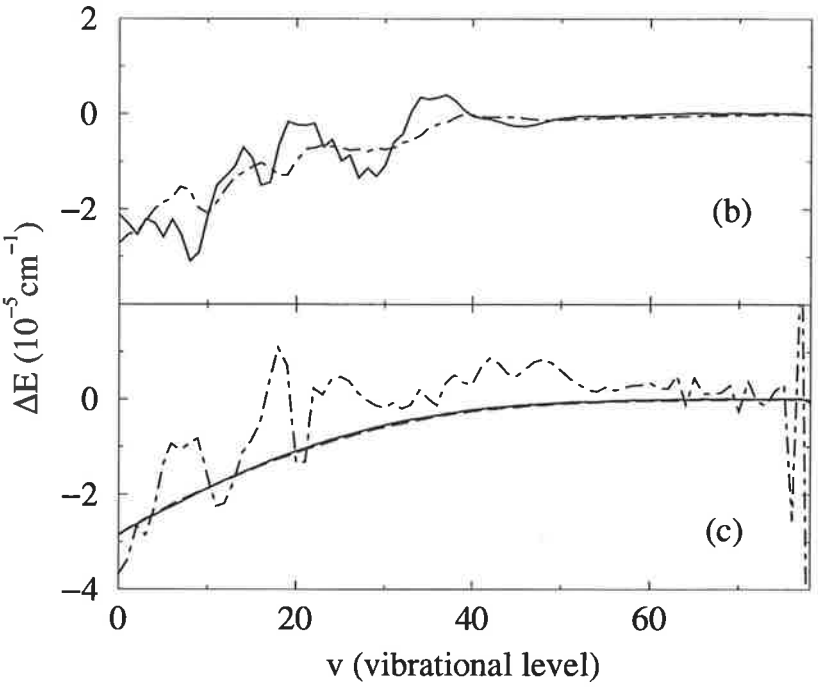

Figure 3.2: Improved calculations with parameters close to parameters of the figure 3.1. The calculations using the Numerov method with 576000 points are chosen as a reference. Two panels correspond to the *b* and *c* panels of the Fig. 3.2. Panels: b) - ΔE, for energies computed by the FGR method with the uniform grid. Solid line: N=953 points ($\beta = 0.418$); dash-dotted line: N=1141 points ($\beta = 0.349$). c) - ΔE, for the FGR method with the mapping defined by Eq. (2.61), considering different values of the parameter β. Dash-dotted line: $\beta = 0.4$, N=233 points; solid line: $\beta = 0.2$, N =465 points; dashed line: $\beta = 0.1$, N=927 points.

Recently (after a publication of the paper [64]), additional accuracy tests has been done using an improved version of the program. A main improvement in the program is a new procedure of calculations of the mapping functions, $f(x), J, J', J''$, from the enveloping potential. This new procedure is described in details in the section 2.8.

Figure 3.2 presents results obtained with the new program. Two panels (*b* and *c*) of the figure correspond to *b* and *c* panels of the Fig. 3.2. The parameters are slightly different on two figures.

- A maximum calculation error for the non-mapped FGR method is the same in new and old calculations with using of the same number of points.

- The accuracy of the mapped FGR method increases essentially in comparison with old results ant it becomes the same as for the non-mapped method. Thus, the mapping does not introduce a significant error into calculations.

- Starting from a density of points corresponding $\beta \leq 0.2$, the difference between energies obtained by two methods does not decrease any more. This fact is preliminary attributed to the error introduced into calculations by the splines procedure, which is used in both methods.

The choice of the Numerov methods a reference for calculations is justified, since this method is stable. It means that computed levels have limits in respect of decreasing of grid step. Increasing the density of points (decreasing the parameter β), the FGR method also demonstrates a stability. The graph 3.3 demonstrates the difference between calculations with two different parameters β. The maximum difference is of the same order of magnitude as for Numerov method with $N = 68000$, 34000 from the graph 3.1. Thus, this order of the error 10^{-7} cm^{-1} is attributed to the procedure of interpolation of potentials and derivatives.

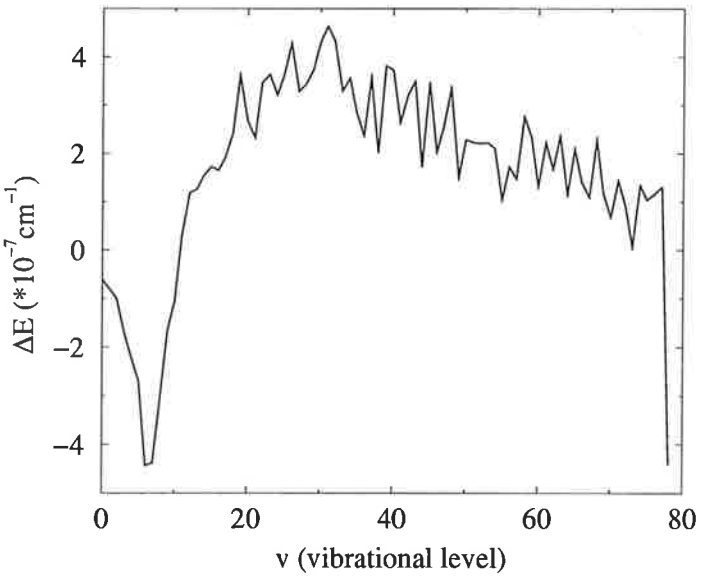

Figure 3.3: The stability of the FGR method. The difference between bound levels calculated in the mapped FGR method with two parameters β 0.07 and 0.1.

3.2 Example of a wave function extending at long range: potential Cs_2 (1_g).

Considering now the example of the potential $Cs_2(1_g, 6s, 6p^2P_{3/2})$[94, 92], we have computed the vibrational levels up to $v = 337$, with a grid of extending from $4.5a_0$ to $500a_0$. The number of points can be reduced from 6500, without coordinate change, to 658 with the simple transformation defined in Eq. (2.61), using a value $\beta = 0.6$ reducing the memory necessary for computation by a factor 120 times. For the chosen example, the highest calculated vibrational level has an energy as small as $E_{337} = -0.0317\ cm^{-1}$, the $v = 0$ level staying at $E_0 = -1359.6804\ cm^{-1}$. The convergence tests show a stability better than $10^{-4}\ cm^{-1}$ when the parameter β is varied from 0.9 to 0.4.The diagonalization procedure yields N eigenvalues, for which only the lower ones correspond to bound states, the upper ones being continuum states up to a positive energy E_β^{max} which depends upon β. The efficiency of the mapping using the real potential is clearly manifested in this example : for the grid considered above, choosing $\beta = 0.6$, mapping using the real potential involve 658 grid points and hence 658 eigenvalues, the upper one lying at an energy $E_\beta^{max} = 12729\ cm^{-1}$. The same calculations with an enveloping potential $-C_3/R^3$ (where we have taken $C_3^{env} = C_3$ so that the enveloping curve differs from the real one only at short and intermediate distances), would require $N = 878$ grid points. The increase in the number of points is not a substantial one, but the maximum energy is now $E_\beta^{max} = 87790\ cm^{-1}$, so that the energy domain spanned by the method is as high as $89000\ cm^{-1}$. Such a large energy range can result into severe inconvenience for application to time-dependent problems.

The repartition of grid points in the example has been illustrated in Fig. 2.3. It is remarkable that vibrational energies can be obtained with accuracy better than $10^{-4}\ cm^{-1}$using only $N = 564$ grid points (with $\beta = 0.9$) for levels with a wave function exhibiting up to 337 nodes. A possible drawback of this achievement could be that N becomes too small for accurate definition of the wave function : we show below that this is not the case.

3.3 Wave function in the mapped FGR method.

In calculations employing a discrete grid, the wave function is represented on a finite set of grid points. Values of the wave function at other distances have therefore to be determined by interpolation. Linear interpolation then yields low quality results (see Fig. 3.4). We describe here a better approach for the interpolation of the wave function in the FGR method, using the intrinsic properties of the Fourier representation [72].

The interpolated wave function in this case is [72]:

$$\psi(q) = \sum_{j=1}^{N} \psi(q_j) sinc\left[\frac{\pi}{\Delta q}(q - q_j)\right], \tag{3.1}$$

where q_j is a working uniform grid (with or without mapping), q is any intermediate point, Δq is a grid step, and we have defined the function $sinc(z) = \frac{sin(z)}{z}$.

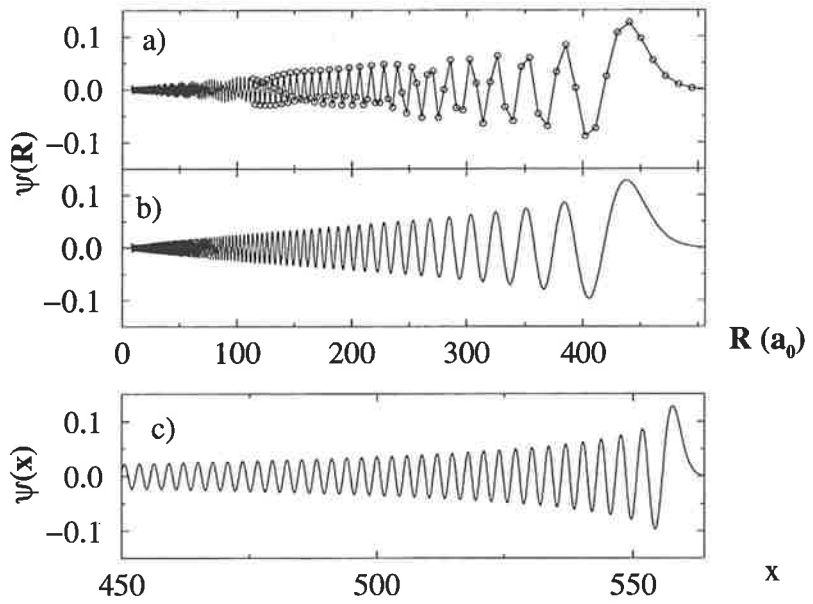

Figure 3.4: The $v = 332$ vibrational wave function for the Cs_2 $(1_g, 6s+6p^2P_{3/2})$ potential (see Fig. 2.1), computed at the grid points defined with the mapping of the Eq. (2.61). Here, $R_{max} = 500a_0$, $N = 564$. a) - wave function at every grid point, with linear interpolation between two points ; b) - wave function interpolated according to Eq. (3.1) choosing $N_{interp} = 10000$ (see text). c) - interpolated wave function in the x variable, showing only the part corresponding to large R. Comparing c) to b), one can appreciate the regularity of the oscillations in the mapped wave function)

In Fig. 3.4 we display the wave function, computed with *sinc* interpolation at a large number ($N_{interp} = 10000$) of q values, for the 333^{st} ($v = 332$) vibrational level of $Cs_2(1_g)$. Comparison with linear interpolation clearly illustrates the good quality of the second interpolation. Of course, we have checked the accuracy of the interpolated wave functions by comparing to standard methods.

In the same figure, we show the influence of the mapping procedure on the shape of the wave function. One can see that the two representations are quite different: the mapping has an effect of "stretching" the grid at smaller distances, where the density of points needs to be large. Indeed, if the unmapped grid has sufficient point density in this region, it has too many points at large distances, where oscillations of the wave function are not so frequent. The mapping procedure eliminates such superfluous points, yielding an uniform distribution of the number of grid points per oscillation. It is remarkable that with mapping good quality wave functions can be obtained with a reduced number of points at each oscillation: indeed, the wave function drawn in Fig. 3.4 has 331 nodes and has been been obtained using only $N = 564$ grid points, that is less than two points per oscillation.

The precision of the FGR method was checked also for wave functions obtained in calculation. The $Na_2(^1\Pi_g, 3s + 3p)$ potential is used again. First, the accuracy of Numerov method is verified. The reference now is a wave function for $\nu = 0$ obtained with $N = 576000$ points. (The further increasing of number of points N

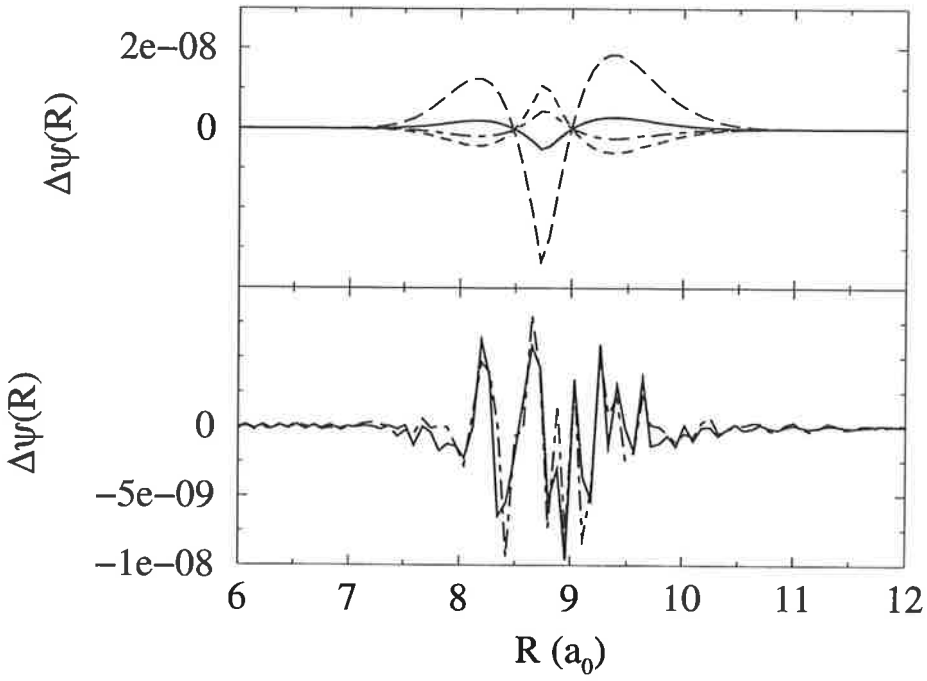

Figure 3.5: The calculation accuracy $\Delta\psi(R)$ of the wave function of $\nu = 0$ vibrational levels of $Na_2(^1\Pi_g, 3s + 3p)$. Upper panned: The reference is the wave function obtained with $N = 576000$ points. Solid line: $N = 288000$ points, dotted line: $N = 144000$ points (the same as for $N = 288000$), dashed line: $N = 72000$ points, long dashed line: $N = 36000$ points, dot-dashed line: $N = 18000$ points. Lower panned: the reference is the $\nu = 0$ wave function obtained in the FGR method with $\beta = 0.07$, $N = 1323$. The difference with wave function obtained for: solid line – $\beta = 0.1$, $N = 927$, dashed line – $\beta = 0.2$, $N = 465$.

in the Numerov method does not improve the result *with the available program of the Numerov method.*) The upper panned of the graph 3.5 shows a comparison with results for different number of points. Thus, the accuracy is limited by error of order 10^{-8}.

The same test was made for the FGR method (the lower panned of the graph 3.5). The interpolation is made according to Eq. (3.1). The error is the same (or slightly less), than the error given by the Numerov method. For a completeness of the description the difference between wave functions obtained in two method with the smallest steps (the graph 3.6) is given. This graph together with the graph 3.7 gives an idea about the mutual trustworthiness of two method. This difference is larger than $\Delta\Psi$ "inside" both methods (graph 3.5). Thus, the best precision of the FGR method *with using the available code and calculated potentials* for calculations of wave functions can be estimated as 10^{-8}.

The graph 3.7 represents the precision of wave function calculations as a function of the parameter β. The reference is the calculations with $\beta = 0.07$. Again, the best precision can be estimated as 10^{-8} for $\beta \leq 0.2$. At the other hand, the wave function is still calculated with a good accuracy $2 \cdot 10^{-5}$ with $\beta = 1$.

In conclusion, it is necessary to mention another method – the recently developed

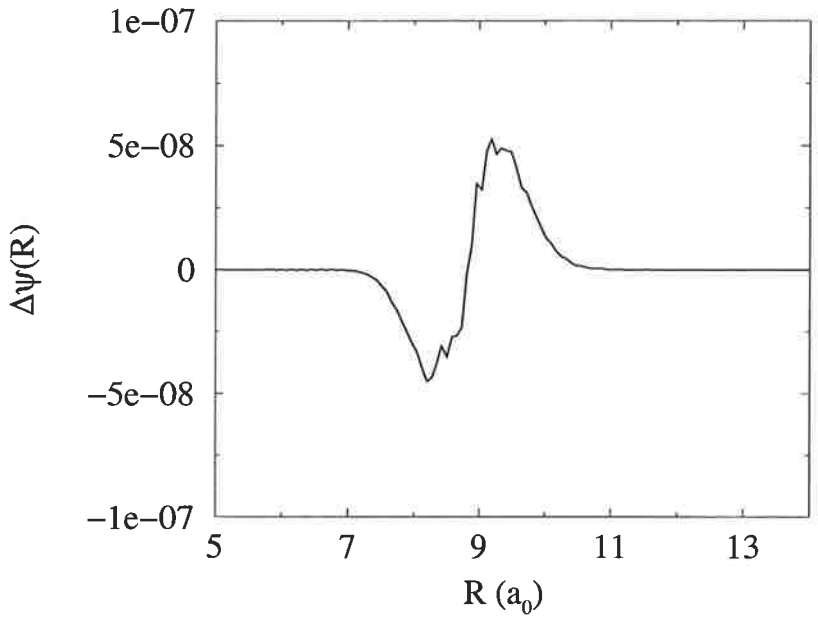

Figure 3.6: The difference between wave functions calculated by two methods. The smallest step is chosen for both methods: $N = 576000$ is used in the Numerov method, $\beta = 0.07$ is chosen for the FGR method. This difference larger than $\Delta\psi$ for each method with indicated parameters. It gives an idea, how small can be β, and what is a order of accuracy of both methods

integral equation method (IEM) by R.Gonzales *et al.* [46]. It is also (as the FGR method) a spectral-type numerical method. Its main feature is that the Schrödinger equation is converted into the integral equation. This integral equation is solved using so-called spectral Clenshaw-Curtis quadrature method. Authors of the mentioned paper compare also a precision of this method with results given by the Numerov method. Two analytical potentials are used for precision tests – $V = l(l+1)/R^2$ (the theoretical solution is available) and $V = 1/(R + R^4)$. Several wave functions with positive asymptotic energies were calculated. The accuracy of IEM was verified comparing these wave functions with theoretical values. The accuracy of Numerov method is better than results presented in the Thesis – of order $0.2 - 0.7 \cdot 10^{-8}$ for $N = 12000 - 410000$. The accuracy of IEM is much better – $1.3 \cdot 10^{-14} - 2 \cdot 10^{-13}$ for different wave functions.

The IEM accuracy is much better than the accuracy of the method considered in the Thesis because IEM uses the analytical potential for tests, but the FGR method is checked here only on numerical potentials. The accuracy tests with analytical potentials were carried out by R. Kosloff [70]. The results is comparable with the work [46] – the accuracy is of order $10^{-14} - 10^{-13}$.

Advantages of IEM are relative simplicity, very high accuracy, a possibility to apply to the scattering at high energies. Nevertheless, a number of disadvantages in comparison with FGR method seem to appear, as follow: calculation only one wave function at one running of the code, impossibility to calculate bound levels and impossibility to generalize for the time-dependent Schrödinger equation and for

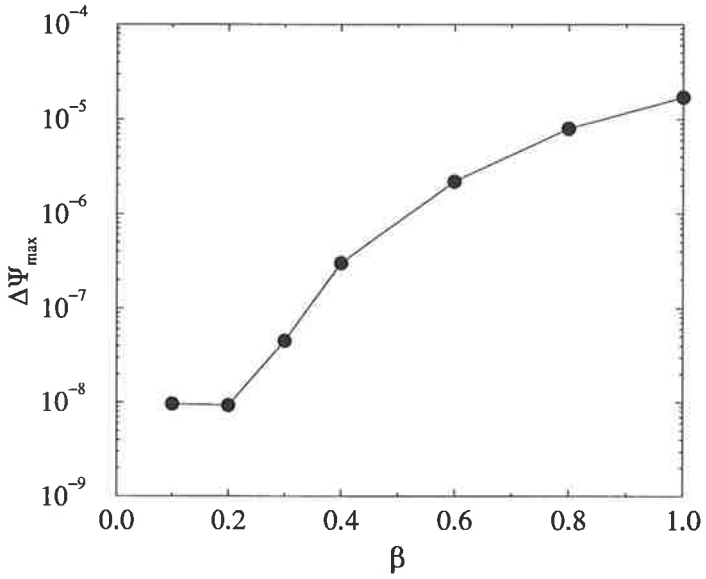

Figure 3.7: The precision of wave function in the FGR method as a function of the parameter β. The reference is the calculations with $\beta = 0.07$

calculation of lifetimes.

3.4 Comparison of methods for calculations of lifetimes

In this section two methods of lifetime calculations for long range potentials are discussed and compared. They are the time-dependent and the time-independent FGR methods, described in sections 2.5 and 2.7. Both of them use the same mapping.

3.4.1 Considering example

The considering system is a two-channel potential of the 0_u^+ $(5S + 5P)$ symmetry of $^{85}Rb_2$. Two potentials $^1\Sigma_u$ and $^3\Pi_u$ having the same dissociation limit are coupled by the constant spin-orbit coupling (for details, see the section 4.2). This coupling corresponds to the spin-orbit splitting of the $5P$ atomic level into two levels - $5P_{1/2}$ and $5P_{3/2}$. Thus, the 0_u^+ $(5S+5P)$ symmetry with accounting of the spin-orbit interaction has two dissociation limits $5S + 5P_{1/2}$ and $5S + 5P_{3/2}$. For a simplicity the first limit will be refereed as $P_{1/2}$, and second as $P_{3/2}$. Diagonalization of such potential (two $^1\Sigma_u$ and $^3\Pi_u$ curves plus the coupling) gives two new curves, which have different dissociation limits – $P_{1/2}$ and $P_{3/2}$. These curves, for a simplicity, will be called also as $P_{1/2}$ and $P_{3/2}$ curves and a corresponding basis of molecular states will be called as the adiabatic representation, since it corresponds to the adiabatic form of the Schrödinger equation. A representation using $^1\Sigma_u$ and $^3\Pi_u$ curves and the coupling will be refereed as diabatic. Vibrational levels with energy between $P_{1/2}$ and $P_{3/2}$

limits have finite lifetimes due to the spin-orbit interaction with continuum spectrum beginning above the $P_{1/2}$ limit. Thus, the accuracy of calculations of lifetimes of these vibrational levels is under consideration in this section.

A choice of the enveloping potential is discussed in the section 2.8 as an example. For Rb($5P$) the atomic spin-orbit splitting is 237.6 cm^{-1}.

A right border of the grid is limited by distances $100 - 200$ a_0.

3.4.2 Time-dependent method

In the time-dependent FGR method the first step in lifetime calculations is a definition of the initial wave function ψ_0. ψ_0 is computed in the time-independent method. The approximated initial wave function ψ_0 could be taken from calculations with the single $P_{3/2}$ potential curve with the energy superior than the $P_{1/2}$ limit . But, since both $P_{1/2}$ and $P_{3/2}$ states are strongly mixed at small internuclear distances, this approximation is very rough. In the calculation it is demonstrated by a non-exponential decaying of the level during the propagation. Thus, the initial wave function must be calculated for two channel potential.

The function ψ_0 is calculated with the mapping providing only bound levels, since without using the optical potential the continuum states are always disturbed by ends of the grid. Thus, only a "bound" part of the pre-dissociated wave will be well presented. The wave function ψ_0 with the energy larger than the first dissociation limit ($P_{1/2}$) contains $0_u^+(P_{1/2})$ component which belongs purely to the continuum (disturbed by ends of the grid). In the adiabatic representation the $P_{1/2}$ component can be separated.

A relative population of two adiabatic components of the pre-dissociated wave function, obtained in the bound state calculations with the finite grid, is defined by the length of the grid. What does not depend on the length of the grid, is a ratio between amplitudes in the interaction region and in the asymptotic region. A lifetime is defined by this relation. The asymptotic amplitude is linked to the flux going out from the interaction region, the last is connected to the lifetime of the state. In the bound calculations the total norm of the wave function is finite and equal to 1, whatever the length of the grid is. Therefore, the relative population of the $P_{3/2}$ component is smaller for larger grid. The Fig. 3.8 shows one pre-dissociated wave function of Rb_2 given by bound calculations in the diabatic and the adiabatic representations. Asymptotic oscillations are very small ($|\psi(R)|^2 = 10^{-5}$) for this wave function and they are not visible on the figure. One can see that the $P_{3/2}$ component (middle right panel) of the total wave function looks like a bound state, whereas its $P_{1/2}$ component (lower right panel) considerably differs from a bound state. As the $P_{1/2}$ component belongs to the continuum, it slightly disturbs the exponential decay of the initial wave function. (The continuum component does not decay exponentially.) Thus, in lifetime calculations, the $0_u^+(P_{1/2})$ component is explicitly eliminated from ψ_0. As the transformation from the diabatic to the adiabatic presentation is known,

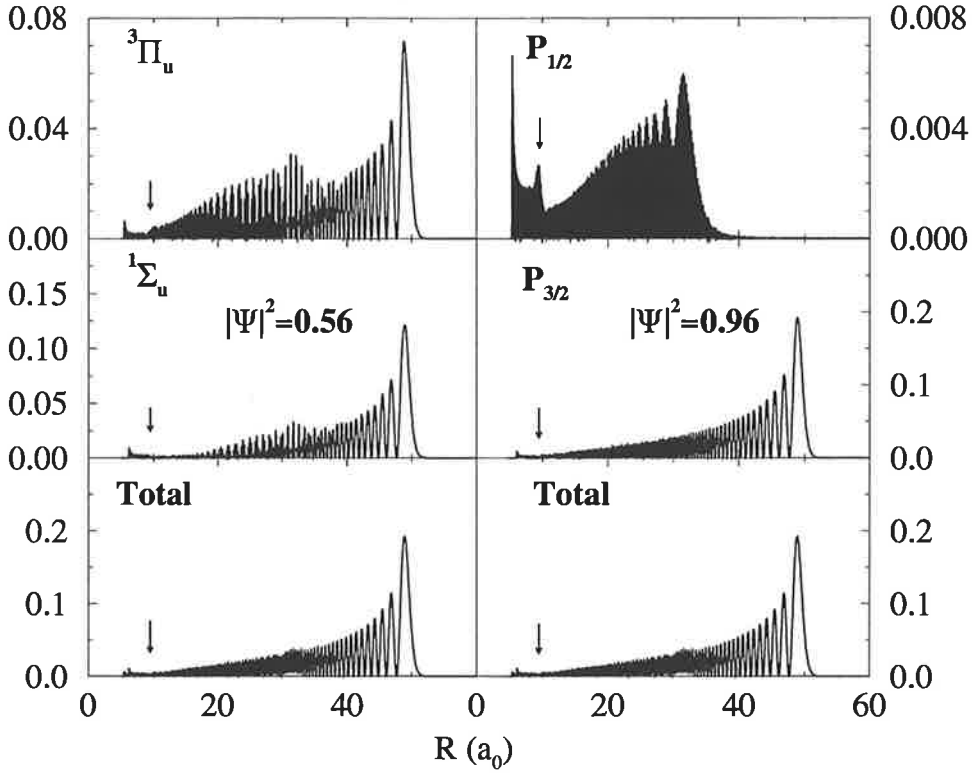

Figure 3.8: Diabatic (left panels) and adiabatic components (right panels) of a two-channels pre-dissociated wave function of $^{87}Rb_2$ (0_u^+); $E = 210.52cm^{-1}$ above the $P_{1/2}$ asymptote. At left panels: up - the $^3\Pi_u$ component, middle - the $^1\Sigma_u$ component, down - the total wave function. At the right: up - the $P_{1/2}$ component, middle - the $P_{3/2}$ component, down - the total wave function. For $^1\Sigma_u$ and $P_{3/2}$ components relative fractions in the total norm are marked. Arrows mark the position of the crossing.

this procedure can be done easily.

$$\vec{\psi}^d \to \vec{\psi}^a,\ \psi^a_{P_{\frac{1}{2}}} = 0, \vec{\psi}^a \to \vec{\psi}^d \tag{3.2}$$

$\vec{\psi}^a$ and $\vec{\psi}^d$ are the initial wave-function ψ_0 in the adiabatic and the diabatic presentations. The figure 2.6 gives examples of the correlation functions for the pre-dissociated levels with energy $E_v = 26.13\ cm^{-1}$ of $^{87}Rb_2$.

The figure shows also the correlation function for the initial state, for which the $P_{1/2}$ component is not extracted . At the beginning, the $P_{1/2}$ component disturbs the exponential decay of the correlation function. A propagation during the time $t \in (0\ ps, 30\ ps)$ works as the time filter for the pre-dissociated wave function [35] — it selects from the initial wave function only a part belonging to the resonance level. After the time $t_0 \approx 30\ ps$, only this resonant pre-dissociated part stays, decaying exponentially. A slope of the curve becomes the same as for the correlation function for the initial wave function belonging "purely" to the $P_{3/2}$ state.

Small oscillations at the bottom of lines on the Fig. 2.6 are due to high frequency components, presented in the initial wave functions. Since grids in the bound calcu-

lation and in time propagation are not the same, the initial wave function ψ_0 in the propagation is transfered from one grid to the other. This transfer introduces new components in the spectrum (mainly, high-frequency components). High components disturb the correlation function and are not eliminated by the time filtering.

The method of the propagation using the Chebyshev expansion is a very precise tool for solution of the time-dependent equation. It is used as a benchmark for other propagation schemes (C. Leforestier *et al.*, [77]). Its uniform error is less than 10^{-14}. In the present calculations there are different sources of errors. First source is a uncertainty of the definition of the slope of $C(t)$ in a logarithmic scale. The second source is disturbing components of the continuum presented in the initial wave function. When the initial wave function is transfered from a grid of the time-independent method into a grid of the time-dependent method, it introduces an additional error due due high frequency components which disturb the exponential decay of a pre-dissociated level. It is a third source of error. Thus, there is a room to improve the present calculations.

3.4.3 Time-independent method

The method of lifetime calculations using the time-independent approach and the optical potential is described is the section 2.5. One advantage of the method is its simplicity. Another and, maybe, the main advantage of the time-independent method in comparison with the time-dependent is that all resonances are extracted during only one running of the program.

In the calculation the optical potential of Eq. (2.129) is used with parameters: $A_5 = 0.00029$, $N = 13.22$, $L = 4.8$ *a.u.*, R_0 is a starting point of the optical potential. R_0 was chosen at 80 a_0. The increasing of R_0 (and the length of the grid) does not sufficiently change results. An increasing of the length L of the optical potential also does not change results, that is in agreement with results of Á.Vibók and G.G.Balint-Kurti [131, 132]. Note, that in the time-independent method one can control the efficiency of the absorbing of the outgoing flux. It can be controlled also in the time-dependent method. If this propagating wave function is not zero at the region behind the optical potential, the absorption does not work properly. The absence of the reflection from the optical potential can be controlled using the analysis of components going back in the asymptotic region before the optical potential. computation It seems that in the time-independent method has smaller of sources of errors than the time-dependent approach.

3.4.4 Comparison of results

The figure 3.9 shows results obtained by two methods. The energy domain corresponds to the splitting between two dissociation limits. The time-independent method computes all resonances at one running of the code, whereas the time-dependent method determines only one lifetime at one running. Therefore, not all resonances have been calculated in the time-dependent method.

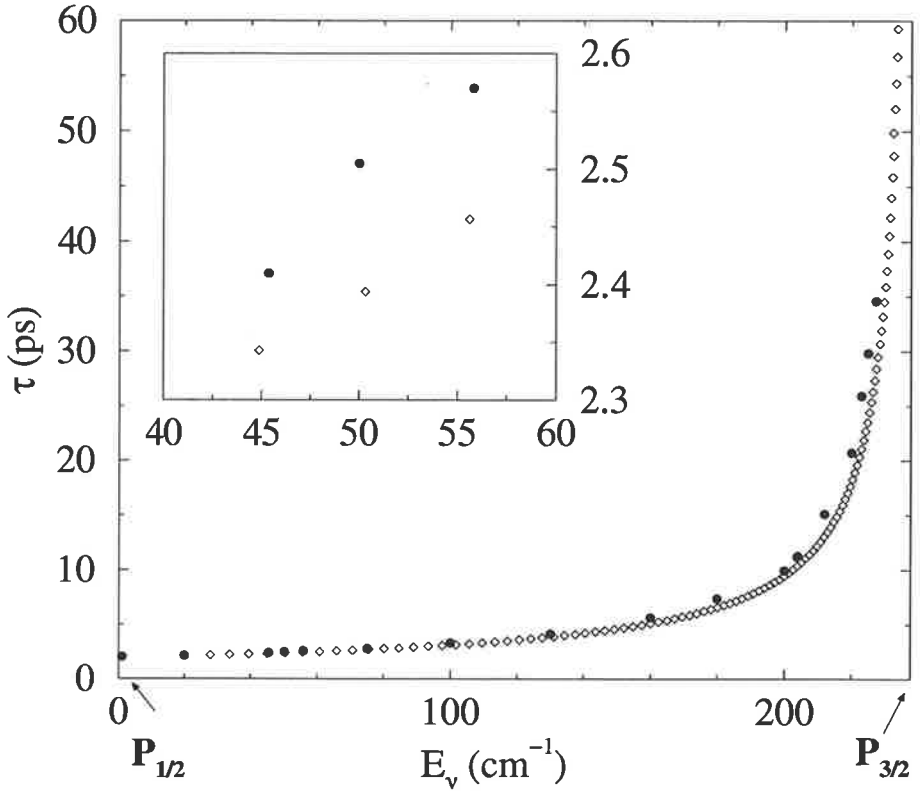

Figure 3.9: Lifetimes of vibrational levels of the 0_u^+ symmetry of $^{85}Rb_2$, calculated by two methods - time-dependent and time-independent. Circles represent the time-dependent calculations; diamonds - time-independent. Inset shows a detailed picture of a part of the whole region.

Although, both methods give comparable results, that proves a capacity for work of both methods, the difference in lifetimes is quite large. It is about 4%. As it was discussed, this error is mainly attributed to the time-dependent method due to the uncertainty of definition of the slope of $C(t)$. This uncertainty of the slope is caused by two factors: by the initial non-exponential decay of ψ_0 and by a limitation of the propagation time (or by a time).

3.5 Conclusion

This chapter examines the precision of the mapped Fourier grid representation method. All tests are made using numerical potentials.

First, the precision of the time-independent method is compared with the integration method of Numerov. It was found that using numerical potentials, precisions of both methods are comparable (of order 10^{-8}) and, probably, are limited by a spline procedure used for calculations of potentials at intermediate points. In principle, the precision of the mapped FGR method with using of analytical potentials should be the same as for the uniform method, i.e. of order 10^{-14}.

The second test concerns a precision of calculations of wave functions. It was

found that the precision of the FGR method (the best is $\approx 10^{-8}$) is not worse than in the Numerov method and even, probably better. The accuracy limit was attributed again to the spline procedure.

Disadvantages of the Numerov method, such as difficulties of a generalization for multichannel potential, difficulties near the dissociation limit and others, are not discussed in the Thesis.

Finally, the precision of the MFGR method in calculations of lifetimes is checked. Two methods of lifetimes calculations are compared. Both, time-dependent and time-independent approaches use MFGR. Results show that both methods give same lifetimes. Unfortunately, there is some discrepancy between results – of order of several percents. The source of error is attributed to the time-dependent approach, in which the lifetime is defined from the correlation function. For a better precision of lifetimes in the time-dependent method the propagation time must be larger.

Chapter 4

Photo-association Spectroscopy of Alkali Diatom near the Dissociation Limit.

The mapped Fourier grid representation method, developed in section 2.1, can be applied to solve the Schrödinger equation of many physical problems. As it was discussed, the method is especially adapted for equations with the long-range potential. This chapter is devoted to an application of the method for the investigation of 0_u^+ spectra of the long-range potentials of Rb_2 and Cs_2. The energy domain under and above the dissociation limit is considered, corresponding to the problems of highly-excited and pre-dissociated vibrational levels.

4.1 Introduction

The symmetry 0_u^+ $(nS + nP)$ of alkali diatoms including, in the diabatic description, two curves ($^1\Sigma_u^+$, $^3\Pi_u$) and a spin-orbit interaction between them, is well known as an example of strong perturbations between vibrational levels of discrete spectra of two molecular states (H. Lefebvre-Brion and R.W. Field [76]). The perturbations are manifested by a non-regular behavior of two vibrational series, not following the dissociation law of Leroy-Bernstein [78].

The perturbations have been intensively studied for all alkali diatoms: many theoretical and experimental studies have been performed for Li_2 [107, 110, 114, 115], Na_2 [37, 61], K_2 [59], Cs_2[130], and Rb_2 [7, 16]. The study of perturbations can help to determine the coupling between molecular states, i.e., the spin-orbit coupling, as it was done, for example, for Na_2 by C. Effantin *et al.* [37].

An equivalent representation of the 0_u^+ symmetry is the adiabatic representation, including two adiabatic curves, asymptotically connected to two different $nS + nP_{1/2}$ and $nS + nP_{3/2}$ dissociation limits of two free atoms, and non-adiabatic coupling between these curves. Over the first dissociation limit, $nS + nP_{1/2}$, the strong non-adiabatic coupling is responsible for the pre-dissociation of vibrational levels, be-

longing to the highest potential curve (asymptotically connected to the $nS + nP_{3/2}$ limit).

The recently developed precise photo-association spectroscopy of cold atoms has opened new possibilities. It became possible to observe vibrational levels close to the dissociation limit and to measure the lifetimes of pre-dissociated levels of different molecular systems, in particular, of the 0_u^+ symmetry. The experimentally measured lifetimes of pre-dissociated levels of the 0_u^+ spectrum have been reported for Rb_2 by R. Cline *et al.* [27] and for K_2 by H. Wang *et al.* [139].

Due to the spin-orbit coupling, the perturbations in spectra of heavy alkali diatoms (Rb and Cs) must be much stronger than for light alkali diatoms. Indeed, C. Amiot *et al.* [7] have recently reported strong perturbations in the experiment with Rb_2, using Fourier transform spectroscopy. The observed perturbations have been successfully interpreted by calculations using the uniform FGR method [7]. The domain of bound energies of vibrational levels from -2500 cm^{-1} to -500 cm^{-1} has been explored.

An example of potential curves of the symmetry for a rubidium diatom is shown at the left panel of the Fig. 4.1 (diabatic curves). The curves diagonalized taking into account the spin-orbit coupling (adiabatic curves) are shown at the right panel of the figure.

The reason of relatively strong perturbations in the 0_u^+ spectra of all alkali diatoms is in the behavior of two potential curves, $^1\Sigma_u^+$ and $^3\Pi_u$, of the 0_u^+ symmetry. The splitting between them is small for a large domain of internuclear distances (approximately from 10 a_0 to 20 a_0). If the spin-orbit coupling between these two molecular states is comparable to the splitting between potential curves (cases of alkali molecules Rb_2 and Cs_2), the strong mixing of vibrational levels of the two molecular states is to be expected. Both molecular states cannot be considered as independent any longer. As a consequence, a spectrum of such a two-channel system presents two series of lines, strongly perturbed by one by other. (The atomic spin-orbit interaction between excited atomic states $^2P_{1/2}$ and $^2P_{3/2}$ is for Rb - 237.6 cm^{-1} and for Cs - 554.1 cm^{-1}.) The strong mixing of molecular states has also an effect on lifetimes of pre-dissociated vibrational levels above the $nS + nP_{1/2}$ dissociation limit.

The goal of this chapter is to study the perturbations and the pre-dissociation in 0_u^+ spectra of heavy alkali diatoms - Rb_2 and Cs_2.

In the present calculation, potential curves at small distances (up to 20 a_0) for Rb_2 and Cs_2 are taken from the accurate *ab initio* pseudo-potential calculations by M. Foucrault *et al.* [43] for Rb_2 and by W. Meyer [94] for Cs_2. The long-range part of the curves is matched to asymptotic curves taken from Ref. [92] (M. Marinescu and A. Dalgarno). The precision of these curves is not sufficient to reproduce the accuracy of high-precision experiments such as the Fourier transform spectroscopy and photo-association experiments. Depth of the wells of the potentials is defined with several cm^{-1} of uncertainty. The position of internal repulsive walls is also not well defined. Another source of uncertainty is the spin-orbit coupling. The coupling is very well known for free rubidium and cesium atoms. But the molecular spin-orbit coupling varies with the distance, since atomic wave functions are disturbed by the presence of the second atom. For Cs_2 there are calculations of W. Meyer [94] describing the

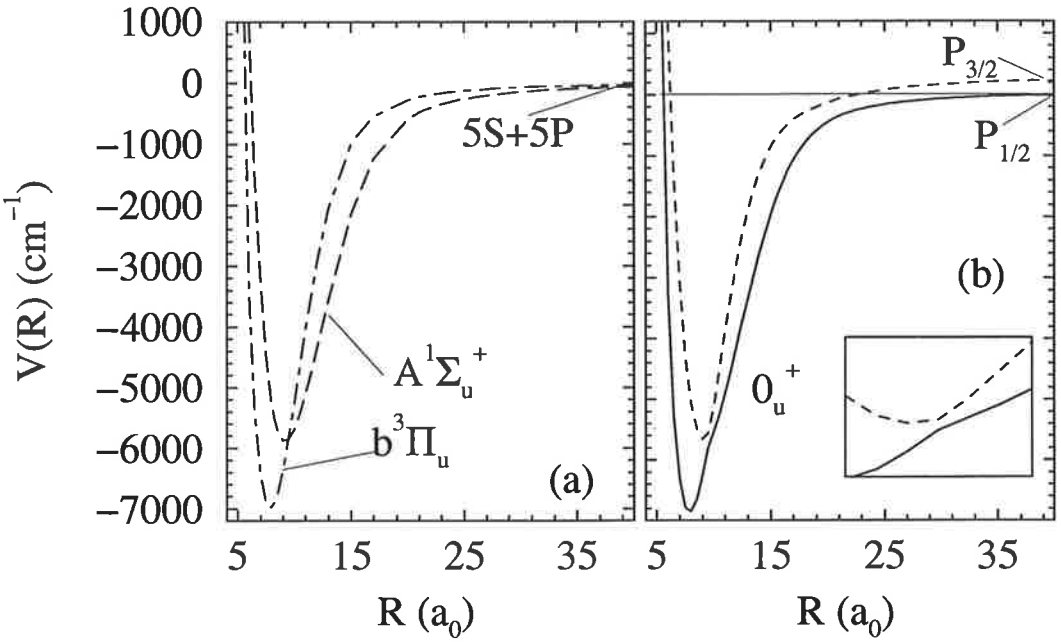

Figure 4.1: Rb_2 potential curves without (a) and with (b) spin-orbit coupling. (a) - Hund's case a $A^1\Sigma_u^+$ $(5S + 5P)$ (broken line) and $b^3\Pi_u$, $(5S + 5P)$ (dash-dotted line) curves from reference [43] (b) Hund's case c $0_u^+(P_{1/2})$ and $0_u^+(P_{3/2})$ potential curves correlated respectively to the dissociation limits $(5S + 5P_{1/2})$ and $(5S + 5P_{3/2})$. The inset at the right panel shows the region of the pseudo-crossing.

variation of the molecular spin-orbit coupling. For rubidium, there is no data.

All these uncertainties influence the results of calculations. An exact comparison with the experiment becomes impossible, especially for low-lying vibrational levels that correspond to motion in the well. Since the asymptotic behavior of the curves is known quite well, highly-excited vibrational levels can be described in calculations much better. For them, the uncertainty of the depth of the well is manifested in a global shift of all these levels. This shift can be described in the frame of the quantum defect theory (QDT). Using QDT, a difference between experimental and theoretical behavior of highly-excited levels can be described by only one parameter – a quantum defect μ (do not confuse with the reduced mass μ). Experiments, considered in this thesis, concern highly-excited vibrational levels of the 0_u^+ symmetry. The uncertainty of the coupling can be described the same way. Namely, for highly-excited levels, the unknown short-range part of the coupling can be represented only by a single parameter, which varies weakly from one vibrational level to an adjacent level.

For two coupled channels, there are three parameters, representing a deviation of numerical and real potentials – two quantum defects, corresponding to two channels and one parameter describing the short-range coupling. Changing slightly the potential and the coupling at small distances, agreement with the experiment for highly-excited levels can be obtained. Assuming that the three parameters change slowly with energy, one can predict the behavior of the vibrational and pre-dissociation series

in energy domains, unreachable by experiment.

The organization of this chapter as follows.

Section 4.2 is devoted to perturbations in the 0_u^+ spectra of Rb_2 and Cs_2. The influence of the masses of different isotopes and the influence of the spin-orbit coupling on the perturbations are investigated. Then a comparison with the experiment [27] (R. Cline *et al.*) is discussed. The strong perturbations in the discrete spectrum obtained in calculations are interpreted in the frame of the two-channel quantum defect theory (2QDT) using the method of the Lu-Fano plot.

Section 4.3 presents lifetime calculations of pre-dissociated levels of Rb_2 and Cs_2 for the same symmetry 0_u^+. The comparison with the experiment of the Heinzen group is discussed. A strong isotopic effect in lifetimes is predicted between isotopes $^{85}Rb_2$ (reduced mass is 77392.38 *a.u.*) and $^{87}Rb_2$ (reduced mass is 79212.88 *a.u.*). The comparison with the experiment of C. Wallace *et al.* [134] is discussed. For Cs_2, a dependence of lifetimes upon the molecular spin-orbit coupling is analyzed. The interpretation of the obtained results is also based on 2QDT. The quantum defect and transition probability are extrapolated continuously through the $nS + nP_{1/2}$ dissociation limit.

4.2 Perturbations in spectra 0_u^+ of Rb_2 and Cs_2.

4.2.1 Perturbations in the Rb_2 spectrum

Details of calculations

The mapped Fourier grid representation method can easily be generalized to calculate the energies of the ro-vibrational level considering several coupled molecular electronic states. We have shown previously [34] that the FGR approach is particularly well-suited for such a goal, compared to more traditional approaches like Numerov integration methods. We describe below calculations considering two coupled states in a diabatic representation. The implementation of the calculation from chapter 2 is straightforward provided the same mapping procedure is applied to both channels. For a grid of N points, we now consider three operators $\mathbf{T}$, $\mathbf{V}(R)$ and $\mathbf{W}(R)$, each represented by a $2N \times 2N$ square matrix as follows:

$$\mathbf{T} = \begin{pmatrix} T_1 & 0 \\ 0 & T_2 \end{pmatrix}; \mathbf{V} = \begin{pmatrix} V_1 & 0 \\ 0 & V_2 \end{pmatrix}; \mathbf{W} = \begin{pmatrix} W_1 & W_{12} \\ W_{12} & W_2 \end{pmatrix} \tag{4.1}$$

The kinetic energy matrix $\mathbf{T}$ is block-diagonal, each block deduced from Eqs. (2.72) and (2.73). The potential energy matrix $\mathbf{V}(R)$ is diagonal in the FGR representation: each diagonal block V_1 and V_2 should contain the mapping of the corresponding potential energy curve. In contrast, in a diabatic representation, the coupling matrix $\mathbf{W}(R)$ contains both diagonal (W_1, W_2) and non diagonal (W_{12} and W_{21}) blocks terms. Obviously, this procedure may be generalized to any number of coupled electronic states. The diagonalization of the full matrix provides the energies of the levels of the coupled system.

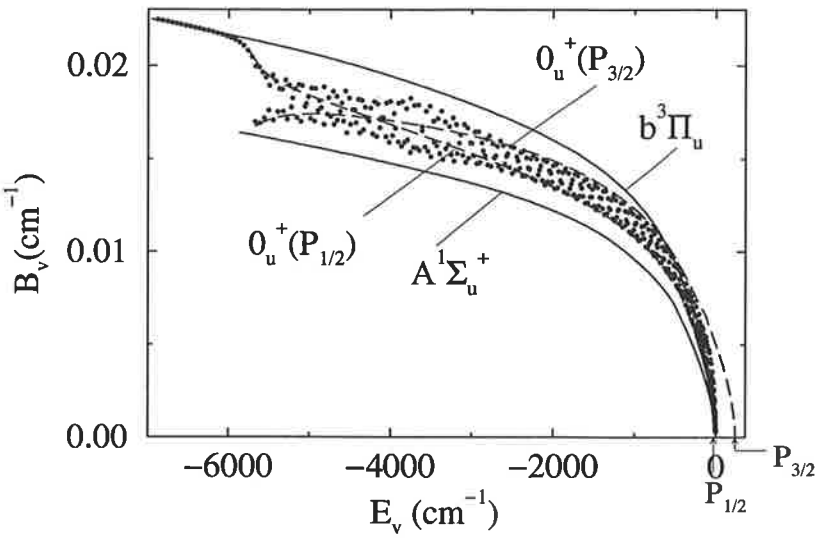

Figure 4.2: Rotational constants B_v (in cm^{-1}) for vibrational levels of the 0_u^+ symmetry of Rb_2 (see the potential curves on Fig. 4.1). Neglecting fine structure coupling (Hund's case a) – full lines; neglecting radial coupling (Hund's case c) – dashed lines; and considering two coupled channels – circles.

The problem is to generalize the mapping procedure: this can be done by considering an enveloping potential adapted to the two different potentials and eventually to the coupling term.

As an example, we use this method for the calculation of the bound vibrational levels of the $A^1\Sigma_u^+(0_u^+)$ and the $b^3\Pi_u(0_u^+)$ excited electronic states in Rb_2, coupled by spin-orbit interaction. Both states are behaving asymptotically as R^{-3}, and are correlated to the first excited dissociation limit $5S + 5P$.

The spin-orbit effective operator is assumed to be R-independent and proportional to the atomic fine structure splitting ΔE_{fs}. The coupling term is then $W_{12} = \Delta E_{fs}\ (\sqrt{2}/3)$, while the energy of the $b^3\Pi_u$ electronic state is corrected by $W_2 = -\Delta E_{fs}/3$, shifting down its dissociation limit. The mapping function is deduced from Eq. (2.63), using for the enveloping potential:

$$V_{env}(R) = \min(V_1(R), V_2(R)),\ R > \min(R_{e1}, R_{e2}) \tag{4.2}$$

$$V_{env}(R) = \min(V_1(R_{e1}), V_2(R_{e2})),\ R < \min(R_{e1}, R_{e2}) \tag{4.3}$$

where R_{e1} and R_{e2} are the positions of the minima of the potential curves $V_1(R)$ and $V_2(R)$ respectively. The potential curves are drawn in Figure 4.1 in Hund's case a ($A^1\Sigma_u^+$ and $b^3\Pi_u$ states) and Hund's case c ($0_u^+(5S + 5P_{1/2,3/2})$) states) representations.

The procedure of choosing of the enveloping potential is discussed in details in section 2.8. The example of the $0_u^+(5S + 5P)$ symmetry of Rb_2 was considered.

Through use of the mapped FGR method, the eigenvalues (4.1) are calculated up to the dissociation limit $(5S + 5P_{1/2})$ hereafter referred to as $P_{1/2}$ limit. (Indeed, our choice

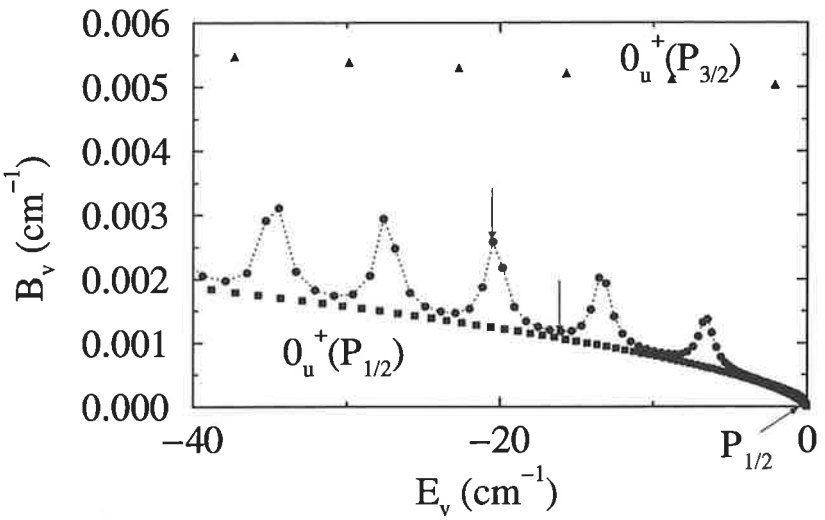

Figure 4.3: Same as figure 4.2, close to the $(5S+5P_{1/2})$ dissociation limit (labeled $P_{1/2}$ and located at energy $E = 0$). Squares and triangles represent B_v for non-coupled $P_{1/2}$ and $P_{3/2}$ potentials respectively.

for an enveloping potential excludes accurate representation of continuum levels.) We have considered a grid extending from 5 to 200 a_0, and found convergence for the value $\beta = 0.5$ of the mapping parameter. With such values, 525 bound vibrational levels can be found, the upper one having a binding energy $E_v(v = 524) = -0.015$ cm^{-1}.

Rotational constants of calculated levels

We present in Figure 4.2 the rotational constants $B_v =< 1/(2\mu R^2) >$ for the vibrational levels of the $^{87}Rb_2$ isotopes (assuming $J = 0$) computed in three different cases: for Hund's case a or Hund's case c coupling schemes, considering two independent vibrational channels and for the coupled channels. The independent channel calculations yield two curves, rather different in case of $A^1\Sigma_u^+$ and $b^3\Pi_u$ channels, more similar and even crossing in case of the $0_u^+(5S+5P_{1/2,3/2})$ channels -hereafter referred to as $0_u^+(P_{1/2})$ and $0_u^+(P_{3/2})$. Coupled-state calculations show that the spin-orbit coupling has a strong effect and introduces important mixing between the two channels, as many B_v values are not lying on any of the four preceding curves. Besides, strong perturbations are found, manifested by oscillations in the computed constants. In contrast with lighter alkali dimers like Li_2 [114, 107], Na_2 [37, 61], K_2 [59], we predict that the whole spectra is concerned by these perturbations, and can not be described neither in the framework of the Hund's case a nor Hund's case c independent channel representation . In a standard spectroscopy experiment, one may expect strong irregularities in the observed spectra, making a full identification very difficult.

An example of the irregularities predicted by the present calculations is analyzed in more details in Fig. 4.3 where we have represented the variation of the rotational constant in the vicinity of the $P_{1/2}$ dissociation limit. Let us note that the mapping represents a

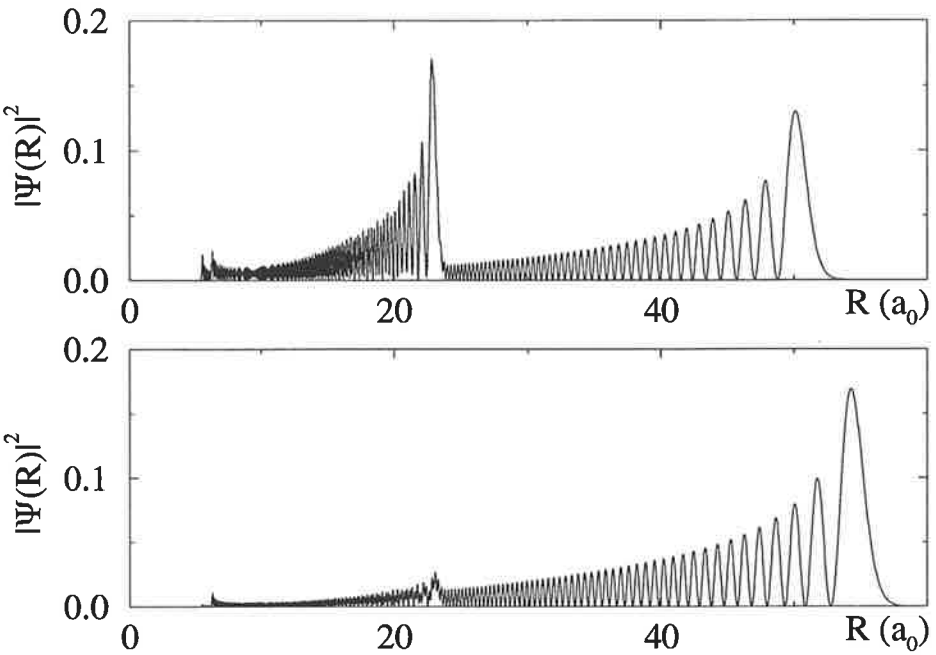

Figure 4.4: Two vibrational wave functions for $Rb_2(0_u^+)$ close to the $P_{1/2}$ dissociation limit. The upper panel shows the wave function with vibrational number $v = 445$ and energy $E_v = -20.414$ cm^{-1} with the relative population of the $P_{3/2}$ component $\int |\Psi_{3/2}(R)|^2 dR = 0.31$. The lower panel – the wave function with $v = 451$, energy $E_v = -15.997$ cm^{-1} with $|\Psi_{3/2}|^2 = 0.033$. The rotational constants for those levels are indicated by arrows in fig. 4.3.

crucial improvement to obtain accurate results in this energy range. The oscillatory behavior of B_v shows that the Hund's case c picture is adapted only to a few levels that we may assign to the lower electronic state $0_u^+(P_{1/2})$, most of the others being perturbed. When the B_v value is minimum, the corresponding wave function is indeed very close to unperturbed vibrational motion in the single channel 0_u^+ $(P_{1/2})$, as is illustrated in Fig. 4.4.

In contrast, the maxima of the oscillations correspond to an important admixture of a 0_u^+ $(P_{3/2})$ wave function, where the vibrational motion is confined to shorter distances, with an outer turning point which in the example chosen for the figure is close to 22 a_0 instead of 50 a_0. Preliminary results [6] seem to confirm this oscillatory behavior of the rotational constant.

Wave function. Relative population of components.

The perturbations of vibrational levels are manifested in the wave functions by comparable relative contributions of both, $P_{1/2}$ and $P_{3/2}$, components. A perturbed level means that its wave function does not belong only to one state, $P_{1/2}$ or $P_{3/2}$. Fig. 4.4 displays wave functions for two vibrational levels near the $P_{1/2}$ dissociation limit. The

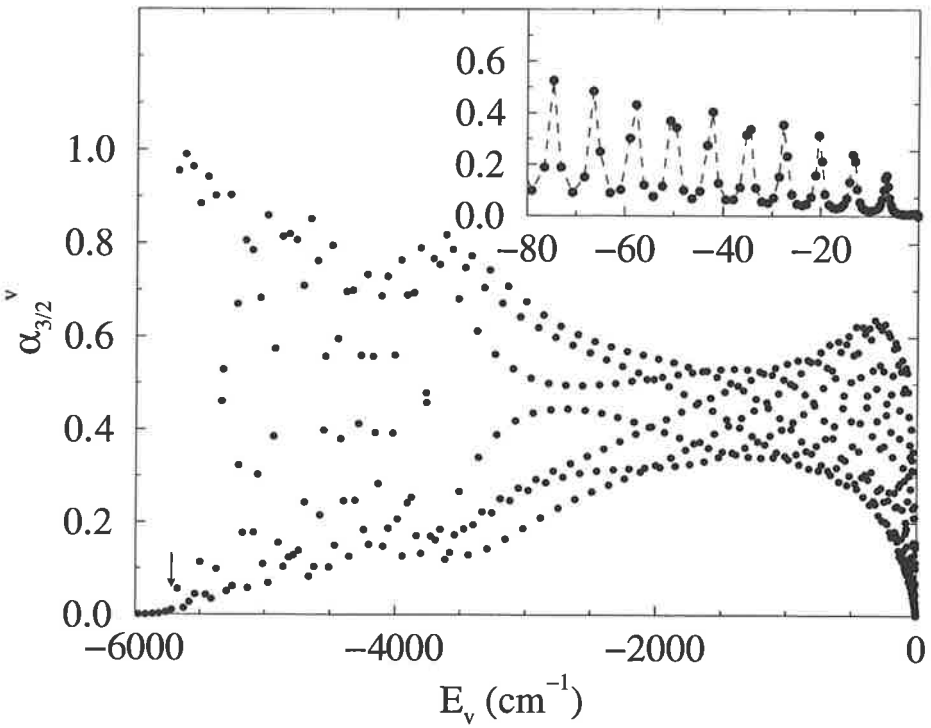

Figure 4.5: The relative population of the $P_{3/2}$ component of the total wave function of $^{87}Rb_2$ (0^+_u) as a function of the binding energy. There is not any bound level with energy > -5715 cm^{-1} (this limit is marked by an arrow and corresponds to the bottom of the well of the $P_{3/2}$ potential), which could be purely the $P_{1/2}$ or $P_{3/2}$ vibrational state. The norm of the $P_{3/2}$ component never becomes 0 or 1. All vibrational levels are perturbed. The inset shows a domain of the energy near the dissociation limit. $P_{3/2}$ levels look like pre-dissociated levels with finite lifetimes.

upper panel represents the wave function for a level with the largest $P_{3/2}$ component (in the considered energy region), corresponding to one maximum of the rotational constants, indicated on the Fig. 4.3 by an arrow. Both components are present. The fraction $\alpha^v_{3/2}$

$$\alpha^v_{3/2} = \int_0^\infty |\Psi^v_{3/2}(R)|^2 dR \tag{4.4}$$

of the $P_{3/2}$ component in the total norm is 0.31. Thus, contributions of both components are comparable. The two maxima of the wave function correspond to different turning points on the two coupled potentials, $0^+_u(P_{1/2})$ and $0^+_u(P_{3/2})$. The lower panel shows the wave function for a level with the smallest $P_{3/2}$ contribution, that corresponds to the minimum of the rotational constant in Fig. 4.3 (also marked by an arrow). Both components are also present, although the first maximum of the wave function corresponding the turning point on the $0^+_u(P_{3/2})$ potential is much smaller, the relative population of the $P_{3/2}$ component being only 0.033.

The effect of the perturbations can be demonstrated also by the relative population of two components of the whole vibrational wave function for the entire range of bound energies. Fig. 4.5 shows the relative population of the $P_{3/2}$ component for all

bound levels. Vibrational levels never become neither purely $P_{3/2}$ levels nor purely $P_{1/2}$ levels – the relative population of the $P_{3/2}$ component almost never becomes 0 or 1.

Close to the $P_{1/2}$ limit, the relative population of the $P_{3/2}$ component tends to 0. Even maximum values of oscillations of the $P_{3/2}$ population become smaller near the $P_{1/2}$ dissociation limit, as the inset of the figure 4.5 demonstrates. It means that for highly-excited $P_{3/2}$ vibrational levels, the coupling with the $P_{1/2}$ molecular state stays strong.

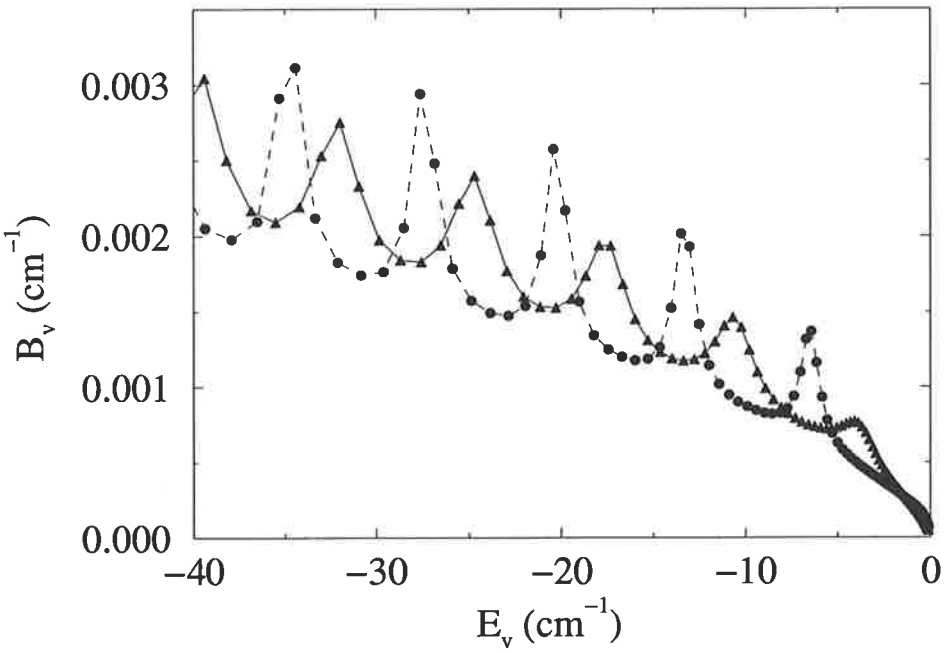

Figure 4.6: Rotational constants of two isotopes, $^{85}Rb_2$ (triangles) and $^{87}Rb_2$ (circles).

Rotational constants for two isotopes of Rubidium

A comparison of rotational constants B_v for two isotopes of Rubidium, $^{85}Rb_2$ and $^{87}Rb_2$, is presented in Fig. 4.6. The distance between consecutive peaks corresponds to the distance between consecutive bound levels calculated for the single $P_{3/2}$ potential. But the "widths" of these peaks are different for two isotopes. For $^{85}Rb_2$ the "widths" are larger (the quantitative estimation will be done below). It means that for $^{85}Rb_2$ more vibrational levels of the $P_{1/2}$ state are perturbed by the coupling with the $P_{3/2}$ channel. Thus, the "effective" coupling in $^{85}Rb_2$ is larger than in $^{87}Rb_2$. (Note that the spin-orbit coupling is the same for both isotopes.) It also means that for pre-dissociated levels lying just over the $P_{1/2}$ limit, the pre-dissociation will be more effective for $^{85}Rb_2$ where the coupling with the continuum states of the $P_{1/2}$ is larger. Thus, the lifetimes of pre-dissociated levels of $^{85}Rb_2$ must be smaller in comparison to the levels of the $^{87}Rb_2$ isotope.

Quasi pre-dissociated levels of the discrete spectrum near the $P_{1/2}$ limit.

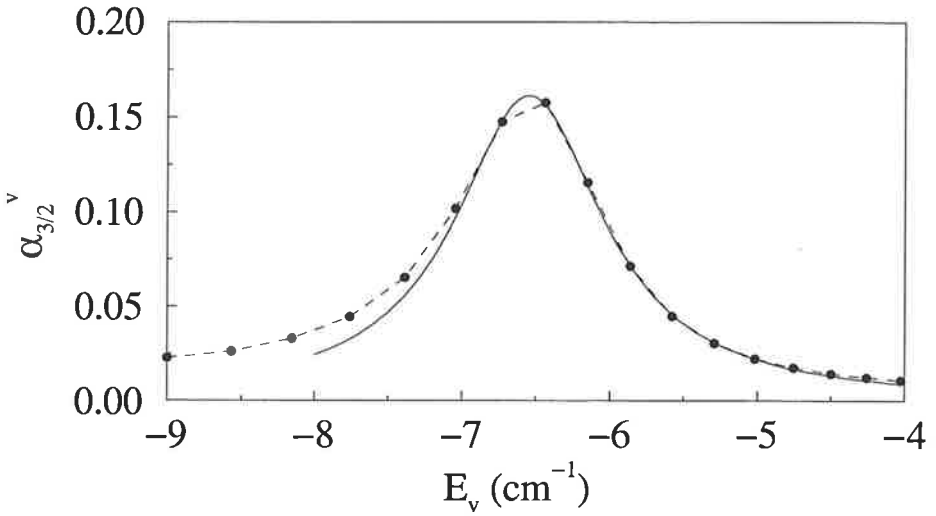

Figure 4.7: The same figure as shown in Fig. 4.5 near the $P_{1/2}$ dissociation limit. Circles represent the relative population of the $P_{3/2}$ component. The solid line is an adjusted function of Eq. (4.5) with $\Gamma = 1.22\ \mathrm{cm}^{-1}$. The left tail of the resonance is not reproduced by the analytical curve because the shape of the resonance is perturbed by a neighboring peak.

Lifetimes of pre-dissociated levels lying near the $P_{1/2}$ dissociation limit can be estimated assuming that the "effective" coupling is not sufficiently different for energies near (over and below) the dissociation limit.

Since the density of $P_{1/2}$ bound levels near the first dissociation limit is much higher than the density of $P_{3/2}$ levels, the discrete spectrum near the $P_{1/2}$ limit can be viewed as a set of $P_{3/2}$ "resonances" situated in the *discretized* continuum of $P_{1/2}$ levels. For such $P_{3/2}$ "resonances", one can determine "widths". Widths can be defined from the decreasing of the relative population of $P_{3/2}$ levels with energy (as it is shown in Fig. 4.5. It can be done only in the region where the density of $P_{1/2}$ levels is quite large.

Fig. 4.7 shows in detail the last $P_{3/2}$ vibrational levels under the $P_{1/2}$ dissociation limit. The shape of the resonance is adjusted by the Lorentzian $L(E)$, describing the decay of the level due to the dissociation:

$$L(E) = \frac{C}{(E - E_0)^2 + (\Gamma/2)^2} \tag{4.5}$$

The width Γ is equal to 1.22 cm^{-1}, corresponding to the lifetime $\tau \approx 4.4\ ps$. This is a very rough estimate of the lifetime. The accurate calculations (the next section) gives $\tau = 4.89$ for the first pre-dissociated levels above the $P_{1/2}$ asymptote.

Interpretation of perturbations using the QDT method.

Figures 4.3 and 4.5 and the previous discussion show that the 0^+_u spectrum near the $P_{1/2}$ dissociation limit can be considered as two strongly-perturbed series of bound

levels corresponding to $0_u^+(P_{1/2})$ and $0_u^+(P_{3/2})$ molecular states. There is an efficient tool for the interpretation of perturbed series – the quantum defect theory (QDT) (see, for example, H. Friedrich [44]). At the beginning, QDT was created for the description of energy levels in the Coulomb potential disturbed at short distances. The theory is based on the fact that shifts of energy levels in the perturbed Coulomb potential in respect to levels in the purely Coulomb potential can be described by only one parameter, which changes weakly with energy of levels. But the theory is easily generalized for other types of potentials.

For the simplicity of the following discussion consider, at first, the case Coulomb potential. In the purely Coulomb potential, $V_0(R) = D - \frac{1}{R}$, bound energies are described by the Rydberg formula:

$$E_n = D - \frac{\mathcal{R}}{n^2} \tag{4.6}$$

where $\mathcal{R}$ is the Rydberg constant.

If the potential $V(R)$ is perturbed at small distances, but it is still coulombic at large distances ($V(R) \rightarrow D - \frac{1}{R}$) the series of bound levels is described by the modified form of Eq. (4.6):

$$E_n = D - \frac{\mathcal{R}}{(n-\mu_n)^2}. \tag{4.7}$$

If the potential $V(R)$ only slightly differs from the the purely Coulomb potential $V_0(R)$, values μ_n (quantum defects of levels) will be almost the same for all levels. At the limit, $n \rightarrow \infty$, values μ_n converge to a constant value. This fact can be understood from the semi-classical Born-Sommerfeld quantization condition. For the purely Coulomb potential the condition is:

$$\frac{1}{2}S_0(E) = \int_a^b \sqrt{2\mu(D - V_0(R))}dR = \pi(n + \mu_{\phi_0}),\ n = 0, 1, 2... \tag{4.8}$$

where μ_{ϕ_0} is a constant, a and b are turning points.

The influence of the short range part of the potential $V(R)$ on positions of the levels can be found by replacing the action S_0 in Eq. (4.8) by the the action S on the potential $V(R)$:

$$\frac{1}{2}S(E) = \int_{a'}^b \sqrt{2\mu(D - V(R))}dR = \pi(n + \mu_{\phi}),\ n = 0, 1, 2... \tag{4.9}$$

It is supposed that the outer turning point b is the same for both $V_0(R)$ and $V(R)$ potential. A difference, $S_{er}(R)$, between $S_0(E)$ and $S(E)$:

$$S_{er}(E) = S(E) - S_0(E) =$$

$$2\int_{a'}^b \sqrt{2\mu(D - V(R))}dR - 2\int_{a'}^b \sqrt{2\mu(D - V(R))}dR \tag{4.10}$$

converge to a constant, when $E \to 0$ and $n \to \infty$. The quantization condition for the potential $V(R)$ can be now written in terms of quantum defects with respect to levels of the non-perturbed potential $V_0(R)$:

$$\frac{1}{2}S(E) = \pi(n + \mu_{\phi_0} + \mu_n),\ n = 0, 1, 2... \tag{4.11}$$

where μ_n is defined by:

$$\mu_n = \frac{1}{2\pi}S_{er}(E_n). \tag{4.12}$$

When $E \to D$, μ_n converge to a constant.

It is useful to complement the quantum defects $\mu_n = \mu(E_n)$, defined at the discrete energies E_n, by a continuous defect function $\mu(E)$ which describes the influence of the short ranged difference between $V_0(R)$ and $V(R)$ potentials. In the semi-classical approximation an extension of the formula for the quantum defect function is:

$$\mu(E) = \frac{1}{2\pi}S_{er}(E). \tag{4.13}$$

From the previous semi-classical discussion, it is clear that quantum defects μ_n and quantum defect function $\mu(E)$ should be equal near the dissociation limit D.

The previous results can be generalized for other long-range potentials. Let potentials $V_0(R)$ and $V(R)$ have the same asymptotic behavior for large R and different behavior at small distances. The potential $V(R)$ is considered as the perturbed $V_0(R)$ potential. Let the bound series of the $V_0(R)$ is $E^{(0)}(n)$. The series can be viewed also as $n^{(0)}(E)$. The potential $V(R)$ determines another progression - $E^{(p)}(n)$ or $n^{(p)}(E)$.

One can define quantum defects $\mu^{(p)}(n)$ of $E^{(p)}(n)$ levels in respect to the series $E^{(0)}(n)$. Considering dependence $E^{(0)}(n^*)$ as a function of the continuous argument n^*, energies $E^{(p)}(n)$ of $V(R)$-levels can be expressed in terms of effective quantum numbers n^* of the $V_0(R)$ (n^* is not necessary an integer number):

$$E^{(p)}(n) = E^{(0)}(n^*). \tag{4.14}$$

Defining quantum defects μ_n as

$$\mu_n = n - n^*, \tag{4.15}$$

bound levels of the potential $V(R)$ can be written as:

$$E^{(p)}(n) = E^{(0)}(n - \mu_n). \tag{4.16}$$

where

$$\mu_n = n - n^* = n - n^{(0)}(E^{(p)}(n)). \tag{4.17}$$

The two last equations are always valid. But they are useful only if quantum defects μ_n change slowly with the energy. If the potentials $V_0(R)$ and $V(R)$ have

the same asymptotic behavior, the main results of the quantum defect theory can be applied to the case.

Using the quantum defects, one can determine the degree of the deviation of the potential $V(R)$ from the $V_0(R)$ potential. If, for some energy domain, the quantum defects μ_n are constant, the potentials can be considered as equivalent. Therefore, the degree of the deviation of $V(R)$ from $V_0(R)$ can be described by a derivative $d\mu_n/dn = \mu(n+1) - \mu(n)$.

If $V_0(R)$ and $V(R)$ have finite number of bound levels, the convergence of μ_n to a constant value should be understood as a small changing of μ_n for the most excited levels.

As an example, the $P_{1/2}$ long-range potential of the 0_u^+ symmetry of Rb_2 is considered. Its asymptotic behavior is C_3/R^3 with $C_3 = 12.268$ a.u. Therefore, the potential C_3/R^3 will be considered as non-perturbed $V_0(R)$. The perturbed potential $V(R)$ will be the $P_{1/2}$ potential.

The $^{85}Rb_2$ isotope is taken for the calculation. The dissociation limit D is chosen at zero.

Positions of bound levels v in C_3/R^3 potential are described by the law of Leroy-Bernstein [78]:

$$E^{(0)}(v) = -[H_3(v_a - v)]^6 \tag{4.18}$$

v_a and H_3 are constants. H_3 is determined as:

$$H_3 = \frac{1}{2}\frac{\Gamma(4/3)}{\Gamma(5/6)}\frac{1}{(C_3)^{1/3}}\left(\frac{2\pi}{\mu}\right)^{1/2} \tag{4.19}$$

For $^{85}Rb_2$, $H_3 = 0.0015453$ *a.u.* or 0.012002 cm$^{-\frac{1}{6}}$.

Therefore, for excited vibrational levels $E^{(p)}(v)$ of the $P_{1/2}$ potential one expects

$$E^{(p)}(v) = E^{(0)}(v - \mu_v) = -[H_3(v_a - (v - \mu_v))]^6 \tag{4.20}$$

where quantum defects depend only weakly upon v.

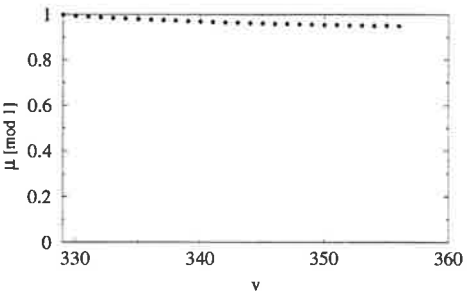

Figure 4.8: Quantum defects μ_v (modulo 1) of vibrational levels of the $P_{1/2}$ state, calculated in respect to levels of the purely C_3/R^3 potential Eq. (4.20).

Fig. 4.8 shows the quantum defects of highest vibrational levels of the $P_{1/2}$ potential, defined from Eq. (4.20). There is a slow variation of the defects due to the small deviation of the potential $P_{1/2}$ from the purely C_3/R^3 curve due to the C_6/R^6 term, present in $P_{1/2}$ potential. The second reason of the deviation is the fact that the $P_{1/2}$ molecular state is determined by the R-depending mixing of components of the $^3\Pi_u$ and the $^1\Sigma$ states, which have different values C_3. The whole $P_{1/2}$ potential can be viewed as the C_3/R^3 potential with R-dependent coefficient C_3.

At small distances (for lower bound energies), the $P_{1/2}$ potential differs markedly from the C_3/R^3 term, which is manifested by the fast variation of quantum defects.

Fig. 4.9 represents the quantum defects (modulo unity) as a function of energy. As one can see, the quantum defect, defined in respect to the pure C_3/R^3 potential, grows on 7 units at the energy domain from $P_{1/2} - 300$ cm^{-1} to $P_{1/2}$.

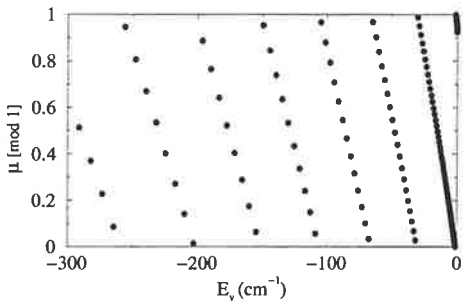

Figure 4.9: the same as the figure 4.8 but for larger domain of energies.

In principle, both potentials, $V_0(R)$ and $V(R)$, can be numerical. In this case, the both progression series $E^{(0)}(v)$ and $E^{(p)}(v)$ are calculated numerically. The use of the quantum defect approach for this case is useful for the fitting of existing potentials to the experimental data.

Consider now a two-channel potential and the generalization of the two-channel quantum defect theory for the non-Coulomb two-channel potential.

The description of the MQDT for the Coulomb potential can be found in the book by H.Friedrich [44].

Some QDT formulas, important for the present consideration, are review below.

Consider, first, two non-coupling Coulomb series following the Rydberg formula:

$$E_i^{(0)}(n) = D_i - \frac{\mathcal{R}}{n^2} \tag{4.21}$$

D_i $(i = 1, 2)$ are two dissociation limits and n are integer numbers. The coupling between these two series leads to the shift of all levels of both series. Perturbed atomic levels are reproduced now by the modified formula:

$$E_i^{(p)}(n) = D_i - \frac{\mathcal{R}}{(n - \tilde{\mu}_i(n))^2} = D_i - \frac{\mathcal{R}}{(n_i^*)^2} \tag{4.22}$$

where n numerates perturbed levels, $\tilde{\mu}_i(n)$ are quantum defects defined in respect to both non-perturbed series.

$$\tilde{\mu}_i(n) = n - n_i^* = n - n_i^{(0)}(E_i^{(p)}(n)) \tag{4.23}$$

Due to the coupling between two potentials, the quantum defects $\tilde{\mu}_i(n)$ in Eq. (4.22), in general, vary strongly with n. In the case of coupled series, the quantum defect theory (A.Giusti-Suzor and U.Fano [45], H.Friedrich [44], M.Aymar *et al.* [11])) gives the connection between effective numbers n_1^* and n_2^*:

$$\tan[\pi(n_1^* + \mu_1)] = \frac{R_{1,2}^2}{\tan[\pi(n_2^* + \mu_2)]} \tag{4.24}$$

where the parameters $R_{1,2}$, μ_1 and μ_2 are varying slowly with energy [44, 45], similarly to the parameter μ_n in the one-channel case ($R_{1,2}$ is not the Rydberg constant $\mathcal{R}$).

The method of the Lu-Fano plot consists in plotting of the dependence $\tilde{\mu}_1(\tilde{\mu}_2)$ (or $n_1^*(n_2^*)$) for perturbed vibrational levels. When the quantum defect $\tilde{\mu}_1$ becomes larger than 1, it means that a new bound state is introduced in the non-perturbed series $\{n_1\}$ due to the coupling with the second series. From the Lu-Fano plot the parameters $R_{1,2}$, μ_1, and μ_2 can be easily extracted.

Parameters μ_1 and μ_2 are the quantum defects, defined with respect to the non-perturbed series. The parameter $R_{1,2}$ is related to the coupling between channels (H. Friedrich [44], H. Lefebvre-Brion and R. Field [76]):

$$| < \Psi_1|H|\Psi_2 > |^2 = \frac{1}{\pi^2} R_{1,2}^2 \tag{4.25}$$

Consider now the case of the 0_u^+ $(nS + nP)$ symmetry of a molecule. As discussed above, the potentials $0_u^+(P_{1/2})$ and $0_u^+(P_{3/2})$ have the asymptotic behavior slightly different from C_3/R^3 and, therefore, can not be described exactly by the Leroy-Bernstein formula. Instead of the Leroy-Bernstein law, Eq. (4.22), the numerical analogue $E^{(0)}(v)$ will be used. Thus, the numerical laws $E_i^{(0)}(v)$ or $v_i^{(0)}(E)$ are determined numerically using the MFGR method. For highly excited vibrational levels, the function $E^{(0)}(v)$ coincides with the formula of Leroy-Bernstein (with a correction of the C_6/R^6 term).

Fig. 4.10 displays a dependence $\tilde{\mu}_1$ (modulo unity) as a function of v_2^* (an analogue of n_2^*) for 0_u^+ of both isotopes of Rb_2 for several perturbed levels (full circles) under the $P_{1/2}$ dissociation limit.

Eq. (4.24) describes the behavior of the effective quantum numbers v_i^* (note that taking the modulo unity function $\{x\} = Mod(x, 1)$ from both side of Eq. (4.23), one gets $\{\tilde{\mu}_i\} = 1 - \{v_i^*\}$). Adjusting the analytical curve

$$\left\{ \mu_1 - \frac{1}{\pi} \arctan \left[\frac{R_{1,2}^2}{\tan[\pi(v_2^* + \mu_2)]} \right] \right\} \tag{4.26}$$

to perturbed vibrational levels, parameters, contained in the formula, are found to be: $\mu_1 = 0.82$, $\mu_2 = 0.185$, $R_{1,2} = 0.74$ for $^{85}Rb_2$ and $\mu_1 = 0.37$, $\mu_2 = 0.64$, $R_{1,2} = 0.47$ for $^{87}Rb_2$. (Parameters v, v_i^* and $\tilde{\mu}_1$ are connected as corresponding parameter in Eq. (4.23).)

Parameters μ_1, μ_2, and $R_{1,2}$ do not significantly change for a large domain of energy from the $P_{1/2}$ limit to -1000 cm^{-1} below it. This domain of energy corresponds to about 70 non-perturbed levels of the $P_{3/2}$ potential from $v = 100$ to $v = 167$ ($v = 168$ for $^{87}Rb_2$), that means that about 70 levels are introduced into the $P_{1/2}$ series.

For the bound levels under the $D_1 = P_{1/2}$ limit, Eq. (4.24) describes the positions of pseudo-resonances in the discrete spectrum. Moreover, it can be considered as a definition of $P_{3/2}$ pseudo-resonances in the $P_{1/2}$ quasi-continuum and well as a definition of $P_{1/2}$ pseudo-resonances in the $P_{3/2}$ quasi-continuum. It does not mater that the density of levels of the "continuum" is smaller than the density of pseudo-resonances.

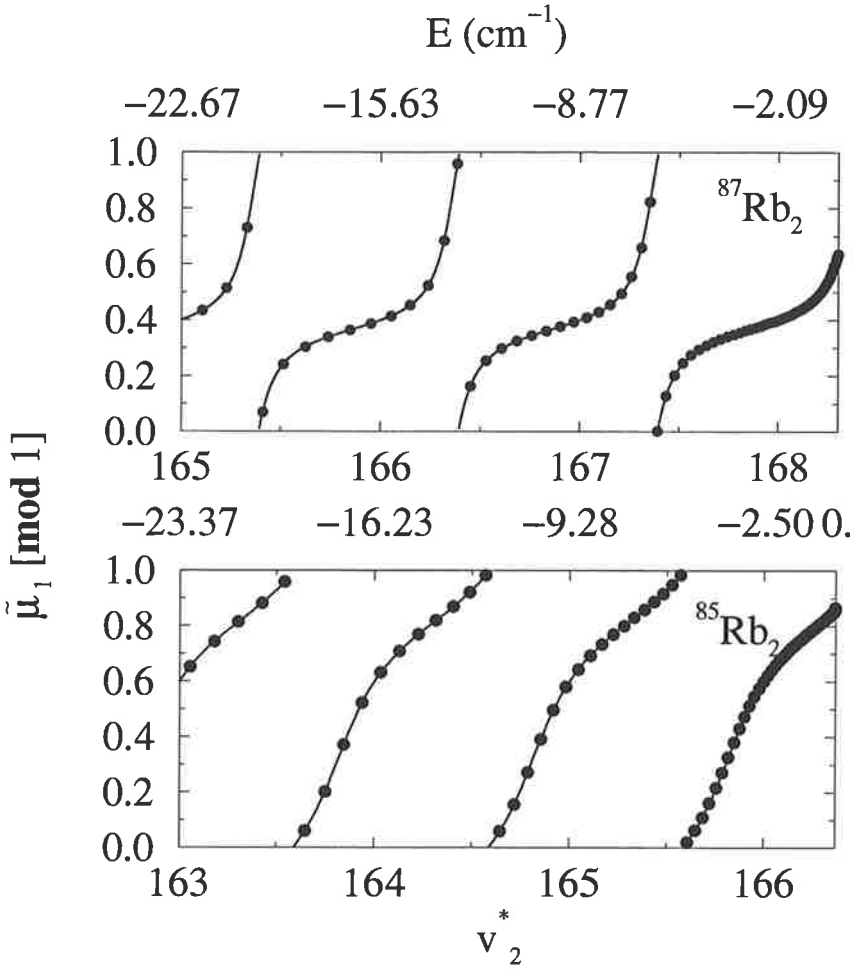

Figure 4.10: The Lu-Fano plot for bound levels for two isotopes of Rb_2. The upper axis of both panels shows energies corresponding to non-perturbed $P_{3/2}$ levels. These levels are shown at lower axes of both panels. Circles represent levels of the coupled 0_u^+ potential. The full lines are the results of the fitting.

Certainly, near the $P_{1/2}$ dissociation limit, only the $P_{3/2}$ pseudo-resonances have a physical sense – they become real resonances above this limit. Positions of $P_{3/2}$ pseudo-resonances in the discrete spectrum are defined from Eq. (4.26) and are described by the condition $\{v_2^*(E_{res}) + \mu_2)\} = 0$, positions of $P_{1/2}$ resonances are defined by $\{v_1^*(E_{res}) + \mu_1)\} = 0$. The 2QDT theory allows to define widths of such resonances [44, 45]. For example, for the $P_{3/2}$ pseudo-resonances widths are defined as:

$$\Gamma(v_2^*) = -\frac{2}{\pi}\frac{dv_2^*}{dv_1^*}\frac{dE}{dv_2} \tag{4.27}$$

where derivatives $\frac{dv_2^*}{dv_1^*}\frac{dE}{dv_2}$ are calculated at points of resonances. At these points, $\frac{dv_2^*}{dv_1^*} = -R_{1,2}^2$. The derivative $\frac{dE}{dv_2}$ is simply difference between consecutive $P_{3/2}$ levels

$\Delta E(P_{3/2})$. Therefore:

$$\Gamma(v_2^*) = \frac{2}{\pi} R_{1,2}^2 \Delta E(P_{3/2}) \tag{4.28}$$

The probability P of transition from the $P_{3/2}$ state to the $P_{1/2}$ state is related to the matrix element $| < \Psi(P_{1/2})|H|\Psi(P_{3/2}) > |^2$ and, as a consequence with $R_{1,2}$. For small P ($P \ll 1$), the relation is:

$$P = 4\pi^2 | < \Psi(P_{1/2})|H|\Psi(P_{3/2} >)|^2 = 4R_{1,2}^2 \tag{4.29}$$

Since the parameter $R_{1,2}$ depends weakly upon the energy, the transition probability varies also weakly with energy.

Above the D_1 threshold, the $P_{3/2}$ pseudo-resonances become real resonances – pre-dissociated levels. Widths and lifetimes of pre-dissociated levels can be estimated using the parameters μ_2, μ_1, and $R_{1,2}$. Consider one, $v_2 = v\ P_{3/2}$ level. A shift of the pre-dissociated level with respect to the non-perturbed level v is defined by the parameter μ_2:

$$\delta E(v) = \mu_2 \frac{dE}{dv_2} \approx \mu_2 (E_{v+1} - E_v), \tag{4.30}$$

the width is defined using the parameter $R_{1,2}$

$$\Gamma(v) = \frac{2}{\pi} R_{1,2}^2 \frac{dE}{dv_2} \approx \frac{2}{\pi} R_{1,2}^2 (E_{v+1} - E_v), \tag{4.31}$$

and the asymptotic shift δ of the pre-dissociated wave function is defined by the parameter μ_1:

$$\delta(v) = \pi \mu_1 \tag{4.32}$$

In section 4.3 the results obtained from the Lu-Fano plot will be compared with the results given by the calculations of pre-dissociated widths of levels over the $P_{1/2}$ dissociation limit.

QDT parameters fitted to the experiment

As described above, the precision of the Mapped FGR method is of order 10^{-5} cm^{-1} that allows comparison with the experiment. For this goal, besides the precise method, one needs the exact potentials. Unfortunately, the potential curves (for Rb_2 and Cs_2) used in the calculations are not very precise in the region of small internuclear distances. For example, the uncertainty of the depth of the well is about several cm^{-1}. Also the position of the inner wall of the potentials is not exactly known.

Thus, there are two outcomes from the this situation. One is to calculate exact curves — it could be a subject of another thesis. The second approach is to try to modify the potential in order to obtain the observed results.

The generalized quantum defect theory can be a very useful tool to fit the results of calculations to experiment. It is especially useful in the case of perturbations and pre-dissociated levels. In the frame of QDT, perturbations and pre-dissociated levels can be described by only few number of parameters (such as μ, $R_{1,2}$), which change slowly from level to level.

Comparison with experiment

There are two experiments with the 0_u^+ symmetry of Rb_2. These are the Fourier transform spectroscopy experiment by C. Amiot *et al.* [7] in the Laboratoire Aimé Cotton and the photo-association spectroscopy experiment carried out by the group of Heinzen [27]. The comparison with the experiment is discussed in this paragraph.

The experiment carried out by C. Amiot et J. Vergès [5, 7] explored the region of bound energies of the 0_u^+ symmetry between -1500 cm^{-1} and -200 cm^{-1} under the $P_{1/2}$ dissociation region for $^{85}Rb_2$, $^{87}Rb_2$ and $^{85}Rb^{87}Rb$ species. Strong perturbations effects have been observed. This effect has been attributed to the strong coupling between molecular states of the 0_u^+ symmetry (C. Amiot *et al.* [7]). The interpretation was done using the 2-coupled-channel calculations together with the uniform FGR method, that allows to calculate vibrational levels up to -500 cm^{-1} under the $P_{1/2}$ limit, that corresponds to the maximum internuclear distance $R_{max} = 20\ a_0$. (The typical number of grid points for such a potential with $R_{max} = 20\ a_0$ is about 1400. The precision of both methods, as it was discussed above, is almost the same.) The results of calculation of Ref. [7] have been also verified using the MFGR method developed in the Thesis. The uniform FGR method gives the same results.

The MFGR method, as it was shown above, allows to include into the consideration the whole spectrum of $0_u^+(Rb_2)$ up to the highest vibrational levels. Therefore, in contrast to the results by Amiot *et al.* [7], here calculations and the analysis of **the entire spectrum** are presented. The analysis of the data of the experiment by C. Amiot will be described in future work.

The second example of comparison with the experiment is a comparison with the photo-association experiment of Heinzen group with the 0_u^+ symmetry of $^{85}Rb_2$ just under the $P_{1/2}$ dissociation limit. These experimental results have been demonstrated firstly at the workshop *"Cold Atomic Collisions: Formation of Cold Molecules"* in March 1999 together with qualitative explanation using similar techniques of calculations (for the method see, for details, Tiesinga *et al* [125]). At the same workshop, the results of calculations described above in the Thesis were presented as a prediction for the behavior of the 0_u^+ symmetry near the dissociation.

The figure 4.11 displays the experimental results (open circles). The behavior of the rotational constants is very irregular. In fact, it means simply, that B_v of coupled channels oscillates between B_v values of non-coupled potentials, as it was discussed above. The results of calculations with the variable spin-orbit coupling is shown also at the same figure. The results of calculations repeat qualitatively the measured data, except the region near the dissociation limit, where, probably another effect is important in the real physical system.

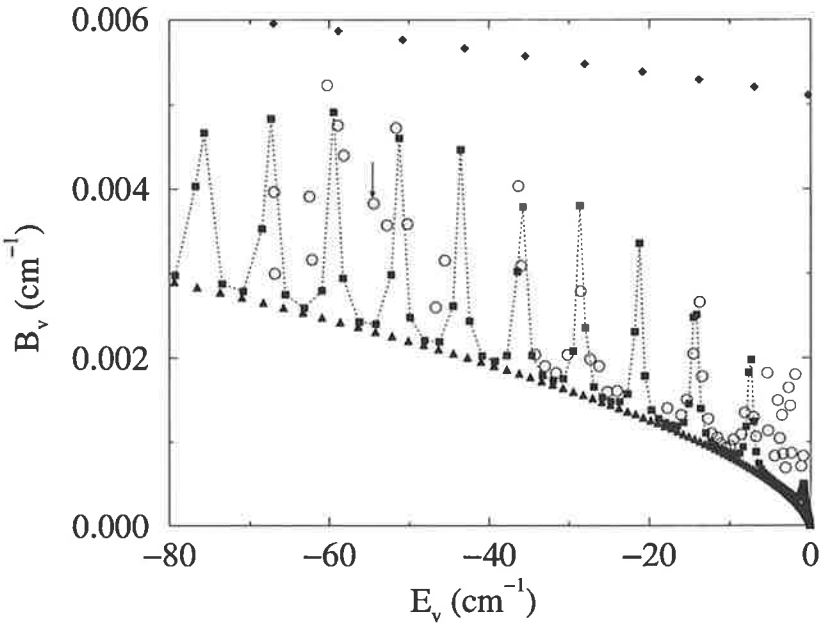

Figure 4.11: The experimental data for dependence $B_v(E_v)$ for 0_u^+ ($^{85}Rb_2$) from [52] (open circles) comparing with the results of calculations (squares). In the calculations, the variable spin-orbit coupling is used (Fig. 4.15). Triangles and diamonds shows also $B_v(E_v)$ for $P_{1/2}$ and $P_{3/2}$ non-coupled potentials.

Comparing the results of calculations with the constant and the variable spin-orbit coupling, it was found that later results are closer to the measured results, even if the variation of the coupling is very approximative. On the other hand, the differences between consecutive levels are not very different for two couplings, since this difference is determined mainly by potential curves, which are the same in both cases. In contrast, rotational constants are more sensitive to the coupling. (In the work by Amiot *et al.* [7], the constant spin-orbit interaction was used.)

Comparing the results of calculation with the experimental data, the potential can be fitted as following. First, the parameters μ_1, μ_2, $R_{1,2}$ are defined for the initial potential used in the calculations. Then, comparing with the experimental data, one estimates discrepancies $\Delta\mu_1$, $\Delta\mu_2$, $\Delta R_{1,2}^2$ between μ_1, μ_2, $R_{1,2}^2$ of calculated and experimental results. The parameter $\Delta\mu_1$ can be defined from a comparison of positions of calculated and measured levels. It can be done quite accurately for low-lying levels (assuming that μ_1 does not change with energy, as predicted by calculations). The parameter $\Delta\mu_2$ is defined quite easily. The defect μ_2 defines the position of the $P_{3/2}$ series in respect to the $P_{1/2}$ dissociation limit. The most efficient way to compare is to represent experimental and theoretical results on one Lu-Fano plot. The needed corrections $\Delta\mu_1$, $\Delta\mu_2$, $\Delta R_{1,2}^2$ will be clearly demonstrated. (The Lu-Fano plot is not done since the exact experimental data are not yet available. The presented experimental results are taken from the graph figure in the paper).

4.2.2 Perturbations in the Cs_2 spectrum

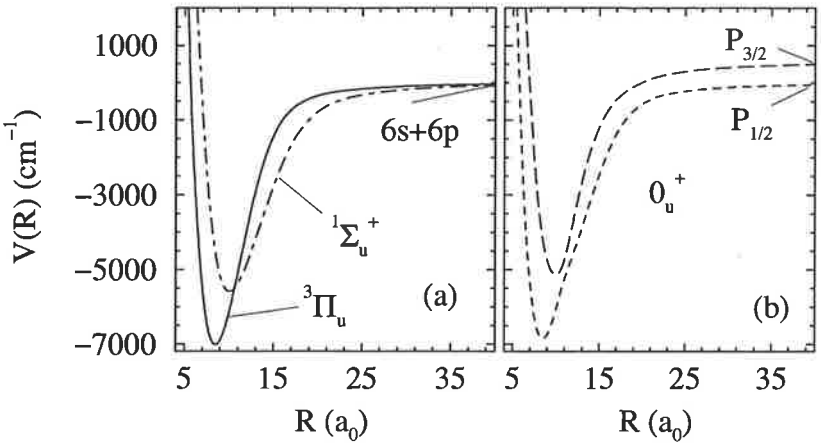

Figure 4.12: Cs_2 potential curves without (a) and with (b) spin-orbit coupling. (a) - diabatic $A^1\Sigma_u^+$ $(6s+6p)$ (dot-dashed line) and $b^3\Pi_u$ $(6s+6p)$ (full line) curves from Ref. [94] (b) adiabatic $0_u^+(P_{1/2})$ (dotted line) and $0_u^+(P_{3/2})$ (dashed line) potential curves correlated respectively to the dissociation limits $(6s+6p\ ^2P_{1/2})$ and $(6s+6p\ ^2P_{3/2})$.

Curves

In this subsection the main results concerning the perturbations in the 0_u^+ $(6S+6P)$ symmetry of Cs_2 are presented.

In the calculation, $^3\Pi_u$ and $^1\Sigma_u$ potentials are taken from accurate quantum chemistry calculations [94] (W. Meyer *et al.*), matched at large R to asymptotic calculations [92] (M.Marinescu and A.Dalgarno). Curves are coupled by the molecular spin-orbit interaction. In present calculation the spin-orbit coupling is chosen to be constant for all internuclear distances. The potential curves of the symmetry 0_u^+ $(6S+6P)$ of Cs_2, used in the calculation, are presented on the figure 4.12. The figure shows curves with (the right panel) and without (the left panel) the molecular spin-orbit interaction. Right curves are obtained from left ones by a diagonalization accounting for the spin-orbit coupling. In the asymptotic region, adiabatic curves are separated by the atomic spin-orbit interaction ($V_{so}(\infty) = P_{3/2} - P_{1/2} = 554.1$ cm^{-1} for Cs). Diabatic curves have the same dissociation limit.

Results for the constant spin-orbit coupling.

Fig. 4.13 demonstrates the rotational constants for non-coupled and coupled potentials of the 0_u^+ symmetry. In comparison with the case of Rb_2, vibrational levels of two molecular states, $P_{1/2}$ (0_u^+) and $P_{3/2}$ (0_u^+), are less perturbed. B_v for coupled potentials is much closer to the curves representing the non-coupled calculations. Vibrational levels of the two series are not so strongly mixed as in the case of Rb_2. There are few vibrational levels with B_v lying far from both curves. Thus, almost all levels can be attributed to one or to the other molecular potential ($P_{1/2}$ or $P_{3/2}$). The non-adiabatic coupling between two adiabatic states, $P_{1/2}$ (0_u^+) and $P_{3/2}$ (0_u^+),

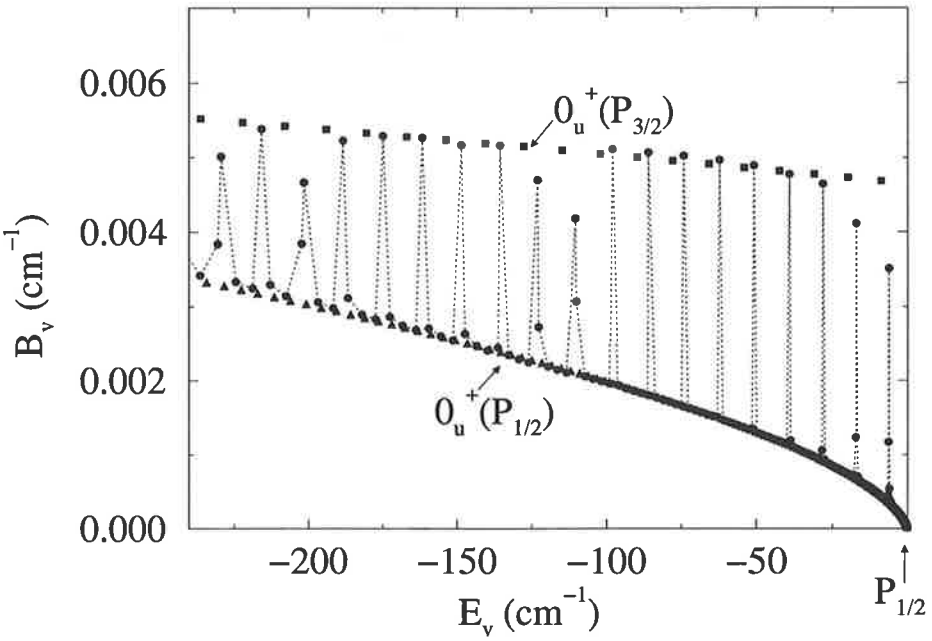

Figure 4.13: Rotational constants B_v of vibrational levels of 0_u^+ symmetry of Cs_2. Triangles and squares show B_v for vibrational levels of non-coupled $P_{1/2}$ and $P_{3/2}$ potentials respectively. Circles represent B_v in coupled channel calculation (the R-independent spin-orbit coupling).

is much weaker than in the case of Rb_2. Thus, for this particular potential with a constant spin-orbit coupling, in contrast to Rb_2, $P_{1/2}$ (0_u^+) and $P_{3/2}$ (0_u^+) are only weakly mixed.

As a consequence, lifetimes of the pre-dissociated levels of $P_{3/2}$ (0_u^+) with energy greater than $P_{1/2}$ must be relatively long. Indeed, as it will be shown in the next section, lifetimes for this potential are longer than 1000 ps.

In order to give a more complete description of the perturbations and compare them with the perturbations in Rb_2, the Lu-Fano plot is shown in Fig. 4.14. The upper panel represents the dependence of $\tilde{\mu}_1(E_c)$ as function of $\{v^*_{P_{3/2}}(E_c)\}$ for the energy domain corresponding to the whole discrete spectrum of the $P_{3/2}$ molecular state. The lower panel shows the region near the $P_{1/2}$ dissociation limit together with the analytical curve of Eq. (4.26).

Most of the levels are situated at vertical $\{v_2\} \approx 0.04$ and horizontal $\{\tilde{\mu}_1\} \approx 0.05$ lines. Thus, quantum defects μ_1, μ_2 are very small. It was found from the fitting procedure of Eq. (4.26) that parameters μ_1 and μ_2 change slowly from 0 to $\mu_1 = 0.0483$, $\mu_2 = -0.046$ when the energy changes from the lowest $P_{3/2}$ level to the $P_{1/2}$ dissociation limit. In contrast, the parameter $R_{1,2}$ varies quite fast and can not be fitted to a unique value. It is demonstrated by the lower panel of Fig. 4.14, where only levels situated between two $P_{3/2}$ resonances, $v_2 = 179$, $v_2 = 182$, are well fitted by the analytical curve. For smaller numbers v_2 the $R^2_{1,2}$ must be larger.

Thus, the effective non-adiabatic coupling in the 0_u^+ symmetry of Cs_2 is much smaller than in case of Rb_2. Matrix elements $R_{1,2}$ differ by a factor 25, giving a

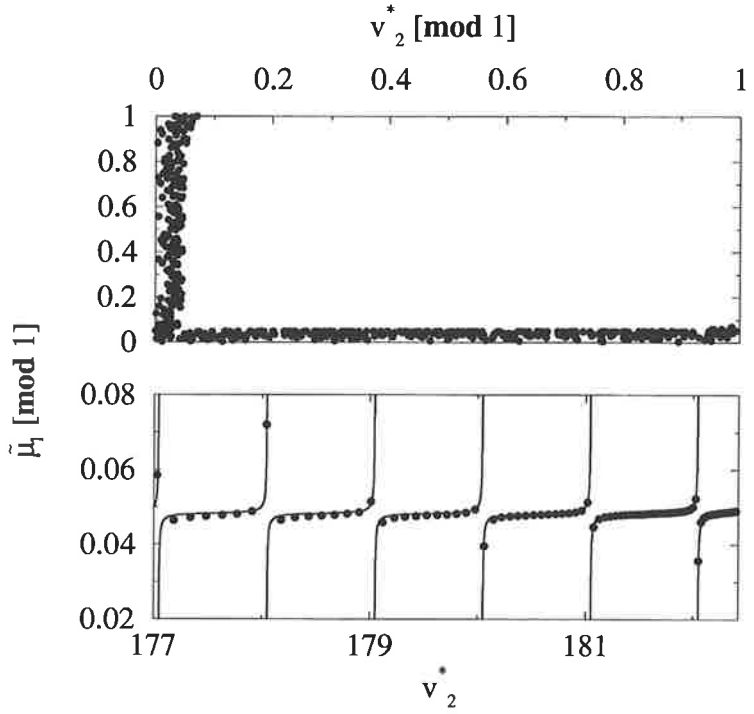

Figure 4.14: The Lu-Fano plot for the 0_u^+ symmetry of Cs_2. Circles represent coupled levels. The upper panel shows quantities of $\tilde{\mu}_1(E_c)$ and $\{v_2^*(E_c)\}$ for the energy domain corresponding to all non-perturbed levels of the state $P_{3/2}$ from $v = 0$ to $v = 182$. The lower panel shows the dependence $\tilde{\mu}_1(v_2^*)$ for the energy region just below the $P_{1/2}$ limit. The full curves represent analytical curve of Eq. (4.26) with parameters $R_{1,2} = 0.03$, $\mu_1 = 0.0483$, $\mu_2 = -0.046$.

difference in transition probabilities of 625 times.

Dependence upon the spin-orbit coupling.

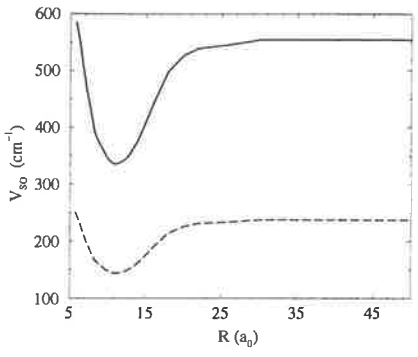

Figure 4.15: The variation of the molecular spin-orbit interaction used in the calculation. Full line - calculated for Cs_2 . Dashed line - for Rb_2.

In previous consideration the spin-orbit coupling was constant. But, in fact, it is varying with the internuclear distance. Since, as it was shown, perturbations strongly depend of the reduced mass of the diatom, it is worth to see whether perturbations depend on the coupling or not.

The reason of a variation of the molecular spin-orbit splitting with the internuclear distance is the fact that the molecular states $^3\Pi_u$ and $^1\Sigma_u$ at small internuclear distances are sufficiently influenced by atomic states more excited than $6P$. For more excited atomic states the spin-orbit coupling is smaller and makes the molecular spin-orbit splitting weaker for short distances.

Here the influence of this factor on the perturbations in the 0_u^+ spectra of Cs_2 and Rb_2 is considered.

The variation of the molecular spin-orbit interaction in Cs_2 was calculated by Meyer [94] and is shown in Fig. 4.15. As there is no corresponding data for Rb_2, the same curve as for Cs_2, scaled for all internuclear distances by factor $V_{SO}(Rb)/V_{SO}(Cs)$ (V_{SO} is atomic spin-orbit interaction) is used for Rb_2. Thus, results for Rb_2 have only the qualitative character.

Fig. 4.16 shows the results of calculations with the constant (upper left panel) and the variable (lower left panel) spin-orbit coupling for Cs_2. The perturbations in Cs_2 are more significant for the case of a variable molecular spin-orbit coupling. With the variable spin-orbit coupling, vibrational levels are perturbed even more than in case of Rb_2. All B_v constants are situated completely non-regularly – both descriptions (diabatic and adiabatic) of the potential cannot approximate the entire coupled situation.

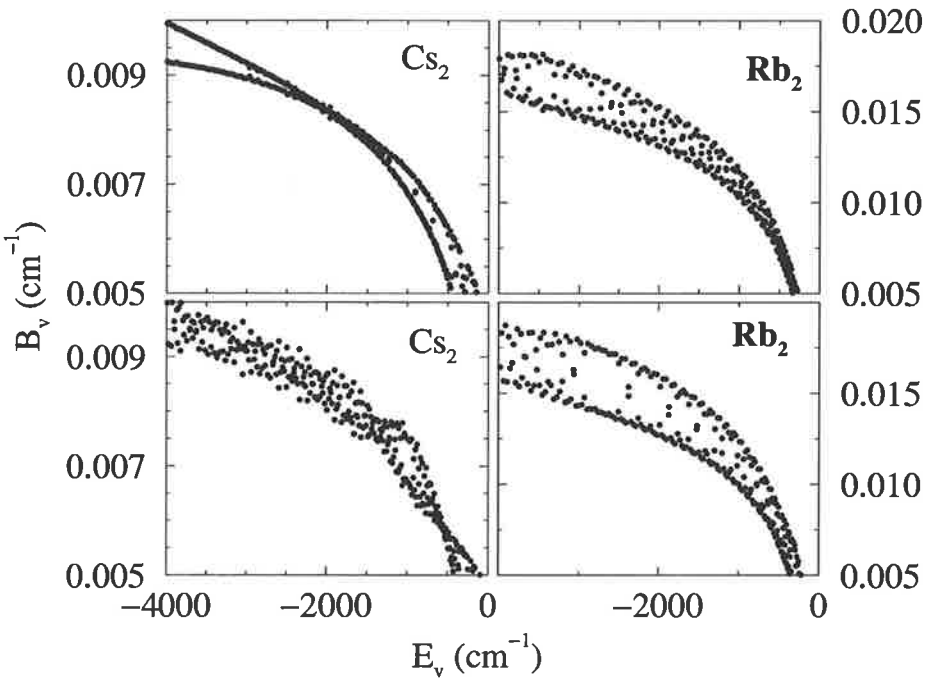

Figure 4.16: Rotational constants for $^{237}Cs_2$ (left panels) and $^{85}Rb_2$ (right panels), calculated using two different molecular spin-orbit couplings. Upper panels show rotational constants for the potential with R-independent molecular spin-orbit interaction, lower panels — with the variable coupling according to the Fig. 4.15

The atomic spin-orbit splitting in Cs_2 is sufficiently large. This constant molecular spin-orbit coupling in Cs_2 is sufficiently strong that the total potential (two curves plus the coupling) can be considered as almost purely adiabatic. The $P_{1/2}$ and $P_{3/2}$ molecular states are only weakly coupled by the non-adiabatic coupling. In contrast to the Rb_2, it that allows to attribute all vibrational levels to one or to another molecular state.

The variable coupling, as it is shown in the figure 4.15, is weaker for small distances. Qualitatively, it can be viewed as if the potential could be considered as a pair of non-coupled diabatic $^3\Pi_u$ and $^1\Sigma_u$ curves at the region of small spin-orbit coupling. It gives perturbations in a corresponding region of energies, i.e. region of vibrational levels for which a short-range part (where the coupling is smaller) of wave functions is quite important. Two $P_{1/2}$ and $P_{3/2}$ channels can not be treated independently any more. For more excited levels, for which wave functions is situated mostly at the region, where the non-adiabatic coupling is small, the non-adiabatic coupling between adiabatic $P_{1/2}$ and $P_{3/2}$ states is much smaller and in this region, $E > -200$ cm^{-1}, perturbations are small.

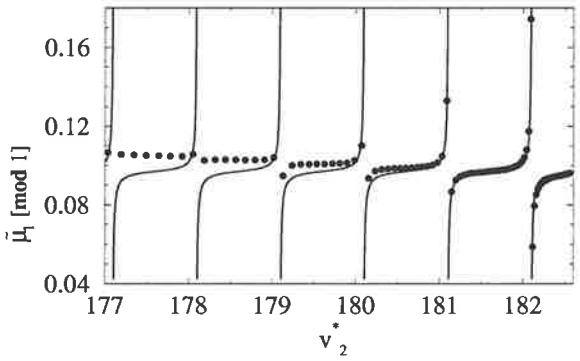

Figure 4.17: Lu-Fano plot for 0_u^+ symmetry of Cs_2 with the variable spin-orbit coupling (full circles), fitted with constant parameters: $R_{1,2} = 0.1$, $\mu_1 = 0.097$, $\mu_2 = -0.096$ (full lines).

This effect is manifested also in the Lu-Fano plot (the Figure 4.17). As one can see from the figure, the parameters $R_{1,2}$, μ_1, μ_2 vary from one quantum number $v(P_{3/2})$ to the consecutive number $v(P_{3/2}) + 1$. It means that adiabatic approximation (two non-coupled, $P_{1/2}$ and $P_{3/2}$, vibrational series) does not work well anymore.

As a result, pre-dissociated levels of the $P_{3/2}$ molecular state with energies above the $P_{1/2}$ limit must have smaller lifetimes in comparison with levels computed for the potential with the constant spin-orbit coupling. The parameters $R_{1,2}$, μ_1, μ_2 determining the positions and widths of resonances above $P_{1/2}$ limit are the following: $R_{1,2} = 0.1$, $\mu_1 = 0.097$, $\mu_2 = -0.096$. But these parameters slowly change with the energy (on 1-5% for two consecutive vibrational levels) and can be considered as constant only for several resonances close to the $P_{1/2}$ threshold.

As another demonstration of the effect of the variable coupling, qualitative calculations for Rb_2 are presented on the right lower panel of Fig. 4.16. The coupling is shown on Fig. 4.15. For Rb_2 vibrational levels also becomes less adiabatic and more close to the levels calculated for non-coupled $^3\Pi_u$ and $^1\Sigma_u$ potentials, especially, in the intermediate region of energies, from -3000 cm^{-1} to -200 cm^{-1}.

4.3 Lifetimes of pre-dissociated levels of 0_u^+ symmetry of Rb_2 and Cs_2.

In the previous section perturbations in the discrete spectrum 0_u^+ were considered. Above the $P_{1/2}$ limit, the mixing between two components, $P_{1/2}$ and $P_{3/2}$ leads to the fact, that bound vibrational $P_{3/2}$ levels are pre-dissociated due to the coupling with the $P_{1/2}$ continuum levels. The $P_{3/2}$ series of vibrational levels lying above the $P_{1/2}$ asymptote becomes a series of resonances.

In this section the pre-dissociation of the $P_{3/2}$ vibrational levels is discussed. First,

the example of Rb_2 is considered. As it was found in the previous section, that perturbations in spectra of two isotopes are different. The parameters μ_1, μ_2, $R_{1,2}$ were extracted from the perturbations in the discrete spectrum, that allows to predict widths and positions of pre-dissociated levels. Since the parameter $R_{1,2}$ is different for two isotopes, the lifetimes for two isotopes should be different (approximately by a factor 3). The variation of the μ_2 parameter must lead to a difference in shifts of pre-dissociated levels in respect of the non-perturbed series.

The results of lifetimes calculations for both isotopes of Rubidium were obtained by two methods - time-dependent and time-independent. The comparison and the effectiveness of two methods have been considered in the chapter 3.

Second example of lifetime calculations is the 0_u^+ symmetry of Cs_2. It was found in the previous section that parameters μ_1, μ_2, $R_{1,2}$ are not constant and they vary at several percents $(1 - 10\%)$ from one vibrational level to the neighboring one. Therefore, the prediction concerning the widths and positions of pre-dissociated levels can be made only for several resonances close to the $P_{1/2}$ limit, for the energy domain from 0 to 100 cm^{-1}. Indeed, the lifetimes calculation will show that the parameters μ_2, $R_{1,2}$ change sufficiently on the energy domain between $P_{1/2}$ and $P_{3/2}$ asymptotes.

Third, the influence of the variable spin-orbit coupling between two states are investigated for both species - Rubidium and Cesium as it was made for the discrete spectrum for Cesium.

4.3.1 Rb_2

This subsection presents first results of lifetime calculation for two isotopes of Rubidium. The results are analyzed using the 2QDT approach, the parameters μ_2 and $R_{1,2}$ are extracted from the results and compared with parameters for the discrete spectrum. Excellent agreement is found. The strong difference in lifetimes (and in $R_{1,2}$) for two isotopes $^{85}Rb_2$ and $^{87}Rb_2$ is discussed and qualitatively explained. A dependence of lifetimes upon the variable coupling between channels is considered. Finally, the comparison with experiment are discussed.

Results of calculations

Fig. 4.18 represents the results of time-independent calculations with the optical potential for pre-dissociated levels located between the $^2S + ^2P_{1/2}$ and $^2S + ^2P_{3/2}$ asymptotes for two isotopes of Rb, $^{85}Rb_2$ with reduced mass $\mu = 77392.376$ $a.u.$ and $^{87}Rb_2$ with $\mu = 79212.883$ $a.u.$. The upper panel of the figure shows lifetimes τ, the lower panel – the widths $\Gamma = \tau^{-1}$ of levels. A relation between τ in ps and Γ in GHz is:

$$\Gamma(GHz) = \frac{1000}{2\pi\tau(ps)} \tag{4.33}$$

The figure also shows the lifetimes and widths (triangles) for $^{85}Rb_2$ with the R-dependent spin-orbit coupling as it is shown at the figure 4.15. The detailed discussion of the influence of the R-dependent spin-orbit coupling will be presented below.

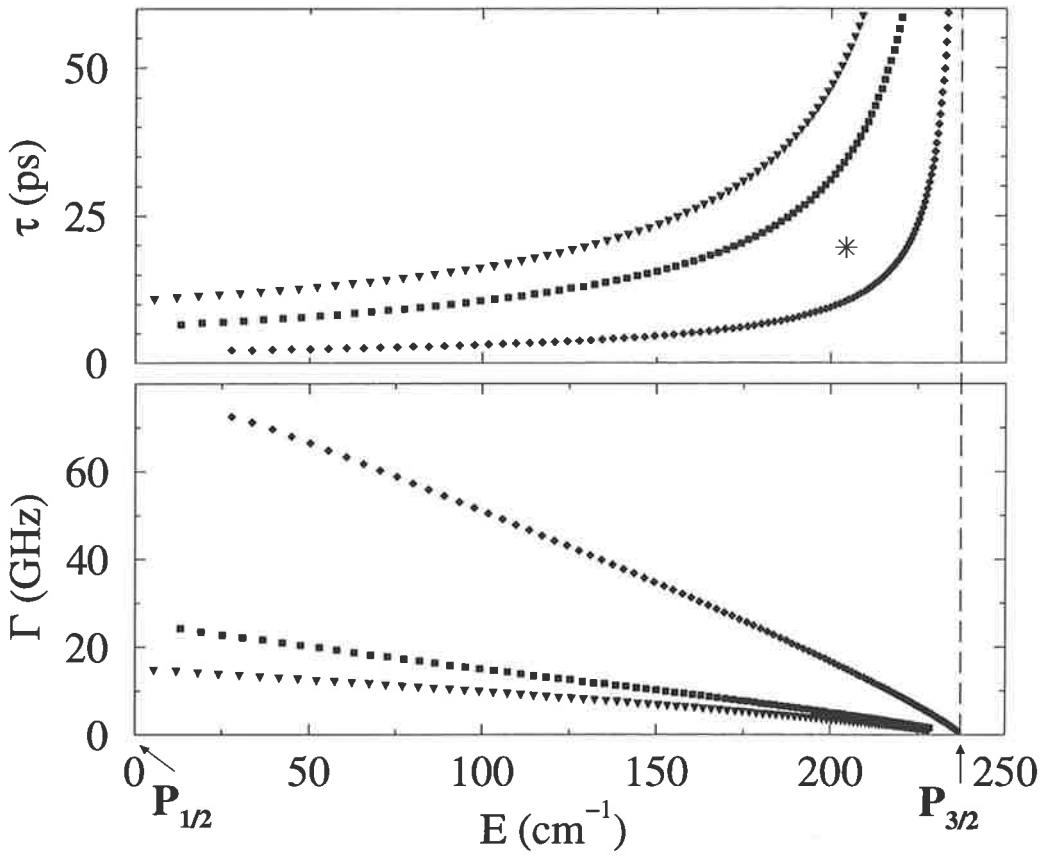

Figure 4.18: Lifetimes (upper panel) and widths (lower panel) of pre-dissociated levels for two isotopes: diamonds - $^{85}Rb_2$, squares - $^{87}Rb_2$. The experimental value for $^{85}Rb_2$ from [27] ($\tau \approx 20\ ps$) is presented by a big star. Triangles represent the model calculations with the variable coupling as it shown at Fig. 4.15 for $^{85}Rb_2$.

Lifetimes are calculated using the time-independent MFGR coupled with the optical potential.

QDT parameters, comparison with the discrete spectrum

Compared with bound vibrational levels of the single $P_{3/2}$ molecular state, vibrational levels, pre-dissociated into the $P_{1/2}$ state, can be characterized by three parameters: μ_1 – the asymptotic phase shifts of the pre-dissociated wave function, μ_2 – the quantum defect, which defines the energetic shift of a level in respect of the corresponding non-coupled $P_{3/2}$ level, $R_{1,2}$, which defines the transition probability and width of the pre-dissociated level. All these parameters are defined from the discrete spectrum and should be continuous when energy cross the $P_{1/2}$ threshold.

Fig. 4.19 shows quantum defects μ_2 for pre-dissociated levels for two isotopes (open diamonds and squares). They are almost constant for all domain of energy between $P_{1/2}$ and $P_{3/2}$ asymptotes. The first calculated value μ_2 for $^{85}Rb_2$ is 0.190, and 0.638 for $^{87}Rb_2$. The value obtained from the discrete spectrum are 0.180 and

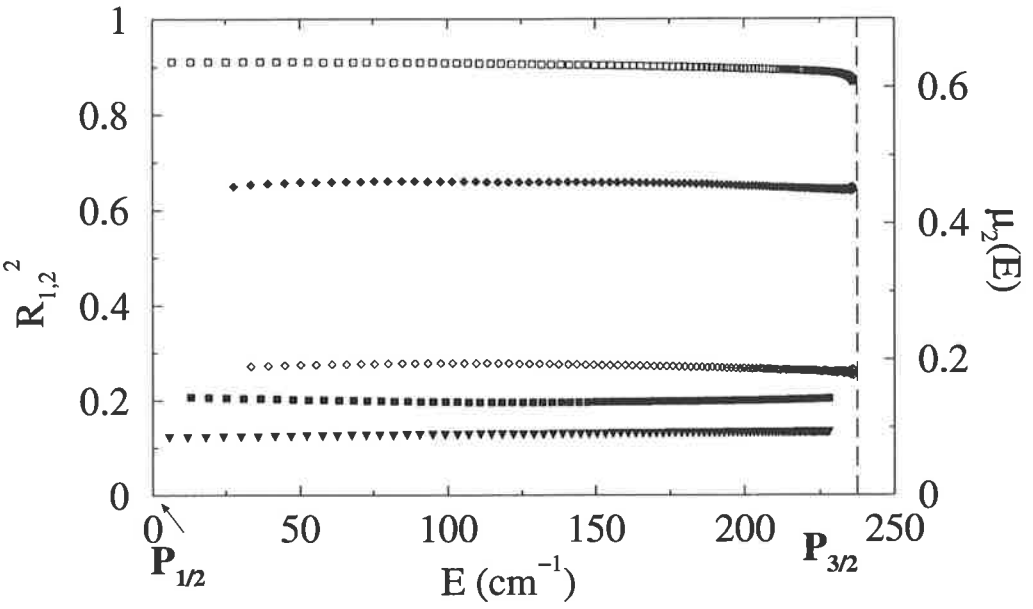

Figure 4.19: The quantum defects μ_2 (open diamonds and squares) and quantities $R^2_{1,2}$ (full figures) for $P_{3/2}$ pre-dissociated levels for $^{85}Rb_2$ (diamonds) and $^{87}Rb_2$ (squares). Triangles represents calculation for $^{85}Rb_2$ with the variable coupling.

0.636 respectively. The figure 4.19 demonstrates also the behavior of the $R^2_{1,2}$. It is almost constant for both isotopes for whole energy domain of pre-dissociated levels. $R^2_{1,2}$, defined for the discrete spectrum using the Lu-Fano plot, is $R^2_{1,2} = 0.547$ for $^{85}Rb_2$ and $R^2_{1,2} = 0.212$ for $^{87}Rb_2$. $R^2_{1,2}$ defined from the lifetime calculation is 0.648 for $^{85}Rb_2$ and 0.207 for $^{87}Rb_2$. As it was found, parameters μ_2, $R^2_{1,2}$ do not change for the energy domain from -1000 cm^{-1} to $P_{1/2}$. They do not change above the $P_{1/2}$ limit up to the $P_{3/2}$ threshold. Therefore, one can say that they stay constant for the range of energies from $P_{1/2} - 1000$ cm^{-1} up to $P_{3/2}$). The parameters μ_1 were not determined. The asymptotic shifts of the $P_{1/2}$ component of the total wave function with and without the coupling should be compared to obtain μ_1 (see Eq. (4.32)).

The previous discussion means that all perturbations in the discrete spectrum, position shifts and line widths can be described only by three parameters μ_1, μ_2 and P (or $R_{1,2}$). In more general case, these parameters vary weakly with the energy, but they change weakly for consecutive levels.

Transition probability

The norm n of a $P_{3/2}$ pre-dissociated level decreases exponentially with the time t:

$$n = n_0 e^{-\frac{t}{\tau}} \tag{4.34}$$

The transition probability P from $P_{3/2}$ state on $P_{1/2}$ during one classical period T_c of oscillation is defined from the rest of the norm $n = 1 - P$ after the time T_c, if the

initial norm was 1:

$$1 - P = e^{-\frac{T_c}{\tau}} = e^{-\Gamma T_c}, \tag{4.35}$$

The period of classical oscillations is:

$$T_c = \sqrt{2\mu} \int_{R_1}^{R^2} \frac{dR}{\sqrt{E - V(R)}}, \tag{4.36}$$

where $V(R)$ is the $P_{3/2}$ potential, R_1 and R_2 are turning points for the energy E. The period T_c is connected with the difference ΔE between consecutive vibrational levels. From the WKB quantization condition [78]:

$$\frac{1}{\Delta E} = \frac{1}{\pi}\sqrt{\frac{\mu}{2}} \int_{R_1}^{R^2} \frac{dR}{\sqrt{E - V(R)}}. \tag{4.37}$$

Then:

$$T_c = \frac{2\pi}{\Delta E}, \tag{4.38}$$

and

$$P = 1 - \exp(-\Gamma T_c) = 1 - \exp\left(-\frac{2\pi\Gamma}{\Delta E}\right). \tag{4.39}$$

Using Eq. (4.31):

$$P = 1 - \exp\left(-4R_{1,2}^2\right). \tag{4.40}$$

For small P ($\frac{2\pi\Gamma}{\Delta E} << 1$):

$$P \approx \frac{2\pi\Gamma}{\Delta E}. \tag{4.41}$$

As the parameter $R_{1,2}$ is almost constant for all pre-dissociated energies, the transition probability is constant also (but it is not small, especially for $^{85}Rb_2$). The transition probability for $^{85}Rb_2$ is 0.93 and for $^{87}Rb_2$ is 0.56.

Since the probability is constant the lifetimes of pre-dissociated levels increases with the energy as the period of classical motion increases:

$$\tau_c = -\frac{T_c}{\ln(1-P)} = -\frac{1}{\ln(1-P)}\frac{1}{3}\sqrt{2\mu\pi}C_3^{\frac{1}{3}}\frac{\Gamma(\frac{5}{6})}{\Gamma(\frac{4}{3})}(E_{P_{3/2}} - E)^{-\frac{5}{6}} = \alpha(E_{P_{3/2}} - E)^{-\frac{5}{6}}. \tag{4.42}$$

The integration is made as in Ref. [78] (R.Leroy and R.Bernstein). The parameter α is 190 $ps(\mathrm{cm}^{-1})^{5/6}$ for $^{85}Rb_2$ and 630 ps $(\mathrm{cm}^{-1})^{5/6}$ for $^{87}Rb_2$. Fig. 4.20 shows the variation of calculated lifetimes together with the fitting function of Eq. (4.42).

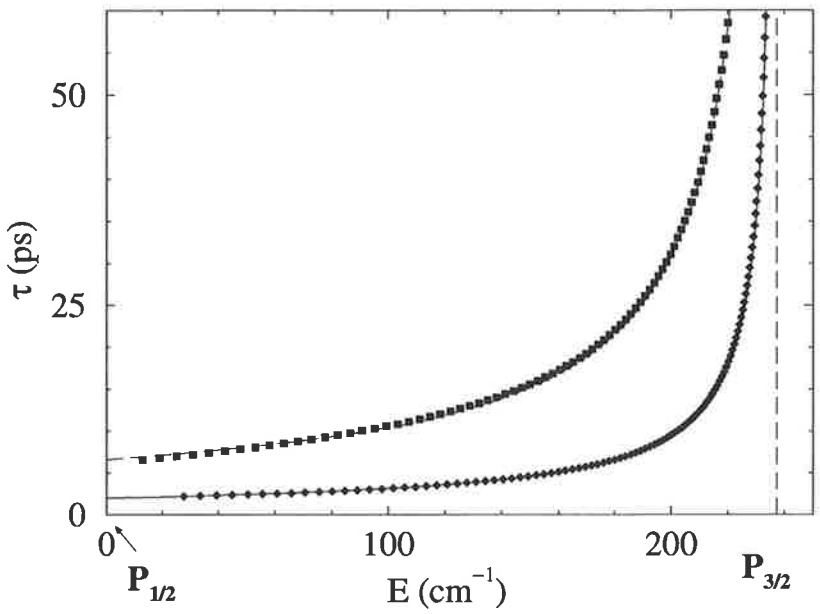

Figure 4.20: Lifetimes of pre-dissociated $P_{3/2}$ levels: $^{85}Rb_2$ - diamonds; and $^{87}Rb_2$ - squares fitted with functions (4.42) with $\alpha = 190\ ps(\mathrm{cm}^{-1})^{5/6}$ for $^{85}Rb_2$ (full line) and with $\alpha = 630\ ps\ (\mathrm{cm}^{-1})^{5/6}$ for $^{87}Rb_2$ (dashed line).

Although the classical approach gives the correct behavior for the lifetime curve, it does not explain the big difference in the lifetimes of two isotopes. The difference between classical periods of oscillations for two isotopes is as small as:

$$\frac{\tau_1}{\tau_2} = \sqrt{\frac{\mu_1}{\mu_2}}. \tag{4.43}$$

For $^{87}Rb_2$ and $^{85}Rb_2$, the difference is lower than 1 %. Lifetimes, calculated in the quantum approach are different with a factor 3.2.

Comparison with the Landau-Zener transition probability

The Landau-Zener probability (P_{LZ}) of transition from the $P_{3/2}$ adiabatic term to the $P_{1/2}$ term during one period of the classical motion is:

$$P = 2P_{LZ}(1 - P_{LZ}) = 0.489 \tag{4.44}$$

where P_{LZ} is a transition probability of one passage through the crossing ($P_{LZ} = 0.573$). The difference for two isotopes is only about 1%. The quantum calculations give a factor 1.7. Thus, this isotopic difference of the lifetimes is a purely quantum effect.

Semi-classical attempt at the explication of the strong isotopic effect

A first natural assumption for the explanation of the isotopic effect is to suppose that the difference between the lifetimes of the isotopes is caused by the difference

between Stueckelberg phases of paths for two isotopes (see, for example, [102, 76]) - a transition probability from the $P_{3/2}$ term to the $P_{1/2}$ term is different because the wave function of one isotope ($^{87}Rb_2$) has a node at the distance of crossing, and the wave function of second ($^{85}Rb_2$) isotope has a maximum there. The phase difference $\Delta\Phi$ between two paths (along $P_{1/2}$ and $P_{3/2}$ terms), accumulated during the passage of region ΔR of internuclear distances, is:

$$\Delta\Phi = \sqrt{2\mu}\int_{\Delta R}\left[\sqrt{E_0 - U_{P_{1/2}}(R)} - \sqrt{E_0 - U_{P_{3/2}}(R)}\right]dR \tag{4.45}$$

This phase is 80 radians. The isotopic difference is about 1 % or 0.8 radian. But the space period (≈ 0.05 *a.u.*) of oscillation of wave function in this region of the potential is much smaller than the width of the coupling ($\approx 1.$ *a.u.*). Thus, the interaction between two terms does not "feel" the nodal structure of both components of the wave function. Another argument against the nodal approach is that one must observe an oscillatory behavior of lifetime with the energy of pre-dissociation. This behavior is monotonous.

The explanation of the isotopic effect in lifetimes

The lifetime is calculated [76] (H.Lefebvre-Brion and R.Field):

$$\tau = \frac{1}{2\pi < \psi'_{P_{3/2},v}|\mathbf{H}|\psi'_{P_{1/2},E} >^2} \tag{4.46}$$

(Here wave functions $\psi'_{P_{3/2},v}$ and $\psi'_{P_{1/2},E}$ are normalized in energy.) In the region ΔR, where the interaction between terms is varying slowly, for the qualitative description of the transition, one can consider the overlap between two components –

$$F = \int_{\Delta R} f(R)dR = \int_{\Delta R} \psi_{P_{3/2},v}\psi_{P_{1/2},E}dR. \tag{4.47}$$

Looking at the potential curves one sees that the crossing occurs in the region where the kinetic energy of highly excited vibrational levels is almost the same for both potentials (in both diabatic and adiabatic representations). It means that both components of a wave function oscillate with almost the same frequency for distance ± 1 a_0. As a consequence, the factor $f(R)$ is modulated by a slow frequency equal to the difference between frequencies corresponding to the motion in the two potential wells. The period of these modulation is of order of 2 *a.u.* near the crossing. Since there is a phase shift between two wave function components, positions of maxima and minima of slow oscillations of $f(R)$ are different for the two isotopes near the crossing. Integrating over the domain of crossing ($\approx 1.$ *a.u.*), we obtain different values F for the two isotopes and, therefore, lifetime for the two isotopes will be different. Fig. 4.21 shows products $f(R)$ for both isotopes. Slow modulations are shifted one in respect to other in the region of the crossing. Outside of the region of the crossing, modulations are much frequent because the separation between potential terms are not small in comparison with the kinetic energy. In panel *c* we

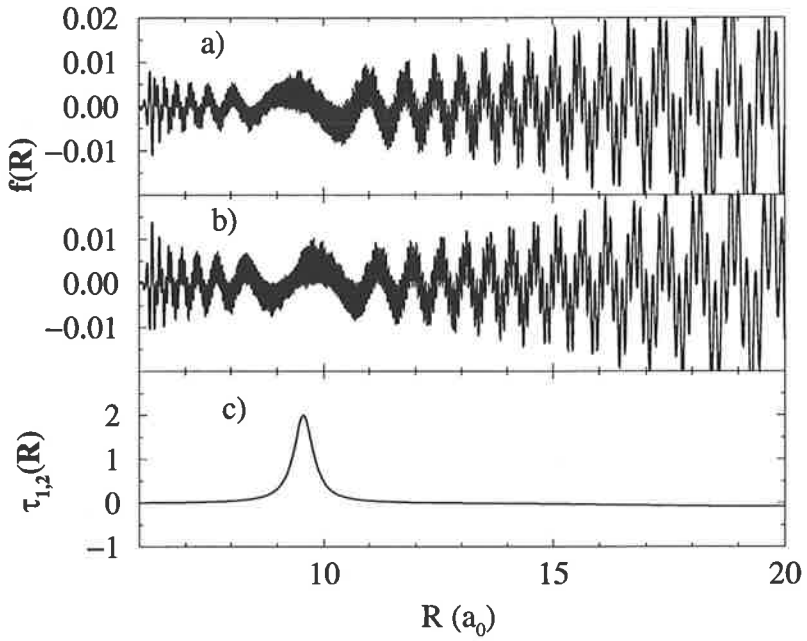

Figure 4.21: The quantity $f(R) = \psi_{E,P_{3/2}}(R)\psi_{E,P_{1/2}}(R)$, calculated for two rubidium isotopes. a – $^{85}Rb_2$ (energy of level $E = 15.7$ cm^{-1} over $P_{1/2}$ limit), b – $^{87}Rb_2$ with the energy $E = 19.4$ cm^{-1}. The panel c represents the non-adiabatic coupling between two components – $P_{1/2}$ and $P_{3/2}$. Transitions occur only in the region where $\tau_{1,2}$ is quite large.

present also the non-adiabatic radial coupling $(\tau_{1,2}(R),)$ between two components of 0_u^+ Rb_2. (We use a form of non-adiabatic coupling V^{na}, where $\tau_{1,2}(R)$ is introduced as : $V^{na} = -\frac{1}{\mu}\tau(R)\frac{d}{dR}$.)

In contrast to the sensitivity of lifetimes to the isotopic mass, there is no significant dependence of the pre-dissociated energy. On the figure 4.22 we present $f(R)$ for three energies near the dissociation limit for $^{87}Rb_2$. For all range of pre-dissociated energies from $P_{1/2}$ to $P_{3/2}$ and even for highly excited bound levels there is no significant shift in positions of maxima and minima of $f(R)$. Therefore, lifetime increase monotonously for energy between $P_{1/2}$ to $P_{3/2}$ limits. *This result means that the phase shift $\Delta_{3/2-1/2}$ between* **two components** *($P_{1/2}$ and $P_{3/2}$) of a wave function in the vicinity of the crossing changes slowly with the pre-dissociated energies and the shift changes fast with the reduced mass.*

Therefore, the standard approach using the Stueckelberg phases and considering simply the nodal structure of wave functions (not the nodal structure of *modulations*), does not work.

The difference between *shifts* $\Delta_{3/2-1/2}$ for two isotopes due to the different Stueckelberg paths is of order 1% or 0.8 radians (Fig 4.21), that gives easily the strong isotopic effect. In this form the approach, using Stueckelberg phases, explains the monotonous lifetime behavior with the pre-dissociated energy and strong dependence of the reduced mass.

In order to demonstrate again the strong isotopic effect, we have calculated life-

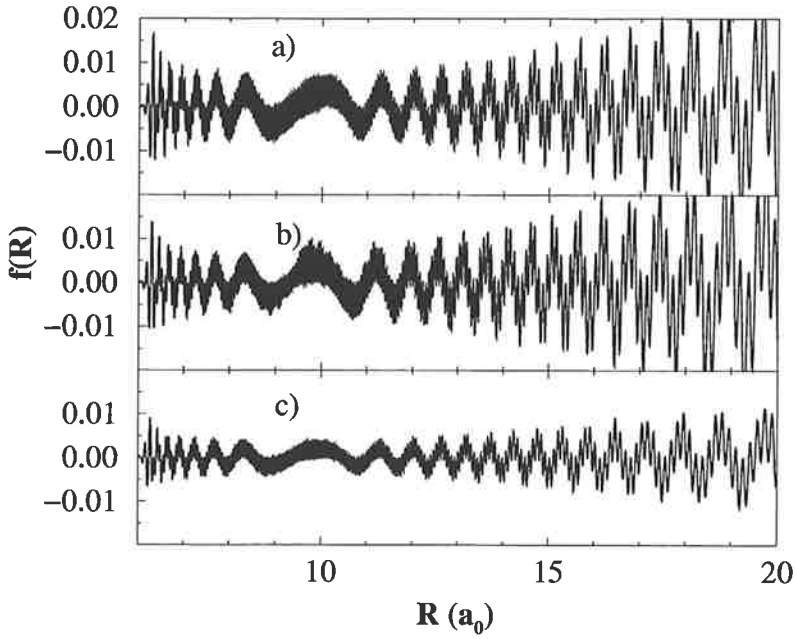

Figure 4.22: Factor $f(R)$, calculated for levels of the 0_u^+ symmetry of $^{87}Rb_2$ with different energy near the $P_{1/2}$ dissociation limit. a – bound level with energy $E = 13.6\ cm^{-1}$, b and c - pre-dissociated levels with energies $E = 19.4\ cm^{-1}$ and $E = 174.1\ cm^{-1}$ respectively. For any energy positions of maxima and minima of the slow modulation stay the same. It provides the monotonic (not oscillating) increasing of lifetimes for the all pre-dissociated levels between $P_{1/2}$ and $P_{3/2}$ limits.

times for fictitious isotopes of Rb_2 with different reduced mass. The lifetimes is very large for an "isotope" with the mass equal to 75000 $a.u.$ ($\alpha = 7000$), but it becomes again small, as for $^{87}Rb_2$, with the mass 70000 $a.u.$

Quantum defects

The qualitative explication of isotopic difference in quantum defects μ_1 and μ_2 can be easily done using the previous consideration, i.e. using the the isotopic difference in the effective coupling between $P_{1/2}$ and $P_{3/2}$.

Consider, for example, the discrete spectrum and the defect μ_2. This quantity is defined in respect to the non-coupled single potential $P_{3/2}$. Following the ordinary definition of the quantum defect (H.Friedrich [44]), μ_2 can be written as:

$$\mu_2 = \frac{1}{\pi}\left[\int_{\bar{R}_1}^{R_2}\sqrt{2\mu(E - V_e(R))}dR - \int_{R_1}^{R_2}\sqrt{2\mu(E - V(R))dR}\right], \tag{4.48}$$

where $V(R)$ is the $P_{3/2}$ potential, $V_e(R)$ is a some fictitious "effective" potential, which has a same effect on the phase shift as the coupling with the $P_{1/2}$ potential. It is clear that at large distances, where the coupling is small and potentials $V(R)$ and $V_e(R)$ are equal, contributions of both integrations Eq. (4.48) are almost equal and compensated. Thus, for different highly-excited vibrational levels μ_2 is almost

the same, but not 0. It gives the constant quantum defect μ_2. The situation does not change when energy becomes larger than the $P_{1/2}$ threshold.

For the defect μ_1 the situation is exactly the same for bound levels. Eq. (4.48) is valuable also for energies above $P_{1/2}$. μ_1 in this region stays the same as for bound levels, but now it means the asymptotic shift (modulo unit) of the wave function. For resonances, similarly to μ_2, it changes slowly with energy.

4.3.2 Cs_2

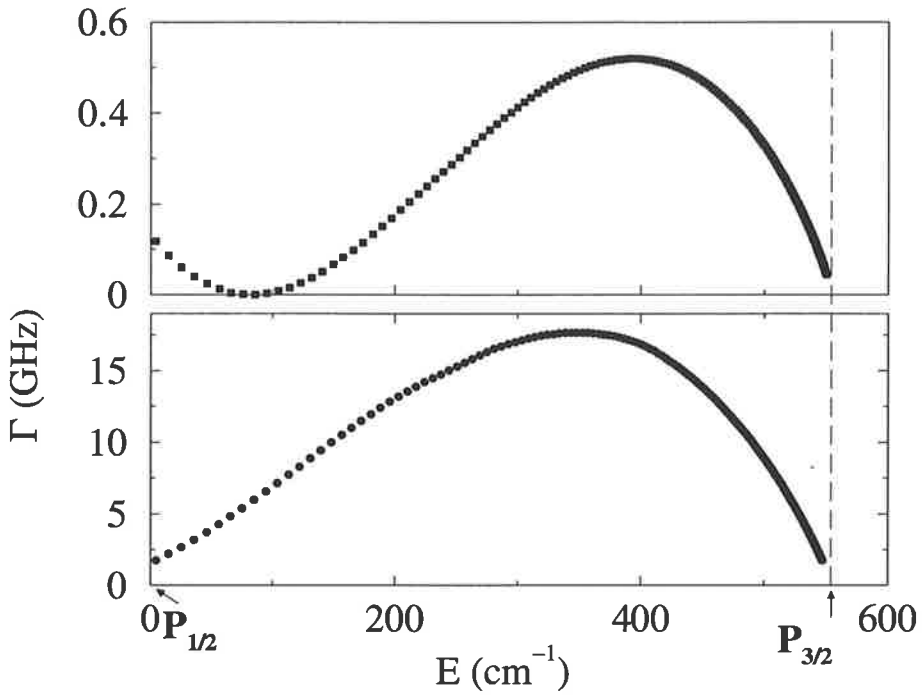

Figure 4.23: Widths of vibrational levels of Cs_2 0_u^+ for two different molecular spin-orbit interactions $V_{SO}(R)$ between $^3\Pi_u$ and $^1\Sigma_u$ curves: circles - the molecular spin-orbit interaction is varying as shown in Fig. 4.15; squares - constant molecular spin-orbit interaction ($V_{SO} = 554.1$ cm^{-1}).

The calculations for the discrete spectrum of the 0_u^+ symmetry of Cs_2 with the constant spin-orbit coupling have shown that the mixing between adiabatic components of vibrational wave functions is much smaller than in the case of Rubidium. Parameters μ_1, μ_2, $R_{1,2}^2$ were found much smaller that 1. The results for rotational constants demonstrate also that vibrational levels of $P_{1/2}$ and $P_{3/2}$ states are only slightly perturbed by the adiabatic coupling between these molecular states. It means that one should expect relatively large lifetimes of pre-dissociated levels in comparison with lifetimes of Rb_2. In contrast, calculations with the same potentials but with the R-dependent spin-orbit coupling demonstrates the very strong mixing of adiabatic (and diabatic) components of vibrational wave functions. The parameter $R_{1,2}$ increases in three times comparing with the case of the constant spin-orbit coupling, what must

give nine times smaller lifetimes for the case of the variable coupling. Another prediction, which can be made using the analysis of the Lu-Fano plots for the discrete spectrum, is that the parameters μ_1, μ_2, $R_{1,2}$ are not constant for both constant and variable coupling. For the Cs_2 they should change slightly with the energy. For pre-dissociated levels just over the $P_{1/2}$ dissociation limit, positions and widths of resonances can be predicted using Eqs. (4.30) and (4.31).

Below, the results of lifetime calculation are presented. For the case of Cesium, the time-independent approach with the optical potential and the mapping is used.

R-independent coupling

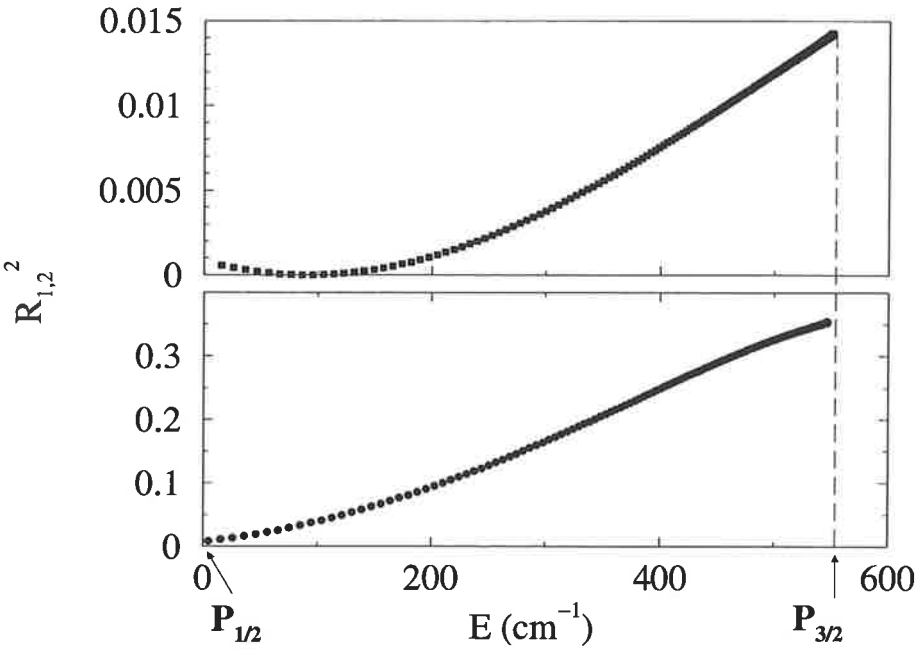

Figure 4.24: The parameter $R_{1,2}^2$ for pre-dissociated levels of the 0_u^+ symmetry of Cs_2 with the constant (upper panel) and the variable (lower panel) spin-orbit coupling.

The upper panel of Fig. 4.23 represents the results of calculations with the constant coupling, corresponding to the atomic spin-orbit coupling $6^2P_{3/2} - 6^2P_{1/2} = 554.1$ cm^{-1} in the free 6^2P atom. As one can see, lifetimes are indeed much larger in comparison with Rb_2. The upper panel of Fig. 4.24 shows the $R_{1,2}^2$ parameter as a function of energy. As in the discrete spectrum, this parameter varies slowly with energy. For neighboring levels, this parameter is almost the same. The small value of $R_{1,2}^2$ demonstrates again that the adiabatic approximation works well for the constant molecular spin-orbit coupling. Another interesting feature of the results is a strong increase of lifetimes ($R_{1,2} \approx 0$) near the energy $E = 140$ cm^{-1}.

R-dependent coupling

The variable spin-orbit coupling changes the order of magnitude of $R^2_{1,2}$. As it can predicted from the bound calculations, the lifetimes of pre-dissociated levels are much smaller than lifetimes for the constant spin-orbit coupling. This result can be explained as following. The reducing of the spin-orbit coupling at small distances leads to the total potential which is "more diabatic" than with the constant coupling. – In the adiabatic representation (two channels $P_{1/2}$, $P_{3/2}$ and the non-adiabatic coupling), a reducing of spin-orbit orbit interactions leads to the increasing of non-adiabatic coupling between $P_{1/2}$, $P_{3/2}$ channels, that leads to more strong perturbations in the spectrum.

4.4 Conclusion

In this chapter it was demonstrated that the mapped time-independent FGR method developed in the Thesis is very powerful tool for calculation of bound and pre-dissociated levels of long-range one- and multi-channel potential.

As an application of the method, the 0^+_u symmetry of two alkali molecules, Rb_2 and Cs_2, has been investigated. Especially, bound and pre-dissociation levels close to the first dissociation limit $P_{1/2}$ have been investigated.

The example of the 0^+_u symmetry was chosen since it demonstrates the strong non-adiabatic coupling between two states, that is manifested in strong perturbations in the discrete spectrum and in the strong pre-dissociation of vibrational levels over the $P_{1/2}$ limit. Therefore in the experiment it is observed that the vibrational series of the discrete spectrum are very irregular, and levels over the $P_{1/2}$ limit are broaden due to the pre-dissociation. Since wave functions of highly excited vibrational levels of the symmetry are situated mainly at large distances, the choice of this potential allows to check once again the method.

The calculations with the rubidium diatom have reproduced the perturbations in the discrete spectrum. Using the method, it was confirmed (as it was done by C.Amiot *et al.*) once again, that the spin-orbit coupling is responsible for the strong perturbations in the spectrum, observed in the experiment.

The same calculations have qualitatively explained also the "strange" behavior of the rotational constant of vibrational levels in $^{85}Rb_2$ near the $P_{1/2}$ dissociation limit, observed in the experiment of the Heinzen group [52].

For the interpretation of the results, the quantum defect theory has been adapted for two perturbed vibrational series. 2QDT allows to parameterize the behavior of the two coupled vibrational series near (below and above) the $P_{1/2}$ dissociation limit only by three parameters, μ_1, μ_2, $R_{1,2}$. Under the dissociation limit these parameters describe shifts of vibrational levels due to the coupling. Above the threshold, the parameters define also lifetimes of pre-dissociated levels. Since these parameters change weakly with the energy, by extracting them from the discrete spectrum, the lifetimes of pre-dissociated levels and asymptotic shifts of corresponding wave functions can be predicted.

In a case of Rubidium, two isotopes have been investigated, $^{85}Rb_2$ and $^{87}Rb_2$. A large difference (3 times) in lifetimes was found for these two isotopes. This result can explain another experimental effect – the isotopic difference in the trap loss in Rubidium [134]. This experimental effect initial was attributed to the different hyperfine structure for two isotopes.

It was investigated an influence of the molecular spin-orbit coupling on perturbations and lifetimes of levels of the 0_u^+ symmetry of Rb_2 and Cs_2. It was found that in Rubidium, the variable spin-orbit coupling does not change qualitatively the results. In contrast, the results for Cs_2 with the constant and variable molecular spin-orbit interaction are very different in the discrete spectrum and in the spectrum of pre-dissociated levels.

Chapter 5

Other Applications of the Mapped Fourier Grid Method.

In the previous chapter, the MFGR method was applied for the detailed investigation of vibrational and pre-dissociated levels of the 0_u^+ symmetry of Cs_2 and Rb_2. In this chapter two other experiments carried out in the laboratory Aimé Cotton are interpreted using the developed method.

5.1 Tunneling in the Cs_2 0_g^- photo-association spectrum.

In the recent photo-association experiment in a cesium trap [41], two vibrational series were observed. These series have been attributed to the 0_g^- $(6S + 6P_{3/2})$ and to the 1_u $(6S + 6P_{3/2})$ molecular states.

The 0_g^- $(6S+6P_{3/2})$ potential curve has two wells separated by a potential barrier at 15 a_0. In the experiment, only vibrational levels of the outer well are observed. This double-well shape of the potential gives rise to a tunneling between the inner and the outer wells for vibrational levels lying under the barrier. The tunneling affects positions of vibrational levels situated near the potential barrier.

In the experiment, besides two vibrational series, which are assigned to two molecular states, the observed spectrum contains two rotational structures, which cannot be assigned to any series.

M. Vatasescu [128, 129] has used MFGR to compute the vibrational levels and their wave functions in the double well of the 0_g^- $(6S + 6P_{3/2})$ potential, showing evidence of tunneling. She demonstrates that multichannel tunneling is important, due to the coupling, in the inner well, between the 0_g^- $(6S + 6P_{3/2})$ and the 0_g^- $(6S + 5D_{3/2})$ molecular states. Due to the tunneling, a part of the wave functions of such levels is in the outer well, and, thus, the levels can be populated in photo-association experiment.

Using the MFGR method and changing slightly the 0_g^- $(6S+5D_{3/2})$ potential and the coupling, M. Vatasescu has fitted calculated positions and rotational constants of

these two levels to the observed ones. She defined also the exact height of the barrier of the 0_g^- $(6S + 6P_{3/2})$ state.

5.2 Symmetry breaking between $B^1\Pi_u$ and $1^1\Pi_g$ states in $^6Li^7Li$.

This section describes another application of the MFGR method – an interpretation of an experiment with the $^1\Pi_u$ – $^1\Pi_g$ $(2S+2P)$ symmetry breaking in the molecule $^6Li^7Li$. The motivation of the this work was a recent experiment by N. Bouloufa, P. Cacciani, and R. Vetter [22] studying the $^1\Pi_u$ symmetry of Li_2. In this experiment, an unexpectedly strong pre-dissociation of vibrational levels of the $^1\Pi_u$ $(2S + 2P)$ electronic state of the isotope $^6Li^7Li$ was observed.

In this section, an explanation is proposed for this strong effect, assuming that the observed pre-dissociation is due to the coupling with the $^1\Pi_g$ $(2S + 2P)$ state. This coupling arises from the $g - u$ symmetry breaking in the $^6Li^7Li$ molecule.

Hereafter in this chapter the origin of the energy will be at the dissociation limit of the $^1\Pi_u$ $(2S + 2P)$ potential, potentials $^1\Pi_u$ $(2S + 2P)$ and $^1\Pi_g$ $(2S + 2P)$ will be called simply as $^1\Pi_u$ and $^1\Pi_g$.

5.2.1 Introduction

The potential $^1\Pi_u$ of Li_2 demonstrates a barrier at the distance 11 a_0 (Fig. 5.1). Due to the barrier, the potential has, for $^6Li^7Li$ and the total momentum $J = 1$, four vibrational levels with the positive energy in addition to 13 bound levels. These levels are pre-dissociated and have finite lifetimes.

Among the four pre-dissociated levels $v = 13 - 16$ $(J = 1)$ of $^6Li^7Li$, only the upper level $(v = 16)$, situated close to the the top of the barrier, is strongly pre-dissociating. Three others have very long lifetimes because the barrier is sufficiently large. With increase of the quantum number J, the energies of all vibrational levels (bound and pre-dissociated) move up. This leads to the fact that for some J the energy of the $v = 12$ levels becomes positive – this level becomes pre-dissociated. Increase of J leads also to the disappearance of the highest $v = 16$ level, when its energy is above the top of the barrier. For very large values $J \sim 70$ the $^1\Pi_u$ does not contain vibrational levels any more.

The pre-dissociation of upper levels for different J values from 1 to 72 has been observed in the experiment by N. Bouloufa *et al.* [22] for $^7Li_2$. The observed pre-dissociation widths have been found in very good agreement with the results of quasi-classical calculations [22]. These calculations show also, that only the pre-dissociation of one the highest level (for a given J) can be observed in the experiment. Widths of other pre-dissociated levels are smaller than the experimental resolution limit, 1 MHz. For simplicity, these levels with very small widths will be referred to VLL-levels (very long-living levels).

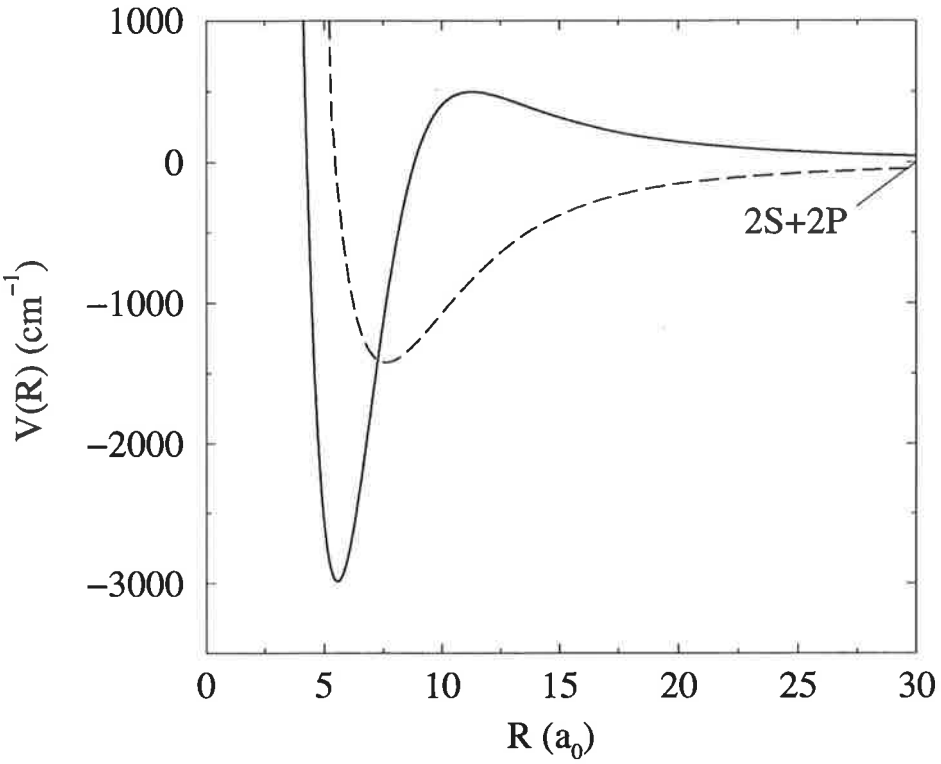

Figure 5.1: Potentials $B^1\Pi_u$ (full line) and $1^1\Pi_g$ (dashed line) of Li_2 $(2S+2P)$.

However, in the same experiment, the pre-dissociation of such VLL-levels for $^7Li^6Li$ was observed. This effect could not be explained by tunneling through the barrier. There are levels lying very close to the dissociation limit with relatively large widths. The largest widths are about 60 GHz.

This observed strong pre-dissociation was the motivation for the present model and calculations.

The explanation of the effect can be done taking into account the fact that nuclei in the $^7Li^6Li$ molecule are not equivalent, so that u and g symmetries no longer correspond to good quantum numbers. The permutation of $2S$ and $2P$ atomic states between two nuclei in the molecule change the total molecular wave function, since these atomic states $2S$ and $2P$ are not the same for nuclei with different mass. The $g-u$ symmetry breaking leads to the coupling between $^1\Pi_u$ and $^1\Pi_g$ molecular states. This coupling causes the pre-dissociation of VLL-levels of the $^1\Pi_u$ molecular states through the $^1\Pi_g$ state.

5.2.2 The pre-dissociation through the potential barrier

First, the results of semi-classical calculations for the upper levels pre-dissociated due to the tunneling effect has been confirmed. In the present calculations the MFGR method with the absorbing potential was used.

For the calculation, the potential $^1\Pi_u$ was taken from Ref. [22], the potential

$^1\Pi_g$ was taken from Ref. [87]. Both potential, fitted to the experiment, are very precise. Bound levels, calculated with the MFGR method using these potentials, and experimental levels are found in agreement, expressed in terms of quantum defects, better than $\mu(v) = 0.04$.

Below, the results of calculations for $^6Li^7Li$ are presented and discussed.

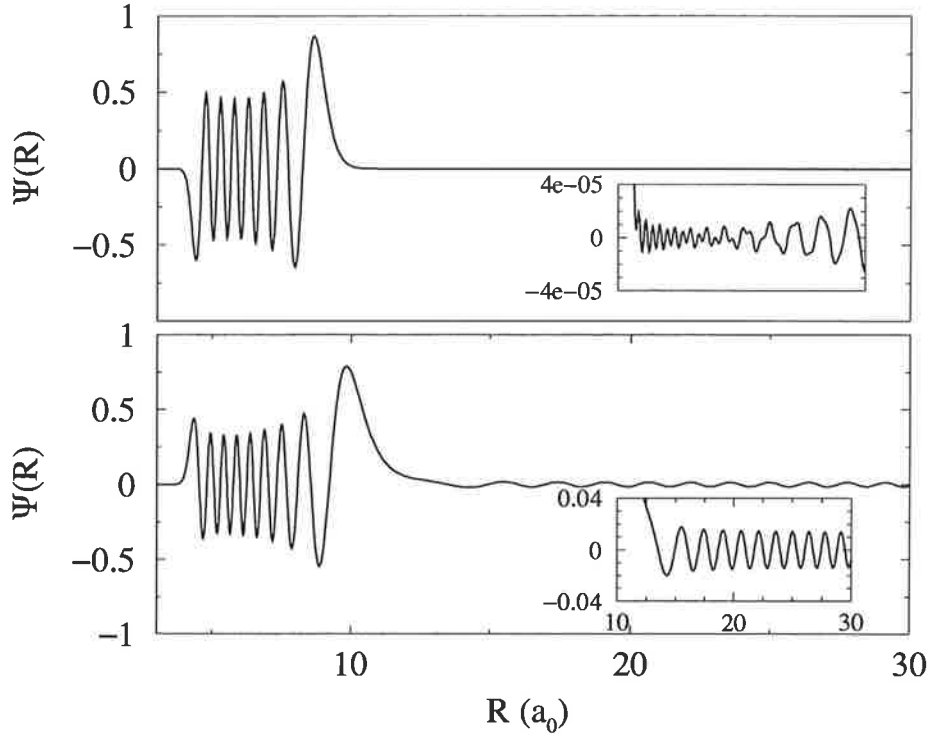

Figure 5.2: Two typical pre-dissociated wave functions of the $^1\Pi_u$ molecular state of $^6Li^7Li$ with $J = 1$. The lower panel shows the wave function of the highest ($v = 16$) pre-dissociation level, the upper panel shows the lowest ($v = 13$) pre-dissociated level. Insets show asymptotic tails of both wave functions.

For calculation of widths the time-independent method with the absorbing potential was used.

The figure 5.2 shows two typical wave functions of pre-dissociated levels, obtained in MFGR calculations for $^6Li^7Li$ only with the $^1\Pi_u$ potential. Both wave functions are normalized to unity in a box from $R = 1a_0$ to $R = 50a_0$. The upper panel of the figure shows the lowest *pre-dissociated* vibrational level with energy 77.3 cm^{-1} for the $J = 1$. The width of the level is 0.3 Hz. The lower panel shows the upper vibrational level, $v = 16$. The energy is 450.3 cm^{-1}, the width is 1.008 GHz. (For $J = 1$, the height of the barrier is 499.5 cm^{-1}.) Two insets show the asymptotic parts of wave functions.

The figure 5.3 shows pre-dissociation widths of seven vibrational levels from $v = 10$ to $v = 16$ as a function of the total rotational momentum.

The plan of the section is following. At the beginning, the pre-dissociation only due to the tunneling through the barrier is considered using the MFGR method. The

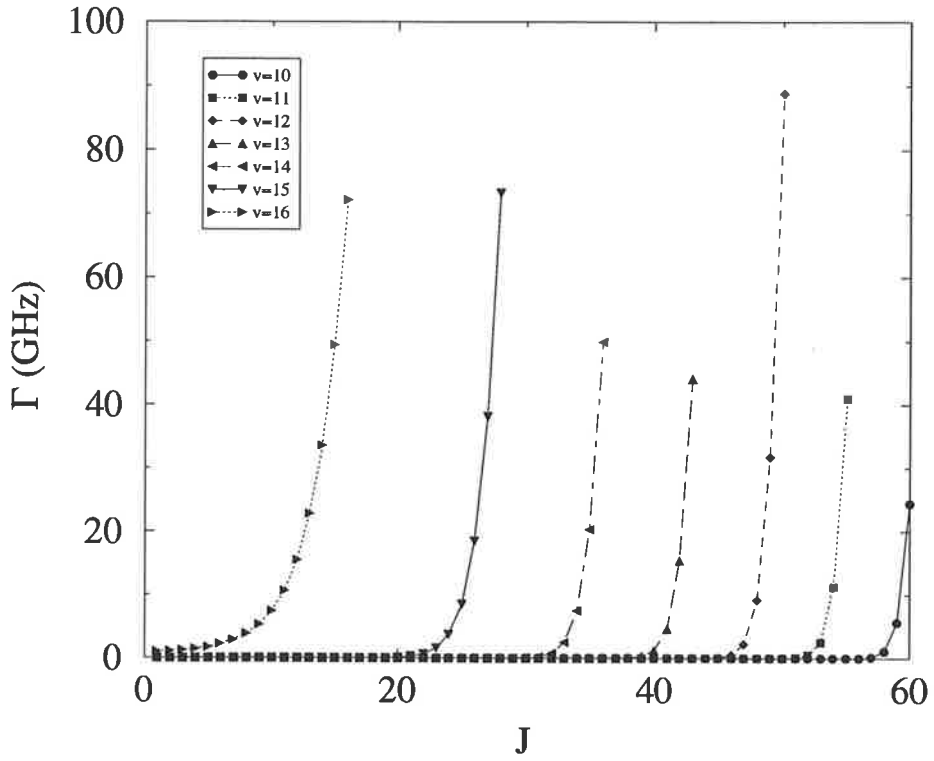

Figure 5.3: Widths of $^1\Pi_u$ ($^6Li^7Li$) levels, pre-dissociated due to the tunneling through the potential barrier, as a function of the total momentum J.

results for $^7Li_2$ are in agreement with the experiment and the semi-classical calculations [22]. Then, a simple model of the symmetry breaking in $^6Li^7Li$ is proposed, and the non-diagonal coupling element of the $^1\Pi_u$–$^1\Pi_g$ interaction is defined, using the isotopic splitting of ^2P and ^2S atomic levels in Lithium. Then, widths of vibrational levels of $^1\Pi_u$, pre-dissociated due to the tunneling and the coupling with the $^1\Pi_u$ state, are calculated, using the MFGR method with the optical potential. The results are compared with the experimental data.

5.2.3 Theoretical model for coupling between $B^1\Pi_u$ and $1^1\Pi_g$ states in $^6Li^7Li$.

The order of the magnitude of the coupling between $^1\Pi_u$ and $^1\Pi_g$ states for large internuclear distances can be estimated from the energy difference between atomic levels for two isotopes. Relation between energies of atomic levels for two isotopes is connected to the relation between reduced (nucleus + electron) masses of isotopes. Since this isotopic difference is small, it can be taken into account as a perturbation. One can still consider two molecular states, $^1\Pi_u$ and $^1\Pi_g$, but now, they are coupled.

The whole potential energy operator of the system $^6Li^7Li$ is written as 2×2 matrix:

$$\hat{V}(R) = \hat{U}(R) + \hat{V}_h, \tag{5.1}$$

In the molecular basis $\hat{U}$ is the potential of non-perturbed system, $^6Li_2$. $\hat{V}_h$ is considered as a small perturbation and it is responsible for the coupling between the states.

$\hat{U}$ in the molecular basis is represented by a matrix containing potentials $^1\Pi_u$ and $^1\Pi_g$ as diagonal elements:

$$\hat{U} = \begin{pmatrix} U_g(R) & 0 \\ 0 & U_u(R) \end{pmatrix}. \tag{5.2}$$

V_h can be defined in the basis of products of atomic states (atomic basis). This basis consists from following electronic states (anti-symmetrized over the permutation of electrons):

$$|a_1>= \frac{1}{\sqrt{2}}(|^6Li, 2S, r_1> |^7Li, 2P, r_2> -|^6Li, 2S, r_2> |^7Li, 2P, r_1>)$$

$$|a_2>= \frac{1}{\sqrt{2}}(|^7Li, 2S, r_1> |^6Li, 2P, r_2> -|^7Li, 2S, r_2> |^6Li, 2P, r_1>) \tag{5.3}$$

r_1 and r_2 are coordinates of electrons.

The two representations (atomic and molecular) are connected through a transformation S:

$$S = \frac{1}{\sqrt{2}} \begin{pmatrix} 1 & 1 \\ 1 & -1 \end{pmatrix}, \tag{5.4}$$

$$\psi_g(R) = \frac{1}{\sqrt{2}}(|a_1> +|a_2>)$$

$$\psi_u(R) = \frac{1}{\sqrt{2}}(|a_1> -|a_2>) \tag{5.5}$$

V_h is diagonal in the atomic basis. Diagonal matrix elements can be calculated in the atomic basis. They are determined by differences of energies of electronic states of atoms with different mass of nuclei:

$$< a_1|V_h|a_1 >= E(^6Li, 2S) + E(^7Li, 2P) - (E(^6Li, 2S) + E(^6Li, 2P)) =$$

$$E(^7Li, 2P) - E(^6Li, 2P) = \epsilon_1$$

$$< a_2|V_h|a_2 >= E(^6Li, 2S) - E(^7Li, 2S) = \epsilon_2 \tag{5.6}$$

In the previous formulae, the quantities ϵ_1 and ϵ_2 are calculated with the condition, that atomic wave functions are not disturbed due to the interaction between atoms. Strictly speaking, it is justified only at infinite separation of atoms. In the following

consideration it is supposed that interaction between atoms does not change atomic $2S$ and $2P$ states. Thus, the quantities ϵ_1 and ϵ_2 will be considered as R-independent.

Thus, the whole potential operator in molecular basis is written:

$$\hat{V}(R) = \begin{pmatrix} U_g(R) & 0 \\ 0 & U_u(R) \end{pmatrix} + S \begin{pmatrix} \epsilon_1 & 0 \\ 0 & \epsilon_2 \end{pmatrix} S^T \tag{5.7}$$

or

$$\hat{V}(R) = \begin{pmatrix} U_g(R) & 0 \\ 0 & U_u(R) \end{pmatrix} + \frac{1}{2} \begin{pmatrix} \epsilon_1 + \epsilon_2 & \epsilon_1 - \epsilon_2 \\ \epsilon_1 - \epsilon_2 & \epsilon_1 + \epsilon_2 \end{pmatrix}. \tag{5.8}$$

The term $\hat{V}_h$ shifts both potentials by the energy $\epsilon_1 + \epsilon_2$ and mixes them by a constant interaction $(\epsilon_1 - \epsilon_2)/2$.

At the infinite separation, the quantity $\epsilon = \epsilon_1 - \epsilon_2$ is determined from Eq. (5.6) as difference between atomic transitions $2P \to 2S$ for two isotopes:

$$\epsilon = v(2P \to 2S)_{^7Li} - v(2P \to 2S)_{^6Li}. \tag{5.9}$$

From the experiment, $\epsilon(\infty) \approx 0.349$ cm^{-1}. On the other hand, since the largest part of wave functions of $^1\Pi_u$ levels are situated at short distances, the matrix element $V_{h,(g,u)} = < \psi_u(v)|\hat{V}_h|\psi_g(v) >$ of transition $^1\Pi_u \to ^1\Pi_g$ between two components, $\psi_u(v)$ and $\psi_g(v)$, of the total wave function $\psi(v)$ is defined by values of ϵ at small distances. For the small internuclear distances, this quantity is not known and, in general, it should be fitted to the observed widths. In the present calculations, the experimental value $\epsilon(\infty) \approx 0.349$ cm^{-1} is used at small distances also.

For the fit the following observations can be useful. The matrix element $V_{h,(g,u)}$ can be written in a form:

$$V_{h,(g,u)} = < V_h >< \psi_u(v)|\psi_g(v) > \tag{5.10}$$

where the value $< V_h >$ is defined as

$$< V_h > = \frac{< \psi_u(v)|\hat{V}_h|\psi_g(v) >}{< \psi_u(v)|\psi_g(v)}. \tag{5.11}$$

The quantity $< V_h >$ can vary from one level to another. Taking the notation $\mathcal{F}$ for the Franck-Condon factor $< \psi_u(v)|\psi_g(v) >$, the matrix element is written as:

$$V_{h,(g,u)} = < V_h > \mathcal{F}. \tag{5.12}$$

Since the value ϵ is small, its small variation does not change the total wave function and the Franck-Condon factor. Therefore, the matrix element varies linearly with ϵ. Widths Γ are defined by the equation

$$\Gamma = 2\pi |V_{h,(g,u)}|^2. \tag{5.13}$$

Increasing ϵ by a given factor leads to an increase of Γ by the square of this factor.

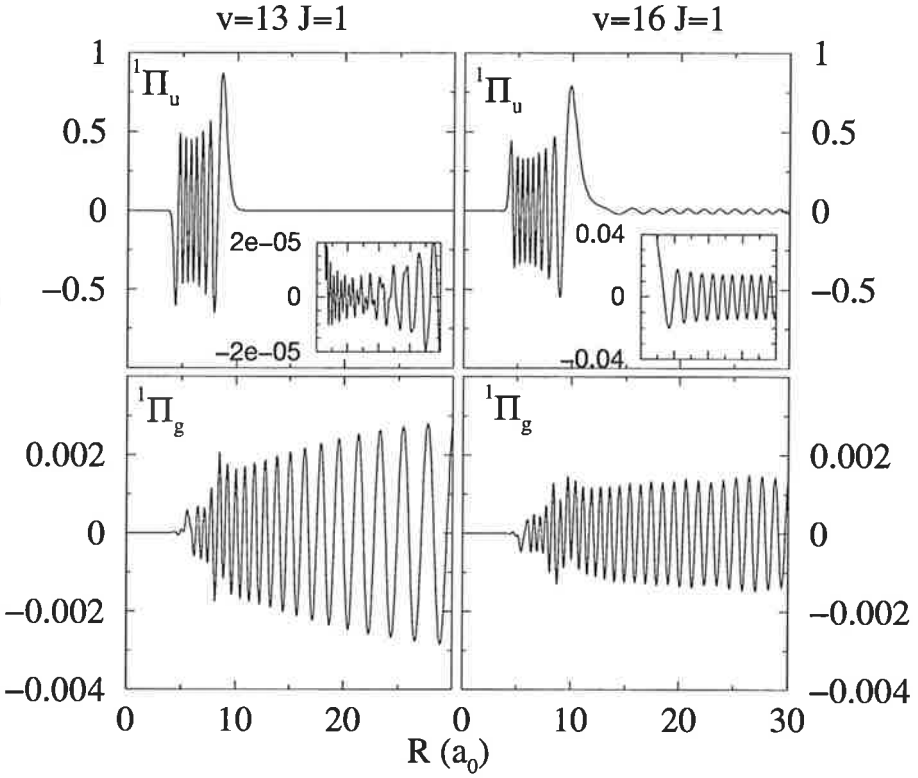

Figure 5.4: Two typical pre-dissociated wave functions of the $^1\Pi_u$ molecular state of $^6Li^7Li$ with $J = 1$ perturbed by the coupling with the $^1\Pi_g$ molecular state. The lower panel shows $^1\Pi_g$-components of wave functions.

5.2.4 Results of calculations

Introducing the described two-channel potential with the coupling V_h into the program of calculations of pre-dissociated levels is performed similarly as it was done for the 0_u^+ symmetry of Cs_2 and Rb_2.

Results of calculations including the coupling with the $^1\Pi_g$ show a large increasing of pre-dissociation widths for VLL-levels. The figure 5.4 shows again pre-dissociated wave functions $v = 13$ and $v = 16$ of the $^1\Pi_u$ state, but now perturbed by the coupling with the $^1\Pi_g$ state. Therefore, both wave functions have a $^1\Pi_g$-contribution. Two lower panels shows these contributions.

Pre-dissociation widths Γ now arise from two sources, from the tunneling and from the dissociation through the $^1\Pi_g$ state. The total width is a sum of widths given by two contributions. Widths due to tunneling are much larger for the highest pre-dissociated levels. Comparing the figure 5.4 with the figure 5.2, one sees that the coupling does not change the short-range parts of $^1\Pi_u$-components of wave functions. In contrast, for the VLL-levels the contribution to the pre-dissociation due to the coupling is much more important than the contribution due to the tunneling. It is manifested in the $v = 13$ wave function. At large distances the amplitude of the $^1\Pi_u$-component is much smaller than the amplitude of the $^1\Pi_g$-component.

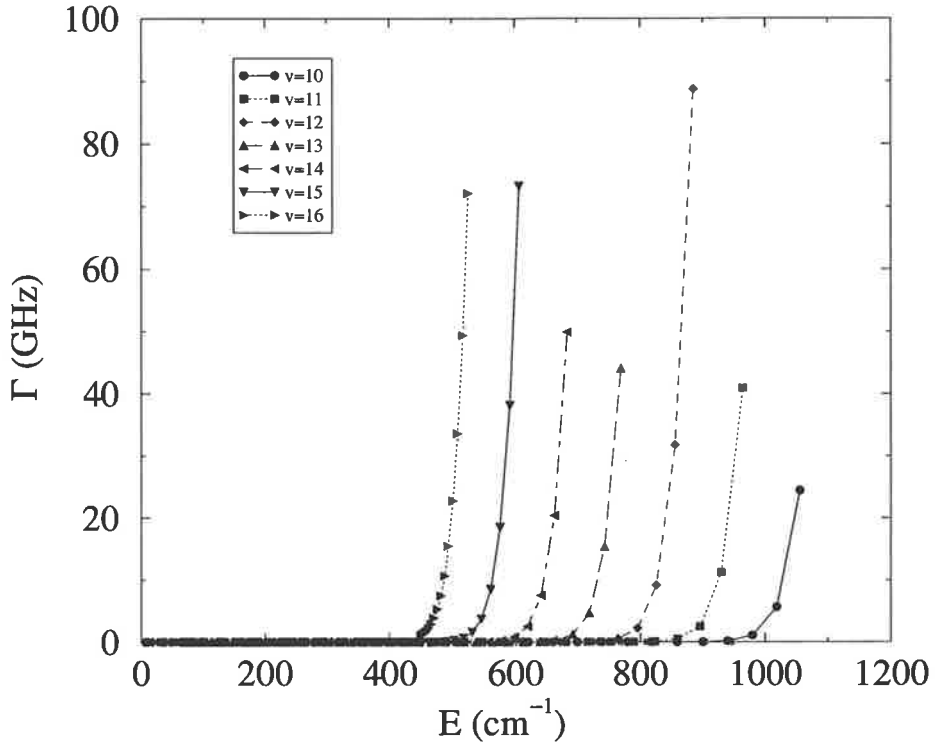

Figure 5.5: The variation of Γ as a function of the energy for vibrational levels $v = 10 - 16$. Calculations with different J from 1 to 60 are represented on the figure.

In order to see a variation of widths for different values of J, calculations were performed for J from 1 to 60. The figures 5.5 and 5.6 represent widths as a function of energy for several pre-dissociated vibrational levels for two different domains of Γ. The first figure shows the region where widths are determined mainly by the tunneling through the barrier. The values of Γ, shown in the plot are almost the same as in Fig. 5.3.

The figure 5.6 shows a region of small widths. In the figure, the competition between two contributions is clearly manifested, when widths caused by tunneling becomes comparable with the widths caused by coupling.

Widths of levels, for which the contribution into the pre-dissociation due to the coupling with $^1\Pi_g$ is larger than the tunneling effect, demonstrate slow variation with J (or with energy). For example, the width of the level $v = 8$, is increasing from 0 MHz at the energy 0 until a value 5 MHz at the energy $E = 300$ cm^{-1}, then it decreases almost to zero again. Other levels display a similar behavior. This behavior is defined by the Franck-Condon factor $\mathcal{F}$, which changes slowly for each level with variation of J.

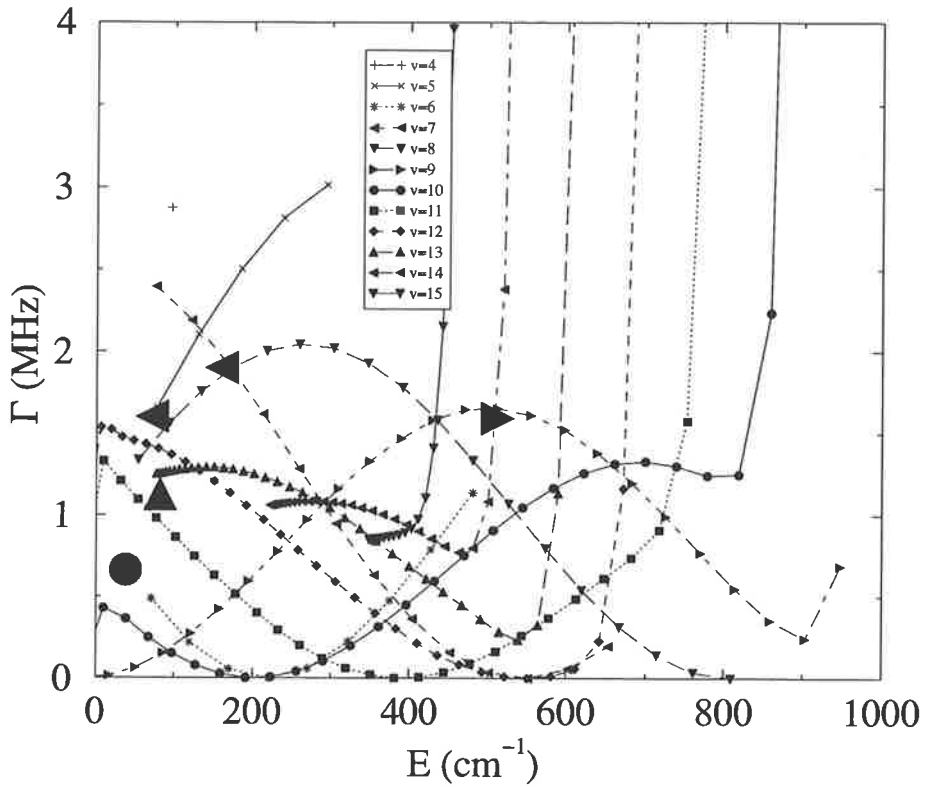

Figure 5.6: Same as the figure 5.5 by for the region of small Γ. Vibrational levels from $v = 4$ to $v = 16$ are represented. Large symbols represent experimentally-observed widths, the convention for their geometric form being the same as for calculated values.

5.2.5 Comparison with the experiment

The goal of the experiment [22]was the spectroscopy of the $^1\Pi_u$ state of $^7Li_2$. The effect of tunneling through the barrier was investigated. The spectroscopy of the $^6Li^7Li$ molecule was also observed due to a small fraction (13%) of $^6Li^7Li$ presenting in a beam. But the signal was weak, so the pre-dissociation was not systematically investigated for this species. In particular, the pre-dissociation due to the coupling with the $^1\Pi_u$ state was not expected.

At the present moment, only a few pre-dissociation rates are experimentally measured for $^6Li^7Li$. In addition, values of the observed pre-dissociation rates are not very precise since the signal-to-noise ratio is small.

The experimentally observed rates are represented by large symbols on Fig. 5.6. The order of magnitude of experimental and calculated values are the same. For a more precise comparison, one needs more precise experimental data. Then fitting of the coupling to the experiment will be possible.

Following the proposed model and the present calculation, a new experiment is prepared now in the Laboratory Aimé Cotton with a purpose of complete investigation of the pre-dissociation of the $^1\Pi_u$ state of $^6Li^7Li$.

5.2.6 Conclusion

In this section the pre-dissociation of vibrational levels of the $^1\Pi_u$ ($^6Li^7Li$) state are discussed. In the experiment the observed widths are much larger than one could expect from the tunneling through the potential barrier of the $^1\Pi_u$ state. In this section, a simple perturbation model, describing this observations is proposed. It is based on the fact that in $^6Li^7Li$ the $^1\Pi_u$ state is coupled with the $^1\Pi_g$ state due to the symmetry breaking under a permutation of non-equivalent nuclei ^6Li and ^7Li. Calculations for two-channel coupled potential, using the MFGR method, have shown a good agreement with experiment data, existing at present. The experiment, preparing now in the Laboratory will allow to compare experimental and theoretical results more closely.

Chapter 6

Conclusion and Perspectives.

The main object of the present Thesis is the development of theoretical and numerical methods for the study of diatomic systems near the dissociation limit. A diatomic system near the dissociation means a molecule in a weakly-bound vibrational level, if the energy is lower than the molecular dissociation limit; two atoms with a small relative kinetic energy, if the energy is slightly larger than the dissociation energy.

A particularity of a diatomic system with energy close to the dissociation is the fact that wave functions of levels with such energies have important long-range tails, located in a region where the kinetic energy is comparable with the energy of the inter-atomic interaction. The C_n/R^n character of the diatomic potential at large distances together with a small relative kinetic energy give at asymptotic region slowly oscillating wave functions. On the other hand, one cannot neglect the short-range part of wave functions, that determines, for example, the asymptotic phase shift. In this region, the inter-atomic motion is faster, and wave functions oscillate more. Thus, a full consideration must take into account both long- and short-range parts of the diatomic potential.

Therefore, the Thesis describes how existing methods of solution of the time-dependent and the time-independent Schrödinger equations are adapted for physical problems, where the both, short-range and long-range parts of the potential is important.

Using the developed method, several applications to experiments with cold alkali molecules near the dissociation limit are considered.

Potential curves needed for applications are taken from different sources. In the present state of quantum chemistry calculations, the accuracy of the potentials is not yet spectroscopic accuracy, but using the generalized quantum defect theory, a qualitative analysis of results and the comparison with the experiment are possible. It is shown, that fitting some parameters, such as quantum defects, an agreement with the experiment can be obtained. The fitting of the quantum defects is made by small change of the potentials at small distances, where *ab initio* potentials have the the largest certainty (about 1 cm^{-1}).

6.1 Results obtained in the Thesis

The main results of the Thesis are the following:

I. The method developed in the Thesis is based of the Fourier Grid Representation (FGR) method [72] (R. Kosloff). An important feature of FGR is its ability to represent a wave function as an expansion on a basis of functions (e^{ipR}) or by values of the wave function on grid points. The ordinary FGR method make use an equally-spaced grid, that corresponds to basis functions with fixed frequencies p.

A new method of representation (the mapped Fourier grid representation) developed in the Thesis is adapted for a Hamiltonian containing a long-range potential. This new representation uses a basis of exponential functions with varying frequencies p, such that these basis functions oscillate more in the region where the maximum possible energy is larger and, therefore, wave functions oscillate more. In a region where oscillations are less frequent, the frequencies of basis functions are smaller. Since a maximum frequency of local oscillations of wave functions is defined by the maximum local kinetic energy, the functional basis is connected to the local kinetic energy. From a grid point of view, the density of grid points is higher in the region where oscillations are more frequent. It means, that the working (mapped) grid is more dense at distances, where the wave function of the most excited bound state oscillates fast, and it is less dense at distances, where the wave function oscillates slowly.

This basis choice reduces the number of basis functions to the minimum, since the basis functions, chosen by this way are adapted to the potential in the most natural way. Typically, the number of basis functions is slightly larger than the number of quantum states and to close the absolute minimum (the number of quantum states is defined by the volume of the phase space of the highest state of the interest).

The eigen-energies and eigen-functions are obtained by a diagonalization of a matrix of the Hamiltonian written in the mapped Fourier grid representation.

The determination of the new (mapped) grid is done numerically, using the maximum possible local kinetic energy. This numerical evaluation of the mapped grid does not introduce an additional error into calculations when a numerical potential is used in the Hamiltonian.

The idea of the mapped Fourier grid is not new. It was discussed by E. Fattal *et al.* [38] and by E. Tiesinga *et al.* [125]). But in these works, the mapping was applied only for very special cases of the potential. They used analytical forms of the mapping adapted to some coordinate regions and did not estimate its efficiency. In contrast, the Thesis present general techniques for determination of the mapping adapted for any potential and for any number of channels.

The proposed method was for one- and two-channel potentials and can be easily generalized for larger number of channels.

With use of the method of optical potential, the mapped time-independent method is adapted for calculations of widths (and lifetimes) of pre-dissociated levels of long-range potentials.

II. It is proposed a simple and effective techniques for the pre-estimation of the

size of needed basis and, thus, the pre-estimation of a calculation cost. The techniques is based on a estimation of the phase space occupied by the Hamiltonian. The shape and volume of the occupied phase space is determined from the maximum local kinetic energy. For this goal the concept of an enveloping potential is introduced. This potential reflects simply the maximum local kinetic energy (multiplied by -1). Use of an enveloping potential is very useful for a problem with several channels, where the maximum local kinetic energy is not always obtained by the minimum of the potential curve.

In the present version of the method, only the classically allowed region is explicitly included into the procedure of determination of the basis. The classically forbidden region is included implicitly when the density ($= 1/\beta$) of points per one de Broglie length is increased.

III. The precision of the mapped time-independent Fourier method, developed in the Thesis is checked. In the present form, the precision is limited by the accuracy of calculations of a potential at grid points, using a spline procedure. Comparing with the Numerov method, it was found that the present precision of bound state calculations with the numerical potential is of order 10^{-7}. But, in principle, if the spline procedure could be avoided, the precision must be of order of the uniform Fourier method, i.e. about 10^{-14} [70].

IV. The same method of representation of wave functions and Hamiltonian with a long-range potential is applied to solution of the time-dependent Schrödinger equation. The MFGR method coupled with the time-propagation approach of R.Kosloff is an efficient tool for the simulation of collisions, when the long-range interaction is important (for example, collisions of cold atoms). Using techniques of extraction of lifetimes from the correlation function, it has been shown that the mapped time-dependent method can be used for lifetime calculations.

Since lifetimes can be calculated by time-dependent and time-independent approaches, these calculations have been used as a test for the reliability of both methods. As an example for the test, the symmetry 0_u^+ was used. Both approaches have given approximately the same results.

As applications of the developed method the following examples are discussed in the Thesis:

I. The symmetry 0_u^+ of two heavy alkali dimer molecules Rb_2 and Cs_2 has been considered. Two vibrational series of spectra of this symmetry are strongly perturbed one by the other for all domain of bound and pre-dissociated energies (approximately for 6000 cm^{-1}) due to the strong non-adiabatic coupling between two adiabatic channels, $0_u^+(P_{1/2})$ and $0_u^+(P_{3/2})$, of the symmetry. The perturbations are manifested by the fact that wave functions of the vibrational levels contain both components, $0_u^+(P_{1/2})$ and $0_u^+(P_{3/2})$, in comparable proportions. Since the vibrational motion is extending at large inter-nuclear distances, the mapped FGR method is especially adapted for this kind of problem.

It was found that the perturbations are much stronger in the case of rubidium. In the spectrum of Rb_2 there are vibrational levels, which cannot be attributed to any

molecular state – the mixing is very strong. In the case of cesium, the non-adiabatic mixing near the first dissociation limit $P_{1/2}$ is much weaker.

A qualitative agreement for Rb_2 has been found between results of calculations and perturbations of highly excited vibrational levels, observed in the photo-association experiment of D. Heinzen *et al.* [52]). Also, the results of calculations by C. Amiot *et al.* [7], explaining perturbations in the low-lying part of the spectrum observed in Fourier Transform experiments (experiment by C. Amiot and J. Vèrges), have been reproduced and confirmed.

The precision of results is limited by the present precision of potentials at short distances. In order to see how the results depend upon the coupling, calculations with R-independent and R-dependent spin-orbit coupling have been done. For cesium, the R-dependence of the molecular spin-orbit coupling has been computed [94]. For rubidium, a model dependence was used (see the Thesis). In the case of cesium, a strong dependence of perturbations upon the coupling was found – with the R-independent spin-orbit coupling, two adiabatic molecular states ($P_{1/2}$ and $P_{1/2}$) of the symmetry almost do not interact, and the perturbations are very weak. In a case of R-dependent spin-orbit coupling, the perturbations are very strong. In contrast, in Rubidium, the R-dependent spin-orbit coupling does not change a picture qualitatively, but do change quantitatively.

II. An analysis of a type of Leroy-Bernstein was applied for obtained results. For one-channel potential, if the potential is not exactly a C_n/R^n curve, instead of the exact Leroy-Bernstein dependence of the level energy, $E(v)$, on the number of a level, v, it is proposed to use the calculated dependence $E(v)$. This numerical dependence is useful for the analysis of shifts of vibrational levels when the potential is changed or perturbed by a coupling with the another potential curve. For this analysis the quantum defect theory is applied.

Using the two-channel quantum defect theory, a whole complexity of perturbations is described by only three parameters, μ_1, μ_2, $R_{1,2}$, weakly depending upon the vibrational levels. Since these parameters stay almost the same when the $P_{1/2}$ threshold is overcome, lifetimes of the pre-dissociated levels, lying just over the $P_{1/2}$ threshold, can be predicted from μ_1, μ_2, $R_{1,2}$, calculated for the discrete spectrum.

It was found for Rb_2, that μ_1, μ_2, $R_{1,2}$ stay almost constant for a large energy domain from $-1000\ cm^{-1}$ under the $P_{1/2}$ limit up to the $P_{3/2}$ limit. These parameter change less than by 1% from one vibrational levels to the neighboring and by 10% for whole this energy domain. For the case of cesium, these parameters are slowly changing (from 1% to 10% for neighboring levels).

An important conclusion of the 2QDT analysis is the fact, that if the asymptotic behavior of potentials is known, only three parameters determine perturbations of highly-excited vibrational levels and the pre-dissociation of resonant levels. Even, if the short-range part of the potential is not known, fitting these parameters, an agreement with the experiment for positions of bound levels can be obtained. Extrapolating these parameters outside the experimentally-accessible energy domain, lifetimes and perturbations can be predicted.

III. Using the developed method together with the optical potential method,

lifetimes of pre-dissociated vibrational levels lying between two thresholds, $P_{1/2}$ and $P_{3/2}$, of the symmetry, have been directly calculated for Rb_2 and Cs_2.

It was found an agreement between lifetimes defined by a direct calculation and with using parameters μ_1, μ_2, $R_{1,2}$, extracted from the discrete spectrum.

Comparing the results of lifetime calculations with the photo-association experimental data for pre-dissociated levels of $^{85}Rb_2$ (D. Heinzen *et al.*), some discrepancy was found. This discrepancy was attributed to the low accuracy of the spin-orbit coupling, used in the calculations. It was shown, that by a small variation of the potential and the coupling, the agreement with the experiment can be obtained.

A large isotopic difference in lifetimes of pre-dissociated levels and in perturbations in the discrete spectrum has been predicted for two isotopes of Rubidium $^{85}Rb_2$ and $^{87}Rb_2$. It should be seen in the photo-association experiment, for example, as a strong difference in a trap loss due to the fine-structure transition. Thus, this effect can explain the difference in the trap loss between ^{85}Rb and ^{87}Rb observed in the experiment by C. Wallace.

IV. Using the mapped Fourier method developed in the Thesis, two vibrational structures observed in the cesium photo-association spectrum have been interpreted by M. Vatasescu *et al.* [129]. These two features are caused by the multi-channel tunneling through the barrier of the 0_g^- state. An analysis of experimental data and a fit of potential have allowed to define the coupling between the 0_g^- $(6s+6P_{3/2})$ and the 0_g^- $(6s+5D_{3/2})$ molecular states and to precise a height of the barrier. (The work has been done by M. Vatasescu.)

V. As another application of the mapped Fourier method, the dissociation of vibrational levels of the $^1\Pi_u$ symmetry of $^6Li^7Li$ due to the interaction with the $^1\Pi_g$ symmetry has been investigated. A simple perturbation model, describing a $g-u$ symmetry breaking in states $^1\Pi_g$ and $^1\Pi_u$ in $^6Li^7Li$, was proposed. Results of calculations explain the dissociation observed in the experiment by P.Cacciani.

6.2 Some perspectives

Among the most close perspectives of the continuation of the work, presented in the Thesis, can be noted following.

I. There are several applications of the mapped Fourier method to experiment, which can and must be considered:

- The interpretation of non-explained lines, experimentally observed in the photo-association spectrum of Cs_2 near the $P_{1/2}$ limit. These lines are, probably, caused by perturbations in the spectrum of one of symmetries of the $6S+6P$ manifold of cesium.

- The detailed analysis of the 0_u^+ spectrum of Rb_2, obtained in the Fourier transform spectroscopy experiment of C.Amiot and J.Vergès and in the experiment of D. Heinzen *et al.*. To improve the potentials and the spin-orbit coupling at small distances comparing with the experiment.

- Investigation of a scheme of formation of cold molecules in the ground molecular state obtained by a spontaneous emission from the excited 0_g^+ $(6S + 6P)$ state. (Rb_2 – the experiment by G.Pichler).

II. A generalization of the mapped Fourier grid representation to multi-dimensional potentials. Advantages of the multi-dimensional mapping are even more essential than in the case of a one-dimensional problem. A multi-dimensional version would allow to solve many problems such as calculations of bound and pre-dissociated vibrational levels of multi-dimensional potentials (triatomic molecules), three-body collisions, calculations of potential curves and surfaces.

III. Since the propagation of wave packets in the solution of time-dependent problems leads to heavy calculations, the creation of a parallel version of the algorithm seems to be useful, especially for multi-dimensional or (and) multi-channel potentials. The parallelization could be useful also for the time-independent approach, if, for example, there are many channels. Now, the parallel version of the propagation code without the mapping is already written on a parallel language BSP. The perspective to unify abilities of the parallel computing with the MFGR seems to be very fruitful.

In conclusion, the Thesis opens very different opportunities for the future: a systematic use of the existing code for calculations of bound states and for the interpretation of experimental spectra, a following theoretical development of the method, and the purely algorithmic work.

6.3 Résumé

L'objectif principal de la Thèse est le développement des méthodes théoriques et numériques pour traiter soit les niveaux de vibration d'une molécule diatomique proche de la limite dissociation, soit les collisions entre atomes froids. Ce travail est motivé par de nombreux résultats expérimentaux récents sur la formation de molécules froides.

Dans les problèmes considères, le mouvement relatif des deux atomes s'étend à de grandes distances internucléaires, où le potentiel est très faible et où la fonction d'onde oscille très lentement, alors que dans la zone interne elle oscille rapidement. Pour résoudre cette difficulté, on a propose une nouvelle méthode de représentation de grille de Fourier ou le pas d'intégration est ajusté sur la longueur d'onde de Broglie locale. On a montré qu'une fonction d'onde peut être représentée avec précision en utilisant moins de deux points par oscillation. La méthode a été appliquée à la prédiction de spectre de photoassociation de Cs_2 et Rb_2 et a l'interprétation d'expérience de la violation de symétrie en Li_2.

Résultats obtenus dans la Thèse.

Résultats principaux obtenus dans la Thèse sont suivants

I. La méthode développée est fondée sur la représentation de grille de Fourier (FGR) [72] (R. Kosloff). Une propriété importante de la FGR est sa capacité à représenter la fonction d'onde comme un développement sur la base des fonctions e^{ipR} ou par ses valeurs sur des points de grille. La méthode FGR originale utilise une grille à pas constant, correspondent à une base des fonctions e^{ipR} avec des fréquences p constantes.

La méthode proposée dans la Thèse (MFGR - FGR avec le "mapping") utilise une grille à pas variable [64]. Pour la représentation par les fonctions de base cela signifie que les fréquences p dépendent de R. Les fonctions $e^{ip(R)R}$ sont choisies de telle façon qu'ils oscillent plus dans la zone R où les fonctions d'onde oscille le plus. Mais la fonction d'onde oscille plus ou l'énergie cinétique est grande. Le pas de la grille et la fréquence locale $p(R)$ sont choisis liés à l'énergie cinétique locale.

Si la base de fonctions (la grille) est choisie à partir de l'énergie cinétique locale, le nombre de fonctions de base (le nombre de points de la grille) est minimum pour un potentiel donne. La base des fonctions (la grille à pas variable) est définie numériquement à partir du potentiel.

Les niveaux liés et les fonctions propres sont détermines par une diagonalisation de la matrice de Hamiltonian, écrite dans représentation MFGR. Pour résoudre de l'équation de Schrödinger dépendent de temps on utilise la même représentation.

La méthode de MFGR est généralisée ensuite à plusieurs voies. En ce cas il faut prendre l'énergie cinétique maximale pour toutes les voies pour ajuster le pas de grille.

En introduisant un potentiel absorbant au bord de la grille, la méthode indépendante du temps est utilisée à calculer des largeurs (des durées de vie) des niveaux

pré-dissociés.

II. Une technique simple et efficace est proposée pour estimer le nombre des fonctions de base (le nombre des points de grille) pour une précision donnée. Ça permet à pré-estimer les efforts numériques pour un potentiel et une précision donnés. La technique est basée sur l'estimation d'espace de phase occupée par le potentiel de l'Hamiltonian. Le volume d'espace de phase est détermine par l'énergie cinétique locale. On a introduit une notation le potentiel enveloppe qui donne la valeur d'énergie cinétique maximale a chaque distance R donne. La définition du potentiel enveloppe est très utile pour les Hamiltonian avec un potentiel a plusieurs voies.

III. La précision de la méthode Mgr est comparée avec la méthode de Numerov. Dans la version présente la précision est limitée par des calculs du potentiel sur les points intermédiaire en utilisant la procédure de spline. L'ordre de grandeur de la précision actuelle des calculs des états liés est de 10^{-7}. In principe, si on évite la procédure de spline, on doit attendre la précision de l'ordre de 10^{-14}, comme pour la méthode FGR ordinaire [70].

IV. La méthode MFGR de représentation des fonctions d'onde et de l'Hamiltonian a été appliquée à l'équation de Schrödinger dépendent de temps [66]. Pour la propagation en temps, l'expansion de Chebyshev de l'opérateur de propagation ést utilisée. La méthode MFGR couplée avec la propagation en temps permet de traiter des collisions a très basses énergies. En utilisant la méthode dépendant du temps, la durée de vie des niveaux pré-dissocies peut être calculée. On a comparé les resultats à ceux qui obtenus par la dépendent de temps pour tester la precision de deux méthodes. Ça a permis à vérifier la surete des résultats donnes par deux méthodes. Comme un exemple, la symétrie 0_u^+ de Rb_2 et Cs_2 est considérée.

Applications de la méthode MFGR sont considérées dans la Thèse.

I. On a étudié le spectre de photoassociation 0_u^+ $(nS+nP)$ des molécules alcalines lourdes, Cs_2 et Rb_2. Les deux voies corrélées aux asymptotes $P_{1/2}$ et $P_{3/2}$ sont fortement couplées, ce qui crée des perturbations dans le spectre sur un domaine d'énergie de plus de 6000 cm^{-1}. Comme le mouvement vibrationnel atteint en ce cas de très grandes distances (potentiel $1/R^3$), la méthode MFGR est particulièrement adaptée.

J'ai trouvé que les perturbations sont plus important pour le rubidium que pour le césium. Des potentiels utilisent pour Rb_2 et Cs_2 ne sont pas très bien connus. La dépendance des positions des niveaux et des perturbations dans le spectre avec de changement des courbes potentiels et du coulage spin-orbite ont été étudiés. Il y a des données expérimentales pour le rubidium: spectres de fluorescence pour les niveaux vibrationnels les plus bas (C. Amiot *et al.* [7]), spectres de photoassociation (D. Heinzen [52]). Un bon accord a été trouvé entre des calculs et expérience. Résultats des calculs pour le césium sont actuellement utilisés pour interpréter les spectres de photoassociation de l'équipe de Pierre Pillet.

II. Une analyse de type de Leroy-Bernstein a été applique aux niveaux calcules. En modifiant du potentiel, un déplacement des niveaux peut être décrit par un seul

paramétrer μ (défaut quantique). L'intérêt d'utiliser du défaut quantique est qu'il varie peu avec l'énergie. Si le comportement du vrai potentiel est connu aux grandes distances et inconnu aux petites distances, en changeant le défaut quantique (le potentiel numérique) on peut arriver à une série vibrationnelle calculée identique à la séries expérimentale. On a généralisé la théorie du défaut quantique pour des potentiels de type non-Rydberg à deux états. Dans ce cas-la on arrive décrire toute la complexité des niveaux perturbés seulement avec trois paramètres μ_1, μ_2, $R_{1,2}$ (défauts quantiques sur les deux voies et couplage). La méthode graphique de Lu-Fano a été appliquée aux perturbations entre deux états moléculaires [65].

On a trouvé des paramètres μ_1, μ_2, $R_{1,2}$ pour la symétrie 0_u^+ de Rb_2 et Cs_2.

Un résultat important de la théorie du défaut quantique a deux états (2QDT) est que si on connaît les paramètres μ_1, μ_2, $R_{1,2}$ juste au-dessous de la première limite de dissociation $nS + nP_{1/2}$, on peut prédire des positions et des largeurs des résonances (niveaux pré-dissocies) au-dessus de lu limite [65].

III. En utilisant la méthode indépendante de temps avec le potentiel absorbant, des largeurs et positions des niveaux pré-dissocies ont été calculées pour la symétrie 0_u^+ de Rb_2 et Cs_2. Un excellent accord a été trouvé entre les paramètres μ_1, μ_2, $R_{1,2}$, définis pour le spectre pré-dissocie et pour le spectre discret. Ca justifie la prédiction des largeurs de résonance à partir de spectre discret.

En comparant les largeurs calculées avec des largeurs expérimentales pour $^{85}Rb_2$ [52] une divergence a été trouvée et attribuée à la précision insuffisante des potentiels et du couplage. J'ai montré que cette divergence peut être éliminée par un petit changement du potentiel.

Un effet isotopique important sur les durées de vie pour deux isotopes de Rubidium, $^{85}Rb_2$ et $^{87}Rb_2$, a été prédit. Cet effet doit être observe dans l'expérience de photoassociation comme une différence en pertes d'atomes due au couplage spin-orbite.

IV. En utilisant la méthode de MFGR deux structures vibrationelles observées dans le spectre de photoassociation du césium, ont été expliquées [129]. Ces deux structures sont attribuées à l'effet tunnel a travers la barrière du potentiel moléculaire 0_g^-. On avait pu même déterminer la hauteur de la barrière d'état 0_g^-.

V. Comme autre application, la pré-dissociation des niveaux vibrationels d'état $^1\Pi_u$ de Li_2 était considérée. La motivation de ce travail était l'expérience du group de Cacciani [22]. Des largeurs des niveaux d'état $^1\Pi_u$ de l'isotope $^6Li^7Li$ près de la limite de dissociation sont beaucoup plus grandes que pour l'isotope $^7Li_2$. On a attribué cet effet a la violation de la symétrie $g - u$. La différence en masse de deux noyaux casse la symétrie et introduit un couplage entre des états $^1\Pi_u$ et $^1\Pi_g$. Dans la Thèse j'ai développé un modèle qui décrit ce couplage. J'ai calculé des largeurs des niveaux pré-dissocies. Un bon accord a été trouvé avec l'expérience [24]. Maintenant, à la suite des résultats obtenus dans la Thèse, une nouvelle expérience se prépare.

Appendix A

Classification and Calculation of Molecular Terms

Since the Thesis refers very often on the Hund's cases a and c of molecular terms, it seems to be useful to bring the details of the construction of Hund's case c curves from Hund's case a and connections between corresponding quantum numbers, nevertheless this scheme of construction is well-known. Thus, this appendix is devoted to a brief description of calculations of electronic molecular terms of symmetries $nS + nP$ and $nP + nP$ of alkali diatoms with accounting the spin-orbit coupling. Curves of the Hund's classification a were used as a starting point.

It is be assumed in the appendix that the total potential operator includes the a potential curves plus the spin-orbit non-diagonal coupling. Since there is no a term of the first derivative in the corresponding Schrödinger equation, this representation will be refereed as diabatic. The c curves are obtained diagonalizing this potential operator. In this representation the potential does not contain non-diagonal terms but the corresponding Schrödinger equation contains the first derivative mixing the molecular states. This representation of the potential will called, as usually, adiabatic representation.

The first part of the appendix is briefly describing the well-known scheme of the construction of electronic molecular wave functions of the diatom (not only alkali) from atomic electronic wave function (see, for instance, the book by E. Nikitin and S. Umanskii [102]). It is given quantum numbers of molecular terms for two Hund's cases – a and c.

The details of calculation c curves and references of sources of a curves are given in the second part of the appendix.

A.1 General scheme of the construction of molecular terms

A.1.1 Symmetry groups and quantum numbers of electronic states of the diatomic system

The classification of molecular terms is directly related to the symmetry group of the system. For homo nuclear diatom the symmetry group is $D_{\infty,h}$ (E.Nikitin and S.Umanskii, [102]). $D_{\infty,h}$ is direct product of symmetry groups: 1) permutations of electrons, 2) rotations around the inter-atomic axis, 3) reflections in any plane containing this axis, and 4) inversion. Thus, correct quantum numbers are following:

- Ω - the absolute value of the projection of the total electronic angular momentum along diatomic axis;
- $\sigma(\sigma = +, -)$ - the character of reflection of the total wave function in the plane containing the diatomic axis;
- $w(w = g, u)$ - the parity of the total wave function on inversion through the center of a diatom;
- δ - others quantum numbers, which can specify different terms inside each symmetry.

The physical conditions of the problem can increase the symmetry of the system, and therefore, the further classification can be done and additional quantum numbers is defined. In the case of interesting , when the spin couples weakly with the orbital momentum, it is appeared the additional group of symmetry – the group of geometric transformation is reduced into the direct product of the group of rotations in the spin space and the group of geometrical transformations acting only in the coordinate space. The corresponding additional classification is a specification of the total spin and the projection of the electronic orbital angular momentum. Quantum numbers in this classifications will be: .

Quantum numbers will be:

- Λ - the absolute value of the projection of the electronic orbital angular momentum along diatomic axis;
- $\sigma'(\sigma' = +, -)$ - the character of reflection of the spatial part of the wave function in the plane containing the diatomic axis;
- $w'(w' = g, u)$ - the parity of the spatial part of the wave function on inversion through the center of a diatom;
- S - the total spin;
- $\delta'(\delta \neq \delta')$ - others quantum numbers, which can specify different terms inside each symmetry.

Let these states are called as a.

In the non relativistic case, the inversion does not involve the spin variables for both classifications. For this reason:

$$w' = w \tag{A.1}$$

A.1.2 Molecular wave functions on large internuclear distance

At large internuclear distances wave functions of atoms are only slightly perturbed one by other, that permits to construct approximate molecular wave function from product of atomic function. Accepting this approximation, the problem of molecular wave functions is reduced to constructing of linear combinations of those product, which transform correctly under group operations, imposed by the symmetry of the diatomic system.

Hund case a

Consider first the Hund's case a, when the spin is independent of the orbital angular momentum.

Let atomic wave functions for atoms A and B will be:

$$|\gamma_1 S_1 m_{S_1} L_1 m_{L_1} >_A$$

$$|\gamma_2 S_2 m_{S_2} L_2 m_{L_2} >_B \tag{A.2}$$

Wave functions of the basis a transforming correctly under the group operations are:

$$|\gamma_1\gamma_2 L\tilde{\Lambda} S m_S >= \hat{A} \sum_{m_{L_1} m_{L_2}} \sum_{m_{S_1} m_{S_2}} C^{L,\Lambda}_{L_1,m_1;L_2,m_2} C^{L,\Lambda}_{\frac{1}{2},m_{S_1};\frac{1}{2},m_{S_2}}$$

$$|\gamma_1 S_1 m_{S_1} L_1 m_{L_1} >_A |\gamma_2 S_2 m_{S_2} L_2 m_{L_2} >_B . \tag{A.3}$$

Here

$$\hat{A} = \frac{1}{\sqrt{2}} \sum_p \delta_p \hat{P} \tag{A.4}$$

is the anti-symmetrization operator, $\hat{P}$ stands for the electron permutation operators, the factor δ_p are +1 for even, and -1 for odd permutations, and the summation is over all permutations of two electrons. The functions (A.3) are antisymmetric with respect to all electrons and correspond to definite values of the total spin S, its projection m_S on the diatomic axis, and the projection $\tilde{\Lambda}$ of the total orbital angular momentum on this axis.

Expressions for quantum numbers

Quantum numbers of wave functions (A.3) are defined symmetry properties of the Clebsh-Gordon coefficients under transformations of the symmetry group of the diatom.

The projection of the orbital angular momentum Λ

$$\Lambda = |\tilde{\Lambda}|, \tag{A.5}$$

Reflection index σ'

For a case $\Lambda = 0$:

$$\sigma' = w_1 w_2 (-1)^L, \tag{A.6}$$

Here w_1 and w_2 are parities of atomic states: $w_{1,2} = (-1)^{L_{1,2}}$.
If $\Lambda \neq 0$ when functions transforming correctly under the action of the operator $\hat{\sigma_v}$:

$$|\gamma_1, \gamma_2, L, \Lambda, S, m_S, p >=$$

$$\left[|\gamma_1, \gamma_2, L, \tilde{\Lambda}, S, m_S > +(-1)^p |\gamma_1, \gamma_2, L, -\tilde{\Lambda}, S, -m_S >\right] / \sqrt{2}$$

$$p = 0, 1 \tag{A.7}$$

i.e.

$$\sigma' = w_1 w_2 (-1)^p (-1)^{L-\Lambda}, \tag{A.8}$$

Parity w'

When atomic states are the same, parity of the molecular state is given:

$$w' = (-1)^{S+L} \tag{A.9}$$

When atomic states are different, functions transforming correctly on inversion:

$$|\gamma_1 \gamma_2 L \tilde{\Lambda} S m_S p_w >=$$

$$\left[|\gamma_1, \gamma_2, L, \tilde{\Lambda}, S, m_S > +(-1)^{p_w} |\gamma_2, \gamma_1, L, \tilde{\Lambda}, S, m_S >\right] / \sqrt{2}$$

$$p_w = 0, 1 \tag{A.10}$$

and parity:

$$w' = w_1 w_2 (-1)^{S_1 + S_2 - S + L_1 + L_2 - L + p_w}. \tag{A.11}$$

Hund case c

When the spin-orbit coupling is comparable or stronger than the electrostatic interaction (Hund's case c), wave functions are constructed by another way. Namely:

$$|\gamma_1, j_1, \gamma_2, j_2, j, \tilde{\Omega} >= \hat{A} \sum_{m_1, m_2} C^{j,\tilde{\Omega}}_{j_1, m_1; j_2, m_2} |\gamma_1, j_1, m_1 >_A |\gamma_2, j_2, m_2 >_B, \tag{A.12}$$

where functions $|\gamma, j, m >$ are constructed from atomic wave functions of Eq. (A.2):

$$|\gamma, j, m >= \sum_{m_L, m_S} C^{j,m}_{L, m_L; S, m_S} |\gamma, S, m_S, L, m_L > \tag{A.13}$$

Expressions for quantum numbers Quantum numbers of wave functions (A.12) are calculated as following.

The projection of the orbital angular momentum Ω

$$\Omega = |\tilde{\Omega}|, \tag{A.14}$$

Reflection index σ

If $\tilde{\Omega} = 0$:

$$\sigma = w_1 w_2 (-1)^j \tag{A.15}$$

When $\tilde{\Omega} \neq 0$ correct wave functions will be:

$$|\gamma_1, j_1, \gamma_2, j_2, j, \Omega, p >=$$

$$\left[|\gamma_1, j_1, \gamma_2, j_2, j, \tilde{\Omega} > + (-1)^p |\gamma_1, j_1, \gamma_2, j_2, j, -\tilde{\Omega} > \right] / \sqrt{2}$$

$$p = 0, 1 \tag{A.16}$$

$$\sigma = w_1 w_2 (-1)^{j-\Omega} \tag{A.17}$$

Parity w

If both atoms are in the same state, parity of molecular state will be:

$$w = (-1)^j \tag{A.18}$$

When identical atoms are in different states, correct functions transforming under inversion are:

$$|\gamma_1, j_1, \gamma_2, j_2, j, \Omega, p_w >= \left[|\gamma_1, j_1, \gamma_2, j_2, j, \tilde{\Omega} > +(-1)^{p_w}|\gamma_2, j_2, \gamma_1, j_1, j, \tilde{\Omega} >\right]/\sqrt{2}$$

$$p_w = 0, 1 \tag{A.19}$$

with parity:

$$w = w_1 w_2 (-1)^{j_1+j_2-j+p_w}. \tag{A.20}$$

A.2 Molecular terms of $nS+nP$ and $nP+nP$ alkali diatoms.

This section is devoted to the details of calculations of c potential curves for $nS+nP$ and $nP+nP$ symmetries of homo nuclear alkali diatoms. The starting a potential curves of Na_2, K_2, Rb_2 and Cs_2, correlating to the $nS+nP$ dissociation limit were accurately computed by the effective potential techniques up to the large internuclear distances, where the curves were continued by C_n/R^n terms with C_n defined by M. Marinescu and A. Dalgarno [92]. At intermediate distances the a potential curves were calculated by S. Magnier *et al* [89] for Na_2, by S. Magnier and Ph. Millié [91] for K_2, and by M.Foucrault *et al* [43] for Rb_2 and for Cs_2. Only c potential curves of Na_2 were considered for the $nP+nP$ symmetry. Corresponding a potential curves were defined by S. Magnier *et al.*

A.2.1 Quantum numbers

$nS+nP$ symmetry

Since for the $nS+nP$ symmetry additional quantum numbers γ of a wave functions are:

$$L_1 = 1,\ L_2 = 0,\ \rightarrow L = 1,\ w_1 w_2 = -1 \tag{A.21}$$

The correct quantum numbers Λ, σ', w' of a wave functions are defined from Eqs. (A.5), (A.6), and (A.11)

$$\Lambda = |\tilde{\Lambda}|$$
$$\sigma' = (-1)^{L+1} =' +'$$

$$w' = (-1)^{S+p_w} \tag{A.22}$$

The correct quantum numbers Ω, σ, w of c wave functions are defined from Eqs. (A.14), (A.15), and (A.20)

$$\Omega = |\tilde{\Omega}|$$
$$\sigma = (-1)^{j+1}$$

$$w = (-1)^{j_1+1/2-j+p_w+1} \tag{A.23}$$

where $j_1 = 1/2$ *or* $3/2$ is a total momentum of the nP atom.

$nP + nP$ symmetry

Additional quantum numbers γ of a wave functions, which are the same for all molecular terms inside the $nP + nP$ symmetry, are:

$$L_1 = L_2 = 1, \rightarrow w_1 w_2 = 1 \tag{A.24}$$

The correct quantum numbers Λ, σ', w' of a wave functions are defined from Eqs. (A.5), (A.6), and (A.9)

$$\Lambda = |\tilde{\Lambda}|$$
$$\sigma' = (-1)^{L}$$

$$w' = (-1)^{S+L} \tag{A.25}$$

The correct quantum numbers Ω, σ, w of c wave functions are defined from Eqs. (A.14), (A.15), and (A.18)

$$\Omega = |\tilde{\Omega}|$$
$$\sigma = (-1)^{j}$$

$$w = (-1)^{j} \tag{A.26}$$

where j is a total momentum of the diatom.

A.2.2 Transformation matrix between a and c bases.

The potential curves with the spin-orbit coupling are calculated by the diagonalizing of the total potential operator:

$$U = \hat{U}^{(a)} + \hat{V}^{SO}, \tag{A.27}$$

where $\hat{U}^{(a)}$ and $\hat{V}^{SO}$ are a potential operator and the operator of the spin-orbit coupling. $\hat{U}^{(a)}$ is diagonal in the a basis, $\hat{V}^{SO}$ is diagonal in the c basis. The transformation between bases is carried out either through the basis of products of atomic

functions using Eqs. (A.3) and (A.12) or directly using the $9-j$ symbol (see the book by E. Nikitin and S. Umanskii [102]). In the Thesis the first approach is used.

The basis of products of atomic wave functions (it will be refereed as AO basis) are defined

$$|L_1, m_{L_1}, m_{S_1}, L_2, m_{L_2}, m_{S_2} >= \hat{A}\,(|L_1, m_{L_1}, 1/2, m_{S_1} >_A |L_2, m_{L_2}, 1/2, m_{S_2} >_B) \tag{A.28}$$

For simplicity these functions will be referred as φ_i^{AO}, functions of basis a as φ_i^a and a notation φ_i^c is for c-basis functions. Here i includes a full set corresponding quantum numbers. All bases have the same number of wave functions.

Equations (A.3), (A.10), (A.7), (A.12), (A.16), and (A.19) defines the connections between wave functions in different bases. For an atom in p-state ($L = 1,\ s = 1/2$) there are 6 states with different projections of the spin and the angular momentum. There are 2 states for s-state ($L = 0,\ s = 1/2$. Hence one has 36 states for $3p + 3p$-manifold. For the $3s + 3p$-manifold with accounting of Eq. (A.10) there are 24 states. Transformations matrixes are:

$$\varphi_i^a = \sum_i T_{i,j}^{AO\to a} \varphi_j^{AO}$$

$$\varphi_i^c = \sum_i T_{i,j}^{AO\to c} \varphi_j^{AO}$$

Where matrix $T^{AO\to a}$ $T^{AO\to c}$ are constructed from evident combinations of the Clebsh-Gordon coefficients. The transformation matrix between c and a bases

$$T^{a\to c} = T^{AO\to c} \left(T^{AO\to a}\right)^{-1} \tag{A.29}$$

In the Thesis, the matrix of the total potential operator is calculated in the a basis. For this, the operator of the spin-orbit coupling is transformed into the a basis and added to a potential curves. Then, this total matrix is diagonalized, giving the adiabatic potential curves.

Appendix B

Adiabatic Schrödinger Equation for the Alkali Diatom

This chapter of the appendix discusses the Schrödinger equation of the diatomic system with accounting the spin-orbit coupling and the Coriolis interaction.

Among alkali diatoms, both interactions are important for K_2 and for Rb_2, for which these interaction are comparable on intermediate internuclear separations. For more light species, Na_2 and Li_2 the spin-orbit interaction is much smaller on in the region of effective transitions between molecular states and, thus, in can be neglected. For Cs_2 in the intermediate region, the spin-orbit coupling is much larger than the Coriolis interaction. In addition, the hyperfine structure becomes comparable with the the Coriolis coupling for the Cesium.

The most general form of the Schrödinger equation for the diatom can be written as (E.Nikitin And S.Umanskii [102]):

$$\mathbf{H}\Psi^{J,M} = E\Psi^{J,M}. \tag{B.1}$$

Where J, M are quantum numbers of integrals of motion – the squared total angular momentum $\mathbf{J}^2$ and its projection J_z on the space-fixed axis Z.

Each symmetry of molecular states specified by the pair of indexes J, M does not interact with others. The molecular states inside one J, M symmetry can be further specified by additional quantum numbers, but in general case there is a coupling between them.

The first step to the system of coupled equation is the definition of the adiabatic states and adiabatic molecular terms. The adiabatic molecular terms are defined as eigenvalues of the electronic part of the Hamiltonian, when the nuclei are supposed to be fixed. The internuclear distance is introduced into the electronic molecular states as a parameter.

$$H_{el}(R)|\gamma(R)>= V_\gamma(R)|\gamma(R)> \tag{B.2}$$

- r is a set of all-electrons coordinates (not specified explicitly here),

- R is a distance between nuclei,
- $H_{el}(R)$ is the electronic Hamiltonian of the system including the spin-orbit coupling,
- $|\gamma(R)>$ is electron wave-function with fixed nuclei – adiabatic states,
- $V_\gamma(R)$ is energy of a state $\gamma(R)>$.

Thus, the set of numbers γ numerates the adiabatic states. (Hereafter, γ will be contains all quantum numbers not specified explicitly.) Since the rotation around the internuclear axis does not change the symmetry, the corresponding quantum number can be specified here - the projection of J on the internuclear axis – Ω. The second quantum number is J as in Eq. (B.1). Since the adiabatic states and terms are defined in the molecular-fixed *MF* basis and Eq. (B.1) is written in the space-fixed *SF* basis one should transform the Schrödinger equation in *MF* basis. The following form of the equation is taken from [102] (E.Nikitin and S.Umanskii).

$$\left(-\frac{1}{2\mu}\frac{d^2}{dR^2}+\frac{J(J+1)-\Omega^2}{2\mu R^2}+V_{\gamma,\Omega,J}\right)\psi_{\gamma,\Omega,J}+$$

$$\sum_{\gamma',\Omega'}\left(<\gamma,\Omega|V_R|\gamma',\Omega'>+<\gamma,\Omega|V_{Cor}|\gamma',\Omega'>\right)\psi_{\gamma',\Omega',J}=i\frac{d}{dt}\psi_{\gamma,\Omega,J}. \tag{B.3}$$

Interaction

$$<\gamma,\Omega|V_R|\gamma',\Omega'>=\delta_{\Omega,\Omega'}(-\frac{1}{\mu}<\gamma,\Omega|\frac{\partial}{\partial R}|\gamma',\Omega'>\frac{d}{dR}$$

$$-\frac{1}{2\mu}<\gamma,\Omega|\frac{\partial^2}{\partial R^2}|\gamma',\Omega'>+\frac{1}{2\mu R^2}<\gamma,\Omega|j_x^2+j_y^2|\gamma',\Omega'>) \tag{B.4}$$

- $\psi_{\gamma,\Omega,J}$ is nuclear wave function,
- j_x, j_y is a operator of the projection of the orbital electronic momentum j on the X and Y axes of body-fixed coordinate system

is a non-adiabatic radial coupling between the states with the same Ω.

Interaction $<\gamma,\Omega|V_{Cor}|\gamma',\Omega'>$ is due to correlation between the motion of electrons and the rotation of internuclear axis:

$$<\gamma,\Omega|V_{Cor}|\gamma',\Omega'>=-\frac{1}{\mu R^2}(\lambda^+(J)<\gamma,\Omega|j_x|\gamma',\Omega+1>\delta_{\Omega+1,\Omega'}+$$

$$\lambda^-(J)<\gamma,\Omega|j_x|\gamma',\Omega-1>\delta_{\Omega-1,\Omega'}) \tag{B.5}$$

$$\lambda^\pm(J)=\sqrt{(J\mp\Omega)(J\pm\Omega+1)} \tag{B.6}$$

From rest of indexes γ the projection ω of the electronic angular momentum on the internuclear axis can be specified. Since the vector of molecular rotation is always orthogonal to the inter atomic axis, it does not give any contribution into the projection of the full momentum on the inter atomic axe. And hence:

$$\omega = \Omega \tag{B.7}$$

Matrix elements $< \gamma, \Omega | j_x^2 + j_y^2 | \gamma', \Omega' >$ and $< \gamma, \Omega | j_x | \gamma', \Omega \pm 1 >$ can be calculated in jj-representation (Hund's case c basis).

Let $\{|\varphi >\}$ is a basis of the c representation, and let two bases MC and c are connected by the transformation $\mathbf{S}$

$$|\gamma >= \sum_{\varphi} S_{\gamma,\varphi} |\varphi > \tag{B.8}$$

The number φ numerates functions $|\varphi >$. The next indexes must be specified explicitly in order to calculate $< \gamma, \Omega | j_x^2 + j_y^2 | \gamma', \Omega' >$ and $< \gamma, \Omega | j_x | \gamma', \Omega \pm 1 >$ elements:

- j_1, j_2 are total momenta of separated atoms,
- j is a sum of j_1 and j_2,
- Ω is a projection of j on the diatomic axe.

The matrix elements are:

$$< \Omega, \varphi | j_x |, \Omega - 1, \varphi' >= \frac{1}{2} \sqrt{(j + \Omega)(j - \Omega + 1)} \delta_{\Omega-1,\Omega'} \delta_{\varphi,\varphi'}. \tag{B.9}$$

And for $< \Omega, \varphi | j_x | \Omega + 1, \varphi' >$:

$$< \Omega, \varphi | j_x | \Omega + 1, \varphi' >= \frac{1}{2} \sqrt{(j + \Omega + 1)(j - \Omega)} \delta_{\Omega+1,\Omega'} \delta_{\varphi,\varphi'}. \tag{B.10}$$

For $j_x^2 + j_y^2$ term:

$$< \varphi, \Omega, j | j_x^2 + j_y^2 | \varphi', \Omega', j' >=< \varphi, \Omega, j | j^2 - j_z^2 | \varphi', \Omega', j' >=$$

$$(j(j+1) - \Omega^2) \delta_{\varphi,\varphi'} \delta_{\Omega,\Omega'} \delta_{j,j'} \tag{B.11}$$

Finally matrix elements of the operator $\mathbf{V}_{Cor}$ is written in $|\varphi >$-basis:

$$< \varphi, \Omega | V_{Cor} | \varphi', \Omega' >= -\delta_{\varphi,\varphi'} \frac{1}{2\mu R^2} (\lambda^+(J) \lambda^+(j) \delta_{\Omega+1,\Omega'}$$

$$+ \lambda^-(J) \lambda^-(j) \delta_{\Omega-1,\Omega'}) \tag{B.12}$$

$$\lambda^{\pm}(j) = \sqrt{(j \mp \Omega)(j \pm \Omega + 1)} \tag{B.13}$$

Operator $\frac{\partial}{\partial R}$ in the basis γ is written:

$$< \gamma|\frac{\partial}{\partial R}|\gamma' >= \sum_{\varphi,\varphi'} S_{\gamma,\varphi}\left(S_{\gamma',\varphi'} < \varphi|\frac{\partial}{\partial R}|\varphi' > + \frac{\partial S_{\gamma',\varphi'}}{\partial R} < \varphi|\varphi' >\right) =$$

$$\sum_{\varphi} S_{\gamma,\varphi}\frac{\partial S_{\gamma',\varphi}}{\partial R} \tag{B.14}$$

because the basis functions if the c basis does not depend of R:

$$\frac{\partial|\varphi >}{\partial R} = 0. \tag{B.15}$$

Operator $\frac{\partial^2}{\partial R^2}$:

$$< \gamma|\frac{\partial^2}{\partial R^2}|\gamma' >= \sum_{\varphi} S_{\gamma,\varphi}\frac{\partial^2 S_{\gamma',\varphi}}{\partial R^2} \tag{B.16}$$

The whole operator $\mathbf{V}_R$:

$$< \gamma,\Omega|\mathbf{V}_R|\gamma',\Omega' >=$$

$$\delta_{\Omega,\Omega'}\frac{1}{2\mu}\sum_{\varphi}\left(-2S_{\gamma,\varphi}\frac{\partial S_{\gamma',\varphi}}{\partial R}\frac{d}{dR} - S_{\gamma,\varphi}\frac{\partial^2 S_{\gamma',\varphi}}{\partial R^2} + S_{\gamma,\varphi}S_{\gamma',\varphi}\frac{j(j+1)-\Omega^2}{R^2}\right) \tag{B.17}$$

Using Eq. (B.8), Eq. (B.5) will be:

$$< \gamma,\Omega|V_{Cor}|\gamma',\Omega' >= -\frac{1}{2\mu R^2}\sum_{\varphi} S_{\gamma,\varphi}S_{\gamma',\varphi}(\lambda^+(J)\lambda^+(j)\delta_{\Omega+1,\Omega'} +$$

$$\lambda^-(J)\lambda^-(j)\delta_{\Omega-1,\Omega'}) \tag{B.18}$$

The full equation has a form:

$$E\psi_{\gamma,\Omega,J} = \left(-\frac{1}{2\mu}\frac{d^2}{dR^2} + \frac{J(J+1)-\Omega^2}{2\mu R^2} + V_{\gamma,\Omega,J}\right)\psi_{\gamma,\Omega,J} +$$

$$\frac{1}{2\mu}\sum_{\gamma',\Omega'}\sum_{\varphi}(\delta_{\Omega,\Omega'}(-2S_{\gamma,\varphi}\frac{\partial S_{\gamma',\varphi}}{\partial R}\frac{d}{dR} - S_{\gamma,\varphi}\frac{\partial^2 S_{\gamma',\varphi}}{\partial R^2} + S_{\gamma,\varphi}S_{\gamma',\varphi}\frac{j(j+1)-\Omega^2}{R^2}) -$$

$$\frac{1}{R^2}S_{\gamma,\varphi}S_{\gamma',\varphi}\{\lambda^+(J)\lambda^+(j)\delta_{\Omega+1,\Omega'} + \lambda^-(J)\lambda^-(j)\delta_{\Omega-1,\Omega'}\})\psi_{\gamma',\Omega',J}. \tag{B.19}$$

For the program it is more convenient a form:

$$-\frac{1}{2\mu}\frac{d^2}{dR^2}\psi_\gamma + \sum_{\gamma'}\left(V^{Mod}_{\gamma,\gamma'} - \frac{1}{2\mu}\left[2\tau^{(1)}_{\gamma,\gamma'}\frac{d}{dR} + \tau^{(2)}_{\gamma,\gamma'}\right]\right)\psi_{\gamma'} = i\frac{d}{dt}\psi_\gamma, \tag{B.20}$$

where

$$V^{Mod}_{\gamma,\gamma'} = \left(\frac{J(J+1)-\Omega^2}{2\mu R^2} + V_\gamma\right) + \frac{1}{2\mu}\sum_{\gamma'}\sum_{\varphi}\delta_{\Omega,\Omega'}S_{\gamma,\varphi}S_{\gamma',\varphi}\frac{j(j+1)-\Omega^2}{R^2}$$

$$-\sum_{\gamma',\Omega'}\sum_{\varphi}\frac{1}{2\mu R^2}S_{\gamma,\varphi}S_{\gamma',\varphi}\{\lambda^+(J)\lambda^+(j)\delta_{\Omega+1,\Omega'} + \lambda^-(J)\lambda^-(j)\delta_{\Omega-1,\Omega'}\} \tag{B.21}$$

and

$$\tau^{(1)}_{\gamma,\gamma'} = \sum_{\varphi} S_{\gamma,\varphi}\frac{\partial S_{\gamma',\varphi}}{\partial R} \tag{B.22}$$

$$\tau^{(2)}_{\gamma,\gamma'} = \sum_{\varphi} S_{\gamma,\varphi}\frac{\partial^2 S_{\gamma',\varphi}}{\partial R^2} \tag{B.23}$$

are the matrices of the non-adiabatic coupling between diabatic components.

For the homo nuclear alkali diatomic system numerating indexes γ and φ besides others explicitly mentioned contains also the following quantum numbers:

- parity of state - w,
- for $\Omega = 0$ - a sign of a state - σ,

Appendix C

Article: *"Mapped Fourier methods for long-range molecules: Application to perturbations in the Rb_2 0_u^+ photo-association spectrum"*

JOURNAL OF CHEMICAL PHYSICS VOLUME 110, NUMBER 20 22 MAY 1999

Mapped Fourier methods for long-range molecules: Application to perturbations in the $Rb_2(0_u^+)$ photoassociation spectrum

V. Kokoouline
Laboratoire Aimé Cotton, Bât. 505, Campus d'Orsay, 91405 Orsay Cedex, France
and The Institute of Physics, Saint-Petersburg State University, Saint-Petersburg 198904, Russia

O. Dulieu
Laboratoire Aimé Cotton, Bât. 505, Campus d'Orsay, 91405 Orsay Cedex, France

R. Kosloff
The Fritz Haber Research Center for Molecular Dynamics, The Hebrew University of Jerusalem, Jerusalem 91904, Israel

F. Masnou-Seeuws[a)]
Laboratoire Aimé Cotton, Bât. 505, Campus d'Orsay, 91405 Orsay Cedex, France

(Received 10 November 1998; accepted 18 February 1999)

Numerical calculations of vibrational levels of alkali dimers close to the dissociation limit are developed in the framework of a Fourier Grid Hamiltonian method. The aim is to interpret photoassociation experiments in cold atom samples. In order to avoid the implementation of very large grids we propose a mapping procedure adapted to the asymptotic R^{-n} behavior of the long-range potentials. On a single electronic potential, this allows us to determine vibrational wave functions extending up to $500a_0$ using a minimal number of grid points. Calculations with two electronic states, $A\ ^1\Sigma_u^+$ and $b\ ^3\Pi_u$ states, both correlated to the $Rb(5s)+Rb(5p)$ dissociation limit, coupled by fine structure are presented. We predict strong perturbation effects in the $Rb_2(0_u^+)$ spectrum, manifested under the $5s$, $5p\ ^2P_{1/2}$ dissociation limit by an oscillatory behavior of the rotational constants. © *1999 American Institute of Physics.* [S0021-9606(99)00519-X]

I. INTRODUCTION

Due to rapid progress in experiments with cold atom samples, there is an important need for modelization and theoretical interpretation. Numerical tools should be constantly refined for the treatment of atomic collisions at very low energy or for the determination of the bound vibrational levels of an alkali dimer close to the dissociation limit. Among the many applications, we may emphasize the following:

(1) The determination of cross sections for fine-structure transitions[1–3] or predissociation[4] in a magneto-optical trap.
(2) The population of vibrational levels of an excited electronic state by photoassociation of cold atoms (see, for instance, Refs. 5–7.
(3) The study of long-lived cold molecule formation by spontaneous emission from the later state, as recently observed.[8]

Grid numerical methods using fast Fourier transform have proved to be very efficient for quantum molecular dynamics.[9,10] Wave functions are then represented on grids with a constant step in the momentum or coordinate spaces. However, their application to the present class of problems is not straightforward due to the coexistence of two regions of space with very different physical properties. There is a long-range region where the relative motion of the atoms is very slow, so that the de Broglie wavelength is very large, up to hundreds of atomic units a_0 ($1a_0=0.052\,917\,72$ nm). In contrast, in the inner region where chemical attractive forces become important, the kinetic energy is large so that the de Broglie wavelength is smaller than $1a_0$. In the long-range region, the interaction potential is decreasing as R^{-n}, R being the internuclear distance: we shall focus on examples for which $n=3$ — relevant to problems with dissociation limit $A(ns)+A(np)$, one alkali atom A being in the ground state, the other in the first excited state—and $n=6$ — relevant to dissociation into $A(ns)+A(ns)$.

As the maximum grid step in the position space is necessarily linked to the maximum momentum p_{max} considered in the physical problem, the choice of a constant grid step leads to the definition of a domain in the phase space with rectangular shape and area $2L\times p_{max}$, where L is the length of the grid in the position space. Therefore this rectangular domain is too extended in the long-range region, where only very small momenta should be included. In order to optimize the efficiency of the representation of the grid, Fattal *et al.*[11] have suggested a mapping procedure, a change of variable dealing for the dependence of the local wavelength with the distance. They give an application to the solution of the Schrödinger equation with a Coulomb potential. Our aim in the present paper is to extend their work to potentials asymptotically varying as R^{-n}, considering both one channel and multichannel applications.

For such potentials, a change of variable, already sug-

a)Electronic mail: fmasnou@lancelot.lac.u-psud.fr

gested in the book of Landau and Lifshitz,[12] has been used by O'Malley *et al.*[13] for electron atom scattering and later on by Gribakin and Flambaum[14] in their semiclassical treatment of cold collisions. Their aim was to obtain analytical solutions in the asymptotic region.

Change of variables for grid-based methods have been analyzed by Bayliss and Turkel[15] and employed by Gygi[16] or, more recently, by Pérez-Jordá[17] for electronic structure calculations as well as by Tiesinga *et al.*[18] for obtaining bound vibrational states of alkali dimers by a filter method. In the latter work, however, the emphasis is more on the filtering method to extract eigenvalues by means of the Green's function approach. The formalism is applied to the many-channel problem of rovibrational levels coupled by hyperfine structure in the vicinity of the first excited asymptote of Na_2. In contrast, our goal in the present paper is to analyze in detail the implementation of a mapping procedure to improve the efficiency of grid method calculations for bound vibrational levels in the class of potentials described above. Starting with a one-channel problem, we shall compare the efficiency of an analytical change of variable, close to the one used in Ref. 18, with a purely numerical one. The accent will be put on the optimization of the phase space occupation, and on the definition of a symmetric representation of the Hamiltonian on the grid convenient for numerical accuracy. Indeed, Tuvi *et al.*[19] have pointed out that a simple change of variables results in non-Hermitian Hamiltonian representation and suggested a way to symmetrize. We shall propose another procedure, better adapted to coupled channels with d/dR radial coupling. Section II is devoted to the description of the mapping procedure, particularly in the case of R^{-3} asymptotic potentials, with an estimation of the occupation of the phase space. In the two following sections we describe applications to the calculation of bound vibrational states, close to the dissociation limit, for examples relevant to photoassociation studies. In Sec. III, we have considered two cases of a single potential corresponding, respectively, to the $^1\Pi_g(3s+3p\,^2P)$ excited state of Na_2, and the $1_g(6s+6p\,^2P_{3/2})$ excited state of Cs_2. Indeed, the spectroscopy of those dimers can be interpreted using Hund's case *a* representation for Na_2 and Hund's case *c* for Cs_2. In contrast, Sec. V is devoted to the study of perturbations in Rb_2 fluorescence spectrum, considering two coupled potentials $0_u^+(5s+5p\,^2P_{3/2})$ and $0_u^+(5s+5p\,^2P_{1/2})$

Atomic units will be used except when otherwise stated.

II. MAPPED FOURIER GRID METHOD

A. Mapping procedure

In order to compute bound vibrational states of a diatomic molecule, a method, originally proposed in Refs. 9 and 20, was further developed by Monnerville and Robbe[21] and by Dulieu *et al.*[22] Let us recall briefly the principle of this method, hereafter referred to as Fourier Grid Method (FGH): the radial Schrödinger equation for eigenvalues problem is written as

$$[\mathbf{T}+\mathbf{V}(R)]\psi(R)=E\psi(R), \tag{2.1}$$

A grid of N points equally spaced over coordinate R is defined as R_i, $(i=1,N)$. We introduce a set of functions defined at the grid points:

$$\varphi_i(R_j)=\delta(R_i-R_j) \quad (i,j=1,N). \tag{2.2}$$

In this basis, both $\mathbf{T}$ and $\mathbf{V}(R)$ are represented by $N\times N$ matrices. The potential operator $\mathbf{V}(R)$ is diagonal in this representation, while the kinetic energy $\mathbf{T}$ is diagonal in the momentum representation, which is connected by a Fourier transform to the coordinate representation. Using well-known properties of the Fourier transform, the elements of the operator $\mathbf{T}$ can be written explicitly as a function of the number of points N—assumed to be even—and total length L of the grid:[23]

$$T_{i,i}=\frac{\pi^2}{\mu L^2}\frac{N^2+2}{6}, \tag{2.3}$$

$$T_{i,j}=(-1)^{i-j}\frac{\pi^2}{\mu L^2}\frac{1}{\sin^2[(i-j)\pi/N]}. \tag{2.4}$$

In Eqs. (2.3) and (2.4), μ is the reduced mass of the system. Eigenvalues E_i are obtained by diagonalization of the $N\times N$ matrix $\mathbf{T}+\mathbf{V}$.

Is is important to note that for the vibrational levels considered, the energy is close to the asymptotic value of the potential, hereafter taken as the energy origin. The maximum kinetic energy in the problem can be estimated by the depth $(V_{\max}-V_{\min})$ of the potential well. In most applications $V_{\max}=0$, nonzero positive values corresponding to situations where the potential has a hump. For a grid of length L, the two-dimension phase space should occupy at least a rectangular-shaped area:

$$A\geqslant Lp_{\max}, \tag{2.5}$$

where $p_{\max}$ is the maximum momentum that has to be considered, corresponding to the maximum value of the kinetic energy:

$$p_{\max}=\sqrt{2\mu(V_{\max}-V_{\min})}, \tag{2.6}$$

In practice, for a grid with N points, with a constant grid step $\Delta R=L/N$, the Fourier method[10] considers a momentum domain extending from $-p_{\text{grid}}$ to $+p_{\text{grid}}$ so that the phase space is a rectangle with area:

$$A_N=2\pi N\hbar=2Lp_{\text{grid}}, \tag{2.7}$$

where, using atomic units, $\hbar=1$. Therefore the constant grid step should verify

$$\Delta R=\frac{\pi}{p_{\text{grid}}}\leqslant\frac{\pi}{\sqrt{2\mu(V_{\max}-V_{\min})}}. \tag{2.8}$$

When the vibrational motion extends at very long range, the length L has to be very large and calculations involve diagonalization of huge matrices $\mathbf{H}=\mathbf{T}+\mathbf{V}$. In fact, the grid contains too many points in the asymptotic region: indeed, at each distance R, the grid step needs only to be small enough to represent correctly the local kinetic energy. It is then sufficient to consider a local grid step $s(R)$ satisfying the condition

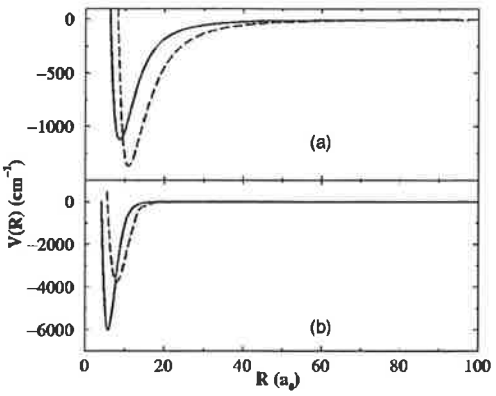

FIG. 1. Examples of potential curves used in the paper. (a) Two potentials with R^{-3} asymptotic behavior. Solid line: $Na_2(^1\Pi_g,3s+3p)$, dashed line: $Cs_2(1_g,6s+6p^2P_{3/2})$. (Indeed, Hund's case *a* representation is better adapted for Na_2 and Hund's case *c* for Cs_2.) (b) Two ground state potentials with R^{-6} asymptotic behavior. Solid line: $Na_2(^1\Sigma_g^+,3s+3s)$, dashed line: $Cs_2(^1\Sigma_g^+,6s+6s)$. For all curves, the energy origin is taken at the dissociation limit.

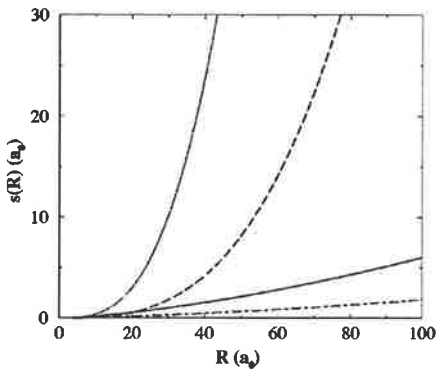

FIG. 2. Variation of the grid step $s(R)$ in the physical grid, for the four potentials in Fig. 1. Dotted line: $Na_2(^1\Sigma_g^+,3s+3s)$, dashed line: $Cs_2(^1\Sigma_g^+,6s+6s)$, solid line: $Na_2(^1\Pi_g,3s+3p)$, dash-dotted line: $Cs_2(1_g,6s+6p^2P_{3/2})$.

$$s(R)=\frac{\pi}{\sqrt{2\mu[V_{\max}-V(R)]}}. \tag{2.9}$$

For the class of problems that we are considering (see Sec. III) the computation effort of the diagonalization procedure scales as the cube of the number of grid points. We propose to apply coordinate transformation in order to "compress" the grid at large distances. To that purpose, we define a transformation function $g(R)$ to set a working grid $x_i=g(R_i)$, $i=1,N$, with a constant step Δx related to the variable step in the physical grid through

$$s(R)=\frac{\Delta x}{g'(R)}. \tag{2.10}$$

The transformation function is obtained, by comparing Eqs. (2.10) and (2.9) as

$$x=g(R)=\int_{R_0}^{R}\frac{\sqrt{2\mu[V_{\max}-V(r)]}}{\pi}dr. \tag{2.11}$$

It is easy to check that in the working grid the minimum step is

$$\Delta x=1. \tag{2.12}$$

In Eq. (2.11), the integration domain starts at a distance R_0 slightly smaller than the position of the repulsive potential wall at short range. Now the physical grid is well adapted to different regions of the potential, since in the asymptotic region the local step $s(R)$ becomes much larger than at short internuclear distances. In Fig. 1, we have illustrated this behavior considering various potentials for Na_2[24] or Cs_2[25] with either R^{-3} or R^{-6} asymptotic behavior. For a constant step $\Delta x=1$ in the working grid, we have represented in Fig. 2 the variation of $s(R)$ as a function of the distance R. The marked dependence upon the value of the n exponent manifests itself clearly, the step $s(R)$ increasing more rapidly with the distance in case of a R^{-6} potential. Besides, due to the mass factor present in Eq. (2.9) the R variation is more rapid for Na_2 than for Cs_2. These features, as well as the role of the position R_0 of the inner repulsive potential wall, will be discussed more explicitly in Sec. II C.

Alternatively, in Eq. (2.9) defining a maximum local grid step, the real potential $V(R)$ can be replaced by another potential $V_{\text{env}}(R)$, provided the local kinetic energy stays larger than or equal to the real one. We shall call $V_{\text{env}}(R)$ an "enveloping potential" as the corresponding potential curve lies below the real one. The local grid step is now such that

$$s_{\text{env}}(R)=\frac{\pi}{\sqrt{2\mu[V_{\max}-V_{\text{env}}(R)]}}\leqslant s(r). \tag{2.13}$$

Therefore the number of points on the grid is necessarily increased compared to the previous one. We discuss in Sec. II C examples where the asymptotic expression of the potential is considered.

Finally, for the discussion of the convergence of the calculations, it is convenient to introduce an auxiliary parameter $\beta_R=s_{\text{env}}(R)/s(R)$. If the enveloping potential differs from the real one, β_R depends upon R, with the restriction $\beta_R\leqslant 1$ so that the number of grid points is sufficient. Moreover, we can, starting from the real potential, calculate $s(R)$, and choose a constant $\beta<1$ (for instance, the minimum value of β_R) in order to define a local grid step such that $s_\beta(R)=\beta s(R)$. It means that the density of points is $1/\beta$ times larger than the critical density defined by (2.12), the step in the working grid being now

$$\Delta x=\beta, \tag{2.14}$$

corresponding in the physical grid to a larger extension of the momentum, from $-p_{\text{grid}}$ to $p_{\text{grid}}=p_{\max}/\beta$.

B. Transformation of the Hamiltonian

Changing in the Schrödinger equation

$$-\frac{1}{2\mu}\frac{d^2}{dR^2}\psi+V(R)\psi=E\psi, \tag{2.15}$$

the variable R into another x with the transformation

$$R=f(x), \quad dR=J(x)dx, \quad J(x)=f'(x), \tag{2.16}$$

one gets

$$\left(-\frac{1}{2\mu J^2}\frac{d^2}{dx^2}+\frac{J'}{2\mu J^3}\frac{d}{dx}\right)\psi+V(x)\psi=E\psi, \tag{2.17}$$

where $J'=dJ/dx$. As discussed in the Appendix, the elements $T_{i,j}$ and $T_{j,i}$ of the kinetic energy operator in the FGH representation are generally different, leading to the diagonalization of a nonsymmetric matrix.

In order to introduce a Hamiltonian matrix symmetric in the FGH representation, we define a new wave function $\phi(x)$:

$$\psi(x)=J^{-1/2}(x)\phi(x), \tag{2.18}$$

so that the Eq. (2.17) becomes

$$\left[-\frac{1}{2\mu J^2}\frac{d^2}{dx^2}+\frac{J'}{\mu J^3}\frac{d}{dx}+V+\frac{1}{2\mu}\left(-\frac{5}{4}\frac{(J')^2}{J^4}+\frac{1}{2}\frac{J''}{J^3}\right)\right]$$

$$\times\phi(x)=E\phi(x). \tag{2.19}$$

We can rewrite this equation in a symmetrical form as

$$\left[-\frac{1}{4\mu}\left(\frac{1}{J^2}\frac{d^2}{dx^2}+\frac{d^2}{dx^2}\frac{1}{J^2}\right)+\bar{V}\right]\phi=E\phi, \tag{2.20}$$

where we have introduced an effective potential by

$$\bar{V}(x)=V(x)+\frac{1}{2\mu}\left(\frac{7}{4}\frac{(J')^2}{J^4}-\frac{1}{2}\frac{J''}{J^3}\right). \tag{2.21}$$

We can check that the indexes i and j now play the same role in the expression of the kinetic operator **T** matrix elements:

$$T_{i,j}=(-1)^{i-j}\frac{\pi^2}{2\mu L^2}\frac{1}{\sin^2[(i-j)\pi/N]}\left(\frac{1}{J_i^2}+\frac{1}{J_j^2}\right), \tag{2.22}$$

if $i\neq j$, while

$$T_{i,i}=\frac{\pi^2}{\mu L^2}\frac{N^2+2}{6}\frac{1}{J_i^2}. \tag{2.23}$$

As a consequence, the FGH representation yields a symmetrical Hamiltonian matrix, so that efficient diagonalization procedures designed for triangular matrices can be implemented.

C. Mapping using R^{-3} and R^{-6} analytical potentials and a repulsive wall

In the derivation of the mapping procedure, we can use as an "enveloping potential" in Eq. (2.13) any analytic potential $V_{\text{env}}(R)=-C_n^{\text{env}}/R^n$, such that the corresponding potential curve lies below $V(R)$.

The Schrödinger equation for a potential with R^{-n} behavior, n being an integer value such that $n\geq 3$, was discussed by many authors: in Refs. 12–14, a change of variable is introduced in order to transform the Schrödinger equation into the Bessel equation for which analytical solutions can be found. In the present approach, performing integration of the right-hand side of Eq. (2.11), we obtain:

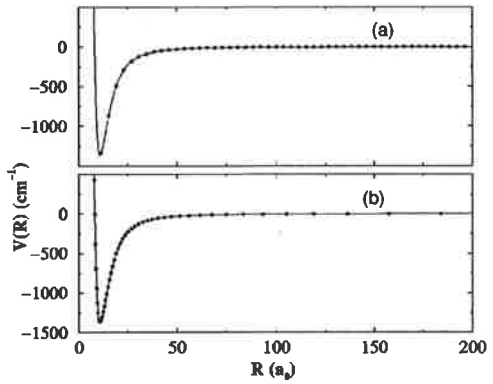

FIG. 3. Distribution of the grid points for a potential with asymptotic R^{-3} behavior: example of $Cs_2(1_g,6s+6p^2P_{3/2})$. (a) Without mapping; (b) with the mapping defined by Eq. (2.24).

$$x_n=g_n(R)=x_{0,n}-\frac{2\alpha_n}{(n-2)}\frac{1}{R^{(n-2)/2}}, \tag{2.24}$$

where we have defined

$$\alpha_n=\frac{\sqrt{2\mu C_n^{\text{env}}}}{\pi}, \tag{2.25}$$

$$x_{0,n}=\frac{2\alpha_n}{(n-2)}\frac{1}{R_0^{(n-2)/2}}. \tag{2.26}$$

Whereas the physical grid is extending from R_0 (chosen at a distance shorter than the position of the repulsive wall of the actual potential) to $R_{\max}$, the new grid is varying from 0 to a maximum value that is limited by the finite value $x_{0,n}$, depending both on the asymptotic behavior of the potential (through α_n and n) and on R_0. There is therefore an accumulation of points in the vicinity of $x_{0,n}$, which is never explicitly reached. At small distances, due to the existence of a repulsive wall in our potential, we do not encounter the problem of the accumulation of points at the origin that had to be considered in Ref. 11 for the Coulomb problem.

The relation between the constant step Δx on the working grid and the variable step $s_n(R)$ on the physical grid is readily obtained as

$$s_n(R)=\frac{R^{n/2}}{\alpha_n}\Delta x. \tag{2.27}$$

The role of the exponent n and of the mass factor in α_n appears clearly in Eq. (2.27) and has been illustrated in Fig. 2. We also display as an example in Fig. 3, in a case where $n=3$, corresponding to the asymptotic behavior of the upper attractive 1_g curve of Cs_2, the repartition of the grid points for the working grid and for the physical grid: the adaptative character of the mapping procedure is demonstrated by the fewer number of points in the working grid when the internuclear distance is increasing. In the case of potential $-C_3^{\text{env}}/R^3$, the change of variable should be

$$x_3=x_{0,3}-2\alpha_3 R^{-1/2}, \tag{2.28}$$

J. Chem. Phys., Vol. 110, No. 20, 22 May 1999

where we have defined $\alpha_3=\sqrt{2\mu C_3^{\rm env}}/\pi$ through Eq. (2.25). The inverse transformation is then analytical:

$$R=f_3(x_3)=\frac{(2\alpha_3)^2}{(x_{0,3}-x_3)^2}. \tag{2.29}$$

As the change of function described in Sec. II B differs from what was proposed in the references quoted above,[12–14] our new Schrödinger equation differs from a Bessel equation. It is more convenient for numerical calculations, as it leads to symmetrical matrices in the FGH representation:

$$\left[-\frac{1}{2\mu}\left(\frac{(x_{0,3}-x_3)^6}{2^7(\alpha_3)^4}\frac{d^2}{dx_3^2}+\frac{d^2}{dx_3^2}\frac{(x_{0,3}-x_3)^6}{2^7(\alpha_3)^4}\right)+\bar{V}(x_3)\right]$$
$$\times\phi(x_3)=E\phi(x_3), \tag{2.30}$$

with new potential $\bar{V}$:

$$\bar{V}(x_3)=V(x_3)+\frac{1}{2\mu}\frac{39}{2^8(\alpha_3)^4}(x_{0,3}-x_3)^4. \tag{2.31}$$

In the new coordinate x_3, the asymptotic behavior of $V(x_3)$ obtained by the transformation of $-C_3/R^3$ is

$$V_{\rm as}(x)=-\frac{1}{2\mu}\frac{4\pi^2}{2^8(\alpha_3)^4}(x_{0,3}-x_3)^6, \tag{2.32}$$

so that when $C_3^{\rm env}=C_3$, the effective potential, in the asymptotic region, may be written:

$$\bar{V}_{\rm as}(x_3)=\frac{1}{2\mu}\left(-\frac{4\pi^2}{2^8(\alpha_3)^4}(x_{0,3}-x_3)^6+\frac{39}{2^8(\alpha_3)^4}(x_{0,3}-x_3)^4\right). \tag{2.33}$$

The matrix elements for the kinetic energy operator are now

$$T_{i,j}=(-1)^{i-j}\frac{\pi^2}{2\mu L^2}\frac{1}{\sin^2[(i-j)\pi/N]}\times\left(\frac{(x_{0,3}-x_{3,i})^6}{2^6(\alpha_3)^4}+\frac{(x_{0,3}-x_{3,j})^6}{2^6(\alpha_3)^4}\right), \tag{2.34}$$

if $i\neq j$, while

$$T_{i,i}=\frac{\pi^2}{\mu L^2}\frac{N^2+2}{6}\frac{(x_{0,3}-x_{3,i})^6}{2^6(\alpha_3)^4}. \tag{2.35}$$

D. Comparison of the numerical and the analytical mapping procedures

The analytic approach enables a simple assessment of the procedure. However, the computing code has to be modified for potentials differing in their asymptotic expression, which is not the case for the general numerical procedure.

Another disadvantage of the analytical approach lies in the definition of an enveloping potential. In many cases, due to the existence of higher-order attractive terms in the multipole expansion, the asymptotic curve $-C_3/R^3$ crosses the $V(R)$ curve. Therefore the value of $C_3^{\rm env}$ should be chosen much larger than the actual C_3 value. For example, as illustrated in Fig. 4, the asymptotic behavior of Na_2 $^3\Pi_u(3s+3p)$ is $-6.48/R^3$,[26] but only the enveloping curve with $C_3^{\rm env}=18.0$ lies under $V(R)$ for all internuclear distances. In the latter case, the use of an enveloping analytical potential in Eq. (2.13) results in a number of grid points four times larger than when the real potential is used in Eq. (2.11). This drawback is particularly important for cases corresponding to small values of R_0, the divergence of C_3/R^3 near the origin resulting in a significant increase of the number of grid points N. Moreover, increasing the phase space of the problem when using small grid steps near the origin may lead to spurious eigenvalues in the numerical diagonalization procedure. It also increases significantly the spectral range of the Hamiltonian operator. This will hinder the use of direct propagation methods.

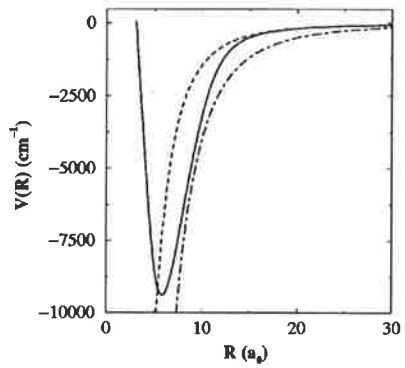

FIG. 4. A comparison of the computed potential curve for $Na_2(^3\Pi_u,3s+3p)$ (Ref. 24) (full line) with the asymptotic curve $V(R)=-C_3/R^3$, $C_3=6.48$ a.u. (dashed line), and the enveloping curve $V(R)=-C_3^{\rm env}/R^3$, $C_3^{\rm env}=18$ a.u. (dash–dotted line).

It seems therefore more convenient to use the real potential in Eq. (2.11). The mapping transformation is calculated for any potential, irrespective of its asymptotic behavior. The integral in Eq. (2.11) and all derivatives of $g(R)$ are then obtained through purely numerical procedures.

E. Occupation of the phase space domain after coordinate transformation

As discussed by Fattal *et al.*[11] and by Kosloff,[10] mapping procedures are capable of optimizing the use of the phase space volume of the representation. As a first approximation, the phase space domain necessary to describe the system can be estimated by considering the classical trajectory corresponding to the highest vibrational level that we want to compute. This is illustrated in Fig. 5, where we have drawn the phase domain in distance R and momentum p spanned by a classical trajectory corresponding to a vibrational motion with binding energy 1.3×10^{-7}, i.e., $E_v=-0.295\,{\rm cm}^{-1}$, in the potential $Cs_2(1_g)$ displayed in Figs. 1 and 2. The shape differs markedly from rectangular, showing that at large distances, due to the very small value of the local momentum, only a very small part of the phase space defined by a grid with a constant grid step is occupied.

The same domain in the new variables x and P_x is presented also. In the working grid, the variable x is defined in

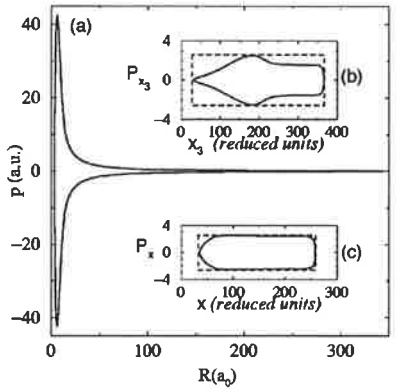

FIG. 5. Solid lines: The classical energy shell in phase space with and without the coordinate transformation, for the vibrational level with binding energy $E_v=-0.295\ \mathrm{cm}^{-1}$ in the attractive potential $Cs_2(1_g,6s+6p^2P_{3/2})$. (a) The main figure shows the energy shell in phase space without any mapping. (b) The upper inset displays the energy shell with the mapping defined by the enveloping potential $-C_3^{\mathrm{env}}/R^3$ with $C_3^{\mathrm{env}}=24.42$. (c) The lower inset displays the energy shell in phase space with the mapping using the real behavior of the potential. The area $S=1034$ a.u. defined by the contour is the same for all three cases. The number of phase cells N_c is connected with S through $S=2\pi*N_c$. Broken lines: The rectangles defining the phase space used in the calculations. One can see that without the mapping a larger phase volume is used in the calculation, that requires proportionally more grid points. The third case is most efficient in that sense.

(2.11) while the variable P_x, canonically conjugated to x in the new phase space, can be found[27] from the Poisson bracket:

$$\frac{\partial P_x}{\partial p}\frac{\partial x}{\partial R}-\frac{\partial x}{\partial p}\frac{\partial P_x}{\partial R}=1. \tag{2.36}$$

As from (2.16) $dR=J(x)dx$ and as $\partial x/\partial p=0$ then

$$P_x=pJ(x). \tag{2.37}$$

In the lower inset of Fig. 5, we display the phase space spanned by the classical trajectory in the new variables x,P_x. The area confined by the contour is the same as in previous case, $S=1034$ a.u., but the shape is now very close to a rectangle.

In the upper inset of the figure we show also the same trajectory in the x_3,P_{x_3} space—using Eq. (2.28) and generalizing Eq. (2.37) for mapping with the analytical enveloping potential $-C_3^{\mathrm{env}}/R^3$, where $C^{\mathrm{env}}=24.42$, larger than the value $C_3=16.2$ associated with the $Cs_2(1_g)$ potential. The contour now differs from a rectangular shape, especially at short x_3, where the extension of the momentum space is due to the overestimation of local kinetic energy. The efficiency of the occupation of the phase space can easily be discussed by comparing the equivalent area $S=1034$ a.u. spanned by the three contours with the area of the rectangles associated to the three grids. In the physical problem, treated with a classical picture, the number of phase cells $N_c=165$ is deduced from the area S through $S=2\pi\times N_c$. Without mapping, the rectangle associated with the physical grid has an area, defined in Eq. (2.5), such that $A\leqslant 28730\approx 2\pi\times 4573$. The numerical treatment should therefore involve at least $N=4573$ grid points. After mapping with enveloping potential, the area spanned by the grid is defined as $A_3^{\mathrm{mapp}}\leqslant 2x_{3,\max}P_{x_{3,\max}}$, so that in the chosen example we have $A_3^{\mathrm{mapp}}\leqslant 1705\approx 2\pi\times 272$, so that the minimum number of grid points is reduced to 272. Finally, when the mapping procedure based on the real potential, the area $A^{\mathrm{mapp}}\leqslant 2x_{\max}P_{x_{\max}}$ now is at least 1077, corresponding to a minimum number of grid points of 172 only, very close to the number $N_c=165$ of cells estimated from the classical phase space restricted to the same energy. The efficiency of the numerical mapping method is therefore clearly demonstrated by this figure.

One should note that this approach to the estimation of phase space confined by the problem is completely classical. It assumes that the quantum density in phase space decays exponentially fast in the classical forbidden region. The definition of the phase space in quantum mechanics was done by Hillery *et al.* in Ref. 28. Using the Wigner distribution function, the exponential decay of the quantum density outside the classical allowed region is clearly evident.[10] If tunneling is important, the phase space region involved, both in coordinate and momentum has to be included in the grid, so that a larger number of grid points should be considered. The introduction of a parameter β, as defined in Eq. (2.14), in order to reduce the step in the working grid is then justified, and this parameter needs to be optimized in the calculations. We describe some examples below.

III. APPLICATION TO THE CALCULATION OF BOUND VIBRATIONAL LEVELS FOR A SINGLE LONG-RANGE POTENTIAL: EXAMPLES FOR Na_2 AND Cs_2

The efficiency and accuracy of the mapped FGH method described above can be checked by comparison with a standard method, such as the well-known Numerov Cooley algorithm,[29] as well as with the usual FGH method.

As discussed in the Introduction, we have chosen two potentials relevant to implementation of spectroscopy experiments, and corresponding to Hund's case *a* representation for Na_2 and Hund's case *c* for Cs_2. We have performed accuracy tests computing the energies of the first 80 vibrational levels in the potential $Na_2\ ^1\Pi_g(3s+3p\ ^2P)$[24] already displayed in Fig. 1 extended at long range by the asymptotic $-6.48/R^3$ curve predicted in Ref. 26. We chose a grid extending from $5.0a_0$ to $90a_0$, and we display in Fig. 6 the results of the convergence tests. The precision of the Numerov method itself is illustrated in the upper panel, where we show that the computed vibrational energies E_v vary by less than $4\times 10^{-7}\ \mathrm{cm}^{-1}$ when the step size is modified from $\Delta R=0.00125a_0$ (68 000 points) to $\Delta R=0.0025a_0$ (34 000 points). The binding energies extend from 1103.78 to 2.44 cm^{-1}. Taking as a reference the first calculations with the Numerov algorithm, we show that a typical $10^{-5}\ \mathrm{cm}^{-1}$ accuracy can be obtained with the FGH method using a constant step and a number of points of the order of 1000.

The convergence tests for the mapped FGH method varying the β parameter are also given in the figure. The same level of accuracy can be reached with $\beta=0.2$ and $N=506$ grid points, thus reducing N by a factor of 2. We should note that the accuracy obtained with $\beta=0.6$ is already

J. Chem. Phys., Vol. 110, No. 20, 22 May 1999

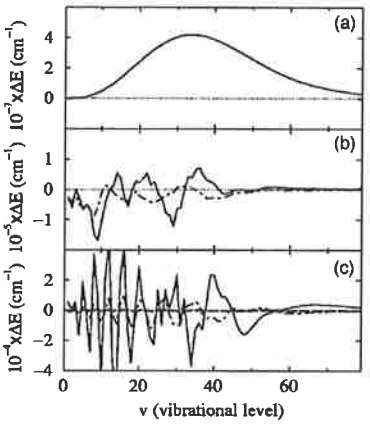

FIG. 6. Accuracy ΔE of the computed energies for the 80 lowest vibrational levels in the $^1\Pi_g(3s+3p)$ potential of Na_2 represented in Fig. 1. The vibrational number v is indicated on the horizontal axis. The uppermost level considered has 2.44 cm^{-1} binding energy. The physical grid is extending from $5a_0$ to $90a_0$. As reference values, we consider energies computed through a Numerov integration on a grid with step $\Delta R=0.00125a_0$ (68 000 points). The three figures represent (a) ΔE, from Numerov integration with $\Delta R=0.0025a_0$ (34 000 points); (b) ΔE, for energies computed by the FGH method with a uniform grid. Solid line: $N=950$ points; dash–dotted line: $N=1140$ points; (c) ΔE, for the FGH method with the mapping defined by Eq. (2.11), considering different values of the parameter β. Solid line: $\beta=0.6$, $N=170$ points; dash–dotted line: $\beta=0.4$, $N=254$ points; dashed line: $\beta=0.2$, $N=506$ points.

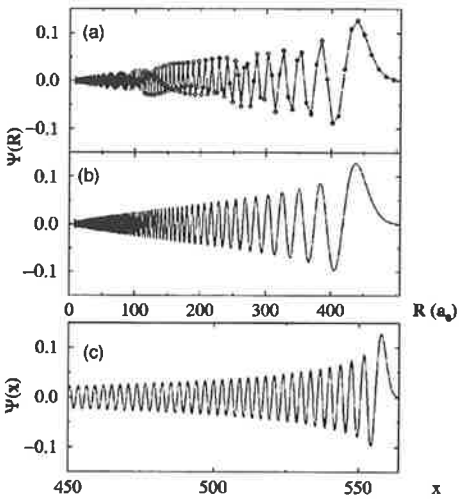

FIG. 7. The $v=332$ vibrational wave function for the $1_g(6s+6p^2P_{3/2})$ potential of Cs_2 (see Fig. 1), computed at the grid points defined with the mapping of Eq. (2.11). Here, $R_{max}=500a_0$, $N=564$. (a) The wave function at every grid point, with linear interpolation between two points; (b) the wave function interpolated according to Eq. (4.1) choosing $N_{interp}=10\,000$ (see the text). (c) The Interpolated wave function in the x variable, showing only the part corresponding to large R. Comparing (c) to (b), one can appreciate the regularity of the oscillations in the mapped wave function.

better than 10^{-3} cm^{-1}, and corresponds only to 170 grid points for the determination of 80 vibrational levels. In contrast, for $\beta=1$, only the 20 lowest levels are obtained accurately, the error on the energy of levels $v\geq 40$ reaching 0.5 cm^{-1}. Finally, we have checked that for $\beta>1$, the method is not even yielding all the eigenenergies.

The calculated error on the energy resulting from the Numerov calculation (Fig. 6) is clearly nonuniform. Indeed, changing the number of grid points modifies the local description of the potential curve, which will affect mainly energy levels with outer turning points located in the region $10a_0<R<16a_0$, where the slope of the potential is large. In contrast, the calculated error in the FGH method is uniformly distributed on all levels, due to the global character of the method.

The latter example is not intended to check the efficiency of the mapping procedure, as the vibrational motion extends only to $90a_0$. Considering now the example of the $1_g(6s+6p^2P_{3/2})$ potential of Cs_2,[25,26] we have computed the vibrational levels up to $v=337$, with a grid extending from $4.5a_0$ to $500a_0$. The number of points can be reduced from 6500, without a coordinate change, to 658 with the simple transformation defined in Eq. (2.11), using a value $\beta=0.6$ reducing the memory necessary for computation by a factor 120. For the chosen example, the highest calculated vibrational level has an energy as small as $E_{337}=-0.0317\,\text{cm}^{-1}$, the $v=0$ level staying at $E_0=-1359.6804\,\text{cm}^{-1}$. The convergence tests show a stability better than 10^{-4} cm^{-1}, when the parameter β is varied from 0.9 to 0.4. The diagonalization procedure yields N eigenvalues, for which only the lower ones correspond to bound states, the upper ones being continuum states up to a positive energy E_β^{max} that depends upon β. The efficiency of the mapping using the real potential is clearly manifested in this example: for the grid considered above, choosing $\beta=0.6$, mapping using the real potential involve 658 grid points and hence 658 eigenvalues, the upper one lying at an energy $E_\beta^{max}=12\,729\,\text{cm}^{-1}$. The same calculations with an enveloping potential $-C_3/R^3$ (where we have taken $C_3^{env}=C_3$ so that the enveloping curve differs from the real one only at short and intermediate distances), would require $N=878$ grid points. The increase in the number of points is not a substantial one, but the maximum energy is now $E_\beta^{max}=87\,790\,\text{cm}^{-1}$, so that the energy domain spanned by the method is as high as 89 000 cm^{-1}. Such a large energy range can result into a severe inconvenience for the application to time-dependent problems.

The repartition of grid points in the example has been illustrated in Fig. 3. It is remarkable that vibrational energies can be obtained with accuracy better than 10^{-4} cm^{-1} using only $N=564$ grid points (with $\beta=0.9$) for levels with a wave function exhibiting up to 337 nodes. A possible drawback of this achievement could be that N becomes too small for an accurate definition of the wave function: we show below that this is not the case.

IV. THE WAVE FUNCTION IN THE FGH METHOD

In calculations employing a discrete grid, the wave function is represented on a finite set of grid points. Values of the wave function at other distances have therefore to be determined by interpolation. Linear interpolation then yields low-

quality results (see Fig. 7). Here we describe a better approach for the interpolation of the wave function in the FGH method, using the intrinsic properties of the Fourier representation.[10]

The interpolated wave function in this case is[10]

$$\psi(q)=\sum_{j=1}^{N}\psi(q_j)\mathrm{sinc}\left(\frac{\pi}{\Delta q}(q-q_j)\right), \tag{4.1}$$

where q_j is a working uniform grid (with or without mapping), q is any intermediate point, Δq is a grid step, and we have defined the function $\mathrm{sinc}(z)=\sin(z)/z$. In Fig. 7, we display the wave function, computed with sinc interpolation at a large number ($N_{\mathrm{interp}}=10\,000$) of q values, for the 333rd ($v=332$) vibrational level of $Cs_2(1_g)$. A comparison with linear interpolation clearly illustrates the good quality of the second interpolation. Of course, we have checked the accuracy of the interpolated wave functions by comparing to standard methods.

In the same figure, we show the influence of the mapping procedure on the shape of the wave function. One can see that the two representations are quite different: the mapping has an effect of "stretching" the grid at smaller distances, where the density of points needs to be large. Indeed, if the unmapped grid has sufficient point density in this region, it has too many points at large distances, where oscillations of the wave function are not so frequent. The mapping procedure eliminates such superfluous points, yielding a uniform distribution of the number of grid points per oscillation. It is remarkable that with mapping, good quality wave functions can be obtained with a reduced number of points at each oscillation: indeed, the wave function drawn in Fig. 7 has 332 nodes and has been been obtained using only $N=564$ grid points, which is less than two points per oscillation.

V. EXAMPLE OF TWO COUPLED STATES: PERTURBATIONS IN Rb_2 SPECTRUM

The mapped Fourier Grid Hamiltonian method presented in the previous section can easily be generalized to calculate the energies of the rovibrational levels considering several coupled molecular electronic states. We have shown previously[2] that the FGH approach is particularly well suited for such a goal, compared to more traditional approaches like Numerov integration methods. We describe here below calculations considering two coupled states in a diabatic representation. The implementation of the calculation from the previous section is straightforward, provided the same mapping procedure is applied to both channels. For a grid of N points, we now consider three operators $\mathbf{T}$, $\mathbf{V(R)}$, and $\mathbf{W(R)}$, each represented by a $2N\times 2N$ square matrix as follows:

$$\mathbf{T}=\begin{pmatrix}T_1 & 0\\ 0 & T_2\end{pmatrix};\quad \mathbf{V}=\begin{pmatrix}V_1 & 0\\ 0 & V_2\end{pmatrix};\quad \mathbf{W}=\begin{pmatrix}W_1 & W_{12}\\ W_{12} & W_2\end{pmatrix}. \tag{5.1}$$

The kinetic energy matrix $\mathbf{T}$ is block diagonal, each block deduced from Eqs. (2.22) and (2.23). The potential energy matrix $\mathbf{V(R)}$ is diagonal in the FGH representation: each diagonal block V_1 and V_2 should contain the mapping of the corresponding potential energy curve. In contrast, in a diabatic representation, the coupling matrix $\mathbf{W(R)}$ contains both diagonal (W_1,W_2) and nondiagonal (W_{12} and W_{21}) blocks terms. Obviously, this procedure may be generalized to any number of coupled electronic states. The diagonalization of the full matrix provides the energies of the levels of the coupled system. The problem is to generalize the mapping procedure: this can be done by considering an enveloping potential adapted to the two different potentials and eventually to the coupling term.

As an example, we use this method for the calculation of the bound vibrational levels of the $A\,^1\Sigma_u^+(0_u^+)$ and the $b\,^3\Pi_u(0_u^+)$ excited electronic states in Rb_2, coupled by spin–orbit interaction. Both states are behaving asymptotically as R^{-3}, and are correlated to the first excited dissociation limit $5s+5p$. It is well known that, due to the spin–orbit coupling between those two states, perturbations[30] are observed in the spectra of all alkali dimer molecules: many theoretical and experimental studies have been performed for Li_2,[31–34] Na_2,[35,36] K_2,[37] Cs_2,[38] while only a single low resolution experiment has investigated this interaction in Rb_2.[39]

In the present work, the Rb_2 potential curves are taken from the accurate *ab initio* pseudopotential calculations of Foucrault *et al.*,[40] matched to the asymptotic curves of Ref. 26. The spin–orbit effective operator is assumed to be R independent and proportional to the atomic fine structure splitting ΔE_{fs}. The coupling term is then $W_{12}=\Delta E_{\mathrm{fs}}(\sqrt{2}/3)$, while the energy of the $b\,^3\Pi_u$ electronic state is corrected by $W_2=-\Delta E_{\mathrm{fs}}/3$, shifting down its dissociation limit. The mapping function is deduced from Eq. (2.13), using for the enveloping potential,

$$V^{\mathrm{env}}(R)=\mathrm{inf}[V_1(R),(V_2(R)],\quad R>\mathrm{inf}(R_{e1},R_{e2}), \tag{5.2}$$

$$V^{\mathrm{env}}(R)=\mathrm{inf}[V_1(R_{e1}),V_2(R_{e2})],\quad R<\mathrm{inf}(R_{e1},R_{e2}), \tag{5.3}$$

where R_{e1} and R_{e2} are the positions of the minima of the potential curves $V_1(R)$ and $V_2(R)$, respectively, while $\mathrm{inf}(a,b)$ means the lower of the two numbers. The potential curves are drawn in Fig. 8 in Hund's case a ($A\,^1\Sigma_u^+$ and $b\,^3\Pi_u$ states) and Hund's case c [$0_u^+(5s+5p^2P_{1/2,3/2})$] states representations. Two aspects need to be discussed in the choice of the enveloping potential in this two-channel problem: first the dissociation limit is now an important issue, as it may introduce significant local kinetic energy. Taking the Hund's case c lower potential curve as an enveloping potential would increase the local kinetic energy, all over the grid, by $2\Delta E_{\mathrm{fs}}/3=158.4.20\,\mathrm{cm}^{-1}$. The introduction of a β factor is increasing the momentum domain to address this issue. Second, in contrast with the previous discussion, we have taken the enveloping curve as constant from the position of the first grid point to the distance of the potential minimum: this introduces only a few (around 20) additional grid points, but from numerical point of view it simplifies markedly the situation in the region of small internuclear distances R, where the real potential is rapidly varying as a function of R.

J. Chem. Phys., Vol. 110, No. 20, 22 May 1999

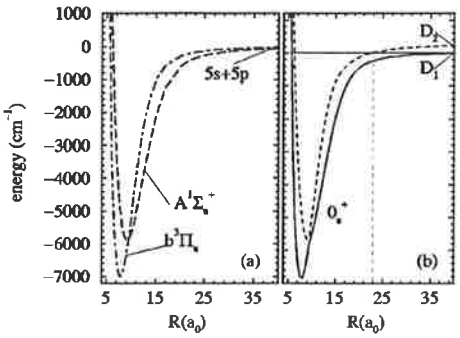

FIG. 8. The Rb_2 potential curves without (a) and with (b) spin–orbit coupling. (a) Hund's case *a* $A\,^1\Sigma_u^+(5s+5p)$ (broken line) and $b\,^3\Pi_u(5s+5p)$ (dash–dotted line) curves from Ref. 40. (b) Hund's case *c* $0_u^+(D_1)$ and $0_u^+(D_2)$ potential curves correlated, respectively, to the dissociation limits $(5s+5p^2P_{1/2})$ and $(5s+5p^2P_{3/2})$. A vibrational level close to the D_1 limit, and its turning point in the $0_u^+(D_2)$ potential, are displayed for illustration.

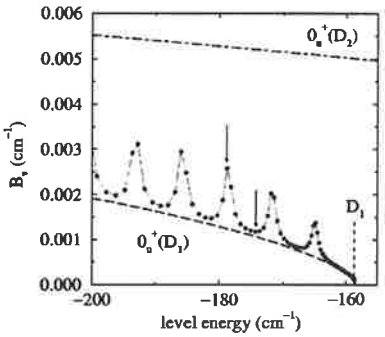

FIG. 10. The same as Fig. 9, close to the $(5s+5p^2P_{1/2})$ dissociation limit (labeled D_1 and located at energy $E=-158.4\,\mathrm{cm}^{-1}$).

Through use of the mapped FHG method, the eigenvalues of the Hamilltonian 5.1 are calculated up to the dissociation limit $(5s+5p^2P_{1/2})$, hereafter referred to as D_1 limit (indeed, our choice for an enveloping potential excludes an accurate representation of continuum levels). We have considered a grid extending from 5 to $200a_0$, and found convergence for the value $\beta=0.5$ of the mapping parameter. With such values, 525 bound vibrational levels can be found, the upper one having a binding energy $E_v(v=524)=-0.015\,\mathrm{cm}^{-1}$.

We present in Fig. 9 the rotational constants $B_v=1/(2\mu\langle R^2\rangle)$ for the vibrational levels (assuming $J=0$) computed in three different cases: for Hund's case *a* or Hund's case *c* coupling schemes, considering two independent vibrational channels and for the coupled channels. The independent channel calculations yield two curves, rather different in the case of $A\,^1\Sigma_u^+$ and $b\,^3\Pi_u$ channels, more similar and even crossing in case of the $0_u^+(5s+5p^2P_{1/2,3/2})$ channels—hereafter referred to as $0_u^+(D_1)$ and $0_u^+(D_2)$. Coupled-state calculations show that the spin-orbit coupling has a strong effect and introduces important –

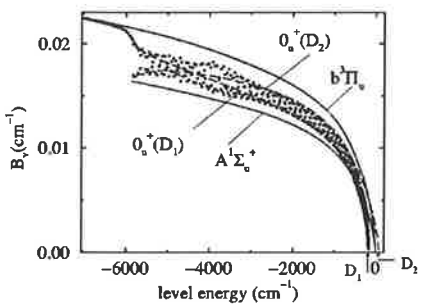

FIG. 9. Rotational constants B_v (in cm^{-1}) for vibrational levels in the Rb_2 $A\,^1\Sigma_u^+$ and $b\,^3\Pi_u$ [or, equivalently, $0_u^+(D_1)$ and $0_u^+(D_2)$] potential curves of Fig. 8 computed: neglecting fine structure coupling (Hund's case *a*: full lines); neglecting radial coupling (Hund's case *c*: dashed lines); and considering two coupled channels (circles). The energy of the levels is referred to the $(5s+5p)$ dissociation limit.

mixing between the two channels, as many B_v values are not lying on any of the four preceding curves. Besides, strong perturbations are found, manifested by oscillations in the computed constants. In contrast with lighter alkali dimers like Li_2,[31,32] Na_2,[35,36] K_2,[37] we predict that the whole spectra is concerned by these perturbations, and can be described neither in the framework of the Hund's case *a* nor Hund's case *c* independent channel representation. In a standard spectroscopy experiment, one may expect strong irregularities in the observed spectra, making a full identification very difficult.

An example of the irregularities predicted by the present calculations is analyzed in more details in Fig. 10, where we have represented the variation of the rotational constant in the vicinity of the D_1 dissociation limit. Let us note that the mapping represents a crucial improvement to obtain accurate results in this energy range. The oscillatory behavior of B_v shows that the Hund's case *c* picture is adapted only to a few levels that we may assign to the lower electronic state $0_u^+(D_1)$, most of the others being perturbed. When the B_v value is minimum, the corresponding wave function is indeed very close to unperturbed vibrational motion in the single channel $0_u^+(D_1)$, as is illustrated in Fig. 11. In contrast, the maxima of the oscillations correspond to an important admixture of a $0_u^+(D_2)$ wave function, where the vibrational motion is confined at shorter distances, with an outer turning point that in the example chosen for the figure is close to $22a_0$ instead of $50a_0$. Preliminary experimental results[41] seem to confirm this oscillatory behavior of the rotational constant.

Above the D_1 dissociation limit, the coupling between the two channels is also responsible for the predissociation of the $0_u^+(D_2)$ bound levels into a continuum of two $ns^2S_{1/2}$ and $np^2P_{1/2}$ free atoms. This process has been recently investigated as a detection tool of K_2 molecules in a photoassociation experiment[42] and could be extended to Rb_2, since the broadening of the 0_u^+ lines in Rb_2 photoassociation spectra has already been reported.[43]

In the present calculations we find that a similar effect still occurs in the continuation of the B_v curve beyond the D_1 dissociation limit, now due to the mixing between continuum wave functions describing the vibrational motion in the $0_u^+(D_1)$ state, with bound vibrational wave functions in

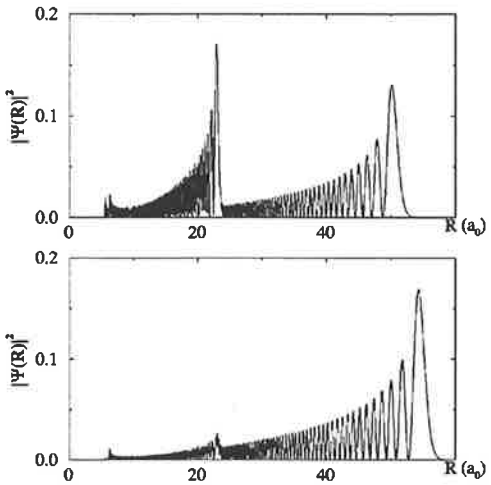

FIG. 11. Two vibrational wave functions for $Rb_2(0_u^+)$ close to the D_1 dissociation limit. The upper panel shows the wave function with vibrational number $v=445$ and energy -178.814 cm^{-1}. The middle panel—the wave function with $v=451$ and energy is -174.397 cm^{-1}. The rotational constants for those levels are indicated by arrows in Fig. 10.

the $0_u^+(D_2)$ state. The present time-independent formalism is not providing information on the predissociation lifetime of such levels. But we can solve the time-dependent Schrödinger equation defined from the Hamiltonian in Eq. (5.1) and from a given eigenfunction taken as an initial state compute the autocorrelation function, as already performed in our previous work.[22] The limited energy range of the representation then appears as an advantage for such calculations. The lifetime is most easily extracted from the exponential behavior of the autocorrelation function, and this example shows clearly the advantage of the technique. Detailed calculations of the lifetimes and analysis of the predissociation process will be published in a forthcoming paper.

VI. CONCLUSION

(i) The theoretical treatment of cold atom collisions and photoassociation processes leads us to treat the relative motion of two nuclei in regions of space where the kinetic energies differ by several orders of magnitude. Grid methods have to be modified by compressing the number of points in order to reduce the computational effort. In the present paper we describe a mapping procedure in which the change of variable closely follows the variation of the local de Broglie wavelength as a function of the internuclear distance. We have discussed the implementation of this procedure within a Fourier Grid Hamiltonian method for determination of energies and wave functions of loosely bound vibrational states in alkali dimer molecules. Reducing by n the number of points in a numerical method relying upon diagonalization procedure results into reducing by n^3 the computational effort.

(ii) In case of single channel calculations, we have discussed two possible choices for the definition of a new grid and transformation of the Hamiltonian: one is using a numerical change of variable considering the real potential of the problem; the other one is analytical and based upon the asymptotic R^{-n} behavior of the potential. The latter procedure was recently used by Tiesinga *et al.*[18] Due to the divergence of R^{-n} at short distances, the numerical mapping procedure has been demonstrated to be more efficient. It yields better optimization of the phase space, and avoids an unnecessary increase of the spectral range of the Hamiltonian.

(iii) We have discussed the convergence tests and accuracy of the method, showing that very accurate results can then be obtained for binding energies and wave functions of vibrational levels, where the classical motion extends as far as $500a_0$, with a minimal number of points, typically less than twice the number of nodes of the wave function.

(iv) The numerical mapping procedure has next been generalized to problems involving several channels, through the use of an enveloping potential. An example of an application to the perturbations in the Rb_2 spectrum has been given. We have shown that the method can easily be extended to the computation of predissociation lifetimes.

(v) In contrast with recent work by Tiesinga *et al.*,[18] the accent in the present paper was put on the mapping procedure rather than the method to extract eigenvalues. We have shown the advantage of maintaining a Hermitian Hamiltonian operator, and discussed the efficiency of a numerical mapping procedure in view of optimizing the representation. The diagonalization procedure, having uniform convergence with respect to eigenvalue extraction, could be used to check the global performance of the mapping. The quality of the wave functions obtained by interpolation using Fourier transformation is also an original aspect of this work.

(vi) In the case of two coupled channels, the method is presently formulated for diabatic calculations. Further development should consider a formulation using the d/dR coupling, where the advantage of the present mapping procedure maintaining a symmetric Hamiltonian operator will clearly be manifested.

(vii) In future work we will address the problem of propagation either for filtering the eigenvalues in a given energy range, in the spirit of Ref. 44, or for the treatment of time-dependent problems related to cold collisions and predissociation. The numerical mapping procedure developed here will help to maintain a small as possible the spectral range of the Hamiltonian.

ACKNOWLEDGMENTS

This work has been made possible through the French Israeli cooperation program Arc en Ciel 1998, which allowed V. K. and F. M-S to work two weeks in Jerusalem. O. D. thanks the Fritz Haber Research Center for hospitality. V. K. is a beneficiary of a grant (bourse de thèse) from a network (''réseau de formation recherche'') funded by the French Ministry of Education.

APPENDIX: THE KINETIC OPERATOR IN THE FGH REPRESENTATION

The Hamiltonian of Eq. (2.17), written in Fourier grid representation, is real but nonsymmetric. In order to show it, we write each term of the Hamiltonian this representation:

$$\langle\varphi_i|-\frac{1}{2\mu J^2}\frac{d^2}{dx^2}|\varphi_j\rangle=\frac{1}{J^2(x_i)}T_{i,j}. \tag{A1}$$

Here elements $T_{i,j}$ are same as in Eqs. (2.3) and (2.4). Indexes i and j are introduced nonsymmetrically because of $1/J^2(x_i)$. The term

$$\langle\varphi_i|\frac{J_x'}{2\mu J^3}\frac{d}{dx}|\varphi_j\rangle=\frac{J'(x_i)}{2\mu J(x_i)^3}\langle\varphi_i|\frac{d}{dx}|\varphi_j\rangle \tag{A2}$$

is also nonsymmetric. (Note that the first derivative in FGH is antisymmetric[19]). Being diagonal, the operator $V(x)$ is symmetric.

Consider now the Hamiltonian of Eq. (2.20). The new potential $\bar{V}$ is diagonal. To evaluate the new kinetic operator, note that for any function $F(x)$ the second derivative in FGH will be

$$F''(x_n)=\left(\frac{d^2}{dx^2}F\right)_n=-\frac{4\pi^2}{NL^2}\sum_{k=-N/2+1}^{N/2}\sum_{s=1}^{N}F(x_s)k^2\exp\left(i\frac{2\pi(n-s)k}{N}\right), \tag{A3}$$

and for $F(x)\varphi_l(x)$ function,

$$\left(\frac{d^2}{dx^2}F(x)|\varphi_l\rangle\right)_n=\left(\frac{d^2}{dx^2}F(x)\varphi_l(x)\right)_n=-\frac{4\pi^2}{NL^2}\sum_{k=-N/2+1}^{N/2}\sum_{s=1}^{N}F(x_s)k^2\times\exp\left(i\frac{2\pi(n-s)k}{N}\right)\varphi_l(x_s). \tag{A4}$$

For the scalar product $\langle|\,|\rangle$:

$$\langle\varphi_m|\frac{d^2}{dx^2}F(x)|\varphi_l\rangle=-\sum_{k=-N/2+1}^{N/2}\sum_{s,n=1}^{N}\frac{4\pi^2}{NL^2}F(x_s)k^2\times\exp\left(i\frac{2\pi(n-s)k}{N}\right)\varphi_m(x_n)\varphi_l(x_s)=-\frac{4\pi^2}{NL^2}F(x_l)\sum_{k=-N/2+1}^{N/2}k^2\exp\left(i\frac{2\pi(m-l)k}{N}\right). \tag{A5}$$

The kinetic operator in the equation is

$$\langle\varphi_m|-\frac{1}{4\mu}\left(\frac{1}{J^2}\frac{d^2}{dx^2}+\frac{d^2}{dx^2}\frac{1}{J^2}\right)|\varphi_l\rangle=\frac{\pi^2}{\mu NL^2}\left(\frac{1}{J^2(x_m)}+\frac{1}{J^2(x_l)}\right)\sum_{k=-N/2+1}^{N/2}k^2\times\exp\left(i\frac{2\pi(m-l)k}{N}\right). \tag{A6}$$

The sum here is[19]

$$\sum_{k=-N/2+1}^{N/2}k^2\exp\left(i\frac{2\pi(m-l)k}{N}\right)=\frac{N(-1)^{l-m}}{2\sin^2[\pi(m-l)/N]},\quad m\neq l; \tag{A7}$$

$$\sum_{k=-N/2+1}^{N/2}k^2\exp\left(i\frac{2\pi(m-l)k}{N}\right)=N\frac{N^2+2}{12},\quad m=l. \tag{A8}$$

From Eqs. (A6)–(A8), we obtain the expressions (2.22) and (2.23) for the kinetic energy operator (2.20). Expressions (2.22) and (2.23) are symmetrical over i and j.

[1] P. S. Julienne and J. Vigué, Phys. Rev. A **44**, 4464 (1991).
[2] O. Dulieu, P. S. Julienne, and J. Weiner, Phys. Rev. A **49**, 607 (1994).
[3] A. Fioretti, J. H. Muller, P. Verkerk, M. Allegrini, E. Arimondo, and P. S. Julienne, Phys. Rev. A **55**, R3999 (1997).
[4] H. Wang, P. L. Gould, and W. C. Stwalley, Phys. Rev. Lett. **80**, 476 (1998).
[5] H. R. Thorsheim, J. Weiner, and P. S. Julienne, Phys. Rev. Lett. **58**, 2420 (1987).
[6] P. D. Lett, K. Helmerson, W. D. Phillips, L. P. Ratliff, S. L. Rolston, and M. E. Wagshul, Phys. Rev. Lett. **71**, 2200 (1993).
[7] R. A. Cline, J. D. Miller, and D. J. Heinzen, Phys. Rev. Lett. **71**, 2204 (1993).
[8] A. Fioretti, D. Comparat, A. Crubellier, O. Dulieu, F. Masnou-Seeuws, and P. Pillet, Phys. Rev. Lett. **80**, 4402 (1998).
[9] R. Kosloff, J. Phys. Chem. **92**, 2087 (1988).
[10] R. Kosloff, in *Dynamics of Molecules and Chemical Reactions*, edited by R. E. Wyatt and J. Z. H. Zhang (Marcel Dekker, New York, 1996).
[11] E. Fattal, R. Baer, and R. Kosloff, Phys. Rev. E **53**, 1217 (1996).
[12] L. D. Landau and E. M. Lifshitz, *Quantum Mechanics: Non-Relativistic Theory* (Pergamon, Oxford, 1965).
[13] T. F. O'Malley, L. Spruch and L. Rosenberg, J. Math. Phys. **2**, 491 (1961).
[14] G. F. Gribakin and V. V. Flambaum, Phys. Rev. A **48**, 546 (1993).
[15] A. Bayliss and E. Turkel, J. Comput. Phys. **101**, 349 (1992).
[16] F. Gygi, Europhys. Lett. **19**, 617 (1992).
[17] J. M. Pérez-Jordá, Phys. Rev. B **58**, 1230 (1998).
[18] E. Tiesinga, C. J. Williams, and P. S. Julienne, Phys. Rev. A **57**, 4257 (1998).
[19] I. Tuvi and Y. B. Band, J. Chem. Phys. **107**, 9079 (1997).
[20] D. T. Colbert and W. H. Miller, J. Chem. Phys. **96**, 1982 (1992); C. C. Martson and G. G. Ballint-Kurti, J. Chem Phys. **91**, 3571 (1989).
[21] M. Monnerville and J. M. Robbe, J. Chem. Phys. **101**, 7580 (1994).
[22] O. Dulieu and P. S. Julienne, J. Chem. Phys. **103**, 60 (1995); O. Dulieu, R. Kosloff, F. Masnou-Seeuws, and G. Pichler, J. Chem. Phys. **107**, 10633 (1997).
[23] R. Meyer, J. Chem. Phys. **52**, 2053 (1970).
[24] S. Magnier, Ph. Millié, O. Dulieu, and F. Masnou-Seeuws, J. Chem. Phys. **98**, 7113 (1993).
[25] W. Meyer (private communication); N. Spiess, Ph.D. thesis, Fachbereich Chemie, Universität Kaiserslautern, 1989
[26] M. Marinescu and A. Dalgarno, Phys. Rev. A **52**, 311 (1995).
[27] L. D. Landau and E. M. Lifshitz *Mechanics* (Pergamon, Oxford, 1965).
[28] M. Hillery, R. F. O'Connell, M. O. Scully, and E. P. Wigner, *Physics Reports* (North-Holland, Amsterdam, 1984), **106**(3), pp. 121–167.
[29] J. M. Blatt, J. Comput. Phys. **1**, 382 (1967).
[30] H. Lefebvre-Brion and R. W. Field, *Perturbations in the Spectra of Diatomic Molecules* (Academic, New York, 1986).
[31] H. Schmidt-Mink, W. Müller, and W. Meyer, Chem. Phys. Lett. **121**, 49 (1985).
[32] W. Preuss and G. Baumgartner, Z. Phys. A **320**, 125 (1985).
[33] S. F. Rice, X. Xie, and R. W. Field, Chem. Phys. **104**, 161 (1986).
[34] I. Schmidt, W. Meyer, B. Krüger, and F. Engelke, Chem. Phys. Lett. **143**, 353 (1988).
[35] C. Effantin, O. Babaky, K. Hussein, J. D'Incan, and R. F. Barrow, J. Phys. B **18**, 4077 (1985).
[36] H. Kato, M. Otani, and M. Baba, Chem. Phys. **89**, 653 (1988).
[37] G. Jong, L. Li, T. J. Whang, W. C. Stwalley, J. A. Loxon, M. Li, and A.

M. Lyyra, J. Mol. Spectrosc. **155**, 115 (1992).
[38] J. Vergès and C. Amiot, J. Mol. Spectrosc. **126**, 393 (1987).
[39] R. P. Benedict, D. L. Drummond, and L. A. Schlie, J. Chem. Phys. **66**, 4600 (1977).
[40] M. Foucrault, Ph. Millié, and J. P. Daudey, J. Chem. Phys. **96**, 1257 (1992).
[41] C. Amiot (private communication).
[42] H. Wang, P. L. Gould, and W. C. Stwalley, Phys. Rev. Lett. **80**, 476 (1998).
[43] R. A. Cline, J. D. Miller, and D. J. Heinzen, Phys. Rev. Lett. **73**, 632 (1994).
[44] M. R. Wall and D. Neuhauser, J. Chem. Phys. **102**, 8011 (1995).

Appendix D

Article: *"Theoretical treatment of channel mixing in excited Rb_2 and Cs_2 ultra-cold molecules. I Perturbations in (0_u^+) photoassociation and fluorescence spectra"*, **Submitted to Phys Rev. A**

Theoretical treatment of channel mixing in excited Rb_2 and Cs_2 ultra-cold molecules. I Perturbations in (0_u^+) photoassociation and fluorescence spectra

V. Kokoouline [1,2], O. Dulieu [1], and F. Masnou-Seeuws [1]
[1] *Laboratoire Aimé Cotton,*
Bât. 505, Campus d'Orsay, 91405 Orsay Cedex, France
[2] *The Institute of Physics, Saint-Petersburg State University,*
Saint-Petersburg 198904, Russia.
(November 23, 1999)

The mapped Fourier grid method, using coordinate adapted to the local de Broglie wavelength associated to the vibrational motion in a molecule, and recently developed by Kokoouline *et al.* [J. Chem. Phys. **110**, 9865(1999)] is used to compute the perturbed binding energies and rotational constants of the Cs_2 0_u^+ $(6s+6p\ ^2P_{1/2,3/2})$ photoassociation spectrum below the lower dissociation limit. The results are shown to be very sensitive to the molecular potential curves and spin-orbit coupling. In the case of Rb_2 0_u^+ $(5s+5p\ ^2P_{1/2,3/2})$, a strong isotopic effect is also predicted. The results can be interpreted in the framework of generalized two-channel quantum defect theory, and generalized Lu-Fano plots are presented. This work suggests that parameters could easily be fitted to experimental spectra, eliminating the difficulties caused by limitations in the accuracy of the short range molecular potentials.

I. INTRODUCTION

An important application of laser cooling techniques for atomic samples is photoassociation spectroscopy [1,2], where two colliding cold alkali atoms absorb a photon red-detuned from the resonance line (or another atomic transition) to create a long range cold molecule in an excited electronic state. The latter rapidly decays by spontaneous emission, yielding usually a pair of free atoms, or in some cases a bound cold molecule in the singlet and triplet ground electronic state [3–5]. The branching ratio between the two kinds of final products is mainly determined by the behavior of the vibrational wave function in the excited state at short and intermediate internuclear distances. As a consequence, in the rapidly growing field of formation of ultra-cold molecules, spectroscopic knowledge appears as a key factor for development of efficient schemes using photoassociation [6–8]. Many accurate experimental data are becoming available, and the challenge for theoretical interpretation is the precise description of both large-amplitude vibrational motion, and coupling between bound and continuum states (Feshbach resonances) in the present situation where the potentials are known accurately only in the asymptotic region of internuclear distances.

In a recent paper [9], hereafter referred to as paper I, we have developed a mapped Fourier grid method for long range molecules and discussed its efficiency in computing vibrational wave functions relevant to the interpretation of photoassociation experiments or cold atomic collisions. As an example of an application to the problem of two-coupled channel, the perturbations in the Rb_2 $0_u^+(\ 5s+5p^2P_{1/2,3/2})$ spectra were considered. Indeed, the symmetry 0_u^+ of alkali dimers is a textbook example of perturbations in molecular spectra (see, for instance, the book of Lefebvre-Brion and Field [10]) due to spin-orbit coupling between the two Hund's case *a* potential curves $A^1\Sigma_u^+$ and $b^3\Pi_u$. In the past few years, various experiments [11–14] have been studying photoassociation of two cold alkali atoms, initially in the ground *ns* electronic state, into a long range dimer molecule of 0_u^+ symmetry. We choose the latter notation as, due to the large value of the spin-orbit coupling for heavy alkali atoms like Rb and Cs, Hund's case *c* is a better adapted representation. Nevertheless, coupling cannot be neglected between the two excited electronic states dissociating into $ns+np\ ^2P_{1/2}$ and $ns+np\ ^2P_{3/2}$, with $n=5,6$ for Rb_2 and Cs_2 respectively. (The two asymptotes will be hereafter referred to as $P_{1/2}$ and $P_{3/2}$). In the experimental data, the importance of such coupling is manifested by strong perturbations in the discrete spectrum recorded either by photoassociation spectroscopy below the $P_{1/2}$ limit [12,15], or by Fourier transform spectroscopy [16]. Another signature is the predissociation broadening of the lines observed in photoassociation spectroscopy [11,13] between the two $P_{1/2}$ and $P_{3/2}$ dissociation limits.

The aim of the present paper is to report for theoretical calculations of the energies, wave functions and rotational constants for vibrational levels in 0_u^+ Cs_2 and Rb_2photoassociation spectra, in order to interpret experiments and to assess the influence of various physical data (potential energy curves, spin-orbit coupling, mass of the nuclei, detuning of the excitation laser) on the resulting perturbations. We shall discuss the possibility of using an asymptotic theory that eliminates the uncertainty in the computed short-range potentials and couplings by defining a few parameters, valid on a broad energy range, that can be fitted to experimental data. In this work, effects linked to rotation or hyperfine structure splitting will be neglected.

The paper is organized as follows : the choice for potential curves and couplings as well as the computing

method is described in Sec.II . Next, Sec.III is devoted to the presentation of results for perturbations in the 0_u^+ spectra of Cs_2 and Rb_2 and their sensitivity to the physical data. Interpretation in terms of generalized two-channel quantum defect theory is proposed in Sec.IV. Atomic units will be used throughout the paper, the distances being in a_0 unit ($1a_0 = 5.29177 \cdot \times 10^{-11} m$).

II. CALCULATION OF THE ENERGIES AND WAVE FUNCTIONS FOR THE EXCITED VIBRATIONAL LEVELS OF Cs_2 AND Rb_2 0_u^+ $(ns + np)$ POTENTIAL CURVES.

A. Potentials and coupling

The ro-vibrational structure in the 0_u^+ $(ns + np\ ^2P_{1/2,3/2})$ spectra, as well as the perturbation and predissociation effects, depend upon the shape of the two electronic potential curves and upon the coupling between them. In the calculations we use potential curves from accurate quantum chemistry calculations [17,18], matched at large internuclear distances to asymptotic calculations [19]. The atomic spin-orbit splitting between excited states $^2P_{1/2}$ and $^2P_{3/2}$ is $\Delta E_{SO} = 237.6\ cm^{-1}$ for Rb and ΔE_{SO}= 554.1 cm^{-1} for Cs.

In case of the Cs_2 dimer, we display in Fig. 1 the two Hund's case *a* potential curves for symmetries $A^1\Sigma_u^+$ and $b^3\Pi_u$, hereafter referred to as *diabatic* curves and labeled $V_A(R)$ and $V_B(R)$ respectively. Also displayed in the figure are the two Hund's case *c* $0_u^+(P_{1/2})$ and $0_u^+(P_{3/2})$ potential curves hereafter referred to as the *adiabatic* curves $V_1(R)$ and $V_2(R)$. Such curves have been determined by diagonalization of the 2 × 2 effective fine structure Hamiltonian, using the R-dependent molecular spin-orbit coupling $W_{12}(R)$ computed in Ref. [18] and displayed in Fig. 2. The curves $V_1(R)$ and $V_2(R)$ present an avoided crossing in the vicinity of $R \approx 11\ a_0$, with a structure markedly depending upon the value of the spin-orbit coupling in this range of distance: we shall compare, as a demonstration of the importance of molecular electronic structure data, results of calculations either using R–dependent coupling $W_{12}(R)$ or taking the constant value $W_{12}(R) = \Delta E_{SO}(\sqrt{2}/3)$ at all internuclear distances. In the latter case, the splitting between the two Cs_2 curves at the crossing point is found ΔE_{SO}=554.1 cm^{-1}, whereas in the former case it is reduced to 335 cm^{-1}. The present calculated potentials should be considered as very accurate, compared to state-of-the-art quantum chemistry calculations. The accuracy was checked by comparison with recent photoassociation experiments [20,8] and found to be a few cm^{-1} in the intermediate range of internuclear distances, where the asymptotic calculations are not yet valid. This accuracy however does not reach the $\approx 0.01\ cm^{-1}$ accuracy of the observed spectra : we shall therefore discuss the sensitivity of the results to small variations in the potential curves, shifting the position of short range repulsive walls by a distance smaller than the estimated accuracy of its position, or modifying the coupling. Calculations have been performed using for the reduced mass μ = 121135.83 a.u. In the case of Rb_2, the potential curves extracted from Ref. [17] and matched at large internuclear distances to the asymptotic curves of Ref. [19] were given in paper I . Due to the lack of data for molecular spin-orbit coupling, we shall use for the discussion a model curve displaying an R-variation similar to the computed cesium curve, where the fine-structure splitting decreases, from the atomic value at infinity to its minimum at a distance R=11 a_0, by a factor 0.61, then increases again. The ratio between the molecular spin-orbit coupling at given R and the atomic value is taken identical for the two atoms, which is a somewhat arbitrary hypothesis. In order to demonstrate the strong isotopic effect, calculations will be performed for both $^{85}Rb_2$ and $^{87}Rb_2$ isotopes, choosing for the reduced mass the values μ = 77392.38 a.u. and μ = 79212.88 a.u. respectively.

B. Calculations: The Mapped Fourier grid representation.

For the calculation of bound levels we solve the time-independent Schrödinger equation with the Fourier grid representation (FGR) method [21–24,9], where the energies and wave functions are obtained by diagonalization of a Hamiltonian operator written in grid representation, either in position or in momentum space. The potential operator is then a diagonal matrix in position space. The kinetic energy operator is diagonal in momentum space and its matrix elements in position space, obtained by Fourier transform, are given in the quoted references. In order to study loosely-bound vibrational levels relevant to photoassociation experiments, with wave functions extending up to several hundreds a_0, we make use of the procedure developed in paper I to define a working grid with a variable step $s_{env}(R)$ adjusted to the variations of the local de Broglie wavelength and defined as :

$$s_{env}(R) = \beta \frac{\pi}{\sqrt{2\mu(V_{max} - V^{env}(R))}}. \qquad (1)$$

For our two-channel problem we choose the enveloping potential $V^{env}(R)$ as the lowest of the two adiabatic curves,

$$V^{env}(R) = V_1(R) - V_1(\infty) \qquad (2)$$

In Eq. (2), $V_1(\infty)$ is the energy of the $P_{1/2}$ asymptote. Therefore in Eq. 1, the maximum value of the potential energy considered in the problem is :

$$V_{max} = V_1(\infty) + \Delta \qquad (3)$$

where we have taken $\Delta = 0$ for bound-state calculations. For predissociation calculations the quantity Δ

should be positive and at least equal to the energy difference between the highest predissociated level considered in the problem and the $P_{1/2}$ asymptote. The local grid step then follows the variation of the inverse of the maximum local classical momentum, while a scaling factor β enables to represent also correctly the non-classical part of the wave function: the present calculations were converged for $\beta = 0.7$.

The numerical method was described extensively in paper I, where details on rubidium calculations were reported. In the case of cesium, calculations were performed for all bound levels up to 0.04 cm^{-1} below the $P_{1/2}$ asymptote, for which the wave function may extend up to 1000 a_0. We were using a physical grid extending from 5 to 1000 a_0, the working grid consisting of N=853 points. The two-channel potential matrix was written in diabatic representation, including both potentials $V_A(R)$ and $V_B(R) - W_{12}(R)/\sqrt{2}$ as diagonal elements, and considering either constant or R-dependent spin-orbit coupling $W_{12}(R)$ non diagonal elements. The energy levels were then determined through diagonalization of the $2N \times 2N$ Hamiltonian matrix. From their values at the N grid points R_j, the wave functions could be interpolated with *sinc* interpolation (where $\mathrm{sinc}(z) = \sin(z)/z$) as described in paper I.

$$\Psi(R) = \sum_{j=1}^{N} \Psi(R_j)\mathrm{sinc}(\pi(R - R_j)/\Delta R)$$

However, for the numerical quadrature to compute the rotational constants $B_v = \langle 1/(2\mu R^2)\rangle$, direct use of the Fourier Grid representation was sufficient:

$$B_v = \sum_{j=1}^{N} |\Psi(R_j)|^2 \frac{1}{2\mu R_j^2} \Delta R \qquad (4)$$

III. PREDICTION OF THE ENERGY LEVELS AND ROTATIONAL CONSTANTS IN Cs_2 AND Rb_2 0_u^+ PHOTOASSOCIATION AND FLUORESCENCE SPECTRA.

A. Perturbations effects in the Cesium spectrum below the $(6s + 6p^2P_{1/2})$ dissociation limit

An example of the results for the positions and rotational constants of the energy levels in the $[-250, -1\ cm^{-1}]$ energy range below the $P_{1/2}$ limit is reported in Fig. 3. When the coupling is neglected, the $P_{1/2}$ series appears as a quasi continuum (spacing between 4 and 0.004 cm^{-1} in the binding energy range considered) with small rotational constants, while the vibrational levels from $v = 163$ to $v = 182$ attributed to the $P_{3/2}$ series are more widely ($\approx$ 13 cm^{-1}) spaced with larger rotational constants. The effect of the coupling results mainly in a shift of the $P_{3/2}$ levels, with strong perturbations in three regions of the considered energy range, too distant to be interpreted as a beating phenomenon between the two vibrational frequencies. We should note that in contrast to the rubidium case discussed in paper I, the rotational constant is oscillating between the two extreme values corresponding to single-channel calculations, showing that nearly pure $P_{1/2}$ and $P_{3/2}$ wave functions still exist when the coupling is turned on. Due to the large value of the classical phase for such highly-excited levels (slightly vibrational numbers v larger than 100), the results are extremely sensitive to the accuracy of the potential: shifting the repulsive wall by only 0.01 a_0 is sufficient to modify the position of the levels and the perturbation structure, as displayed in Fig. 4. Therefore, in the present state of *ab initio* calculations, it is not realistic to hope to find agreement between theory and experiment as far as absolute values for the positions of the energy levels are concerned. We shall discuss in Sec. IV B how to develop a procedure using knowledge of the asymptotic part of the potentials only and depending upon parameters fitted to experimental data.

Finally, the results appear to be very sensitive to the choice of the spin-orbit coupling. This is illustrated in Fig. 5 where we compare for the entire spectral range the variation of rotational constants with variable spin-orbit coupling as well as with a constant spin-orbit coupling. In the latter case, except in the region close to the dissociation limit, the perturbations are weak and the rotational constants curves in Fig. 5(b) look qualitatively similar to two unperturbed Hund's case c series, as displayed in Fig. 5(a) . The validity of the latter interpretation is not surprising because of the large value of the spin-orbit splitting in the cesium atom. It is striking that when a R-dependent spin-orbit coupling is introduced, as the splitting between adiabatic curves (see the inset of Fig. 1 (c)) in the region of the avoided crossing is reduced by 40%, the behavior becomes qualitatively different. The perturbation structure, now visible in the totality of the spectral range in Fig. 5 c) is clearly manifesting the breakdown of the picture of two uncoupled Hund's case c adiabatic curves.

B. Isotopic effect in the perturbations of the rubidium spectrum

A different qualitative behavior is found in the rubidium case : the perturbations in the Rb_2 0_u^+($5s + 5p^2P_{1/2,3/2}$) spectra computed in paper I with a constant spin-orbit coupling are softened when one introduces a model R-dependence for the spin-orbit coupling (see Fig. 2), in which for a given R the ratio to the atomic value is arbitrarily the same as in the cesium *ab initio* calculations. Strong perturbations are visible (Fig. 6(b)) in the energy positions and rotational constants for vibrational levels computed with constant spin-orbit coupling. In fact, due to the smaller value of the atomic fine-structure

splitting in the rubidium case (237.6 cm^{-1} instead of 554.1 cm^{-1}), the picture of two uncoupled Hund's case c adiabatic curves is even less valid than for cesium. As a consequence, introduction of an R-dependent spin-orbit coupling results into further reduction of the coupling in the region where the two diabatic $A\ ^1\Sigma_u^+$ and $b\ ^3\Pi_u$ curves are crossing, so that the computed energies and rotational constants displayed in Fig. 6(c), although manifesting strong perturbations, do look qualitatively closer to calculations for two Hund's case a uncoupled channels. As a relatively larger decrease of the spin-orbit coupling would reduce the perturbations even further, it is clear that accurate molecular calculations are needed, or, alternatively fitting procedure to experimental data [16].

As an illustration of the importance of channel mixing, we have analyzed the vibrational wave functions, in a 6000 cm^{-1} energy range below the $P_{1/2}$ dissociation limit, obtained in two-coupled-channel calculations with constant spin-orbit coupling. In order to estimate the proportion of population on the each channel, for a given vibrational level, we write the two-channel wave function as:

$$\Phi_v = \Psi^v_{1/2}(R)|1\rangle + \Psi^v_{3/2}(R)|2\rangle \tag{5}$$

In Eq. 5, $|1\rangle$ and $|2\rangle$ correspond to the two electronic states $0_u^+(P_{1/2})$ (potential $V_1(R)$) and $0_u^+(P_{3/2})$ (potential $V_2(R)$) respectively, readily obtained as R-dependent linear combinations of the two diabatic states. Then the relative population of the $P_{3/2}$ channel is simply computed as :

$$\alpha^v_{3/2} = \int_0^\infty |\Psi^v_{3/2}(R)|^2 dR \tag{6}$$

The energy variation of $\alpha^v_{3/2}$, represented in Fig. 7, appears very irregular. Except at very large detunings where the energy lies below the bottom of the V_2(R) potential curve, the relative population $\alpha^v_{3/2}$ never becomes 0 or 1. Therefore, the wave function can never be identified as belonging purely neither to the $P_{3/2}$ nor to the $P_{1/2}$ channel, showing that all vibrational levels are perturbed in the wide (5715 cm^{-1}) energy range between the bottom of the $P_{3/2}$ well and the $P_{1/2}$ dissociation limit. Such behavior has indeed been recently observed by Fourier transform spectroscopy [16] in the [-2500, -1000 cm^{-1}] energy range below the $P_{1/2}$ limit.

Due to the large values of the phases involved for vibrational quantum numbers larger than 100, the sensitivity to potential data would be important for rubidium, but was already discussed in cesium case. A further important result is obtained in the rubidium case where a strong isotopic effect is present. We have displayed in Fig. 8 prediction of the variation of the rotational constants for $^{85}Rb_2$ and $^{87}Rb_2$ in the energy range lying 40 cm^{-1} below the $P_{1/2}$ dissociation limit. The energy behavior looks like a series of resonances, the width being significantly ($\approx$ 50%) smaller for the heavier isotope. Indeed, the curves could be interpreted as Feshbach resonances due to the coupling between a quasi-continuum $P_{1/2}$ series and a discrete $P_{3/2}$ series. Such analysis can be done by fitting the peaks in the energy variation of the relative population $\alpha^v_{3/2}$ defined in Eq.6 by a Lorentzian formula,

$$L(E) = \frac{C}{(E - E_{res})^2 + (\Gamma/2)^2} \tag{7}$$

We have displayed in Fig. 9 an example of such a fit. For $^{85}Rb_2$, we have considered a peak with a maximum located at $E_{res} = -3.87$ cm^{-1}: the fitted width is $\Gamma = 2.4cm^{-1}$, and would correspond to a lifetime $\tau \approx 2.2$ ps. For $^{87}Rb_2$ the peak is located at $E_{res} = -6.38$ cm^{-1}, and the width is reduced to 1.1 cm^{-1}, corresponding to a lifetime $\tau \approx 4.83$ ps. Such results and their possible extrapolation to the situation of a real continuum above the $P_{1/2}$ dissociation limit will be discussed in further work devoted to predissociation calculations [25]. The analogy with Feshbach resonances will be continued in the following section where we analyze our results in the framework of a generalization of the theoretical tools formerly developed for Rydberg series.

IV. LONG-RANGE ANALYSIS AND GENERALIZED TWO-CHANNEL QUANTUM DEFECTS

Due to the long-range extension of the vibrational motion for the levels considered in the present work, interpretation of the progression of the energy values as a function of vibrational numbering in terms of an asymptotic law such as the well known Le Roy-Bernstein formula [27] provides a powerful tool to analyze computed results. Besides giving greater insight into the physics of the problem, it should provide a way to bypass the difficulty linked to the inaccuracy of short range potentials at the scale of present experimental precision by suggesting parameters which could be fitted to experiment in the spirit of quantum defect theory [26].

A. Interpretation of the single-channel results from the Le Roy-Bernstein model : generalized quantum defect

We first have checked the behavior of the two computed unperturbed vibrational series $0_u^+(P_{1/2})$ and $0_u^+(P_{3/2})$, corresponding to motion in the single-channel potentials $V_1(R)$ and $V_2(R)$ respectively. Indeed, for a potential with asymptotic $-C_3/R^3$ behavior, the energy of an excited vibrational level is simply linked to the vibrational number v by the analytical formula proposed by Le Roy and Bernstein [27]:

$$E(v) = D - (H_3(v_D - v))^6 \tag{8}$$

In Eq. 8, D is the dissociation energy, H_3 is a constant and v_D is an usually non-integer number such that:

$$E(v_D) = D \tag{9}$$

In contrast with the Rydberg law for a $1/R$ potential, the energy is related to a positive power of v, so that the series is finite. We shall call v_{max} the number of the last vibrational level for a potential containing $v_{max}+1$ vibrational levels. It is then straightforward to define a generalized quantum defect μ^{LB} through:

$$\mu^{LB} = v_D - v_{max} \tag{10}$$

If we modify the short range potential, for instance by changing the depth of the well, this number changes but the law in Eq. 8 only depends upon the difference in number between the last levels. Following recent work by Crubellier *et al.* [28] on scattering length, we can change the numbering of the levels by comparing the number of nodes of a given vibrational wave function to the number of nodes of the last vibrational level, numbered $n = 0$. The next to last level will be numbered $n = 1$, and so on, so that the new numbering is related to the previous one by:

$$n + v = v_{max} \tag{11}$$

The advantage of such numbering is that the theory presented below is still valid when only a limited number of levels below the dissociation limit are computed or determined experimentally, or when the potential is modified in the short-range region.

The Le Roy-Bernstein law for the energies $E^{LB}(v)$ of the excited vibrational levels v is then simply written:

$$n^*_{LB} = n + \mu^{LB} = v_D - v = \frac{(D - E^{LB}(v))^{1/6}}{H_3} \tag{12}$$

implying that the quantity on the right hand side of Eq.12 is a linear function of v crossing the horizontal axis at $v = v_D$. We have checked over which energy range below the dissociation limit our computed vibrational energies $E(v)$, obtained from single-channel calculations for the potential $V_1(R)$ in the Rb_2 case, verify this law. For that purpose, we may extract a computed quantum defect $\eta^{LB}(E)$ for the level with quantum number $n = v_{max} - v$ from the relation:

$$n^*(E) = n + \eta^{LB}(E) = \frac{(V_1(\infty) - E(v))^{1/6}}{H_3} \tag{13}$$

Choosing the value $C_3 = 12.268$ a.u [19] for the asymptotic coefficient in the potential $V_1(R)$ yields $H_3 = 0.0015453 a.u.$ (or $H_3 = 0.012002(cm^{-1})^{1/6}$) for the $^{85}Rb_2$ isotope. We have represented in Fig. 10 the variation of the quantity $n^* = n + \eta^{LB}(E) = v_D - v$ as a function of the vibrational number v, demonstrating a quasi-linear variation for $v > 180$ up to our last computed level $v = 376$, strictly linear for $v > 250$. The extrapolated curve cuts the horizontal axis at $v_D = 412.9 \pm 0.1$, yielding v_{max}=412, and the relation $n = 412 - v$. The quantum defect $\eta^{LB}(E)$ is then computed from Eqs. 11, 10, 13 and is found slowly varying as a function of E (or n) from its limit $\mu^{LB} = 0.9$ at $E = V_1(\infty)$. From the energy variation of $\eta^{LB}(E)$, Fig. 11, it is clear that except at energies close to the dissociation limit $[(V_1(\infty) - E(v) < 1\ \mathrm{cm}^{-1}]$, the computed quantum defect is not a constant, showing that the Le Roy Bernstein law is not verified. This result is not surprising as:

- The adiabatic curve $V_1(R)$ is obtained through diagonalization of the effective fine structure Hamiltonian between the two diabatic electronic states with potential curves $V_A(R)$ and $V_B(R)$. The latter have very different asymptotic behaviors, the C_3 coefficients determined in Ref. [19] being 18.404 and 9.202 respectively. Due to the R-dependence of the mixture between the two states, the C_3 coefficient for 0_u^+ states departs from its asymptotic value 12.268 at distances smaller than $150 a_0$.

- Furthermore, for binding energies larger than 1 cm^{-1}, corresponding to an outer classical turning point for the vibrational motion located at internuclear distances smaller than 150 a_0, the C_6 terms can no longer be neglected in the expansion.

We therefore have considered another possibility for interpretation in terms of generalized quantum defects through a numerical law , obtained from our computed values $E(v)$. As previously, we first determine the vibrational numbers v_D and v_{max} from the linear variation of the quantity $(V_1(\infty) - E(v))^{1/6}/H_3$ close to the dissociation limit. This defines a quantum defect:

$$\eta = v_D - v_{max} \tag{14}$$

η is equal to the asymptotic value $\eta^{LB}(E = (V_1(\infty))$ of the quantum defect relative to the Le Roy-Bernstein law defined in Eq. 13. The numerical law for the energy variation of the effective quantum numbers $n^* = v_D - v$ is then simply:

$$n + \eta = n^* = f((V_1(\infty) - E(v)) \tag{15}$$

In Eq. 15 η is now constant on the whole energy range. In such an interpretation, the isotopic dependence for the rubidium dimer can be understood easily. Indeed, an increase of 2.4 % in the mass results into a modification of 1.2 % in the phase which is proportional to $\sqrt{\mu}$:for vibrational levels $v \approx 400$, where the semi-classical phase is of the order of 400π, this results into a change of $4.8\ \pi$ in the phase, which means a strong modification (0.8) in the single channel quantum defect. We shall see below how the coupling is also modifying the quantum defect.

B. Generalized Lu-Fano plots for two-coupled channel calculations

These results suggest another way of visualizing and possibly determining the coupling between two channels, in the spirit of early work on quantum defect theory [29–31]. We first determine the energies E_{v_1} and E_{v_2} for the vibrational levels of the two unperturbed series v_1 and v_2 corresponding to single channel vibrational motion in the adiabatic potentials $V_1(R)$ and $V_2(R)$ respectively, with different dissociation limits $V_1(\infty)$ and $V_2(\infty)$. Using the different asymptotic coefficients $C_3^1 = 12.268$ and $C_3^2 = 15.334$, we may analyze the results as previously to determine the quantum defects η_1 and η_2 from Eq. 14 and the effective (non-integer) quantum numbers $n_1^* = v_{D_1} - v_1$ and $n_2^* = v_{D_2} - v_2$. It is then straightforward, from the variation of the binding energies of the vibrational levels in the two series, to define the two numerical laws for the two effective quantum numbers $n_1^* = f_1(V_1(\infty) - E_{v1})$ and $n_2^* = f_2(V_2(\infty) - E_{v2})$ of Eq. 15.

Considering now the results of the coupled equations, we obtain a series of levels v, with computed energies E_v that we analyze with respect to both $P_{1/2}$ and $P_{3/2}$ unperturbed series. Rather than the numbering v, it is more convenient to use the two previous numerical laws to define, for each level, two effective quantum numbers :

$$\nu_1^*(E_v) = f_1(V_1(\infty) - E_v) \tag{16}$$

and

$$\nu_2^*(E_v) = f_2(V_2(\infty) - E_v) \tag{17}$$

By comparing the energy E_v to the energies of the non-perturbed series, we find the two closest larger energies E_{v1} and E_{v2}. From the effective quantum numbers $n_1^*(E_{v1})$ and $n_2^*(E_{v2})$, we define two additional quantum defects $\tilde{\mu}_1(E_v)$ and $\tilde{\mu}_2(E_v)$.

$$\tilde{\mu}_1(E_v) = \nu_1^* - n_1^*(E_{v1}) \tag{18}$$

and

$$\tilde{\mu}_2(E_v) = \nu_2^* - n_2^*(E_{v2}) \tag{19}$$

These quantum defects are simply interpreted as level shifts due to the coupling between the two channels. Each level is now analyzed with two references, and when comparing for instance to the $P_{3/2}$ series, we find several levels with the same principal quantum number and different quantum defects. In order to visualize perturbations in a more intuitive way, we can represent them on a Lu-Fano plot, where the horizontal axis displays the vibrational number $v_2 = v_{D2} - n_2^*$, to make the link with the unperturbed $P_{3/2}$ series, while the vertical axis corresponds to the additional quantum defect $\tilde{\mu}_1$ on channel 1. When the quantum defect reaches the value 1, a new level is introduced in the series, and this is visualized by a jump in the curve back to the value 0.

Such a plot for Cs_2 is reproduced in Fig. 12. For calculations using constant spin-orbit coupling, most levels can be identified as belonging to a $P_{1/2}$ series, with a constant quantum defect 0.05 corresponding to a shift of the levels, while a few $P_{3/2}$ levels have energies differing very little from the unperturbed ones. A positive quantum defect results into an increase of the binding energies of the levels. When the variable spin-orbit coupling is introduced, the perturbations are stronger, and it is more difficult to identify two series. This picture is presently being used to analyze photoassociation spectra observed in a cold cesium sample [32].

The Lu-Fano plots for the two isotopes of the rubidium dimer are displayed in Fig. 13. In the spirit of two-channel quantum defect theory [26], it should be possible, for any set of coupled potentials with asymptotic behavior similar to $V_1(R)$, and $V_2(R)$ to fit the curves in order to extract from such graphs an estimation of the coupling from the equation :

$$tan[\pi(-n_1^* + \mu_1)] = \frac{R_{1,2}^2}{tan[\pi(-n_2^* + \mu_2)]} \tag{20}$$

In the present work, we have simply looked whether an empirical fit of our two channel results $E(v)$, computed with one particular set of potentials $V_1(R)$ and $V_2(R)$, could yield a set of effective parameters. Such a fit can indeed be found in a wide energy range (down to 1000 cm^{-1} below the $P_{1/2}$ dissociation limit), spanning ≈ 70 vibrational levels of the $P_{3/2}$ unperturbed series (for single channel motion in the $V_2(R)$ potential). The curves were fitted within 1% accuracy with the following parameters:

- For $^{85}Rb_2$

$$\mu_1 = 0.82,\ \mu_2 = 0.185,\ R_{1,2} = 0.74 \tag{21}$$

- For $^{87}Rb_2$

$$\mu_1 = 0.37,\ \mu_2 = 0.64,\ R_{1,2} = 0.47 \tag{22}$$

This result shows again the very strong isotopic effect in rubidium. It demonstrates that the computed results can be fitted in terms of a few parameters, which could possibly be applied to analysis of experiments. Further work will show how accurate experimental results obtained in a limited spectral range can be extrapolated outside this spectral range. Furthermore, close to the dissociation limit, analysis of the pseudo-resonances observed in experiment will yield parameters that can be extrapolated above the dissociation limit to determine the predissociation lifetimes. This aspect will be discussed in a forthcoming paper [25].

V. CONCLUSION AND PERSPECTIVES

As an application of the mapped Fourier grid method, developed in paper I, we have presented and analyzed results of two-coupled-channel calculations for the binding energies, wave functions, and rotational constants of the vibrational levels in the 0_u^+ spectra, below the $(ns + np^2P_{1/2})$ dissociation limit of Cs_2 ($n = 6$) and Rb_2 ($n = 5$) diatomic molecules. For heavy dimers, although there exists a strong spin-orbit coupling between two Hund's case a potential curves, yet the picture of two Hund's case$c$ uncoupled adiabatic channels is never valid and perturbations are present extending over all the spectral range (i.e. 5200 cm^{-1} in the case of Cs_2 and 5700 cm^{-1} in the case of Rb_2). This channel mixing is manifested through the irregularities of the rotational constants which keep oscillating between a small value corresponding to $0_u^+(^2P_{1/2})$ unperturbed series and a larger one corresponding to $0_u^+(^2P_{3/2})$ series. These oscillations have already been observed by Fourier transform spectroscopy [16]. The effect of the coupling can also be estimated by analyzing the energy variation of the proportion of the $P_{3/2}$ component in the two-channel wave function, which oscillates between 0 and 1. In the Cs_2 case most values stay close either to 0 or to 1, while for Rb_2 intermediate values are obtained for all levels, the amplitude of the oscillations being smaller so that the maxima and minima still correspond to strong channel mixing. The results are very sensitive to the shape of the potential energy curves and to the R-dependence of the spin-orbit coupling. An important result is the strong isotopic effect found in Rb_2, which allows to predict a marked difference in the predissociation lifetimes.

Indeed, close to the $P_{1/2}$ dissociation limit, the splitting between vibrational levels decreases below 0.1 cm^{-1} and the perturbations can be analyzed as a $P_{3/2}$ vibrational series perturbed by a quasi-continuum $P_{1/2}$ series. The pseudo-resonances give indications about the order of magnitude of the predissociation lifetime and its strong dependence on potential parameters or isotopic mass.

All the results can be interpreted in the framework of a two-channel generalized quantum defect theory, where due to the large value of the phase the quantum defect is shown to be very sensitive to the short range part of the potential. As a simple analytical Le Roy-Bernstein law cannot be used to fit the single-channel results, we have proposed a numerical law to define a generalized quantum defect. The advantage of our derivation is that it can be applied to any combination of long range potentials and that it is no longer necessary to know all the vibrational levels from $v = 0$, a numbering from the dissociation limit being sufficient. We presented an adaptation of Lu Fano plots to show the perturbations in a graph that can be related to quantum defect theory. An important result is that the curves on such graphs can indeed be fitted, on a wide (1000 cm^{-1}) energy range, by 3 parameters equivalent to two generalized quantum defects and one coupling parameter. This method could be used to bypass the difficulties arising from the present limitations in accuracy of short range potentials by defining parameters that can be directly fitted to experiments. Use of such parameters to predict predissociation lifetimes above the $P_{1/2}$ dissociation limit and possibly fine structure transition cross sections above the $P_{3/2}$ dissociation limit will be the subject of forthcoming papers. The explanation of the strong isotopic effect in the measured trap loss [33] in a rubidium magneto-optical trap could be linked to the isotopic effect predicted in the present paper for the perturbations in the photoassociation spectra. Indeed, dynamical coupling between the two $0_u^+(ns + np^2P_{1/2,3/2})$ adiabatic curves has been predicted as the main mechanism for fine structure transitions in collisions between ground state ns and excited $np^2P_{1/2,3/2}$ heavy alkali atoms [34,35] .

VI. ACKNOWLEDGMENTS

Stimulating discussions with our colleagues Claude Amiot, Claude Dion, Ronnie Kosloff, Eliane Luc and Carl Williams are gratefully acknowledged. V. Kokoouline thanks the French Embassy in Russia, Laboratoire Aimé Cotton and the " Societé de Secours des Amis des Sciences" for financial support.

[1] H. R. Thorsheim, J. Weiner, and P. S. Julienne, Phys. Rev. Lett. **58**, 2420 (1987).
[2] P. D. Lett, K. Helmerson, W. D. Philips, L. P. Ratliff, S. L. Rolston, and M. E. Wagshul, Phys. Rev. Lett. **71**, 2200 (1993).
[3] A. Fioretti, D. Comparat, A. Crubellier, O. Dulieu, F. Masnou-Seeuws, and P. Pillet, Phys. Rev. Lett. **80**, 44202 (1998).
[4] T. Takekoshi, B. M. Patterson, and R. J. Knize, Phys. Rev. A **59**, R5 (1999).
[5] N. Nikolov, E. E. Eyler, X. Wang, H. Wang, W. C. Stwalley, and P. L. Gould, Phys. Rev. Lett. **82**, 703 (1999).
[6] Y. B. Band and P. S. Julienne, Phys. Rev. A **51**, R4317 (1995).
[7] J. T. Bahns, W. C. Stwalley, and P. L. Gould, to appear in Adv. At. Mol. Opt. Phys. (1999).
[8] M. Vatasescu, O. Dulieu, C. Amiot, D. Comparat, C.Drag, V. Kokoouline, F. Masnou-Seeuws, and P. Pillet, Phys. Rev. A , *submitted.*
[9] V. Kokoouline, O. Dulieu, R. Kosloff, and F. Masnou-Seeuws, J. Chem. Phys. **110**, 9865 (1999).
[10] H. Lefebvre-Brion and R.W. Field ,Perturbations in the Spectra of Diatomic Molecules (Academic Press, New York, 1986).
[11] R.A. Cline, J. D. Miller, and D. J. Heinzen, Phys. Rev. Lett. **73**, 632 (1994).

[12] J.G.C. Tempelaars, R.S. Freeland, R.A. Cline, D.J. Heinzen, E. Tiesinga, C.J. Williams, and P. S. Julienne, (to be published) , *private communication.*
[13] H. Wang, P. L. Gould, and W. C. Stwalley, Phys. Rev. Lett.**80**, 476 (1998).
[14] D. Comparat, C.Drag, A. Fioretti, O. Dulieu, and P. Pillet, J. Molec. Spect. **195**, 229 (1999).
[15] P. Pillet (1999), *private communication.*
[16] C. Amiot, O.Dulieu, and J.Vergès, Phys. Rev. Lett. **83**, 2316 (1999).
[17] M. Foucrault, Ph. Millié, and J. P. Daudey, J. Chem. Phys. **96**, 1257 (1992).
[18] N. Spies, Ph.D. thesis, Fachbereich Chemie, Universität Kaiserslautern, 1989 and W. Meyer, *private communication.*
[19] M. Marinescu and A. Dalgarno, Phys. Rev. A **52**, 311 (1995).
[20] A. Fioretti, D. Comparat, C.Drag, C. Amiot, O. Dulieu, F. Masnou-Seeuws, and P. Pillet, Eur. Phys. J. D **5**, 389 (1999).
[21] R. Kosloff, J. Phys. Chem. **92**, 2087 (1988).
[22] C. C. Marston and G.G. Balint-Kurti, J. Chem. Phys. **91**, 3571 (1989) .
[23] M. Monnerville and J. M. Robbe, J. Chem. Phys. **101**, 7580 (1994).
[24] O. Dulieu and P. S. Julienne, J. Chem. Phys. **103**, 60 (1995).
[25] V. Kokoouline, O. Dulieu, R. Kosloff and F. Masnou-Seeuws, in preparation .
[26] H. Friedrich, "Theoretical atomic physics", Springer, New York, (1998).
[27] R.J. Le Roy and R.B. Bernstein, J. Chem. Phys. **52**, 3869 (1970).
[28] A. Crubellier, O. Dulieu, F. Masnou-Seeuws, M. Elbs, H. Knöckel, and E. Tiemann, Eur. Phys. J. D **6** 211, (1999).
[29] K. T. Lu and U. Fano, Phys. Rev. A **2**, 81 (1994).
[30] M. J. Seaton, Rep. Prog. Phys. **46**, 167 (1994).
[31] M. Aymar, C. H. Greene, and E. Luc-Koenig, Rev. Mod. Phys. **68**, 1015 (1996).
[32] P. Pillet, to be published.
[33] C.D. Wallace, T.P. Dinneen, K.Y.N. Tan, T.T. Grove, and P.L. Gould, Phys. Rev. Lett. **69**, 897 (1992).
[34] E.I. Dashevskaya, A.I. Voronin, and E. E. Nikitin, Can. Journ. Phys., **47**, 1237.
[35] P. S. Julienne, and J. Vigué, Phys. Rev. A **44**, 4464 (1991).

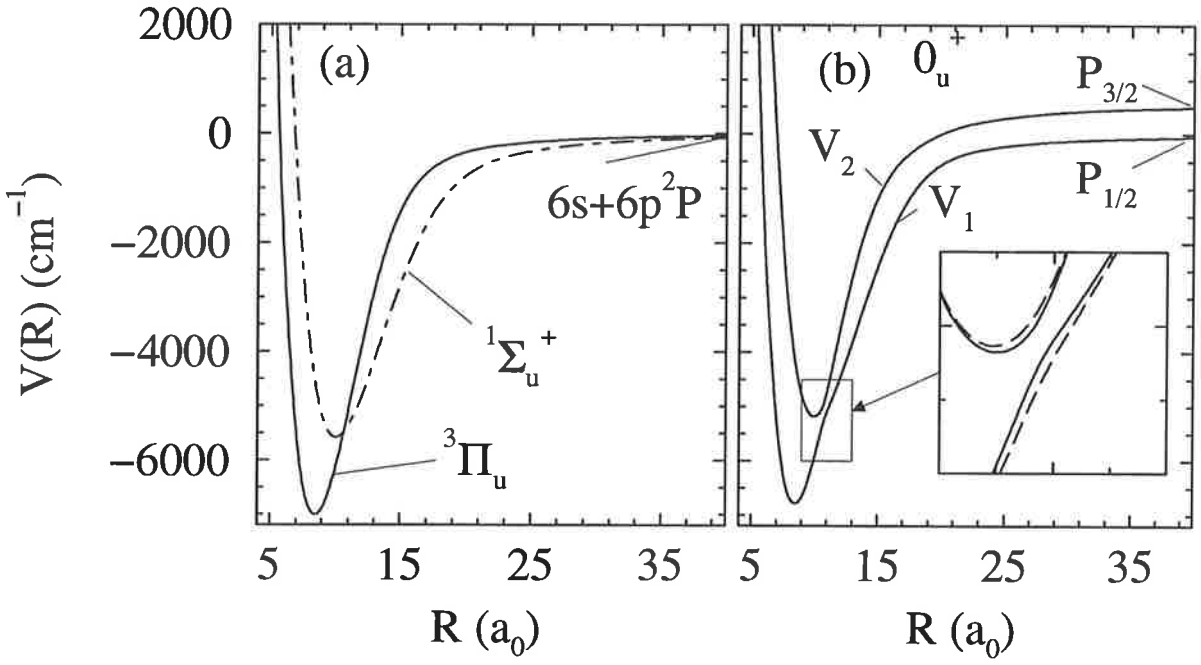

FIG. 1. Cs_2 potential curves from Ref. [18] computed without (a) and with (b) spin-orbit coupling. (a) - Hund's case *a* $A^1\Sigma_u^+$ $(6s + 6p)$ (dash-dotted line) and $b^3\Pi_u$ $(6s + 6p)$ (solid line) curves from Ref. [18]. (b) - Hund's case *c* $0_u^+(P_{1/2})$ and $0_u^+(P_{3/2})$ potential curves (solid lines) correlated respectively to the dissociation limits $(6s+6p\,^2P_{1/2})$ and $(6s+6p\,^2P_{3/2})$. The two curves, referred to as $V_1(R)$ and $V_2(R)$ in the text, display an avoided crossing which is represented in the inset: there, the solid curves have been computed with a molecular R-dependent spin-orbit coupling (see Fig. 2 below), while the broken curves correspond to calculations assuming a constant spin-orbit coupling.

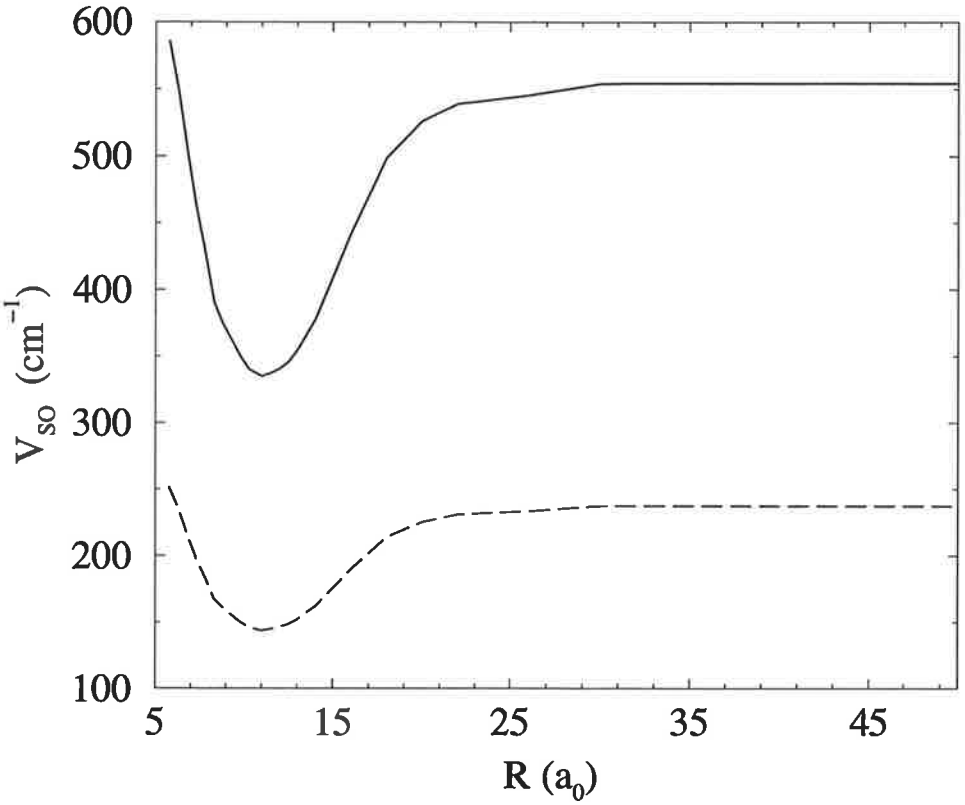

FIG. 2. Variation of the spin-orbit coupling $W_{1,2}(R)$ used in the calculations as a function of internuclear distance R. The quantity represented is $V_{SO}(R) = (3/\sqrt{2})W_{1,2}(R)$ which is asymptotically equal to the atomic spin-orbit splitting ΔE_{SO}. Full line - calculations of Ref. [18] for Cs_2 . Dashed line - for Rb_2, model curve scaled from the Cs_2 curve and fitted at infinity to the rubidium atom spin-orbit splitting.

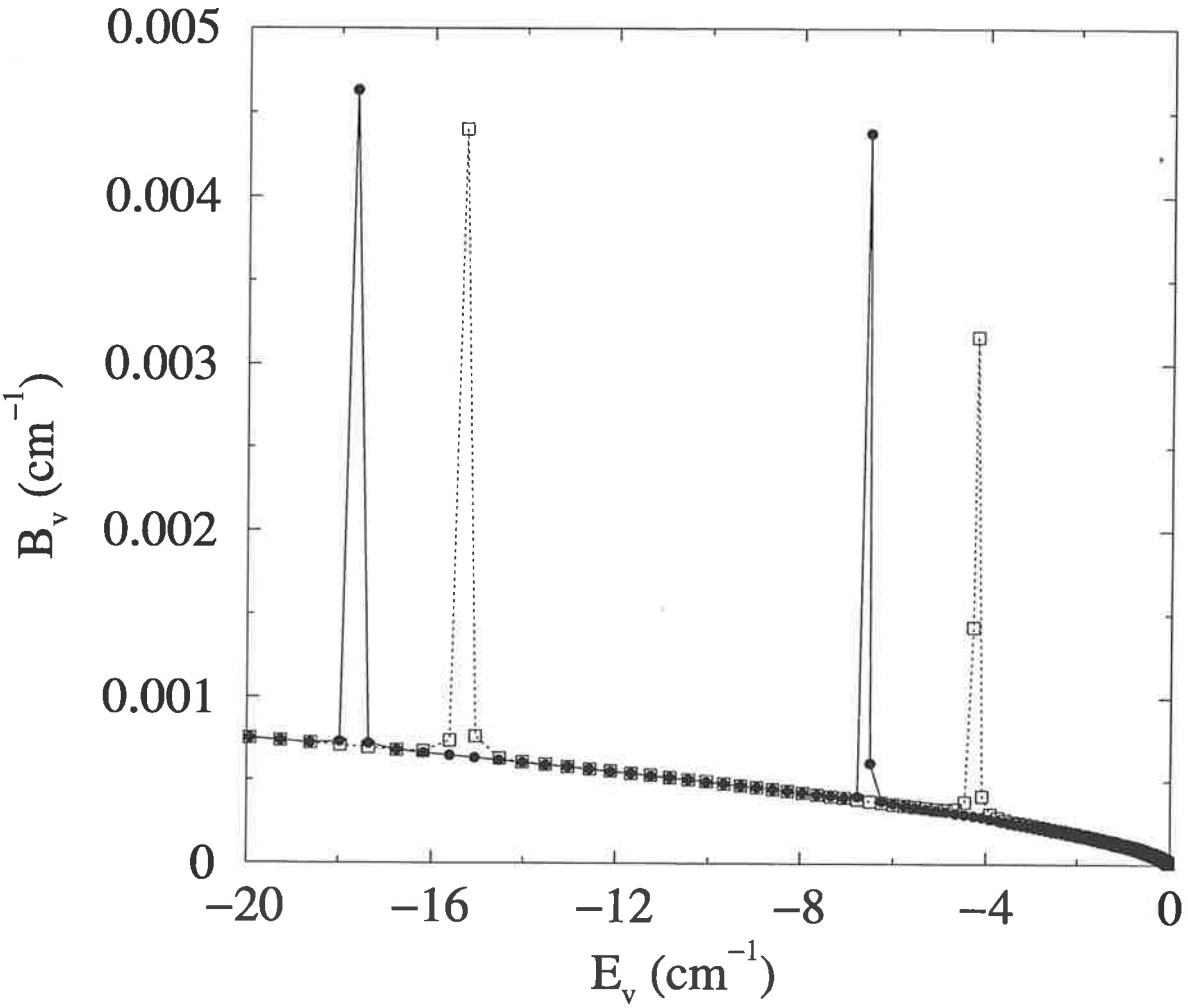

FIG. 4. Sensitivity of the perturbation effects upon the potential curves. Black circles : rotational constants and energy levels computed by two-coupled-channel calculations and already displayed in Fig. 3. White squares: same calculations with slightly modified potential curves, the repulsive wall being shifted by 0.01 a_0.

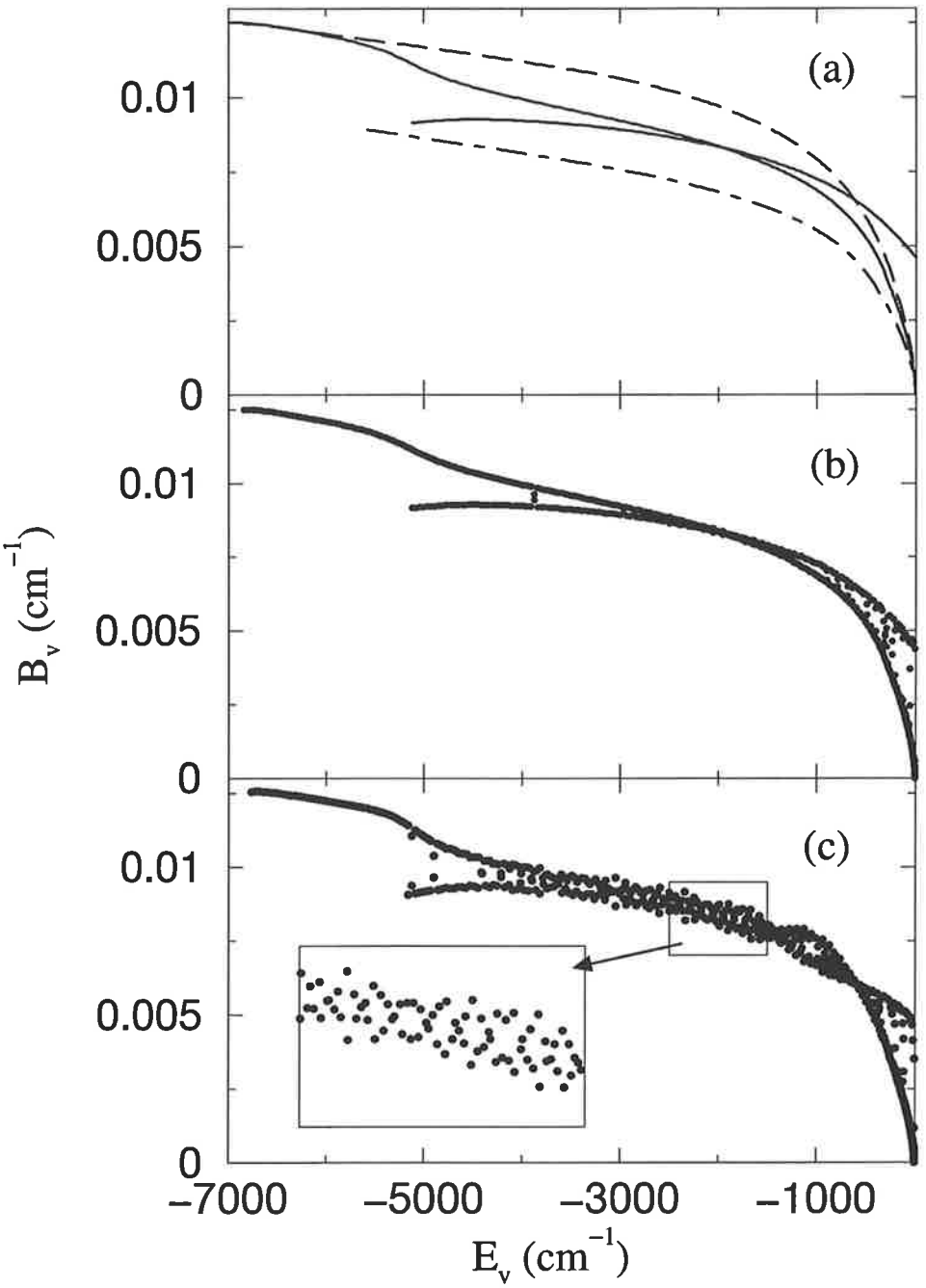

FIG. 5. Influence of channel coupling on the perturbations in the Cs_2 (0_u^+) spectrum.
(a) Rotational constants calculated for two uncoupled channels; solid curves, Hund's case c $0_u^+(P_{1/2})$ and $0_u^+(P_{3/2})$ channels; dashed curve, $b^3\Pi_u$ and, dot-dashed curve, $A^1\Sigma_u^+$ Hund's case a channels. (b) Calculations using atomic (R-independent) spin-orbit coupling. The results look qualitatively similar to two Hund's case c unperturbed vibrational series. (c) Calculations considering R-dependent spin-orbit coupling (see Fig. 2). The perturbations are more visible, as is manifest in the inset.

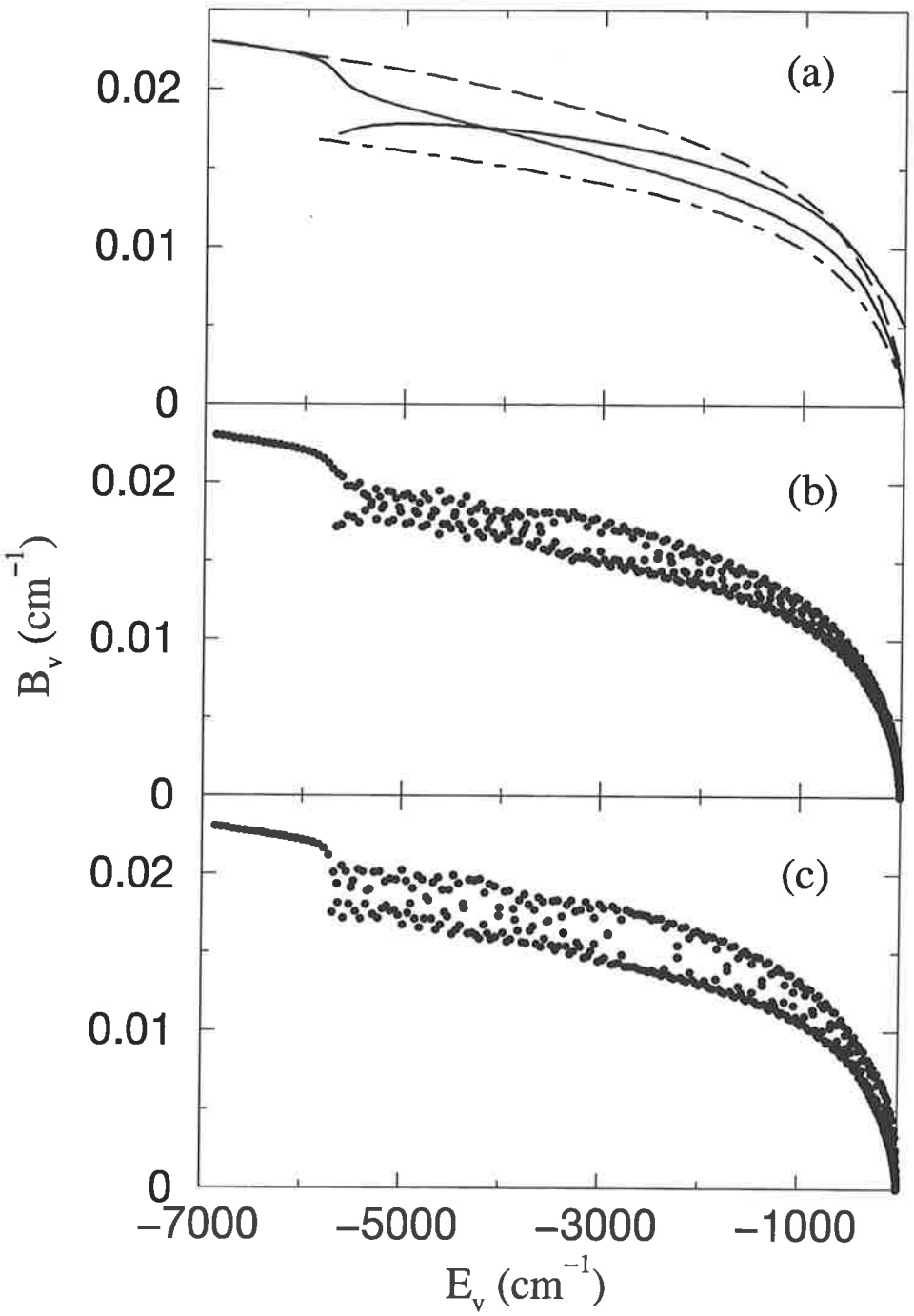

FIG. 6. Influence of channel coupling on the perturbations in the $^{85}Rb_2$ (0_u^+) spectrum.
(a) Rotational constants calculated for two uncoupled channels; solid curves, Hund's case c $0_u^+(P_{1/2})$ and $0_u^+(P_{3/2})$ channels; dashed curve, $b^3\Pi_u$ and, dot-dashed curve, $A^1\Sigma_u^+$ Hund's case a channels. (b) Calculations using atomic (R-independent) spin-orbit coupling. Strong perturbations are manifested in the results. (c) Calculations considering a model R-dependent spin-orbit coupling (see Fig. 2). The perturbations are reduced, the variation of the rotational constants looking qualitatively closer to the Hund's case a behavior represented in (b).

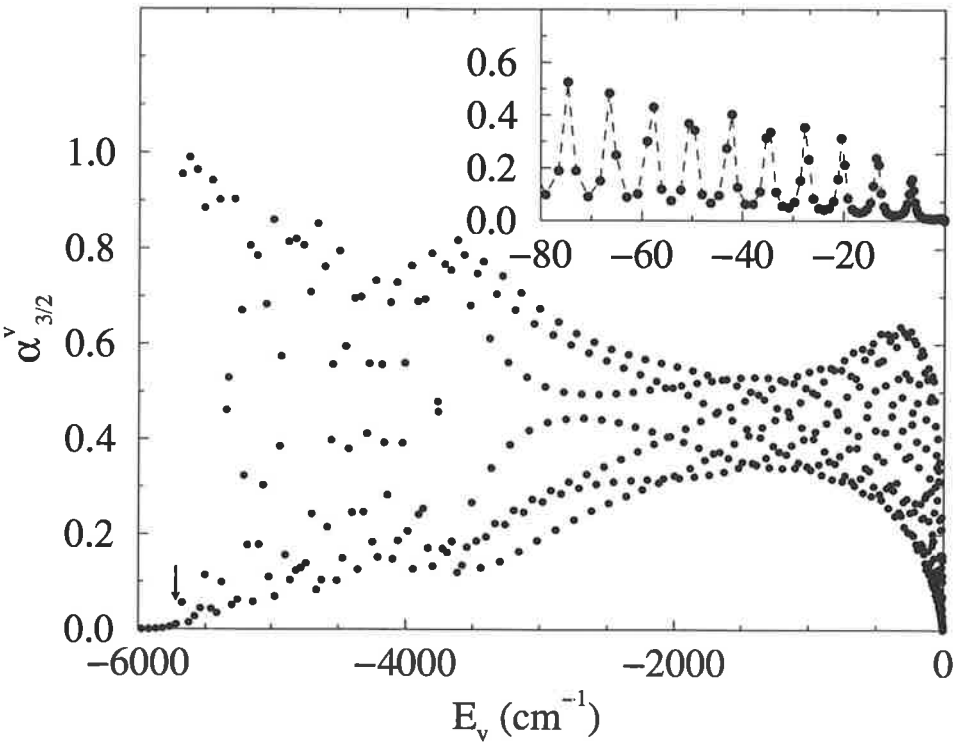

FIG. 7. Variation of the relative population $\alpha^v_{3/2}$ of the $P_{3/2}$ component in the two-channel 0^+_u ($^2P_{3/2}$) and 0^+_u ($^2P_{1/2}$) vibrational function of $^{87}Rb_2$, as a function of the binding energy E_v relative to the $P_{1/2}$ dissociation limit . The inset shows the energy range close to this limit. The arrow indicates the energy $E = -5715$ cm^{-1} of the bottom of the well of the $P_{3/2}$ potential $V_2(R)$. Above this energy, not a single level can be identified as a pure $P_{1/2}$ or $P_{3/2}$ vibrational level.

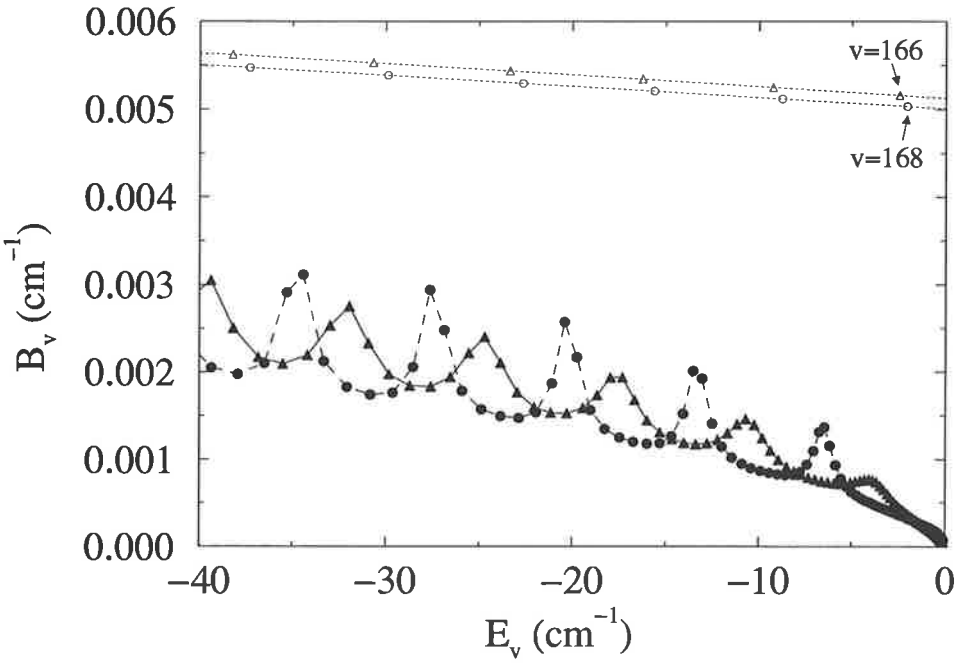

FIG. 8. Isotopic effect on the variation of rotational constants and binding energies for vibrational levels below the $(5s + 5p^2P_{1/2})$ dissociation limit of Rb_2 : black triangles, $^{85}Rb_2$; black circles, $^{87}Rb_2$. In order to identify the resonances, we have indicated by white triangles and squares results of calculations for single-channel $0_u^+(^2P_{3/2})$. Calculations were performed with a constant spin-orbit coupling.

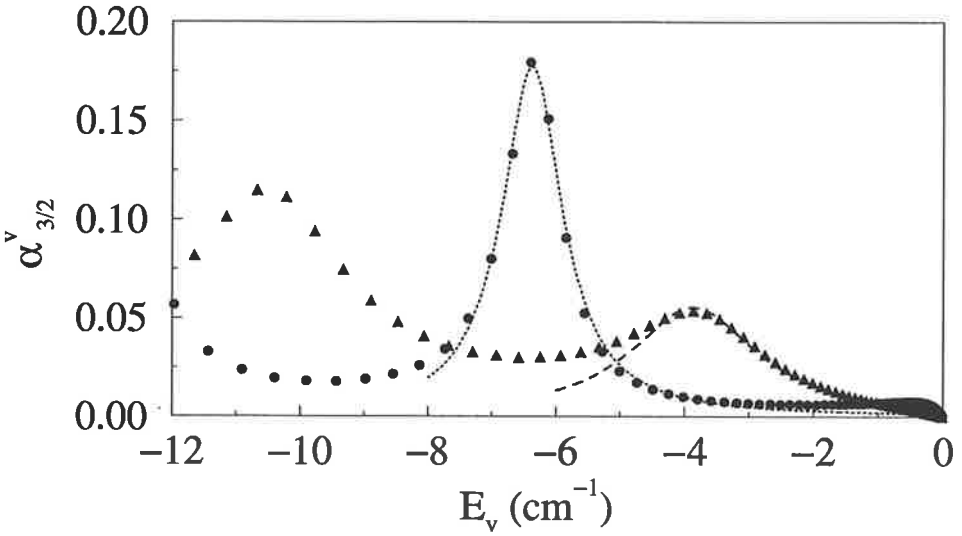

FIG. 9. Isotopic effect in the resonant behavior of the two-channel vibrational wave function. As in Fig. 7, we have represented the relative population $\alpha^v_{3/2}$ of the $P_{3/2}$ channel as a function of the binding energy for: $^{85}Rb_2$ (triangles) and $^{87}Rb_2$ (circles). Lines represent the result of the fit (see the text).

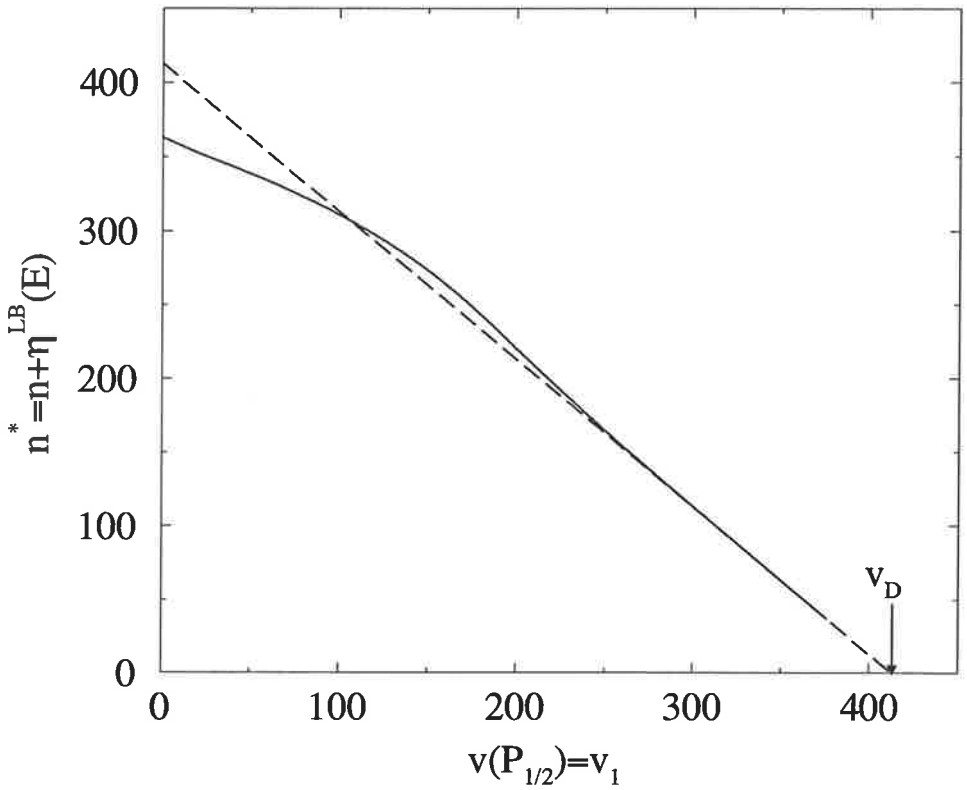

FIG. 10. Validity of the Le Roy-Bernstein law and definition of a quantum defect for vibrational levels in a single $^{85}Rb_2$ $0_u^+(^2P_{1/2})$ adiabatic potential. Variation of the quantity $n^* = n + \eta^{LB}(E)$ as defined in Eq. 13 as a function of the vibrational number v. The curve has been extrapolated in the region of the last vibrational levels up to the value $v_D = 412.9 \pm 0.1$.

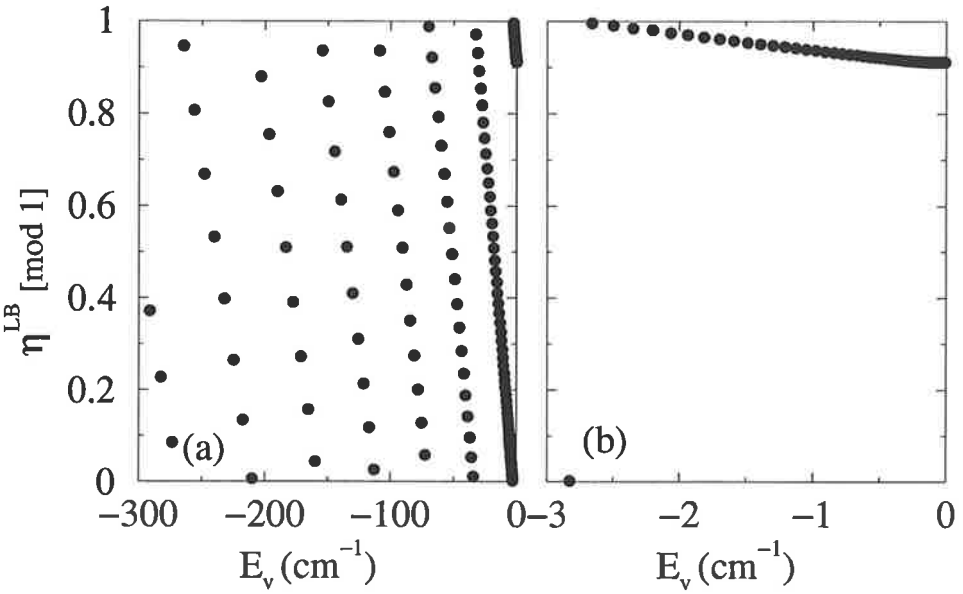

FIG. 11. Energy variation of the computed quantum defect (see Eq.13) for vibrational levels in the adiabatic potential $V_1(R)$ of $^{85}Rb_2$. The quantum defect has been represented modulo(1), showing that the deviation from pure Le Roy-Bernstein law introduces up to 7 levels in the energy range considered.

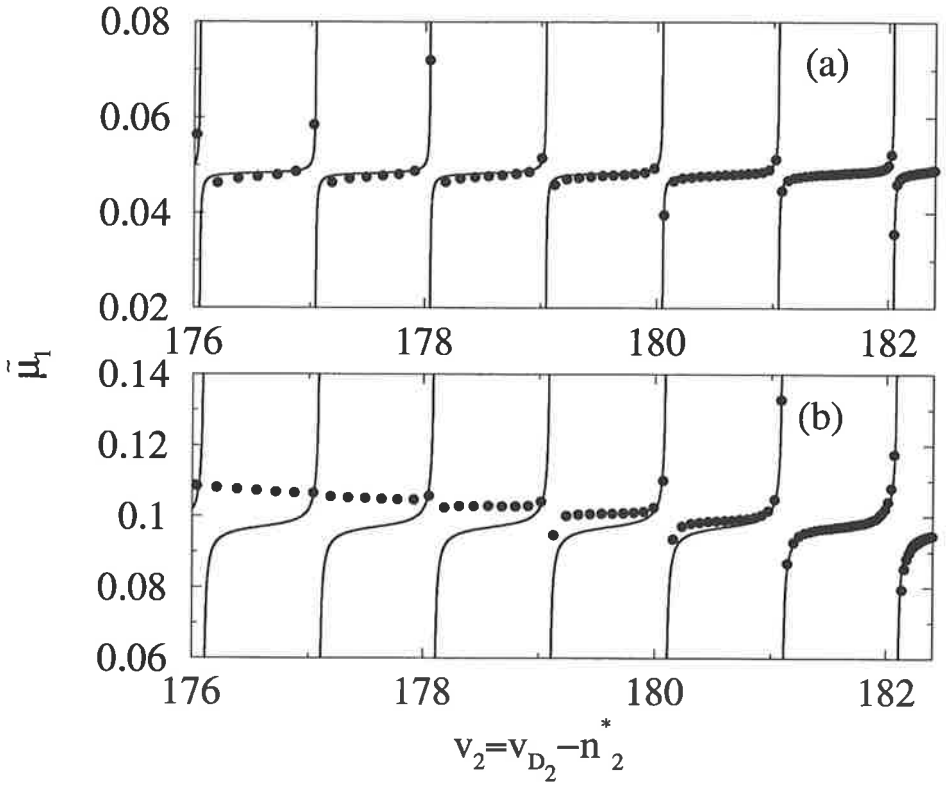

FIG. 12. Lu-Fano plot for the quantum numbers of the vibrational levels obtained by two 0_u^+ coupled channel calculations for Cs_2. On the horizontal axis the lower scale is the quantum number $v_2 = v_{D2} - n_2^*$, where $v_{D2} = 512.0$. The vertical scale is the quantum defect $\tilde{\mu}_1$, obtained by comparing the perturbed series to the unperturbed $P_{1/2}$ series. The calculations are using either variable spin-orbit coupling (top Figure) or constant spin-orbit coupling (bottom Figure)

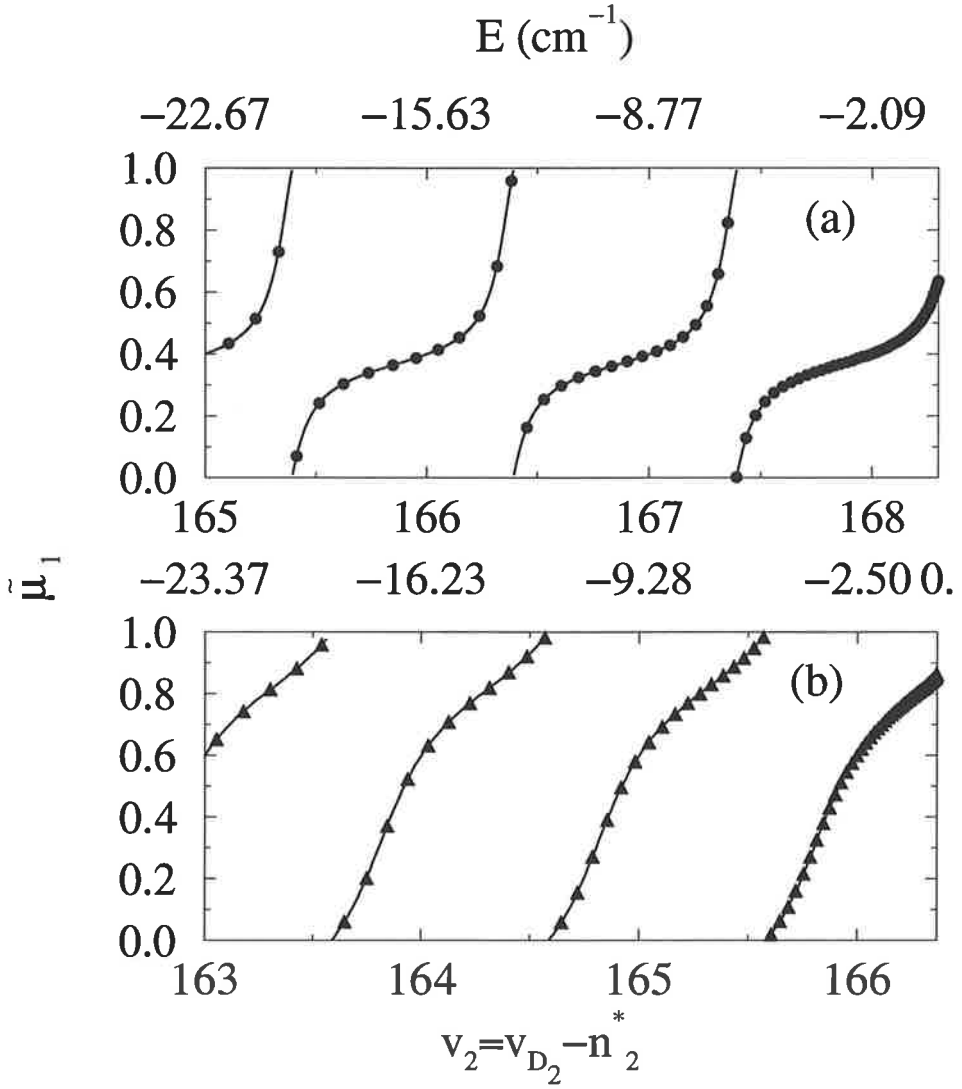

FIG. 13. Lu-Fano plot for the quantum numbers of the vibrational levels obtained by two 0_u^+ coupled channel calculations for : black triangles, $^{85}Rb_2$; black circles, $^{87}Rb_2$. On the horizontal axis the lower scale is the quantum number $v_2 = v_{D2} - n_2^*$ (where v_{D2} =389.1 for $^{85}Rb_2$ and 393.7 for $^{87}Rb_2$) for the unperturbed $P_{3/2}$ series, corresponding to vibrational motion in the adiabatic potential $V_2(R)$. The upper scale is the binding energy relative to $P_{1/2}$ dissociation limit. The vertical scale is the quantum defect μ_1 obtained by comparing the perturbed series to the unperturbed $P_{1/2}$ series.

List of Figures

1.1 The first experiment using the Doppler cooling. Schematic drawing of the vacuum chamber, intersecting laser beams and atomic beam [145]. 10

1.2 The photo-association scheme. The energy ω_a corresponds to the atomic transition $nS \rightarrow nP$. Photon ω_b ($\omega_b < \omega_a$) is the photo-association step. It populates a ro-vibrational level ν_b, J_b of the upper molecular state $nS+nP$ starting from the two free atoms with the asymptotic kinetic energy E. 11

1.3 Potential curves of Rb_2 correlated to the $5S + 5P$ dissociation limit of free atoms, calculated without the spin-orbit interaction. (Calculated by Foucrault *et al.* [43] at small distances and by M.Marinescu and A.Dalgarno [92] at large distances.) . 12

1.4 The Rb_2 potential curves calculated from curves presented on the Fig. 1.3 with accounting of the spin-orbit coupling (details of calculations are in the Appendix). 13

1.5 Diagram of the Cs_2 optical transitions and molecular states relevant for the photo-association experiment. The vibrational level shown represents schematically a level of one of the four curves. Spontaneous emission leads to: (i) trap-loss by desexcitation in two free atoms occurring from the four curves. (ii) and (iii) formation of translationally cold molecules in the $X^1\Sigma_g^+$ and $a^3\Sigma_u^+$, by desexcitation of the 1_u and 0_g^- states respectively. (Taken from [42]) 15

2.1 Examples of potential curves used in the paper. a) Two potentials with R^{-3}asymptotic behavior. Solid line: Na_2 $(^1\Pi_g, 3s + 3p)$, dashed line: $Cs_2(1_g, 6s + 6p^2P_{3/2})$. b) Two ground state potentials with R^{-6} asymptotic behavior. Solid line: $Na_2(^1\Sigma_g^+, 3s+3s)$, dashed line: $Cs_2(^1\Sigma_g^+, 6s + 6s)$. For all curves, the energy origin is taken at the dissociation limit. 35

2.2 Variation of the grid-step $s(R)$ in the physical grid, for the four potentials in Fig. 2.1. Dotted line: $Na_2(^1\Sigma_g^+, 3s + 3s)$, dashed line: $Cs_2(^1\Sigma_g^+, 6s + 6s)$, solid line: $Na_2(^1\Pi_g, 3s + 3p)$, dash-dotted line: $Cs_2(1_g, 6s + 6p^2P_{3/2})$. 36

2.3 Distribution of the grid points for a potential with asymptotic R^{-3} behavior: example of $Cs_2(1_g, 6s + 6p^2P_{3/2})$. a) - without mapping; b) - with the mapping defined by Eq. (2.74). 39

2.4 Comparison of the computed potential curve for Na_2 $(^3\Pi_u, 3s, 3p)$ [89] (full line) with the asymptotic curve $V(R) = -C_3/R^3$, $C_3 = 6.48$ $a.u.$, (dashed line) and the enveloping curve $V(R) = -C_3^{env}/R^3$, $C_3^{env} = 18$ $a.u.$ (dash-dotted line). . 41

2.5 Solid lines: The classical energy shell in phase space with and without the coordinate transformation, for the vibrational level with binding energy $E_u = -0.295\ cm^{-1}$ in the potential Cs_2 $(1_g, 6s, 6p^2P_{3/2})$. a) - The main figure shows the energy shell in phase space without any mapping. b) - The upper inset displays the energy shell with the mapping defined by the enveloping potential $-C_3^{env}/R^3$ with $C_3^{eff} = 24.42$. c)- The lower inset displays the energy shell in phase space with the mapping using the real behavior of the potential. The area $S = 1034\ a.u.$ defined by contour is the same for all three cases. The number of phase cells N_c is connected with S through $S = 2\pi * N_c$. Broken lines: The rectangles defining the phase space used in the calculations. One can see that without the mapping a larger phase volume is used in the calculation, that requires proportionally more grid points. The third case is most efficient in that sense. 42

2.6 Two examples of $C(t)$ for one pre-dissociated level of 0_u^+ $(5S + 5P)$ symmetry of $^{87}Rb_2$. The energy of the level is 26.13 cm^{-1} over the $P_{1/2}$ dissociation limit. Full line – the initial wave function is purely pre-dissociated, dot-dashed line corresponds to the initial wave function containing the non-pre-dissociated $P_{1/2}$ component. 58

2.7 The enveloping potential (the dashed line) for the one-channel potential (solid line). 61

2.8 The enveloping potential for the one-channel potential with a hump. 61

2.9 The enveloping potential for the potential with a hump and a well. 62

2.10 The analytical enveloping potential. 62

2.11 The enveloping potential for the two-channel adiabatic potential. The enveloping potential follows the behavior of the lower potential. 64

2.12 Efficiency of smoothness of the enveloping potential calculated for two-channel system 0_u^+, $5S + 5P$ of Rb_2. Upper panel: full lines – potential curves of the 0_u^+ symmetry, dashed line – non-smoothed enveloping potential, dot-dashed line - smoothed potential according to Eq. (2.168) with $a = 2\ a_0$. Lower panel: Curves represented the quantity $J'(x)$ as a functions or R. Full line is $J'(x)$ calculated from the non-smoothed V_{env}, dot-dashed line represents the smoothed $\tilde{V}_{env}$. . . . 65

3.1 Accuracy ΔE of the computed energies for the 80 lowest $Na_2(1_g)$ vibrational levels in the $Na_2(^1\Pi_g, 3s+3p)$ potential. The three figures represent a) - ΔE, from Numerov integration with $\Delta R = 0.0025$ (34000 points). b) - ΔE, for energies computed by the FGR method with uniform grid. Solid line: N=950 points; dash-dotted line: N=1140 points. c) - ΔE, for the FGR method with the mapping defined by Eq. (2.61), considering different values of the parameter β. Solid line: $\beta = 0.6$, N=170 points; dash-dotted line: $\beta = 0.4$, N =254 points; dashed line: $\beta = 0.2$, N=506 points. 68

3.2 Improved calculations with parameters close to parameters of the figure 3.1. The calculations using the Numerov method with 576000 points are chosen as a reference. Two panels correspond to the *b* and *c* panels of the Fig. 3.2. Panels: b) - ΔE, for energies computed by the FGR method with the uniform grid. Solid line: N=953 points ($\beta = 0.418$); dash-dotted line: N=1141 points ($\beta = 0.349$). c) - ΔE, for the FGR method with the mapping defined by Eq. (2.61), considering different values of the parameter β. Dash-dotted line: $\beta = 0.4$, N=233 points; solid line: $\beta = 0.2$, N =465 points; dashed line: $\beta = 0.1$, N=927 points. 69

3.3 The stability of the FGR method. The difference between bound levels calculated in the mapped FGR method with two parameters β 0.07 and 0.1. 70

3.4 The $v = 332$ vibrational wave function for the Cs_2 $(1_g, 6s+6p^2P_{3/2})$ potential (see Fig. 2.1), computed at the grid points defined with the mapping of the Eq. (2.61). Here, $R_{max} = 500a_0$, $N = 564$. a) - wave function at every grid point, with linear interpolation between two points ; b) - wave function interpolated according to Eq. (3.1) choosing $N_{interp} = 10000$ (see text). c) - interpolated wave function in the x variable, showing only the part corresponding to large R. Comparing c) to b), one can appreciate the regularity of the oscillations in the mapped wave function) 72

3.5 The calculation accuracy $\Delta\psi(R)$ of the wave function of $\nu = 0$ vibrational levels of $Na_2(^1\Pi_g, 3s + 3p)$. Upper panned: The reference is the wave function obtained with $N = 576000$ points. Solid line: $N = 288000$ points, dotted line: $N = 144000$ points (the same as for $N = 288000$), dashed line: $N = 72000$ points, long dashed line: $N = 36000$ points, dot-dashed line: $N = 18000$ points. Lower panned: the reference is the $\nu = 0$ wave function obtained in the FGR method with $\beta = 0.07$, $N = 1323$. The difference with wave function obtained for: solid line – $\beta = 0.1$, $N = 927$, dashed line – $\beta = 0.2$, $N = 465$. 73

3.6 The difference between wave functions calculated by two methods. The smallest step is chosen for both methods: $N = 576000$ is used in the Numerov method, $\beta = 0.07$ is chosen for the FGR method. This difference larger than $\Delta\psi$ for each method with indicated parameters. It gives an idea, how small can be β, and what is a order of accuracy of both methods 74

3.7 The precision of wave function in the FGR method as a function of the parameter β. The reference is the calculations with $\beta = 0.07$ 75

3.8 Diabatic (left panels) and adiabatic components (right panels) of a two-channels pre-dissociated wave function of $^{87}Rb_2$ (0_u^+); $E = 210.52cm^{-1}$ above the $P_{1/2}$ asymptote. At left panels: up - the $^3\Pi_u$ component, middle - the $^1\Sigma_u$ component, down - the total wave function. At the right: up - the $P_{1/2}$ component, middle - the $P_{3/2}$ component, down - the total wave function. For $^1\Sigma_u$ and $P_{3/2}$ components relative fractions in the total norm are marked. Arrows mark the position of the crossing. 77

3.9 Lifetimes of vibrational levels of the 0_u^+ symmetry of $^{85}Rb_2$, calculated by two methods - time-dependent and time-independent. Circles represent the time-dependent calculations; diamonds - time-independent. Inset shows a detailed picture of a part of the whole region. 79

4.1 Rb_2 potential curves without (a) and with (b) spin-orbit coupling. (a) - Hund's case a $A^1\Sigma_u^+$ $(5S + 5P)$ (broken line) and $b^3\Pi_u$, $(5S + 5P)$ (dash-dotted line) curves from reference [43] (b) Hund's case c $0_u^+(P_{1/2})$ and $0_u^+(P_{3/2})$ potential curves correlated respectively to the dissociation limits $(5S + 5P_{1/2})$ and $(5S + 5P_{3/2})$. The inset at the right panel shows the region of the pseudo-crossing. 83

4.2 Rotational constants B_v (in cm^{-1}) for vibrational levels of the 0_u^+ symmetry of Rb_2 (see the potential curves on Fig. 4.1). Neglecting fine structure coupling (Hund's case a) – full lines; neglecting radial coupling (Hund's case c) – dashed lines; and considering two coupled channels – circles. 85

4.3 Same as figure 4.2, close to the $(5S + 5P_{1/2})$ dissociation limit (labeled $P_{1/2}$ and located at energy $E = 0$). Squares and triangles represent B_v for non-coupled $P_{1/2}$ and $P_{3/2}$ potentials respectively. 86

4.4 Two vibrational wave functions for $Rb_2(0_u^+)$ close to the $P_{1/2}$ dissociation limit. The upper panel shows the wave function with vibrational number $v = 445$ and energy $E_v = -20.414$ cm^{-1} with the relative population of the $P_{3/2}$ component $\int |\Psi_{3/2}(R)|^2 dR = 0.31$. The lower panel – the wave function with $v = 451$, energy $E_v = -15.997$ cm^{-1} with $|\Psi_{3/2}|^2 = 0.033$. The rotational constants for those levels are indicated by arrows in fig. 4.3. 87

4.5 The relative population of the $P_{3/2}$ component of the total wave function of $^{87}Rb_2$ (0_u^+) as a function of the binding energy. There is not any bound level with energy > -5715 cm^{-1} (this limit is marked by an arrow and corresponds to the bottom of the well of the $P_{3/2}$ potential), which could be purely the $P_{1/2}$ or $P_{3/2}$ vibrational state. The norm of the $P_{3/2}$ component never becomes 0 or 1. All vibrational levels are perturbed. The inset shows a domain of the energy near the dissociation limit. $P_{3/2}$ levels look like pre-dissociated levels with finite lifetimes. . 88

4.6 Rotational constants of two isotopes, $^{85}Rb_2$ (triangles) and $^{87}Rb_2$ (circles). . . . 89

4.7 The same figure as shown in Fig. 4.5 near the $P_{1/2}$ dissociation limit. Circles represent the relative population of the $P_{3/2}$ component. The solid line is an adjusted function of Eq. (4.5) with $\Gamma = 1.22$ cm^{-1}. The left tail of the resonance is not reproduced by the analytical curve because the shape of the resonance is perturbed by a neighboring peak. 90

4.8 Quantum defects μ_v (modulo 1) of vibrational levels of the $P_{1/2}$ state, calculated in respect to levels of the purely C_3/R^3 potential Eq. (4.20). 93

4.9 the same as the figure 4.8 but for larger domain of energies. 94

4.10 The Lu-Fano plot for bound levels for two isotopes of Rb_2. The upper axis of both panels shows energies corresponding to non-perturbed $P_{3/2}$ levels. These levels are shown at lower axes of both panels. Circles represent levels of the coupled 0_u^+ potential. The full lines are the results of the fitting. 96

4.11 The experimental data for dependence $B_v(E_v)$ for 0_u^+ ($^{85}Rb_2$) from [52] (open circles) comparing with the results of calculations (squares). In the calculations, the variable spin-orbit coupling is used (Fig. 4.15). Triangles and diamonds shows also $B_v(E_v)$ for $P_{1/2}$ and $P_{3/2}$ non-coupled potentials. 99

4.12 Cs_2 potential curves without (a) and with (b) spin-orbit coupling. (a) - diabatic $A^1\Sigma_u^+$ $(6s + 6p)$ (dot-dashed line) and $b^3\Pi_u$ $(6s + 6p)$ (full line) curves from Ref. [94] (b) adiabatic $0_u^+(P_{1/2})$ (dotted line) and $0_u^+(P_{3/2})$ (dashed line) potential curves correlated respectively to the dissociation limits $(6s + 6p\ ^2P_{1/2})$ and $(6s + 6p\ ^2P_{3/2})$. 100

4.13 Rotational constants B_v of vibrational levels of 0_u^+ symmetry of Cs_2. Triangles and squares show B_v for vibrational levels of non-coupled $P_{1/2}$ and $P_{3/2}$ potentials respectively. Circles represent B_v in coupled channel calculation (the R-independent spin-orbit coupling). 101

4.14 The Lu-Fano plot for the 0_u^+ symmetry of Cs_2. Circles represent coupled levels. The upper panel shows quantities of $\tilde{\mu}_1(E_c)$ and $\{v_2^*(E_c)\}$ for the energy domain corresponding to all non-perturbed levels of the state $P_{3/2}$ from $v = 0$ to $v = 182$. The lower panel shows the dependence $\tilde{\mu}_1(v_2^*)$ for the energy region just below the $P_{1/2}$ limit. The full curves represent analytical curve of Eq. (4.26) with parameters $R_{1,2} = 0.03$, $\mu_1 = 0.0483$, $\mu_2 = -0.046$. 102

4.15 The variation of the molecular spin-orbit interaction used in the calculation. Full line - calculated for Cs_2 . Dashed line - for Rb_2. 102

4.16 Rotational constants for $^{237}Cs_2$ (left panels) and $^{85}Rb_2$ (right panels), calculated using two different molecular spin-orbit couplings. Upper panels show rotational constants for the potential with R-independent molecular spin-orbit interaction, lower panels — with the variable coupling according to the Fig. 4.15 103

4.17 Lu-Fano plot for 0_u^+ symmetry of Cs_2 with the variable spin-orbit coupling (full circles), fitted with constant parameters: $R_{1,2} = 0.1$, $\mu_1 = 0.097$, $\mu_2 = -0.096$ (full lines). 104

4.18 Lifetimes (upper panel) and widths (lower panel) of pre-dissociated levels for two isotopes: diamonds - $^{85}Rb_2$, squares - $^{87}Rb_2$. The experimental value for $^{85}Rb_2$ from [27] ($\tau \approx 20\ ps$) is presented by a big star. Triangles represent the model calculations with the variable coupling as it shown at Fig. 4.15 for $^{85}Rb_2$. 106

4.19 The quantum defects μ_2 (open diamonds and squares) and quantities $R_{1,2}^2$ (full figures) for $P_{3/2}$ pre-dissociated levels for $^{85}Rb_2$ (diamonds) and $^{87}Rb_2$ (squares). Triangles represents calculation for $^{85}Rb_2$ with the variable coupling. 107

4.20 Lifetimes of pre-dissociated $P_{3/2}$ levels: $^{85}Rb_2$ - diamonds; and $^{87}Rb_2$ - squares fitted with functions (4.42) with $\alpha = 190\ ps(\mathrm{cm}^{-1})^{5/6}$ for $^{85}Rb_2$ (full line) and with $\alpha = 630\ ps\ (\mathrm{cm}^{-1})^{5/6}$ for $^{87}Rb_2$ (dashed line). 109

4.21 The quantity $f(R) = \psi_{E,P_{3/2}}(R)\psi_{E,P_{1/2}}(R)$, calculated for two rubidium isotopes. a – $^{85}Rb_2$ (energy of level $E = 15.7\ \mathrm{cm}^{-1}$ over $P_{1/2}$ limit), b – $^{87}Rb_2$ with the energy $E = 19.4\ \mathrm{cm}^{-1}$. The panel c represents the non-adiabatic coupling between two components – $P_{1/2}$ and $P_{3/2}$. Transitions occur only in the region where $\tau_{1,2}$ is quite large. 111

4.22 Factor $f(R)$, calculated for levels of the 0_u^+ symmetry of $^{87}Rb_2$ with different energy near the $P_{1/2}$ dissociation limit. a – bound level with energy $E = 13.6\ \mathrm{cm}^{-1}$, b and c - pre-dissociated levels with energies $E = 19.4\ \mathrm{cm}^{-1}$ and $E = 174.1\ \mathrm{cm}^{-1}$ respectively. For any energy positions of maxima and minima of the slow modulation stay the same. It provides the monotonic (not oscillating) increasing of lifetimes for the all pre-dissociated levels between $P_{1/2}$ and $P_{3/2}$ limits. 112

4.23 Widths of vibrational levels of Cs_2 0_u^+ for two different molecular spin-orbit interactions $V_{SO}(R)$ between $^3\Pi_u$ and $^1\Sigma_u$ curves: circles - the molecular spin-orbit interaction is varying as shown in Fig. 4.15; squares - constant molecular spin-orbit interaction ($V_{SO} = 554.1$ cm^{-1}). 113
4.24 The parameter $R^2_{1,2}$ for pre-dissociated levels of the 0_u^+ symmetry of Cs_2 with the constant (upper panel) and the variable (lower panel) spin-orbit coupling. 114

5.1 Potentials $B^1\Pi_u$ (full line) and $1^1\Pi_g$ (dashed line) of Li_2 ($2S + 2P$). 119
5.2 Two typical pre-dissociated wave functions of the $^1\Pi_u$ molecular state of $^6Li^7Li$ with $J = 1$. The lower panel shows the wave function of the highest ($v = 16$) pre-dissociation level, the upper panel shows the lowest ($v = 13$) pre-dissociated level. Insets show asymptotic tails of both wave functions. 120
5.3 Widths of $^1\Pi_u$ ($^6Li^7Li$) levels, pre-dissociated due to the tunneling through the potential barrier, as a function of the total momentum J. 121
5.4 Two typical pre-dissociated wave functions of the $^1\Pi_u$ molecular state of$^6Li^7Li$ with $J = 1$ perturbed by the coupling with the $^1\Pi_g$ molecular state. The lower panel shows $^1\Pi_g$-components of wave functions. 124
5.5 The variation of Γ as a function of the energy for vibrational levels $v = 10 - 16$. Calculations with different J from 1 to 60 are represented on the figure. 125
5.6 Same as the figure 5.5 by for the region of small Γ. Vibrational levels from $v = 4$ to $v = 16$ are represented. Large symbols represent experimentally-observed widths, the convention for their geometric form being the same as for calculated values. . 126

Bibliography

[1] E.R.I. Abraham, W.M. Ritchie, W.I. McAlexander, and R.G. Hulet, J. Chem. Phys. **103**, 7773 (1995).

[2] E.R.I. Abraham, W.I. McAlexander, H.T.C. Stoof, and R.G. Hulet, Phys. Rev. A **53**, 3092-3097 (1996).

[3] M. Abramowitz and I.A. Stegun (Eds.), *Handbook of Mathematical Functions*, National Bureau of Standards, Dover, New York, 1974.

[4] J. Alvarellos and H. Metiu, J. Chem. Phys. **88(8)**, 4957-4966 (1988).

[5] C. Amiot and J. Vergès, Chem. Phys. Lett. **274**, 91 (1997).

[6] C. Amiot, private communication

[7] C. Amiot, O.Dulieu, and J.Vergès, Phys. Rev. Lett. **83** 2316-2319 (1999).

[8] M.H. Anderson, J.R. Ensher, M.R. Matthews, C. E. Wieman, Science **269**, 198 (1995).

[9] A. Aspect, E. Arimondo, R. Kaiser, N. Vansteenkiste, and C. Cohen-Tannoudji, Phys. Rev. Lett. **61**, 826-829 (1988).

[10] A. Aspect, E. Arimondo, R. Kaiser, N. Vansteenkiste, and C. Cohen-Tannoudji, Jour. Opt. Soc. Amer. B **6**, 2112-24 (1989).

[11] M. Aymar, C.H. Greene, and E. Luc-Koenig, Rev. Mod. Phys. **68**, 1015-1124 (1995).

[12] M. Baer J. Chem. Phys. **15**, 49 (1976).

[13] J.T. Bahns, W.C. Stwalley, and P.L. Gould, J. Chem. Phys. **104**, 9689-9697 (1996).

[14] U. Banin, A. Bartana, S. Ruhman, and R. Kosloff, J. Chem. Phys. **101**, 8461-8481 (1994).

[15] A. Bayliss and E. Turkel, J. Comp. Phys. **101**, 349 (1992).

[16] R.P. Benedict, D.L. Drummond, and L.A. Schlie, J. Chem. Phys. **66**, 4600 (1977).

[17] R.H. Bisseling, R. Kosloff, and J. Manz, J. Chem. Phys. **83**, 993 (1985).

[18] J.M. Blatt, J.Comp.Phys. **1**, 382 (1967).

[19] R. Blatt, G. Lafyatis, W.D. Phillips, S. Stenholm, and D.J. Wineland, Phys. Scripta **T22**, 216-223 (1988).

[20] C.Boisseau, thesis (1998)

[21] C. Boisseau, E. Audouard, and J. Vigue, Europhys. Lett. **41(4)**, 349-354 (1998).

[22] N. Bouloufa, P. Cacciani, R. Vetter, and A. Yiannopoulou, J. Chem. Phys. **111**, 1926-1936 (1999).

[23] C.C. Bradley, C.A. Sackett, J.J. Tollett, and R.G. Hulet, Phys. Rev. Lett. **75**, 1687 (1995).

[24] in preparation.

[25] R. Chen, H. Guo, Chem. Phys. Lett. **261**, 605-611 (1996).

[26] S. Chu-S, A. Ashkin, J.E. Bjorkholm, J.P. Gordon, L. Hollberg, Laser Spectroscopy VII. *Proceedings of the Seventh International Conference.* Springer-Verlag, Berlin, West Germany, 18-19 (1985).

[27] R.A. Cline, J. D. Miller, and D. J. Heinzen, Phys. Rev. Lett. **73**, 632 (1994).

[28] C. Cohen-Tannoudji, and W.D.Phillips, Physics Today, p. 33, October (1990).

[29] C. Cohen-Tannoudji, R. Kaiser, K. Molmer, C. Salomon, N. Vansteenkiste, Annales de Physique **15**, 25-30 (1990).

[30] D. T. Colbert and W. H. Miller, J. Chem. Phys. **96**, 1892 (1992).

[31] D. Comparat, C. Drag, A. Fioretti, O. Dulieu, and P. Pillet, to be published (1999).

[32] R. Côté and M.J. Jamieson, J. Comp. Phys. **118**, 388 (1995).

[33] K.B. Davis, M. Mewes, M.R. Andrews, N.J. Drutten, D.S. Durfee, D.M. Kurn, and W. Ketterle, Phys. Rev. Lett. **75**, 3969 (1995).

[34] O.Dulieu and P.S. Julienne, J. Chem. Phys, **103**, 60 (1995).

[35] O. Dulieu, R. Kosloff, F. Masnou-Seeuws and G. Pichler, J. Chem. Phys. **107**, 10633 (1997).

[36] B. K. Elza and B. Ritchie, Phys. Rev. A **48(4)**, 2940-4966-2945 (1993).

[37] C. Effantin, O. Babaky, K. Hussein, J. D'Incan, and R.F. Barrow, J. Phys. B: Atomic Molecular and Optical Physics **18**, 4077 (1985).

[38] E. Fattal, R. Baer, and R. Kosloff, Phys. Rev. E **53**, 1217-1227 (1996).

[39] E. Fattal, Thesis (1996).

[40] A. Fioretti, J. H. Müller, P. Verkerk, M. Allegrini, E. Arimondo, and P. S. Julienne, Phys. Rev. a **49**, 607 (1997).

[41] A. Fioretti, D. Comparat, A. Crubellier, O. Dulieu, F. Masnou-Seeuws, and P. Pillet, Phys. Rev. Lett. **80**, 4402 (1998).

[42] A. Fioretti, D. Comparat, C. Drag, C. Amiot, O. Dulieu, F. Masnou-Seeuws, and P. Pillet, Eur. Phys. J. D **5**, 389-403 (1999).

[43] M. Foucrault, Ph. Millié, and J. P. Daudey, J. Chem. Phys. **96**, 1257 (1992).

[44] H. Friedrich, *Theoretical Atomic Physics*, Springer-Verlag, Berlin (1998).

[45] A. Giusti-Suzor and U. Fano, J. Phys. B **17**, 215-230, 4267-4275, 4277-4283 (1984).

[46] R.A. Gonzales, J. Eisert, I. Koltracht, M. Neumann, and G. Rawitscher J. Comp. Phys. **134**, 134-149 (1997).

[47] G.F. Gribakin and V.V. Flambaum, Phys. Rev. A **48**, 546 (1993).

[48] F. Gygi, Europhys. Lett. **19**, 617 (1992).

[49] T.W. Hansch, A.L. Schawlow, Opt. Comm. **13**, 68-9 (1975).

[50] R. Heather and H. Metiu, J. Chem. Phys. **86**, 5009 (1987).

[51] R.A. Cline, J. D. Miller and D. J. Heinzen, Phys. Rev. Lett. **71**, 2204 (1993).

[52] D.J. Heinzen, J.G.C. Tempelaars, and R.S. Freeland, *workshop on cold atomic collisions and formation of cold molecules. Les Houches*, (1999).

[53] M. Hillery, R.F. O'Connell, M.O. Scully, and E.P. Wigner, Physics Reports **106(3)**, 121-167, Amsterdam (1984).

[54] Y. Huang, D.J. Kouri, J. Chem. Phys. **101**, 10493-10506 (1994).

[55] G. Inoue, J.K. Ku, and D.W.Setser J. Chem. Phys. **76**, 733-734, (1982).

[56] P.S. Julienne and R. Heather, Phys. Rev. Lett. **67**, 2135-2138 (1991).

[57] P. S. Julienne and J. Vigué, Phys. Rev. A **44**, 4464 (1991).

[58] G. Jolicard, E.J. Austin, Chem. Phys. Lett. **121**, 106 (1985).

[59] G. Jong, L. Li, T.J. Whang, W.C. Stwalley, J.A. Loxon, M. Li, and A.M. Lyyra, J. Mol. Spectrosc. **155**, 115 (1992).

[60] R. Kaiser, N.Vansteenkiste, A. Aspect, E. Arimondo, and C. Cohen-Tannoudji, Zeitschrift Physik D **18**, 17-24 (1991).

[61] H. Kato, M. Otani, and M. Baba, Chem. Phys. **89**, 653 (1988).

[62] G. Katz, R. Baer, and R. Kosloff, Chem. Phys. Lett. **239**, 230-236 (1995).

[63] W. Ketterle, K.B. Davis, M.A. Joffe, A. Martin, and Pritchar, Phys. Rev. Lett. **70**, 2253-2256 (1993).

[64] V. Kokoouline, O. Dulieu, R. Kosloff, and F. Masnou-Seeuws, J. Chem. Phys. **110**, 9865 (1999).

[65] V. Kokoouline, O. Dulieu, and F. Masnou-Seeuws, in preparation.

[66] V. Kokoouline, O. Dulieu, R. Kosloff, and F. Masnou-Seeuws, in preparation.

[67] D. Kosloff and R. Kosloff, J. Comp. Phys. **52**, 35-53 (1983).

[68] D. Kosloff and R. Kosloff, J. Comp. Phys. **63**, 363-376 (1986).

[69] R. Kosloff, J. Phys. Chem. **92**, 2087 (1988).

[70] R. Kosloff, C.Cerjan (ed.), Kluwer Academic Publishers, 175-194 (1993).

[71] R. Kosloff, Annu. Rev. Phys. Chem. **45**, 145-178 (1994).

[72] R. Kosloff in *R.E. Wyatt and J.Z.H. Zhang editors, Dynamics of Molecules and Chemical Reactions, Marcel Dekker*, New York 1996.

[73] D.J. Kouri, W. Zhu, Y. Huang, and D.K. Hoffman, Chem. Phys. Lett. **220**, 312-318 (1994).

[74] L.D.Landau and E.M.Lifshitz, *Mechanics* Oxford, Pergamon, (1965).

[75] L.D.Landau and E.M.Lifshitz, *Quantum Mechanics: Non-Relativistic Theory* Oxford, Pergamon, (1965).

[76] H. Lefebvre-Brion and R.W. Field, *Perturbations in the spectra of diatomic molecules*, Academic Press, Inc, U.S., (1986).

[77] C. Leforestier, R. H. Bisseling, C. Cerjan, M. D. Feit, R. Friesner, A. Guldberg, A. Hammerich, G. Jolicard, W. Karrlein, H.-D. Meyer, N. Lipkin, O. Roncero, and R. Kosloff, J. Comp. Phys. **94**, 59-80 (1991).

[78] R.J. LeRoy and R.B. Bernstein, J. Chem. Phys. **52**, 3869-3879 (1970).

[79] R.J. LeRoy, J. Chem. Phys. **73**, 6003-6012 (1980).

[80] V.S. Letokhov, Pis'ma Zh. Eksp. Teor. Fiz., **7(9)**, 348-351 (1968) (in Russian); [JETP Lett. **7**, 272-274 (1968)].

[81] V.S. Letokhov, *Proceed. of the Conf. "Methods of Spectroscopy without Doppler Broadening of Excited Levels of Simple Molecules"* (Aussois, France, May 23-26, 1973), 127-138, (1974); Laser and Unconventional Optics, **46**, 3-27 (1973).

[82] V.S. Letokhov, V.G.Minogin, and B.D.Pavlik, Zh. Eksp. Teor. Fiz. **72(4)**, 1328-1341 (1977) (in Russian).

[83] P. D. Lett, K. Helmerson, W. D. Philips, L. P. Ratliff, S. L. Rolston, and M. E. Wagshul, Phys. Rev. Lett. **71**, 2200 (1993).

[84] P. D. Lett, P.S. Julienne, and W.D. Phillips, Ann. Rev. Phys. Chem. **46**, 423-452 (1995).

[85] J.C. Light, I.P. Hamilton, and J.V. Lill, J. Chem. Phys. **82(3)**, 1400 (1984).

[86] J.V. Lill, G.A. Parker, and J.C. Light, Chem. Phys. Lett. **89**, 483 (1982).

[87] C. Linton, F. Martin, R. Bacis, and J. Verges, J. Mol. Spectr. **142**, 340-375 (1990).

[88] E. Luc-Koenig, M. Aymar, and J.M. Lecomte, J. Phys. B **27**, 2447-2469 (1994).

[89] S. Magnier, Ph. Millié, O. Dulieu, and F. Masnou-Seeuws, J. Chem. Phys. **98**, 7113 (1993).

[90] S. Magnier, M. Aubert-Frécon, O. Bouty, F. Masnou-Seeuws, Ph. Millié, and V.N. Ostrovsky, J. Phys. B: At. Mol. Opt. Phys, **27**, 1723, (1994).

[91] S. Magnier and Ph. Millié, Phys. Rev. A **54** 204, (1996).

[92] M. Marinescu and A. Dalgarno, Phys. Rev. A **52**, 311 (1995).

[93] W.I. McAlexander, E.R.I. Abraham, N.W.M. Ritchie, C.J. Williams, H.T.C. Stoof, and R.G. Hulet, Phys. Rev. A **51**, R871-R874.

[94] W. Meyer, (Private communication).:N. Spiess, Ph. D thesis, Fachbereich Chemie, Universität Kaiserslautern, (1989).

[95] R. Meyer, J. Chem. Phys. **52**, 2053 (1970).

[96] J.D. Miller, R.A. Cline, and D.J. Heinzen, Phys. Rev. A **A47**, R4567-R4570 (1993).

[97] P.A. Molenaar, P. van der Straten, and H.G.M. Heideman, Phys. Rev. Lett. **77(8)**, 1460 (1996).

[98] M. Monnerville, Thesis, Université Bordeaux I (1991).

[99] M. Monnerville and J. M. Robbe, J. Chem. Phys. **101**, 7580 (1994).

[100] M. Monnerville and J.M. Robbe, Eur. Phys. J. D **5**, 381-387 (1999).

[101] A.P. Mosk, M.W. Reynolds, T.W. Hijmans, and J.T.M. Walraven, Phys. Rev. Lett. **82**, 307 (1999).

[102] E.E. Nikitin and S.Ya. Umanskii. *Theory of Slow Atomic Collisions.* Springer-Verlag, Berlin, (1984).

[103] A.N. Nikolov, E.E. Eyler, X.T. Wang, J. Li, H. Wang, W.C. Stwalley, and P.L. Gould, Phys. Rev. Lett. **82(4)**, 703-706 (1999).

[104] T.F. O'Malley, L. Spruch, and L. Rosenberg, Journ. Math. Phys. **2**, 491 (1964).

[105] J.M. Pérez-Jord'a, Phys. Rev. B **58**, 1230 (1998).

[106] P. Pillet, A. Crubellier, A. Bleton, O. Dulieu, P. Nosbaum, I. Mourashko, and F. Masnou-Seeuws, J. Phys. B **30**, 2801-2820 (1997).

[107] W. Preuss and G. Baumgartner, Z. Phys. A, **320**, 125 (1985).

[108] W.H. Press, S.A. Teukolsky, W.T. Vetterling, and B.P. Flannery, *Numerical Recipes in C*, Second edition, Cambridge University Press, (1995).

[109] L.P. Ratliff, M.E. Wagshul, P.D. Lett, S.L. Rolston, and W.D. Phillips J. Chem. Phys. **101**, 2638-2641 (1994).

[110] S.F. Rice, X. Xie, and R.W. Field, Chem. Phys. **104**, 161 (1986).

[111] A.L. Roche, and J. Tellinghuisen, Mol. Phys. **38**, 129 (1979); Chem. Phys. **104**, 161 (1986).

[112] H. Scheingrager and C.R. Vidal. J. Chem. Phys. **66**, 3694-3704 (1977).

[113] U. Schlöder, H. Engler, U. Schünemann, R. Grimm, and M. Weidemüller, Eur. Phys. J. D **7**, 331-340 (1999).

[114] H. Schmidt-Mink, W. Müller, and W. Meyer, Chem. Phys. Lett. **121**, 49 (1985).

[115] I. Schmidt, W. Meyer, B. Krüger, and F. Engelke, Chem. Phys. Lett. **143**, 353 (1988).

[116] J.P. Shaffer, W.Chalupczak, and N.P.Bigelow, Phys. Rev. Lett. **82(6)**, 1124-1127 (1999).

[117] V. Sidis, Adv. in At., Mol., and Opt. Phys. **26**, 161-208 (1989).

[118] T.E. Simos and G. Mousadis, Mol. Phys. **83**(6), 1145 (1994).

[119] T.E. Simos, Int. J. Quant. Chem **68**, 191 (1998).

[120] F.T. Smith, Phys. Rev. **179**, 111 (1969).

[121] W.C. Stwalley and H. Wang, J. Mol. Spectr. **195**, 194-228 (1999).

[122] T. Takekoshi, B.M. Pattersom, and R.J. Knize, Phys. Rev. Lett. **81**, 5105 (1998); Phys. Rev. A **59**, R5 (1999).

[123] H. Tal-Ezer and R. Kosloff, J. Chem. Phys. **81(9)**, 3967-3971 (1984).

[124] D.J. Tannor, D.E. Weeks, J. Chem. Phys. **98(5)**, 3884-3893 (1993).

[125] E. Tiesinga, C.J. Williams, and P.S. Julienne, Phys. Rev. A **57(6)**, 4257 (1998).

[126] H.R. Thorsheim, J. Weiner, and P. S. Julienne, Phys. Rev. Lett. **58**, 2420 (1987).

[127] I. Tuvi and Y. B. Band, J. Chem. Phys. **107**, 138 (1997).

[128] M. Vatasescu, Thesis, Université Paris XI (1999).

[129] M. Vatasescu, O. Dulieu, C. Amiot, D. Comparat, C. Drag, V. Kokoouline , F. Masnou-Seeuws, and P. Pillet, accepted in Phys. Rev. Let. (2000).

[130] J. Vergès and C. Amiot, J. Mol. Spectrosc. **126**, 393 (1987).

[131] Á. Vibók and G.G. Balint-Kurti, J. Phys. Chem. **96**, 8712-8719 (1992).

[132] Á. Vibók and G.G. Balint-Kurti, J. Chem. Phys. **96**, 7615-7622 (1992).

[133] M. R. Wall and D. Neuhauser, J. Chem. Phys. **93**, 8011 (1995).

[134] C.D. Wallace, T.P. Dinneen , K.-Y.N. Tan, T.T. Grove, and P.L. Gould, Phys. Rev. Lett. **69(6)**, 897 (1992).

[135] H. Wang, P. L. Gould, and W. C. Stwalley, Phys. Rev. A **53**, R1216-R1219 (1996).

[136] H. Wang, P. L. Gould, and W. C. Stwalley, Z. Phys. D**36**, 317-323 (1996).

[137] H. Wang, P. L. Gould and W. C. Stwalley, J. Chem. Phys. **106** 7899-7912 (1997).

[138] X. Wang, H. Wang, P. L. Gould, W. C. Stwalley, E. Tiesinga, and P.S. Julienne, Phys. Rev. A **57**, 4600-4603 (1998).

[139] H. Wang, P. L. Gould, and W.C. Stwalley, Phys. Rev. Lett. **80**, 476 (1998).

[140] H. Wang and W. C. Stwalley, J. Chem. Phys. **108**, 5767 (1998).

[141] D.E. Weeks, D.J. Tannor, Chem. Phys. Lett. **207(4-6)**, 301-308 (1993).

[142] J. Weiner, V.S. Bagnato, S. Zilio, and P.S. Julienne, Rev. Mod. Phys. **71**, 1 (1999).

[143] D.J. Wineland, H.G. Dehmelt, J. Appl. Phys. **46**, 919-930 (1975).

[144] Workshop *Cold Atomic Collisions: Formation of Cold Moleculed=s.* Les Houches, 1999.

[145] Website of the Royal Swedish Academy of Science, http://www.kva.se/

[146] Online Handbook *The Data Analysis BriefBook* http://www.cern.ch /RD11/rkb/AN13pp/

Abstract.

The main goal of the Thesis is the development of theoretical and numerical approaches to the problem of vibrational levels of a diatomic molecule near the dissociation limit and to the problem of collisions between two cold atoms. This work was motivated by numerous recent experimental results on the formation of cold molecules.

In the considered problem, the relative motion of two atoms reaches very large internuclear distances, where the potential is very weak and where the wave function oscillates very slowly. On the other hand, in the internal zone, the wave function oscillates fast. For a solution of this problem, a new method of the Fourier grid representation is proposed. The grid step of the new representation is adapted to the local de Broglie wave length. It is demonstrated that the wave function can be accurately represented using less than two grid points per one oscillation. The method allows to determine positions of *all* bound levels, positions and widths of pre-dissociated levels, long-range wave functions ($> 1000\ a_0$) for the one- or multi-channel potential. The method is applied to the prediction of photoassociation spectra of Cs_2 and Rb_2 and to the interpretation of the experiment of the symmetry breaking in Li_2. The perturbations in the spectra of Rb_2 and Cs_2 are discussed in a frame of the Generalized Quantum Defect Theory.

Keywords

Collisions of cold atoms	Fourier Grid Representation
Photoassociation of cold atoms	Mapped grids
Lon-range vibrational motion	Generalized Quantum Defect Theory
Long-range potential	Lu-Fano plot
Cold molecules	

Résumé.

L'objectif principal de la Thèse est le développement des méthodes théoriques et numériques pour étudier soit les niveaux de vibration d'une molécule diatomique proche de la limite dissociation, soit les collisions entre atomes froids. Ce travail est motivé par de nombreux résultats expérimentaux récents sur la formation de molécules froides.

Dans les problèmes considérés, le mouvement relatif des deux atomes s'étend à de grandes distances internucléaires, où le potentiel est très faible et où la fonction d'onde oscille très lentement, alors que dans la zone interne elle oscille rapidement. Pour résoudre cette difficulté, on a proposé une nouvelle méthode de représentation de grille de Fourier où le pas d'intégration est ajusté sur la longueur d'onde de Broglie locale. On a montré qu'une fonction d'onde peut être représentée avec précision en utilisant moins de deux points par oscillation. La méthode permet de calculer la position de *tous* les niveaux liés, la position et la largeur des niveaux pré-dissociés, des fonctions d'onde très étendues (plus de 1000 a_0) pour un système à une ou plusiers voies. La méthode a été appliquée à la prédiction des spectres de photoassociation de Cs_2 et Rb_2 et à l'interprétation d'une expérience de violation de symétrie dans Li_2. Les perturbations dans les spectres de Cs_2 et Rb_2 sont modélisées dans le cadre de la Théorie de Défaut Quantique généralisé.

Mots-clés

Collisions entre atomes froids
Photoassociation d.atomes froids
Mouvements vibrationnels de grande élongation
Potentiels à long - portée
Molécules froides
Représentation de grille de Fourier
Grilles transformées
Théorie de Défaut Quantique généralisé
Graphiques de Lu-Fano